HEAT CAPACITY MEASUREMENTS OF Sr_2RuO_4 UNDER UNIAXIAL STRESS

You-Sheng Li

A Thesis Submitted for the Degree of PhD
at the
University of St Andrews

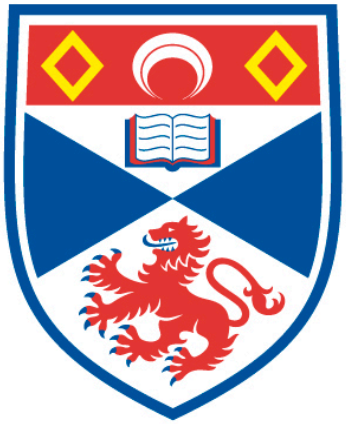

2018

Heat Capacity Measurements of Sr_2RuO_4 under Uniaxial Stress

You-Sheng Li

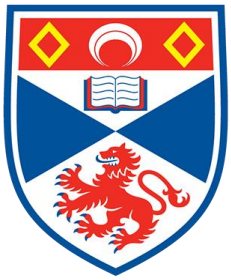

University of
St Andrews

This thesis is submitted in partial fulfilment for the degree of

Doctor of Philosophy (PhD)

at the University of St Andrews

October 2018

Candidate's declaration

I, You-Sheng Li, do hereby certify that this thesis, submitted for the degree of PhD, which is approximately 36,000 words in length, has been written by me, and that it is the record of work carried out by me, or principally by myself in collaboration with others as acknowledged, and that it has not been submitted in any previous application for any degree.

I was admitted as a research student at the University of St Andrews in November 2013.

I received funding from an organisation or institution and have acknowledged the funder(s) in the full text of my thesis.

Date Signature of candidate

Supervisor's declaration

I hereby certify that the candidate has fulfilled the conditions of the Resolution and Regulations appropriate for the degree of PhD in the University of St Andrews and that the candidate is qualified to submit this thesis in application for that degree.

Date Signature of supervisor

Permission for publication

In submitting this thesis to the University of St Andrews we understand that we are giving permission for it to be made available for use in accordance with the regulations of the University Library for the time being in force, subject to any copyright vested in the work not being affected thereby. We also understand, unless exempt by an award of an embargo as requested below, that the title and the abstract will be published, and that a copy of the work may be made and supplied to any bona fide library or research worker, that this thesis will be electronically accessible for personal or research use and that the library has the right to migrate this thesis into new electronic forms as required to ensure continued access to the thesis.

I, You-Sheng Li, have obtained, or am in the process of obtaining, third-party copyright permissions that are required or have requested the appropriate embargo below.

The following is an agreed request by candidate and supervisor regarding the publication of this thesis:

Printed copy

Embargo on all of print copy for a period of 2 years on the following ground(s):

- Publication would preclude future publication

Electronic copy

Embargo on all of electronic copy for a period of 2 years on the following ground(s):

- Publication would preclude future publication

Title and Abstract

- I agree to the title and abstract being published.

Date Signature of candidate

Date Signature of supervisor

Underpinning Research Data or Digital Outputs

Candidate's declaration

I, You-Sheng Li, understand that by declaring that I have original research data or digital outputs, I should make every effort in meeting the University's and research funders' requirements on the deposit and sharing of research data or research digital outputs.

Date Signature of candidate

Permission for publication of underpinning research data or digital outputs

We understand that for any original research data or digital outputs which are deposited, we are giving permission for them to be made available for use in accordance with the requirements of the University and research funders, for the time being in force.

We also understand that the title and the description will be published, and that the underpinning research data or digital outputs will be electronically accessible for use in accordance with the license specified at the point of deposit, unless exempt by award of an embargo as requested below.

The following is an agreed request by candidate and supervisor regarding the publication of underpinning research data or digital outputs:

Embargo on all of electronic files for a period of 2 years on the following ground(s):

- Publication would preclude future publication

Date Signature of candidate

Date Signature of supervisor

Abstract

The most-discussed pairing symmetry in Sr_2RuO_4 is chiral p-wave, $p_x \pm ip_y$, whose degeneracy is protected by the lattice symmetry. When the lattice symmetry is lowered by the application of a symmetry-breaking field, the degeneracy can be lifted, potentially leading to a splitting of the superconducting transition. To lift the degeneracy, the symmetry breaking field used in this study is uniaxial stress. Uniaxial stress generated by a piezo-electric actuator can continuously tune the electronic structure and *in situ* lower the tetragonal symmetry in Sr_2RuO_4.

Previous studies of magnetic susceptibility and resistivity under uniaxial stress have revealed that there is a strong peak in T_c when the stress is applied along the a-axis of Sr_2RuO_4. In addition, it has been proposed that the peak in T_c coincides with a van Hove singularity in the band structure, and measurements of H_{c2} at the maximum T_c indicate the possibility of an even parity condensate for Sr_2RuO_4 at the peak in T_c.

In this thesis, the heat capacity approach is used to study the thermodynamic behavior of Sr_2RuO_4 under uniaxial stress applied along the crystallographic a-axis of Sr_2RuO_4. The first thermodynamic evidence for the peak in T_c is obtained, proving that is a bulk property. However, the experimental data show no clear evidence for splitting of the superconducting transition; only one phase transition can be identified within the experimental resolution. The results impose strong constraints on the existence of a second phase transition, i.e. the size of the second heat capacity jump would be small or the second T_c would have to be very close to the first transition. In addition to these results, I will present heat capacity data from the normal state of Sr_2RuO_4. The experimental results indicate that there is an enhancement of specific heat at the peak in T_c, consistent with the existence of the van Hove singularity. The possibility of even parity superconductivity at the maximum T_c has also been investigated. However, the heat capacity measurements are shown to be relatively insensitive to such a change, so it has not been possible to obtain strong and unambiguous evidence for whether it takes place or not.

Acknowledgements

I would like to express my sincere gratitude to people who helped and supported me during my PhD study at University of St Andrews and, mostly, at the Max Planck Institute for Chemical Physics of Solids in Dresden.

First and foremost I would like to thank my supervisor Andrew Mackenzie, who offer guidance and support during my time as student. I am amazed by his physical insight and I have learned a lot during discussions with him. He also gave me great opportunity to attend conferences and summer schools, which did broaden my horizons. This is the world I could have not imagined. This projected was also supervised by Michael Nicklas and Clifford Hicks. Michael Nicklas introduced me the knowledge of heat capacity measurements and gave me many good advices on the experiments. This new technique would have not been possible without the strain apparatus designed by Clifford Hicks. I appreciate his effort and I learned many important knowledge of design rules as well as strain measurements from him. I benefited a lot from having discussions with all of them. I would also like to thank them for giving me the chance to explore the ideas in my way.

This project would have not been possible without the help from a number of great people. I thank Alexandra Gibbs, Yoshiteru Maeno and Naoki Kikugawa, who provided the excellent single crystals for my study. I would like to thank Robert Borth, who helped me solve the technical problems and who introduced me low temperature techniques. I appreciate the help from Ulrike Stockert, who helped me calibrate the thermocouple and analyze the data. I improved my Labview skill by learning from Thomas Lühmann and Moritz Besser. I learned the Laue diffraction from Dmitry Sokolov. I appreciate the help from Mark Barber, Daniel Brodsky, Alexander Steppke and Lishan Zhao, who shared their knowledge on strain techniques and sample preparations. The technical staffs in the cryogenics service as well as the mechanical and electric workshops offered great supports. This project, especially, heavily relies on the constant supply of the liquid helium. I am grateful for their hard work and effort to keep everything running smoothly. The administrative staffs in St Andrews and Dresden are very helpful. I would like to thank Claudia Strohbach, Petra Laqua and Uta Prautzsch in Dresden and Julie Massey, Christine Edwards and Wendy Clark in St Andrews for their excellent support during my time on both places. There are too many to list explicit here but I thank all my colleagues for their help, advice and friendship.

I would like to take this opportunity to give a special thanks to Yen-Chun Fu, whose support, encouragement and understanding are invaluable. Finally, I would like to thank my family, who support me to pursue what I would like to do.

Funding

This work was supported by the St Leonard's scholarship, the Engineering and Physical Sciences Research Council via the Scottish Condensed Matter Centre for Doctoral Training under grant EP/G03673X/1, and the Max Planck Society.

Research Data access statement

Research data underpinning this thesis are available at **https://doi.org/10.17630/464447c9-ac13-4a06-8a1a-e495cfd45f00**

Table of Contents

Chapter 1 Introduction

Superconductivity, known for the ability to carry current without loss and the ability to expel magnetic flux, is one of the most fascinating phenomena in nature. It was discovered in 1911 by Heike Kamerlingh Onnes [1], who observed in mercury a sudden drop in the resistance to a value below the experimental detection limit at a temperature near 4.2 K. Meissner and Ochsenfeld in 1933 [2] discovered that magnetic flux was expelled from a superconductor when it went into the superconducting state in the presence of a magnetic field. The first 70 years of research on superconductors resulted in the discovery of low temperature superconductors. A breakthrough happened when Bednorz and Müller discovered $La_{2-x}Ba_xCuO_4$ in 1986 with a superconducting transition temperature (T_c) of approximately 30 K [3]. Shortly afterwards, T_c = 92 K, beyond the liquid nitrogen temperature, was found in $YBa_2Cu_3O_{7-\delta}$ [4], motivating scientists to look for higher T_c materials. T_c in this family of the superconductors, cuprate superconductors, has reached about 130 K at ambient pressure [5] and about 160 K under external pressure [6]. In addition to cuprate superconductors, heavy fermion superconductors [7]–[10] and iron-based superconductors [11]–[16] were also found.

The microscopic picture of superconductivity remained a puzzle until Bardeen-Cooper-Schrieffer (BCS) theory was proposed in 1957 [17]. Prior to the BCS theory, L. N. Cooper had demonstrated that two electrons with opposite spins in the presence of the Fermi surface with any arbitrarily weak attractive interaction are paired to form a bound state or a Cooper pair. In BCS theory, the Cooper pairs form a coherent collective state with a superconducting gap which acts as a macroscopic quantum object. Conventional superconductors can be described by BCS theory well.

In the BCS theory, the Cooper pairs are electrons paired with opposite spins but, in general, electrons with equal spin pairing are also possible. Thus, the Cooper pairing symmetry can be divided into two categories if the spin-orbital interaction is weak and the lattice preserves the inversion symmetry—spin singlet and spin triplet. Since electrons are fermions, the pair wave function needs to be antisymmetric under the parity operation. The orbital part of the pair wave function has the parity of $(-1)^l$ according to the angular quantum number l. Consequently, the spin singlet state is associated with orbital states whose angular quantum number is even ($l = 0, 2,$ etc. and traditionally they are labelled as $s, d,$ etc.), whereas the spin triplet states are associated with orbital states whose angular quantum number is odd ($l = 1, 3,$ etc. and traditionally they are labelled as $p, f,$ etc.). The early discovered superconductors such as lead and niobium were *s*-wave superconductors or 'conventional' superconductors in which the attraction came from the

electron-phonon interaction. Superconductors having non *s*-wave pairing symmetry are unconventional. One of the famous examples is the cuprate superconductors. Many of them have been demonstrated to have *d*-wave pairing [18]. However, the conventional electron-phonon mechanism cannot account for the formation of Cooper pairs in this type of material. Thus, the mechanism for the cuprate superconductors is still actively debated even after three decades of research. Up until now, most of the discovered superconductors have spin singlet Cooper pairing. Only a few of them are thought to have spin triplet order parameters. Strontium ruthenate (Sr_2RuO_4) [19] is one of these exceptional superconductors, and was proposed to be a *p*-wave superconductor as long ago as 1995 [20]. Since then, considerable experimental and theoretical research has been performed in an effort to understand its pairing symmetry but it is still actively debated.

In parallel to the discovery of the new superconductors, the development or improvement of experimental techniques enables new physics to be accessed. Strain or stress techniques are prominent examples since they can change the electronic structure of materials. In the case of superconductors, the superconducting transition temperature can be changed dramatically. The T_c of FeSe under hydrostatic pressure can be raised from 8 K up to 37 K [21]. More strikingly, it has been discovered in the past few years that H_2S under hydrostatic pressure of 150 GPa has superconducting transition at 203 K [22]. Strain can also be introduced by the lattice mismatch between the substrate and the deposited material. J.-P. Locquet *et al.* [23] demonstrated that the T_c of $La_{1.9}Sr_{0.1}CuO_4$ was increased from 25 K to 49 K by epitaxial strain. In this study, the technique used is uniaxial stress, which is a directional probe, in contrast to the hydrostatic pressure and epitaxial strain.

Uniaxial stress can distort the lattice in a chosen direction, and changes the overlap of the electron orbitals between the neighboring sites. In strongly correlated materials, electrons are not free-electron-like but, instead, they hop from one site to the next. Electronic structure is strongly influenced by the overlap between the nearest neighbor sites. Therefore, uniaxial stress can have strong effect on these materials. For example, a typical band width for a strongly correlated material could be several eV. Distorting the lattice by 1% would cause approximately 1% change in the band width which is about 10 meV every 1 eV. This 10 meV scale is equivalent to a thermal energy of about 120 K or Zeeman splitting under a magnetic field of about 170T.

Uniaxial stress can lower the lattice symmetry and lift the point group symmetries. In a superconductor, the order parameter symmetry is associated with this point group symmetry. For example, a superconductor having the property of breaking time reversal symmetry has a complex order parameter, which requires two degenerate states protected by the symmetry of the lattice. This degeneracy will be lifted when the lattice symmetry is lowered by means of the symmetry-breaking field, leading to a split of the superconducting transition.

In this study, I will investigate Sr_2RuO_4, which, as well has being *p*-wave, has been postulated to break time reversal symmetry in the superconducting state [24], [25], suggesting that it has a

complex and degenerate order parameter. My aim is to lift the degeneracy, by applying uniaxial stress along the *a*-axis, while studying the heat capacity. However, this presents considerable experimental difficulties because of the very strong thermal coupling of the sample to the uniaxial stress apparatus. Therefore, the first challenge is to develop a feasible method of heat capacity measurement under such strongly non-adiabatic conditions. Besides, the proposed splitting of the superconducting transition could be small. Hence, the second challenge is to increase the experimental resolution for detecting small features in the heat capacity. I will detail these technical challenges, describe what has been achieved and present the results and discussions in the following chapters.

In Chapter 2, I will briefly review the physical properties of Sr_2RuO_4 in the normal state and in the superconducting state. Then, I will discuss the effect of the uniaxial stress when the lattice symmetry is lowered and review the recent uniaxial stress experiments which motivate this research work.

In Chapter 3, I will describe the heat capacity measurements under uniaxial stress. I will demonstrate how to perform measurements under strongly non-adiabatic conditions. Before showing the measurements under uniaxial stress, I will introduce the working principle of the strain apparatus. Then, I will describe an important approach to measure the heat capacity purely from the homogeneous part of the sample when it is under uniaxial stress. The second challenge of this study was to increase resolution for probing small features. Therefore, I will describe several issues and the achievements on the sample preparation and measurement configurations.

In Chapter 4, I will present the results of the heat capacity measurements of Sr_2RuO_4 under uniaxial stress. The main purpose of these measurements was to look for a possible signature of a splitting of the superconducting transition after the lattice symmetry was lowered by the application of uniaxial stress. In addition, the previous uniaxial stress experiments using electrical resistivity and magnetic susceptibility approaches have raised two further questions, which are connected to the existence of a van Hove singularity and the possibility of a pairing symmetry change in strained Sr_2RuO_4. I will discuss these issues in light of the measured data.

Finally, I will close with chapter 5, in which I will present my conclusions on this technique and the experimental results. In addition, I will point out possible future works on Sr_2RuO_4 and related materials.

Chapter 2 Sr_2RuO_4

2.1 Introduction

In the thesis, I focus on strontium ruthenate Sr_2RuO_4, which is proposed to be one of the unconventional superconductors. This compound was discovered by Maeno *et al.* in 1994 [19]. Although it shares the same crystal structure as the cuprates which were discovered by Bednorz and Müller [3], its T_c is far smaller than that in cuprates and its pairing symmetry is believed to be different from that in the cuprates as well. It has been proposed to be a candidate for *p*-wave superconductivity by Rice and Sigrist [20], who made an analogy to the superfluid ^{3}He, a well-established p-wave in atomic Cooper pairing. Since then, many research works have been made experimentally and theoretically to try to unveil the physical properties of Sr_2RuO_4. The normal state properties are well established. It is a Fermi liquid and its band structure has been understood accurately and precisely. However, the symmetry of the Cooper pairing is still under debate. In the following I will briefly introduce the normal state properties of Sr_2RuO_4 and then move on to the superconducting state properties. With the knowledge of the superconducting order parameter in Sr_2RuO_4, the effect of a symmetry-breaking field can be introduced. I will introduce the theoretically proposed effect on the order parameter of Sr_2RuO_4 under uniaxial stress and then describe the existing experiments which motivate this research work.

2.2 Normal state properties

Figure 2.1 shows the crystal structure of Sr_2RuO_4. It is a body-centered tetragonal lattice with a = 3.862Å, c = 12.722 Å. Similar to the cuprates, this material is highly two-dimensional. Figure 2.2 shows the in-plane and out-of-plane resistivity as function of temperature. It is much more highly conductive in the RuO_2 planes than perpendicular to them. Both the in-plane resistivity ρ_{ab} and out-of-plane resistivity ρ_c show metallic behavior and follow the form of $\rho_0 + AT^2$ at temperatures below 30 K. The resistivity anisotropy $\rho_{0,c}/\rho_{0,ab} > 1000$. The T^2-dependence is a characteristic behavior of a Fermi liquid. In addition, the *T*-linear coefficient γ in specific heat and of the spin susceptibility χ_s are strongly enhanced at low temperature, suggesting an enhancement of quasiparticle mass, also consistent with Fermi liquid theory [26].

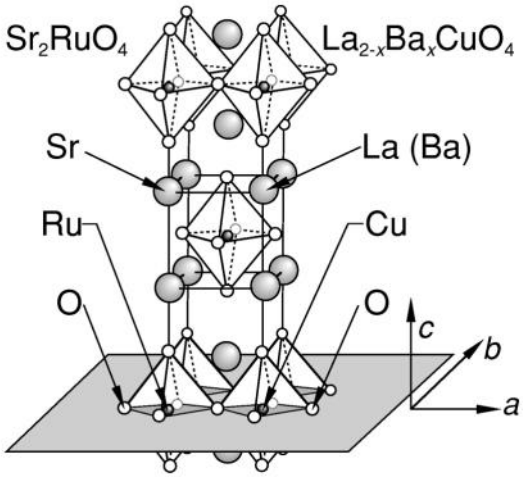

Figure 2.1: The layered perovskite structure of Sr_2RuO_4, which has the same structure as $La_{2-x}Ba_xCuO4$. Reproduced from [27].

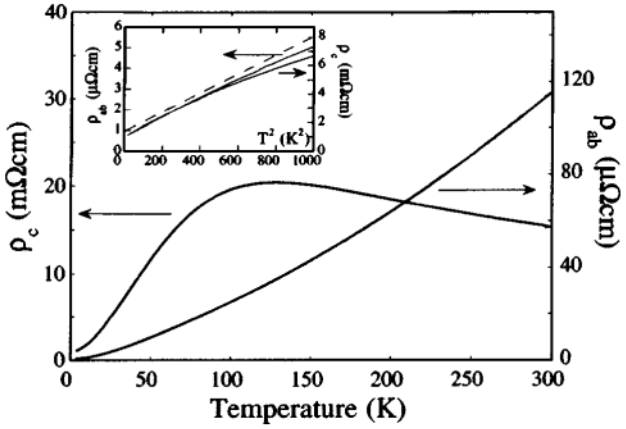

Figure 2.2: The *ab*-plane and *c*-axis resistivity data for Sr_2RuO_4. The inset shows ρ_{ab} and ρ_c as a function of T^2 in the low temperature range. The dashed line is a guide for the T^2 dependence. Reproduced from [28].

Band structure

In Sr_2RuO_4, the electrons hop primarily within the Ru-O layer and the coupling between the layers is weak. This leads to a weak dispersion of the energy bands along the k_z-direction so the band structure is quasi-two-dimensional. The electronic states come from Ru 4*d* orbitals. Ru is sitting in octahedra formed by oxygens atoms. The crystal field in this environment splits the five degenerate *d* states into higher e_g states $(d_{x^2-y^2}, d_{z^2})$ and low-lying t_{2g} states (d_{xy}, d_{xz}, d_{yz}) in which four valence electrons are distributed. The d_{xz} orbitals lie mostly in the *xz*-plane. The overlaps are mainly between the nearest neighbors along the *x*-axis. The band dispersion depends mainly on k_x and forms an open Fermi sheet perpendicular to the k_x-axis. Similarly, d_{yz} forms an open Fermi sheet perpendicular to k_y-axis. d_{xz} and d_{yz} hybridize and form α and β sheet as shown in Figure 2.3(b). In contrast, d_{xy} orbitals overlap not only between near neighbors on both *x*- and *y*-axis but also between the next nearest neighbors since the lobes are aligned along the diagonal directions. Therefore, the d_{xy} based band forms a cylinder-like Fermi sheet denoted as γ-sheet shown in Figure 2.3(a).

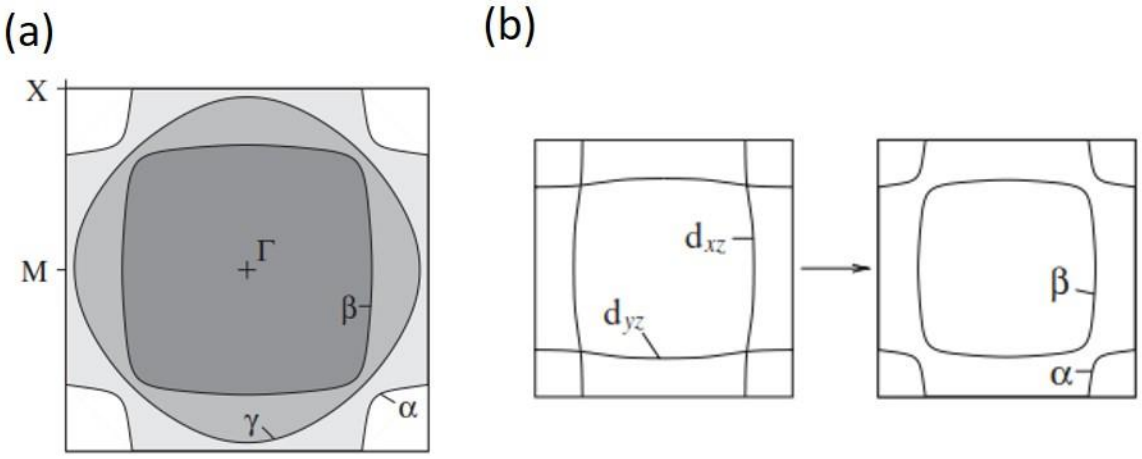

Figure 2.3: (a) A sketch of the Fermi Surfaces in Sr_2RuO_4. (b) The d_{xz} and d_{yz} orbitals hybridize to form α and β sheets. Reproduced from [29].

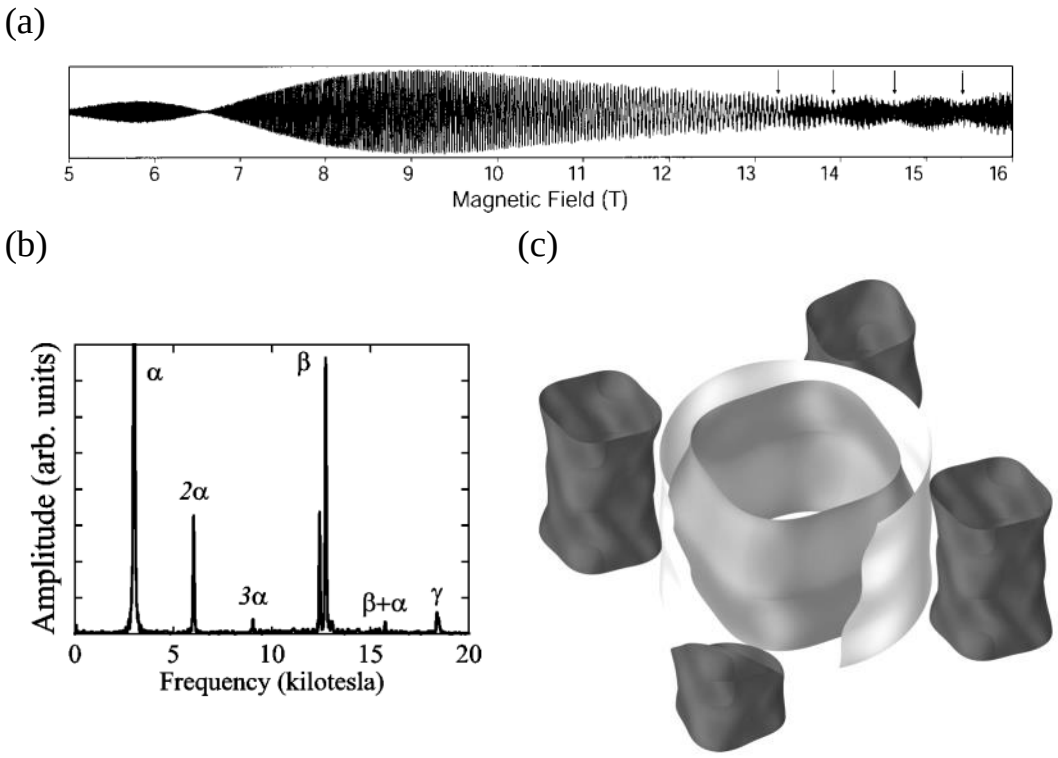

Figure 2.4: (a) Typical dHvA quantum oscillation data from a pure Sr_2RuO_4 single crystal. Reproduced from [30]. (b) Fourier transformation of the dHvA data showing three fundamental frequencies which are related to α, β and γ Fermi sheets. Reproduced from [31] (c) The Fermi surfaces determined by quantum oscillations. The corrugation due to k_z dispersion is exaggerated by a factor of 15 for clarity. The square cylinder in the center is the β sheet which is surrounded by the γ sheet, the circular cylinder, and the α sheet is shown by the four dark cylinders at corners. Reproduced from [27] based on [29].

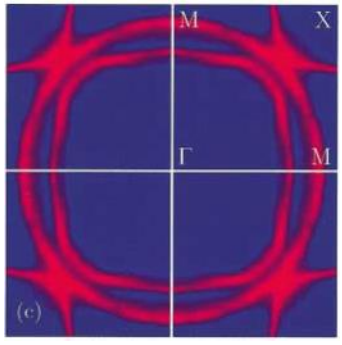

Figure 2.5: The Fermi surfaces of Sr_2RuO_4 measured by ARPES. Reproduced from [32].

Angle-resolved photoemission spectroscopy (APRES) and quantum oscillations can probe the Fermi surfaces. The former is surface sensitive and the latter is bulk sensitive. Figure 2.4(a) show typical de Haas van Alphen (dHvA) oscillations as a function of magnetic field. Landau levels passing successively through the Fermi surface cause oscillations of the density of states at the Fermi energy. The fundamental oscillation frequencies from each Fermi sheet can be retrieved after Fourier transformation as shown in Figure 2.4(b). In a more detailed angular dependence study by C. Bergemann *et al*.[30]., the weak k_z dispersion on the Fermi surfaces could be resolved in great details. Figure 2.4(c) shows the Fermi surfaces deduced by the dHvA measurements, which consists of three quasi-two-dimensional Fermi sheets α, β and γ with corrugations along the k_z-direction. This basic topography is confirmed by the APRES measurements [32] as shown in Figure 2.5. An important feature of the Sr_2RuO_4 band structure is that the γ-sheet is in proximity to the van Hove singularity (vHS) at the M-point of the Brillouin zone. Replacing Sr^{2+} in Sr_2RuO_4 with La^{3+} gives extra electrons, raising the filling at the Fermi level. By doping La-atoms into Sr_2RuO_4, the γ-sheet can be forced to reach the vHS. APRES results on $Sr_{2-y}La_yRuO_4$ indicate that the vHS is ≈14 meV above the Fermi energy [33].

2.3 Superconductivity of Sr_2RuO_4

2.3.1 Non-magnetic impurity effect on superconductors

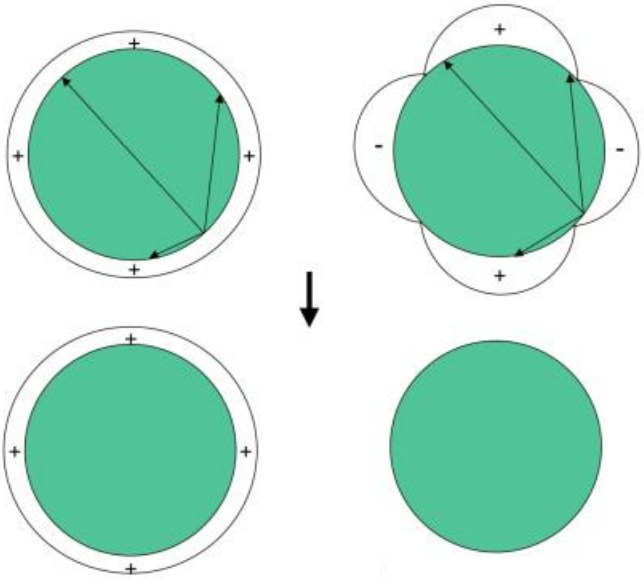

Figure 2.6: Illustrations for s- and d-wave superconductors under strong elastic scattering due to impurities in the crystal lattice. Reproduced from [27].

One way to distinguish whether a superconductor is unconventional or not is the non-magnetic impurity effect. Impurities in the lattice cause elastic scattering and can lead to a strong suppression of T_c in unconventional superconductors but little or no effect in conventional superconductors. Figure 2.6 shows sketches of a conventional (*s*-wave) and an unconventional (*d*-wave) superconductor undergoing strong elastic scattering, which mixes all *k*-states on the Fermi surface and gives an average on the superconducting gap. In an isotropic *s*-wave case, the strong scattering does not change the amplitude of the superconducting gap because the phase is the same around the Fermi surface. However, in the *d*-wave case, the strong scattering averages the superconducting gap to zero, causing a strong suppression of T_c, because the phase is different between the adjacent lobes. More generally, the non s-wave order parameter for unconventional superconductors vanishes under strong *k*-space averaging and gives a strong suppression of T_c because the phase varies around the Fermi surface and, as a result, the summation of the superconducting gap over the Fermi surface is zero.

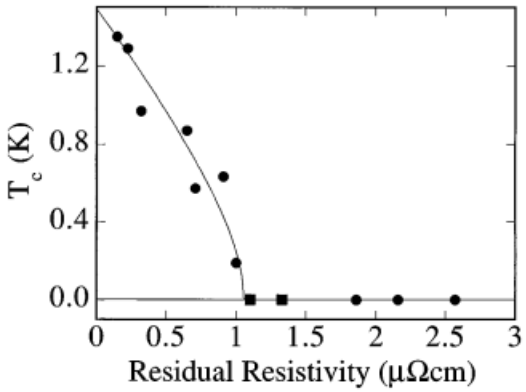

Figure 2.7: The impurity effect on Sr_2RuO_4. The superconducting transition T_c is plotted as a function of the residual resistivity for single crystals with different impurity levels. The solid line is a fit to the data based on the Abrikosov-Gor'kov pair-breaking function. Reproduced from [34].

Mackenzie *et al*. [34] studied the non-magnetic impurity effect on Sr_2RuO_4. Figure 2.7 shows T_c as a function of the residual resistivity for different single crystals with different levels of impurities. T_c is strongly suppressed with an increase of the residual resistivity. To observe superconductivity, a residual resistivity less than 1 μΩcm is needed. The solid line is a fit to the data based on the Abrikosov-Gor'kov pair-breaking function and indicates that the optimal T_c in the clean limit is 1.5 K. The strong suppression of T_c to zero on increasing the impurity level suggests that Sr_2RuO_4 is an unconventional superconductor.

2.3.2 Nuclear magnetic resonance Knight shift

A Cooper pair is composed of two electrons whose spin state (for weak spin-orbit coupling and lattice with inversion symmetry) is either spin singlet or spin triplet. A direct approach to probe the spin configuration is to measure spin susceptibility χ_s in the superconducting state. In a metal, when magnetic field is applied, the Fermi surface is polarized due to the Zeeman splitting. The energy of spin-up electrons is lowered by $\mu_B H$ whereas that of the spin-down electrons is raised by $\mu_B H$. In a spin-singlet superconductor, electrons are paired with opposite spin ($k\uparrow, -k\downarrow$) when it goes into the superconducting state. When a spin-polarized metal goes into a spin-singlet superconducting state, the superconducting condensation energy and the Zeeman splitting energy compete with each other. At low temperatures and small applied field, the condensation energy overpowers the Zeeman splitting and thus the susceptibility χ_s goes to zero. In a spin-triplet superconductor, Cooper pairs can be paired with equal spin and in this case they are exempted from

the pair-breaking mechanism by the Zeeman splitting. Therefore, the spin susceptibility remains the same across T_c.

A convenient way to study susceptibility is usually to use a SQUID magnetometer. However, the Meissner effect cancels out the applied field by generating screening currents on the surface of the superconductor. In type I superconductors, no field can penetrate inside in an ideal case. In type II materials, vortices can thread though the superconductor if the applied field exceeds H_{c1} but the signal is still dominated by screening currents. To avoid this effect, the nuclear magnetic resonance (NMR) Knight shift, K_s, can be used to study the spin susceptibility χ_s because K_s is proportional to χ_s.

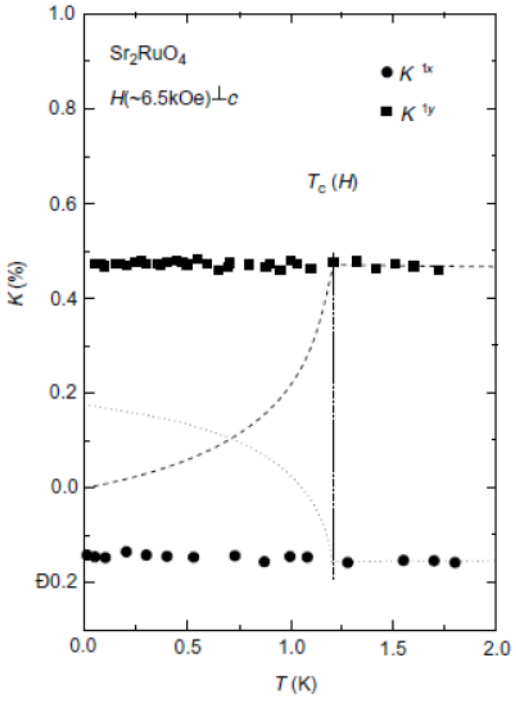

Figure 2.8: NMR Knight shift as a function of temperature for the different oxygen sites at low temperatures. The broken lines indicate the expected responses for the spin-singlet $d_{x^2-y^2}$ state. Reproduced from [35].

K. Ishida *et al*. [35] performed a NMR Knight shift measurements on Sr_2RuO_4 as shown in Figure 2.8. The broken lines are the expected curves for the spin singlet $d_{x^2-y^2}$ state. The NMR Knight shift remains unchanged across T_c and clearly shows that Sr_2RuO_4 is a spin-triplet superconductor.

2.3.3 Time reversal symmetry breaking

If a material breaks time reversal symmetry (TRS), there is a spontaneous magnetic field built in. In a superconductor, if it breaks TRS, magnetic moments develop in the domains but the Meissner effect will compensate this magnetic response and thus there is no net magnetic field inside a superconductor. However, in real materials, there are imperfections, e.g. impurities, vacancies, surfaces, etc., so the screening due to Meissner effect is not perfect and thus there is still expected to be a small detectable signal.

Muon Spin Relaxation (μSR)

The life time of a muon is about 2.2 μs. When a muon is implanted into a material, it interacts with the local magnetic field and decays with a positron in the direction correlated with the spin direction of the muon. The local magnetic field information can be analyzed by recording the positron emission direction as function of time, because the muon spin precesses in the local magnetic field.

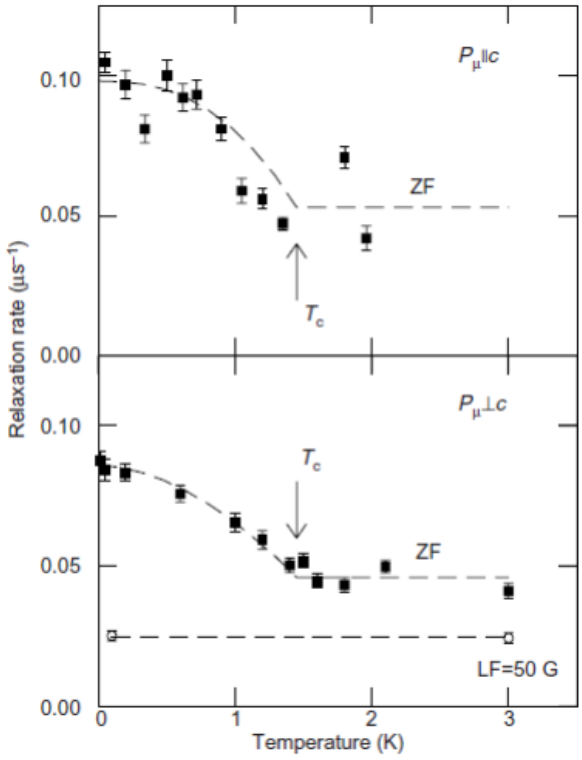

Figure 2.9: Zero-field muon spin relaxation for the muon spin polarization $P_{\mu||c}$ (top) and $P_{\mu\perp c}$ (bottom). T_c is indicated by arrows. The open circles in the bottom panel are the data for the

relaxation rate under a magnetic field of 50 G applied perpendicular to the *c* axis. Reproduced from [24].

The first μSR study on Sr_2RuO_4 was performed by G. M. Luke *et al.* [24]. Figure 2.9 shows the μSR precession rate as a function of temperature for the muon spin polarization $P_{//c}$ (top panel) and $P_{//\perp c}$ (bottom panel). The T_c's determined by *in situ* susceptibility measurements are indicated by arrows in both panels. The onset of a gradually increase in relaxation rate is coincident with T_c in both polarizations. It means that there is a spontaneous magnetic moment developing below T_c. The open circles in the bottom panel are measurements under magnetic fields $H_{\perp c}$ of 50G. The relaxation rate is reduced, indicating that the magnetic moment is static on the order of micro-seconds. These results suggest that TRS is broken in the superconducting state.

Polar Kerr effect

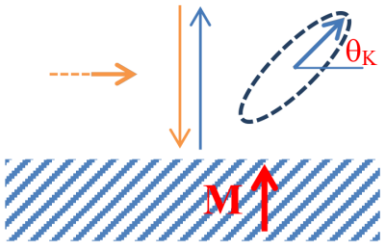

Figure 2.10: A schematic diagram of the polar Kerr effect. When a light is incident on a magnetic material, the linear polarized light is reflected as elliptical light with a rotation angle θ_k, which is known as Kerr angle.

Another approach to study TRS breaking is to measure the Kerr rotation as shown in Figure 2.10. When linearly polarized light is incident on a material with a magnetic moment *M*, the reflected light is polarized elliptical with a rotation angle given by the Kerr angle θ_K, whose value is related to the magnetic moment in the sample.

Jing Xia *et al.* [25] studied the polar Kerr effect on Sr_2RuO_4 as shown in Figure 2.11. They measured both the Kerr angle and in-plane resistivity. T_c from the in-plane resistivity coincides with the onset of the Kerr rotation. The Kerr angle (on the left) is rotated when the sample becomes superconducting (on the right). The dashed line is a fit of a BCS-like temperature dependence. The increase of the Kerr angle below T_c suggests that a magnetic moment appears in the superconducting state and that the TRS is broken.

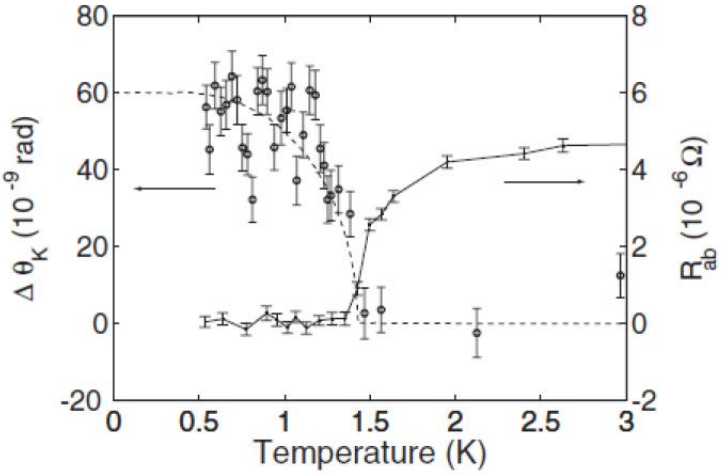

Figure 2.11: Temperature dependences of the polar Kerr rotation and the resistance. Reproduced from [25].

2.3.4 The chiral *p*-wave $p_x \pm ip_y$ state

The vanishing T_c in the impurity effect shows that Sr_2RuO_4 is an unconventional superconductor. The spin susceptibility remaining unchanged across T_c in NMR Knight shift suggests that the Cooper pairing in Sr_2RuO_4 is spin triplet. Both μSR (zero field) and Kerr rotation show an increase below T_c, suggesting that a magnetic moment appears below T_c and that TRS is broken in the superconducting state. There are a number of possible choices for spin triplet order parameters, as listed in ref. [27]. However, the most discussed pairing symmetry in Sr_2RuO_4 is the chiral *p*-wave $p_x \pm ip_y$ or, in terms of the *d*-vector notation appropriate for triplet order parameters,

$$\boldsymbol{d} = \Delta_0(k_x \pm ik_y)\hat{\boldsymbol{z}} \tag{2-1}$$

On a single circular Fermi surface, the magnitude of this order parameter is isotropic $\Delta_0\sqrt{k_x^2 + k_y^2}$, which is the same as that of a s-wave order parameter, but its phase varies continuously with the polar angle ϕ. The term chirality comes from picking up a different phase $\pm\phi$ around the Fermi surface. The orbital part $k_x \pm ik_y$ has states with $L_z = \pm 1$ and $\hat{\boldsymbol{z}}$ represents the spin state having superposition of states $|\uparrow\uparrow\rangle$ and $|\downarrow\downarrow\rangle$. Figure 2.12 shows a sketch of Cooper pairs for $\boldsymbol{d} = \Delta_0(k_x \pm ik_y)\hat{\boldsymbol{z}}$. The large arrows denote the direction of $\boldsymbol{d}$ or L_z and the small arrow denotes the direction of the spins.

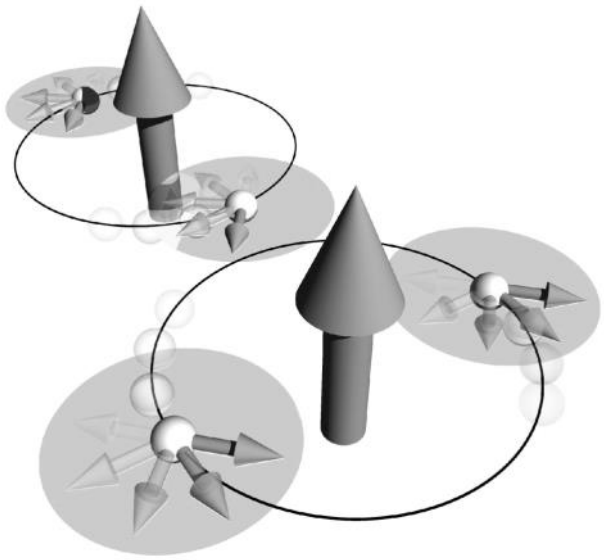

Figure 2.12: A sketch of Cooper pair for $\boldsymbol{d} = \Delta_0(k_x \pm ik_y)\hat{\boldsymbol{z}}$. Reproduced from [27].

2.3.5 Heat capacity

Heat capacity is an essential approach to study the thermodynamic properties of superconductors because they have a phase transition at T_c. In conventional superconductors, the order parameter is s-wave which is nodeless. Around a circular Fermi surface, an isotropic gap[1] opens below T_c. To excite a quasiparticle, it takes energy to overcome this superconducting gap. At very low temperature, the superconducting gap is fully opened and the thermal energy is smaller than the gap. As a result, the number of thermally excited quasiparticles become exponentially small and the heat capacity at very low temperature depends exponentially on temperature. In addition, the heat capacity jump $\Delta C/C$ at T_c in a weak coupling limit is 1.43, which can be derived by the BCS theory [36]. In nodal superconductors, there are nodes at certain directions. For example, in a $d_{x^2-y^2}$-wave material, there are nodes at ±45° and ±135°. Quasiparticles can be thermally excited at nodal directions regardless of how low the temperature is and, thus, the heat capacity displays a power-law behavior. The exponent of temperature T differs depending on the nodal structure. Equation (2-2) describes the heat capacity as a function of T at very low temperature for different gap structures [37].

$$\left.\frac{C_s}{C_n}\right|_{T\to 0} \sim \begin{cases} \exp\left(-\frac{\Delta}{T}\right), \text{isotropic gap} \\ T^2, \text{gap with point nodes} \\ T, \text{gap with line nodes} \end{cases} \tag{2-2}$$

[1] $p_x \pm ip_y$ and $d_{x^2-y^2} \pm id_{xy}$ also give an isotropic gap on a simple circular Fermi surface.

Therefore, heat capacity measurements can give important information on the gap structures depending on the low temperature behaviors, although it should be noted that the powers quoted above are in the extreme clean limit, and can change in the presence of disorder [37].

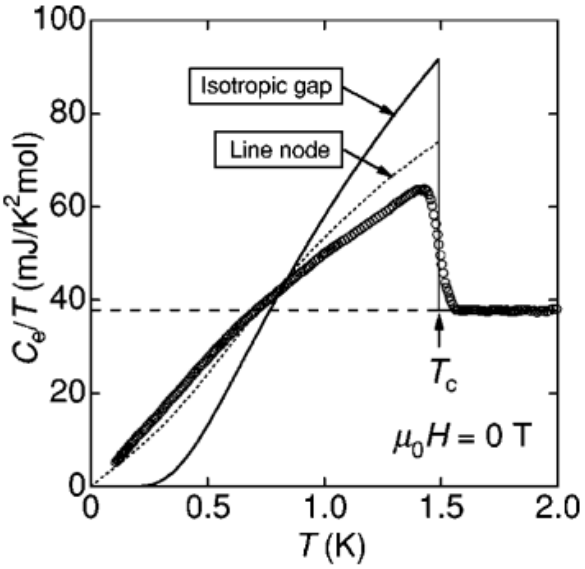

Figure 2.13: Electronic heat capacity of Sr_2RuO_4 with T_c = 1.48 K for H = 0 T. The solid line and the dotted lines show the predictions for an isotropic gap and a gap with line nodes in the cylindrical Fermi surface respectively. Reproduced from [27].

Heat capacity measurements on Sr_2RuO_4 have been reported by many authors but one of the most cited results is that obtained by S. Nishizaki *et al*.[38]. Figure 2.13 shows their electronic specific heat data and the predictions for an isotropic gap (solid line) and a gap with line nodes on a cylindrical Fermi surface (dotted line). No indication of exponential behavior was observed down to the lowest achievable temperature. Instead, C_e/T exhibits a linear T dependence, suggesting the existence of line nodes on the Fermi surface. The predicted curves, none of which fit to the data, are based on a single band calculation. However, Sr_2RuO_4 is a multi-band material which complicates the superconducting properties. The isotropic gap in chiral *p*-wave order parameter is based on a simple circular Fermi surface. In the real situation, the density of states varies in all three bands and the interactions in these bands are complicated, so nodes or gap minima can happen at certain positions in k-space. Figure 2.14 shows the results of calculations for the chiral *p*-wave order parameter [39], [40]. The calculated C/T agrees well compared with the experimental data. The heat capacity is dominated by the γ sheet and the nodes on the β sheet and the gap minima on the α sheet lead to the linear T dependence in the low temperature range. Figure 2.15 shows another possible configuration for the chiral *p*-wave order parameter in Sr_2RuO_4 based on weak-coupling calculations [41]. For the calculation there are again nodes or gap minima on the β sheet.

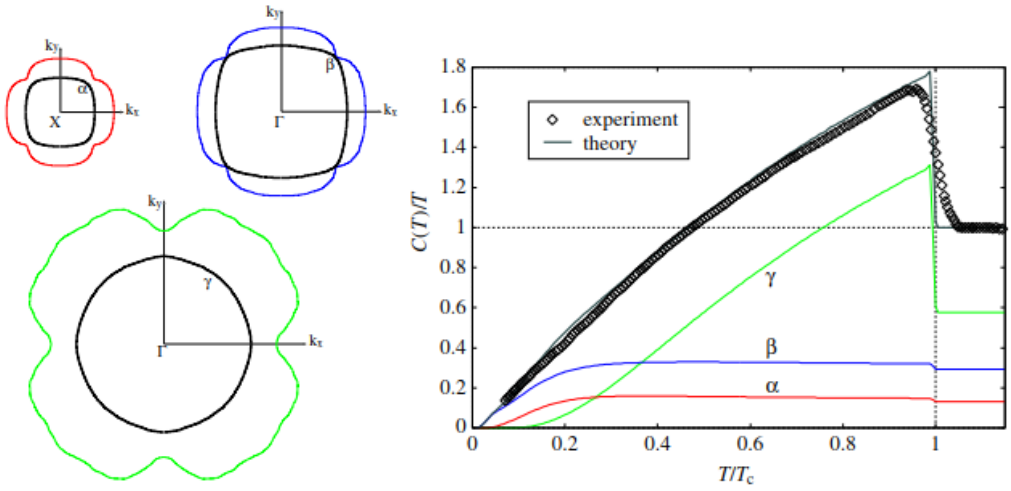

Figure 2.14: (a) The predicted gap magnitudes on the three Fermi surfaces. The black solid lines represent the Fermi surfaces. The colored lines represent the dependence of the gap magnitudes around the Fermi surfaces. (b) The calculated C/T compared to the experimental data. Reproduced from [42] based on [39], [40].

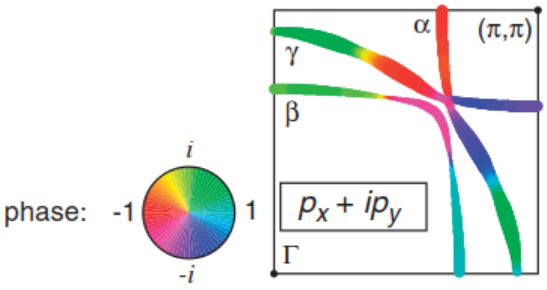

Figure 2.15: Weak-coupling calculations for the chiral *p*-wave order parameter in Sr_2RuO_4. Reproduced from [41].

2.3.6 Some discrepancies with the chiral *p*-wave interpretation and other possible pairing symmetries

Phase sensitive experiments can provide important information about the order parameter of the unconventional superconductors. It is well known that the cuprate superconductors belong to $d_{x^2-y^2}$-wave class of order parameter [18]. Many experiments suggest the existence of nodes but that alone is not sufficient to prove a $d_{x^2-y^2}$-wave order parameter because it could also be an anisotropic *s*-wave order parameter with very deep minima. To solve this issue, phase sensitive experiments are needed. In $YBa_2Cu_3O_{7-\delta}$, corner junctions [43] and tri-crystal rings [44] have shown that the order parameter is dominantly *d*-wave. Later, J. R. Kirtley *et al*. [45] used angle-resolved phase-sensitive techniques to determine the detailed pairing symmetry in $YBa_2Cu_3O_{7-\delta}$. In principle, the same procedures could also be applied to Sr_2RuO_4. However, most of the techniques are based on thin films. For Sr_2RuO_4, it is very challenging to obtain superconducting thin films because T_c is very sensitive to impurities. K. D. Nelson *et al*. [46], instead, used a single crystal to perform Josephson interferometry with a SQUID geometry, a circuit including a superconducting loop interrupted by two Josephson junctions. The superconducting loop was composed of a conventional superconductor $Au_{0.5}In_{0.5}$ and a Sr_2RuO_4 single crystal with junctions on the (100) and (-100) faces. A π-phase difference was observed in their SQUID device, consistent with the expectations for a $p_x \pm ip_y$ order parameter. Later, Žutić and Mazin [47] pointed out that $d_{xz} \pm id_{yz}$ order parameter is consistent with this experimental result as well, because small misalignments could happen during the junction fabrication process.

Heat capacity measurements show a linear T dependence in the low temperature as mentioned above. Another interpretation is the existence of the *symmetry protected* line nodes. E. Hassinger *et al*. [48] by thermal conductivity approach suggest vertical line nodes in the gap structures, e.g. $d_{x^2-y^2}$ *or* d_{xy}, and rule out the chiral *d*-wave state, $d_{xz} \pm id_{yz}$. However, $d_{x^2-y^2}$ or d_{xy} itself is a singlet pairing state and does not break time reversal symmetry. To reconcile these key experiments, they pointed out two possible *f*-wave states which have chiral *p*-wave characteristic and vertical line nodes, namely $(k_x \pm ik_y) \times (k_x^2 - k_y^2)$ and $(k_x \pm ik_y) \times k_x k_y$.

The order parameter $p_x \pm ip_y$ breaks TRS and carries a magnetic moment. In principle, edge currents would be generated automatically around the sample or around the boundaries of magnetic domains to cancel the internal field in the superconducting state (Meissner effect). μSR estimates that a field strength of about 0.5G develops in the superconducting state. In principle, this field should be detectable by other magnetic measurement approaches. However, scanning SQUID and Hall probe measurements [49]–[52] observed a much lower value (<1%) than that estimated by the μSR experiments.

The chiral *p*-wave order parameter has two degenerate components and in principle by applying a symmetry breaking field the degeneracy will be lifted. Agterberg [53] proposed that this could be done by applying an in-plane magnetic field. Experimentally, a bicritical point has been found at approximately (0.8 K and 1.2 T) with a very accurate field alignment [38], [54], [55]. A splitting of the transition has been found in heat capacity measurements below 0.8 K but this is not considered to be a symmetry-breaking-field induced splitting because the size of the splitting and the heat capacity jumps are not consistent with the predictions. Besides, the bicritical point is not part of predictions by Agterberg. Later, it was found that the transition below 0.8K is first order [56], [57]. The first order behavior can be explained by Pauli limiting, implying the pairing symmetry is spin-singlet. To explain the first order nature with the chiral *p*-wave in Sr_2RuO_4, a new concept called the *inter-orbital effect* has been proposed by Ramires and Sigrist [58].

2.4 Sr_2RuO_4 under uniaxial stress

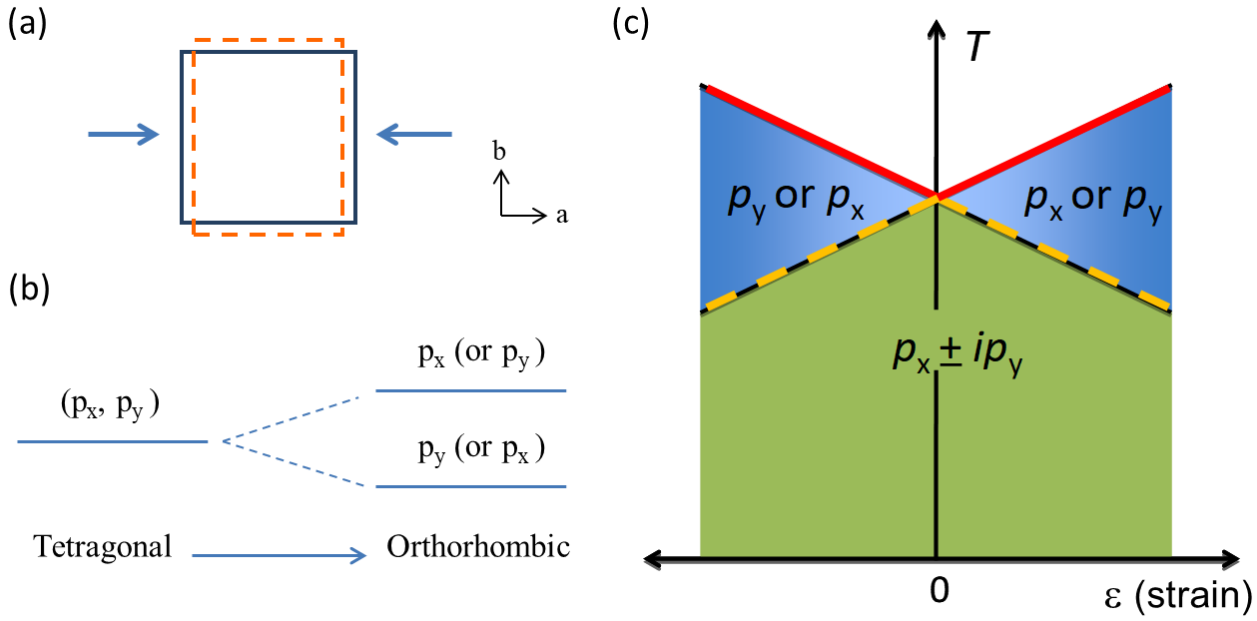

Figure 2.16: (a) A schematic diagram for the lattice distortion under uniaxial stress. (b) A degenerate state $(p_x,\ p_y)$ splits into p_x and p_y states when the lattice is distorted from tetragonal to orthorhombic symmetry. (c) An expected phase diagram for a $p_x \pm ip_y$ superconductor. The red line denotes the upper T_c and the dashed yellow line denotes the lower T_c.

Figure 2.16(a) shows a schematic diagram for lattice distortion. Suppose that a compressive strain is applied along the *a*-axis: the square lattice deforms into a rectangular lattice. The change of the lattice symmetry changes the physical properties as shown in Figure 2.16(b). (p_x, p_y) is an irreducible representation under tetragonal symmetry. When the lattice symmetry changes from tetragonal to orthorhombic, (p_x, p_y) is no longer irreducible and breaks into two irreducible representations p_x and p_y. The order parameters p_x and p_y are degenerate and have the same T_c in a material with tetragonal symmetry. When a strain is applied, the degeneracy breaks and one of the order parameters has a higher T_c and the other has a lower one. The difference in T_c is predicted to be proportional to the lattice distortion [59] and Figure 2.16(c) shows the expected phase diagram which illustrates the concept. There are two phase boundaries, the upper T_c and lower T_c, as shown by the red line and the dashed yellow line respectively, and a cusp at zero strain. The linear dependence and the existence of the cusp are the key features of the prediction for the $p_x \pm ip_y$ order parameter. The easy ways to measure T_c are resistivity and susceptibility. However, these two approaches are sensitive to only the upper T_c because once one of the order parameters sets in, the whole material becomes superconducting. The order parameter $p_x \pm ip_y$ breaks time reversal symmetry so muon spin relaxation or Kerr rotation can probe the lower T_c. Since the upper and lower T_c are thermodynamic phase transitions, heat capacity can probe both boundaries.

2.4.1 Sr_2RuO_4 under both tensile and compressive strains

The linear strain dependence and cusp are key features in the phase diagram shown in Figure 2.16(c). Hicks *et al*. [60] have measured the magnetic susceptibility of Sr_2RuO_4 under both tensile and compressive strains. Figure 2.17(a) and (b) show T_c against sample strain applied along the [100]- and the [110]-directions respectively. Firstly, no cusp is observed around zero strain. Secondly, although it is clear in panel (a) that T_c is enhanced under both compressive and tensile strain along the [100]-direction, this enhancement is quadratic instead of linear, as shown in panel (c). Therefore, Hicks *et al*. speculated that there may be a modified phase diagram, taking the quadratic dependence into account, as shown in Figure 2.18(a). In this picture, the cusp appears to be weak and can be rounded by strain inhomogeneities.

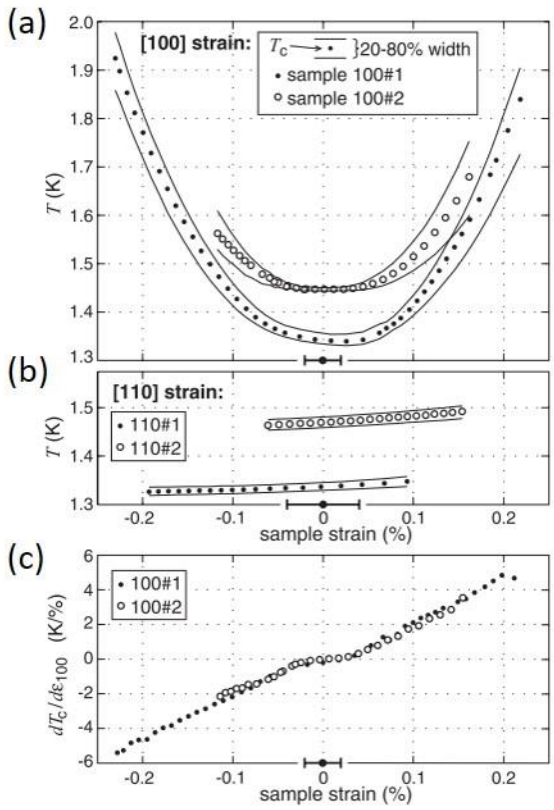

Figure 2.17: T_c against strain for different samples of Sr_2RuO_4 (a) along [100] and (b) along [110] directions. (c) The first derivative of the curves in panel (c). Reproduced from [60].

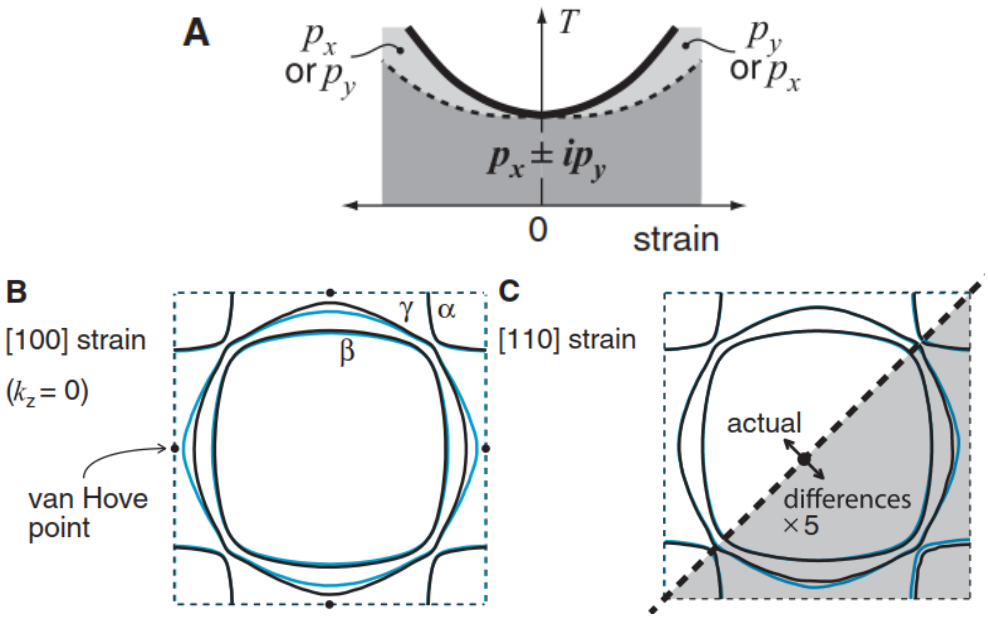

Figure 2.18: (a) A modified phase diagram of Sr_2RuO_4 which takes the quadratic dependence into account. (b) and (c) The calculated Fermi surfaces with (blue lines) and without (black lines) the strain applied along the [100] and the [110] directions, respectively. Reproduced from [60].

The proposed $p_x \pm ip_y$ order parameter should have a similar response along the [100] and [110] directions because the symmetry is lowered in both cases. However, T_c has a weak dependence when the strain is applied along the [110]-direction. This difference suggests that T_c is affected by the tetragonal lattice symmetry. Figure 2.18 (b) and (c) show the calculated Fermi surfaces under 0.5% compression (black) and tension (blue) along the [100]- and the [110]-directions respectively. In panel (b), the γ-sheet approaches the van Hove singularity (vHS), causing an increase of the density of states (DoS) under [100]-strain, whereas in panel (c), the change of the DoS is small under [110]-strain. The simulations suggest that the strong increase of T_c is related to the increase of the DoS at the vHS, an issue that I will address later with new experiments.

Since there is a strong increase of T_c when the applied strain is along [100]-direction, it was intriguing to probe the properties of a sample to which higher strains were applied. These follow-up experiments were performed by A. Steppke *et al*. [41]. Figure 2.19 shows T_c against strain for different samples. T_c is enhanced with increasing compression and reaches at maximum of $T_c \approx 3.4$ K at ε_{xx} = -0.6%. Two samples have been investigated beyond ε_{xx} = -0.6% and show a rapid suppression of T_c.

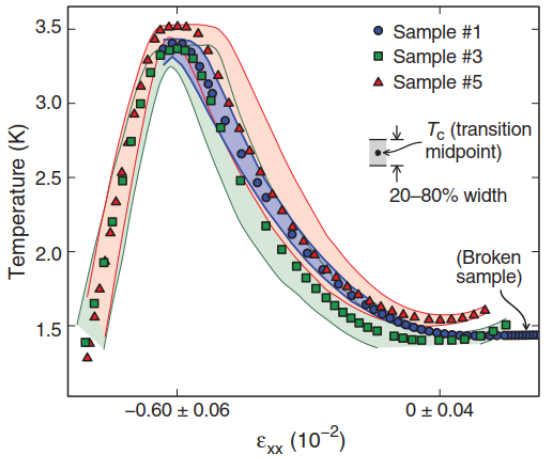

Figure 2.19: T_c against strain for different Sr_2RuO_4 samples. The applied strain is along the [100]-direction. Reproduced from [41].

The DoS increases when a Fermi surface approaches a van Hove singularity. According to the BCS theory, the gap size is related to the DoS and T_c is proportional to the gap size:

$$\Delta_0 = 1.764 k_B T_c = 2\hbar\omega_D e^{-\frac{1}{N(0)V}} \tag{2-3}$$

where Δ_0 is the superconducting gap at T = 0 K, ω_D is the Debye frequency, $N(0)$ is the DoS at the Fermi surface, and V is the attractive potential. Qualitatively speaking, T_c is enhanced when the Fermi surface approaches the van Hove point. However, the standard BCS expressions are based on a single band metal with a circular Fermi surface, while there are three Fermi sheets in Sr_2RuO_4 and therefore, the abovementioned descriptions can only serve as a guideline. To study this issue in more detail, T. Scaffidi and colleagues have performed calculations taking the multi-sheet Fermi surfaces of Sr_2RuO_4 into account [41].

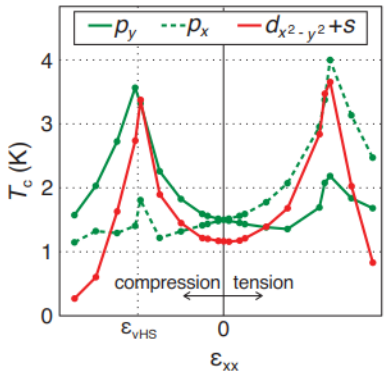

Figure 2.20: Theoretical results of T_c against strain based on weak-coupling renormalization group calculations with two different order parameters, $p_x \pm ip_y$ (green) and $d_{x^2-y^2}$ (red). $p_x \pm ip_y$ splits into p_x and p_y and $d_{x^2-y^2}$ turns into $d_{x^2-y^2} + s$ under strain. Reproduced from [41].

Figure 2.20 shows the calculation of T_c against strain. (p_x, p_y) is an irreducible representation under tetragonal lattice symmetry. When a strain, either tension or compression, is applied along [100], the lattice changes from tetragonal to orthorhombic and (p_x, p_y) breaks into p_x and p_y which are irreducible representations under orthorhombic lattice symmetry. Hence, there is a splitting of T_c. $p_y(p_x)$ condenses at higher temperature under compression (tension) than $p_x\,(p_y)$. Another possible pairing symmetry is $d_{x^2-y^2}$ which becomes $d_{x^2-y^2} + s$ under strain. T_c peaks at the vHS in both scenarios. Another notable feature is that the *p*- and *d*-wave states are nearly degenerate at the vHS. This indicates the possibility of a pairing symmetry change as a function of strain.

2.4.2 Pairing symmetry in Sr_2RuO_4 at the maximum of T_c

In singlet superconductors, if a small magnetic field polarizes the Fermi surface, electrons are paired and condense with a cost of magnetic energy. When the magnetic energy is greater than the superconducting condensation energy, the Cooper pairs are destroyed. This mechanism is known as the spin limit or Pauli limit for the critical field H_{c2} and the phase transition in this case is first order. In contrast, the Pauli limit does not apply for the equal spin paired component of the order parameter in triplet superconductors. For a simple weak-coupled superconductor with an isotropic gap, the Pauli limit is approximately the value in $T_c \times 1.8$ T/K, which is known as Clogston-Chandrasekhar limit [61]. In a multi-band superconductor, an averaging across the different bands is expected and a deviation, within a factor of order one, from 1.8 T/K is reasonable.

In type II superconductors, vortices thread through the sample, each with a flux quantum Φ_0 and a normal core $\sim\xi^2$, where ξ is the coherence length. The applied field at which the sample is completely filled with vortices and the superconductivity is destroyed is the critical field $H_{c2} = \Phi_0/2\pi\xi^2$. This is known as the orbital limit and the phase transition in this case is thought to be second order. The critical field in most of superconductors is determined by the orbital limit and this is the case in 1.5K-Sr_2RuO_4 for the field applied along the *c*-axis.

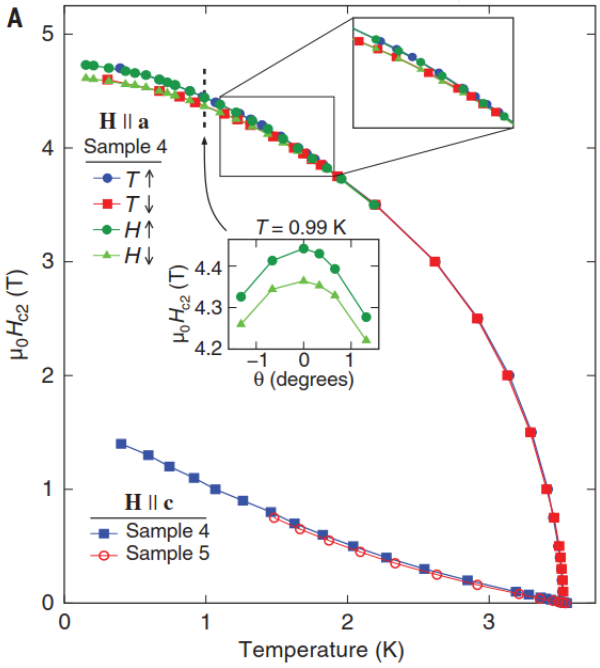

Figure 2.21: $\mu_0 H_{c2}$ as a function of temperature at the peak in T_c for field $H||a$ and $H||c$. The inset shows the hysteresis near $\theta = 0°$. Reproduced from [41].

Figure 2.21 shows the H_{c2} as a function of temperature for a strained Sr_2RuO_4 at the maximum $T_c = 3.4$K with the applied field along the *a*- and *c*-axes. The extrapolated $H_{c2||c}$ and $H_{c2||a}$ at $T = 0$ K are ≈1.5 T and 4.7 T. The anisotropy $\Gamma = H_{c2||a}/H_{c2||c}$ in 3.4K-Sr_2RuO_4 is ≈3 and is strongly reduced compared to the unstrained Sr_2RuO_4 whose value is ≈20. DFT calculations suggest that the band structure in 3.4K Sr_2RuO_4 is still two dimensional. The slope dH_{c2}/dT near T_c in the in-plane direction is far larger than that in the out-of-plane direction. The reduction of Γ in 3.4K-Sr_2RuO_4 is not compatible with the orbital limit. Instead, a first order behavior in $H_{c2||a}$ below 1.8 K has been observed and $H_{c2}/T_c \cong 1.4$ which is not far from the Clogston-Chandrasekhar limit 1.8. Both results support the Pauli limit scenario and a singlet pairing in 3.4K-Sr_2RuO_4.

The authors of Ref. [41] proposed an experimental approach to distinguish between the different pairing symmetries. In the orbital limit case, $H_{c2} = \Phi_0/2\pi\xi^2$. The coherence length ξ in the BCS theory depends on the ratio of Fermi velocity v_F to the magnitude of the superconducting gap $\xi = \hbar v_F/\pi\Delta$ and $v_F \propto 1/N(0)$, where $N(0)$ is the DoS at the Fermi surface. Therefore, H_{c2} is proportional to an average of the superconducting gap with a DoS weighting factor, $(N(0)|\Delta|)^2$. In BCS theory, $\Delta(0) = 1.764 k_B T_c$ and therefore $H_{c2}/T_c^2 \propto N(0)^2$. If the superconducting gap changes only by multiplying a constant factor, namely the gap increasing without changing its symmetry, H_{c2}/T_c^2 remains the same if the DoS does not change. However, in Sr_2RuO_4, the DoS increases when the Fermi surface approaches the vHS and causes H_{c2} to have an additional weighting at the vHS. For even-parity pairing symmetry, the gap is large in the region near the vHS. In contrast, for odd-parity pairing symmetry, the superconducting gap will be zero at the vHS by symmetry because the vHS is invariant under inversion. It is, therefore, expected that H_{c2} will grow more than linearly in T_c^2 for even parity pairing symmetry and less for odd parity pairing symmetry.

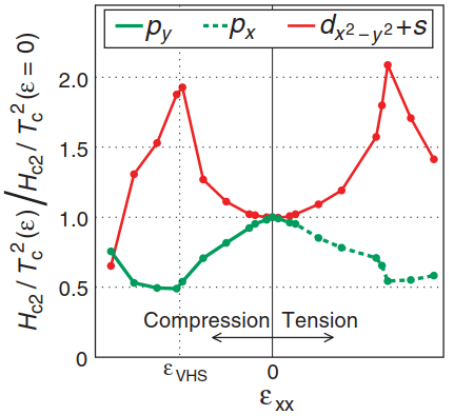

Figure 2.22: Theoretical predictions of H_{c2}/T_c^2 as a function of strain for odd and even parities. The value on the *y*-axis is normalized to that at zero strain. Reproduced from [41].

Figure 2.22 shows theoretical calculations of H_{c2}/T_c^2 as a function of strain for $p_x \pm ip_y$ (odd-parity) and $d_{x^2-y^2}$ (even-parity) pairing symmetry. The results are normalized to the unstrained value. $p_x \pm ip_y$ breaks into p_x or p_y under strain and meets the symmetry requirement imposed on the vHS, whereas $d_{x^2-y^2}$ has small amount of s mixture in the orthorhombic symmetry. H_{c2}/T_c^2 under strain is enhanced for even parity and reduced for odd parity. Experimentally, H_{c2}/T_c^2 in 3.4K-Sr_2RuO_4 is enhanced by a factor 3.6. It is therefore intriguing to measure H_{c2} as a function of strain and calculate whether H_{c2}/T_c^2 is reduced at intermediate strain or not.

The first order transition for $H_{||a}$, the size of the $H_{c2||a}$ and the enhancement of $H_{c2||c}/T_c^2$ suggest even parity pairing symmetry in 3.4K-Sr_2RuO_4. There are two consequences related to unstrained 1.5K- Sr_2RuO_4. First, since the most-discussed pairing symmetry in Sr_2RuO_4 is $p_x \pm ip_y$, which is a spin triplet paired state, there will be a triplet-to-singlet transition at intermediate strain. Second, the first order behavior was observed in 1.5K-Sr_2RuO_4 as well, which can be interpreted as a result of singlet pairing, and this provides the other possibility that the parity remains unchanged between 1.5K- and 3.4K-Sr_2RuO_4. If this is the case, a number of key experiments would need alternative explanations. The evidences of breaking TRS in 1.5K-Sr_2RuO_4 can be accommodated by chiral d-wave $d_{xz} \pm id_{yz}$ [47]. However, the NMR Knight shift, the evidence for triplet pairing, would need a different interpretation.

2.5 Summary

In this chapter, I began with a description of the normal state of Sr_2RuO_4 then spent the rest describing its superconducting properties. Sr_2RuO_4 has a layered perovskite structure and a tetragonal lattice. Electrons are hopping within the Ru-O layers, making it a highly 2D material. Both in-plane and out-of-plane resistivity data at low temperature show a T^2 dependence, which indicates the existence of a Fermi liquid. The Fermi surface consists of three sheets, α, β and γ, whose existence has been nicely verified by APRES and quantum oscillation experiments.

In the absence of strong spin-orbit coupling and inversion symmetry breaking, the Cooper pair wave function can be decomposed into an orbital and a spin part. NMR Knight shift experiments suggest that the pairing in the spin part is triplet. μSR and Kerr rotation studies suggest that TRS is broken in the superconducting state and that the orbital part of the order parameter is a complex. The most-discussed pairing symmetry is the chiral p-wave state $p_x \pm ip_y$, whose gap is isotropic on a circular Fermi surface and whose phase changes with respect to the polar angle θ. However,

heat capacity data at low temperatures show a linear T dependence. This linear dependence can be explained by the complexity of the band structure, indicating the existence of line nodes even within a chiral p-wave scenario. In addition to heat capacity, E. Hassinger *et al.* suggest that the line nodes are vertical on the basis of the analysis of thermal conductivity experiments. To reconcile line nodes with TRS breaking, they pointed out two possible f-wave states, $(k_x \pm ik_y) \times (k_x^2 - k_y^2)$ and $(k_x \pm ik_y) \times k_x k_y$. Phase sensitive experiments suggest that there is a π-phase difference between the opposite sites of the Fermi surface, providing an evidence for a chiral p-wave or f-wave order parameter. However, Žutić and Mazin pointed out that chiral d-wave might also be consistent with the experiments. The existence of a chiral p-wave order parameter suggests the existence of a circulation current around the chiral domains because of the Meissner effect but scanning SQUID and Hall probe experiments observed a signal less than 1% of the value estimated on the basis of μSR studies. Agterberg proposed that an in-plane magnetic field should be able to lift the degeneracy of $p_x \pm ip_y$ but the results from heat capacity measurements were not consistent with the theoretical prediction. There is therefore still no consensus on the pairing symmetry of Sr_2RuO_4 after more than two decades of research.

Lastly, the degeneracy of (p_x, p_y) should be lifted by uniaxial stress. The predicted linear ε dependence and the cusp around zero strain were not observed, and the authors of Ref. [60] proposed a modified phase diagram by taking the quadratic dependence into account. Whether or not there is another transition below the observed transition is an open question. A strong peak in T_c has been observed under higher compressive strain. The enhancement of T_c can be understood as an increase of DoS near the vHS. Whether or not the peak in T_c coincides with the vHS is a further open question. The first order behavior in $H_{c2||a}$, the size of H_{c2} and the enhancement of $H_{c2||a}/T_c^2$ suggest that the pairing symmetry in 3.4K-Sr_2RuO_4 is even parity. Whether or not there is a triplet-to-singlet pairing symmetry change is an open question. The status of the pairing symmetry in Sr_2RuO_4 becomes *even odder* [62].

Several open questions have been raised by the existing strain measurements and they motivate this research work. In my study, I used the heat capacity approach to probe the responses of Sr_2RuO_4 under strain. In the following, I will describe the experimental methods and details for heat capacity measurements of Sr_2RuO_4 under uniaxial stress in Chapter 3, and I will present and discuss my results in Chapter 4.

Chapter 3
Heat Capacity Measurements under Uniaxial Stress

3.1 Introduction

The experimental challenge of this project is, "Is it possible to do heat capacity measurements of a sample under strongly non-adiabatic conditions?"

Conventionally, people do measurements with a thermally-isolated system so that they can control and calculate the heat input and measure the temperature increase. Figure 3.1.1 shows an example of a conventional setup for heat capacity measurements. A sample is glued on top of a platform, in this case a silver plate, and a heater and thermometer are glued on the back side. The whole system is then suspended by very low thermal conductance wires, e.g. Kevlar wires, which decouple the system from the environment. The decay time following the input of some heat is defined by

$$\tau = \frac{C_{system}}{k_{bath}} \tag{3-1}$$

where τ is the decay time, C_{system} is the heat capacity of the system which contains the heat capacity of sample and the addenda, and k_{bath} is the thermal conductance to the environment. The decay time is adjustable by choosing different materials. For a well thermally-isolated setup, the decay time can be hours and a heat pulse method can be used to heat up the platform and read out the temperature increase. If the decay time is in range of seconds, a relaxation time method can be used because the heat capacity is related to the relaxation time. The thermal coupling between system and environment is weak in both cases. In this study, however, this coupling is strong. In order to apply strain on a sample, there is inevitably physical contact to the sample whose thermal conductance cannot be kept low. Figure 3.1 shows the setup of the strain measurements. A sample is sitting across the gap between the strain cell anvils and glued at both ends with Stycast 2850FT. These two Stycast contacts whose thermal conductivity are ~10^{-2} W/m-K served as the thermal barrier and create huge thermal coupling to the environment. In contrast, the thermal barrier in conventional cases are the suspension wires and a typical thermal conductivity is four orders of magnitude higher, about 10^{-6} W/m-K. Therefore, the setup used for this measurement is under

strongly non-adiabatic conditions. Conventional methods cannot be used because the decay time, about 1 ms, is too fast. To solve this issue, I have employed an AC method. In this Chapter, I will introduce the relevant methods in more depth, to demonstrate how my central technical challenge can be overcome.

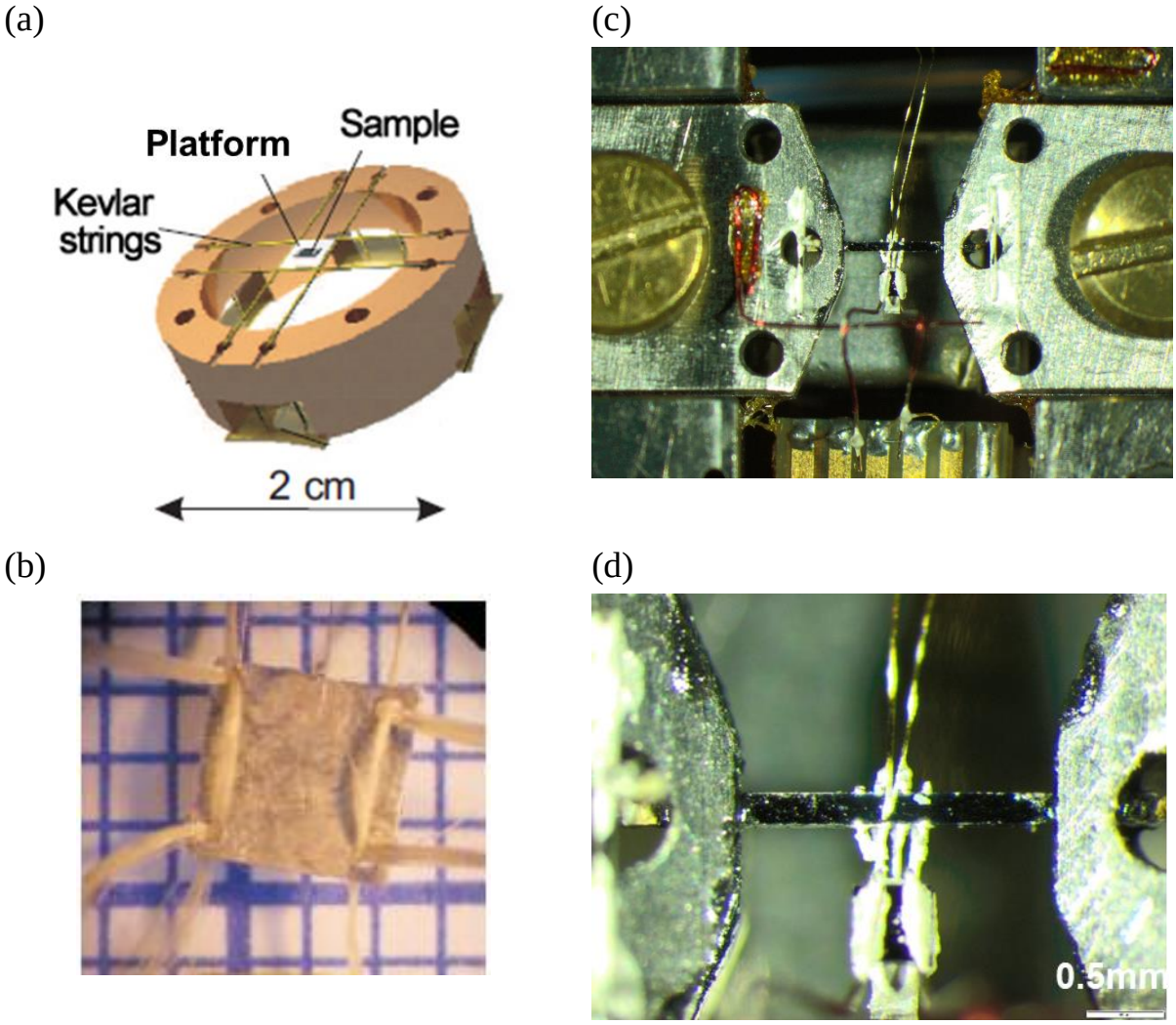

Figure 3.1: (a) A schematic diagram for a conventional setup for heat capacity measurements. Reproduced from [63]. (b) A photograph for the sample platform. Reproduced from [63]. (c) A photograph for a strongly non-adiabatic setup for heat capacity measurements under uniaxial stress. (d) A photograph for a sample with two ends fixed on the anvils.

3.2 Heat capacity measurements

3.2.1 Adiabatic method

By definition, heat capacity is the amount of heat put into a sample, ΔQ, divided by the amount of temperature raised, ΔT.

$$C(T) = \lim_{\Delta T \to 0} \frac{\Delta Q}{\Delta T}$$

In this method, the system is designed to be thermally isolated from the environment and hence the applied heat stays inside the system. To achieve this requirement, the thermal conductance to the environment is very low. This is usually achieved by high vacuum and using very low thermal conductive wires, e.g. Kevlar wires.

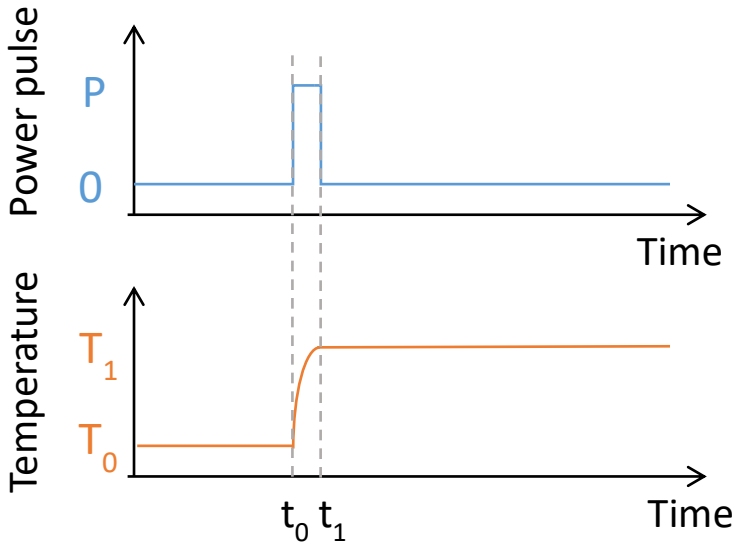

Figure 3.2: Sample temperature as a function of time when a heat pulse is applied in the adiabatic method.

Figure 3.2 depicts the temperature trace of a measurement. A heat pulse is applied to a sample from time t_0 to t_1 and the temperature is increased from T_0 to T_1. The heat pulse is switched off after t_1 and the temperature decays exponentially to the bath temperature. The decay time in this case is on the order of hours and the measurement time is on the order of seconds. Therefore, most of the applied heat still stays inside the system and the heat capacity is $P(t_0 - t_1)/(T_1 - T_0)$.

3.2.2 Relaxation time method

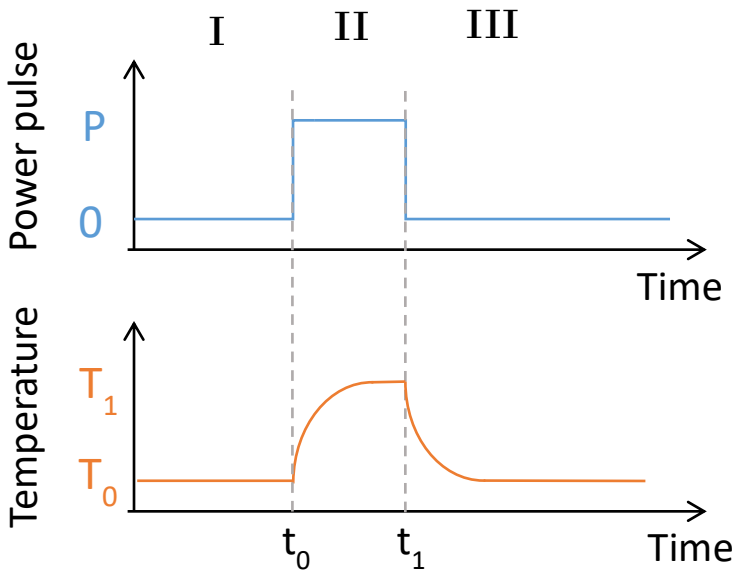

Figure 3.3: Sample temperature as a function of time in the relaxation time method. A continuous heat pulse is applied in phase II and no heat is applied in phase I and III.

If the decay time of a system is on the order of seconds, the relaxation time method can be applied. This method was proposed by R. Bachmann *et al*. [64]. Figure 3.3 shows the concept of this method. In the phase I, no heat is applied and sample is in equilibrium with the bath at temperature T_0. At time t_0, the power is turned on and the sample temperature goes up and saturates at T_1. At time t_1, the power is switched off and the temperature goes down and eventually equilibrium is re-established with the bath at temperature T_0.

In phase II, the temperature rises exponentially as:

$$T(t) = T_1 + (T_0 - T_1)e^{-\frac{k}{C}(t-t_0)} \quad \text{for } t_0 < t < t_1. \tag{3-2}$$

In phase III, the temperature decays exponentially as:

$$T(t) = T_0 + (T_1 - T_0)e^{-\frac{k}{C}(t-t_2)} \quad \text{for } t > t_2 \tag{3-3}$$

In equations (3-2) and (3-3), k is thermal conductance of the system to bath and C is heat capacity of the system (the sum of C_{sample} and $C_{addenda}$). By fitting the measured data with the two formulae, one can obtain the relaxation time

$$\tau = \frac{C}{k} \tag{3-4}$$

In each measurement, T_1 is usually 1 to 2% higher than T_0 and in this temperature range C can be viewed as a constant. k is determined by the equation:

$$k = \frac{\dot{Q}}{\Delta T} \tag{3-5}$$

k and $C_{addenda}$ are known parameters which can be measured in advance and thus one can obtain heat capacity of the sample.

3.2.3 AC calorimetry

P. F. Sullivan and G. Seidel [65] made a breakthrough in the field and proposed a new way to measure heat capacity of a sample. Instead of applying constant power to samples, they applied an alternating power. Figure 3.4 shows the schematic diagram of this method.

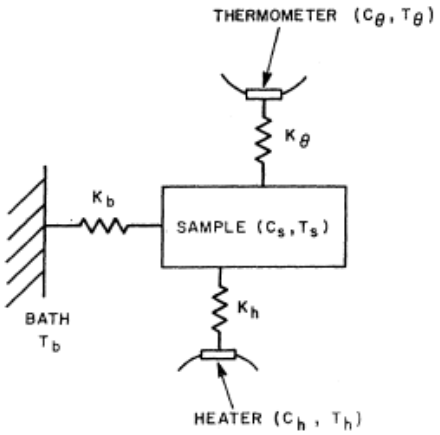

Figure 3.4: A schematic diagram for ac calorimetry. Reproduced from [65].

There is a sample with heat capacity C_s at temperature T_s. A heater (C_h, T_h) and a thermometer (C_θ, T_θ) are thermally coupled, with conductances k_h and k_θ, respectively, to the sample. The whole system is thermally coupled with conductance k_b, to bath at temperature T_b. In this method, the heat input oscillates as

$$\dot{Q} = Q_0 \left[\cos\left(\frac{1}{2}\omega t\right)\right]^2 \tag{3-6}$$

and one would like to read out the temperature from thermometer T_θ. To get a good heat capacity measurement, the heat input is kept small and thus the temperature variation, ΔT, is small compared to the temperature T. $\Delta T/T$about 1% is usually the case and thus in this temperature range one can assume that the heat capacity (C_s, C_h, C_θ) and the thermal conductances (k_s, k_h, k_θ) are constant. The differential equations for each component are the following

$$C_h \dot{T_h} = Q_0 \left[\cos\left(\frac{1}{2}\omega t\right)\right]^2 - k_h(T_h - T_s) \tag{3-7}$$

$$C_s \dot{T_s} = k_h(T_h - T_s) - k_b(T_s - T_b) - k_\theta(T_s - T_\theta) \tag{3-8}$$

$$C_\theta \dot{T_\theta} = k_\theta(T_s - T_\theta) \tag{3-9}$$

After solving equations (3-7) to (3-9), the solution for the temperature T_θ has the following form:

$$T_\theta = T_b + \frac{Q_0}{2k_b} + \frac{Q_0}{2\omega C}(1-\delta)\cos(\omega t - \alpha) \tag{3-10}$$

where

$$C = C_s + C_h + C_\theta \tag{3-11}$$

$$\begin{aligned} 1-\delta = \Bigg[& 1 + \frac{\tau_\theta^2\left(1+2\frac{k_\theta}{k_b}\right)}{\tau_b^2} + \frac{1}{\omega^2\tau_b^2} \\ & + \omega^2\left[\left(\frac{C_s + C_h}{C}\right)^2 \tau_\theta^2 + \left(\frac{C_s + C_\theta}{C}\right)^2 \tau_h^2\right. \\ & \left. + \frac{\tau_\theta^2\tau_h^2}{\tau_b^2}\left(1 + 2\frac{k_b(k_\theta + k_h) + k_\theta k_h}{k_b^2}\right)\right] + \omega^4\tau_\theta^2\tau_h^2\left(\frac{C_s}{C}\right)^2 \Bigg]^{-1/2} \end{aligned} \tag{3-12}$$

and $\tau_b = C/k_b, \tau_h = C_h/k_h, \tau_\theta = C_\theta/k_\theta$,where τ_b, τ_h and τ_θ describe the time scales for heat propagating into bath, heater and thermometer, respectively.

Equation (3-12) describes a general form for $1-\delta$. Although it looks complicated, in a real setup, some of terms are negligible.

a) The mass of a sample is often larger than the mass of the heater and the thermometer. Furthermore, the specific heat of the sample in this study, Sr_2RuO_4, is larger (55 mJ/mol-K at 1 K) than that of the heater and the thermometer (<1 mJ/mol-K at 1 K). Therefore, it is safe to make an assumption that $C_s \gg C_h$ and C_θ.
b) τ_b, τ_h and τ_θ describe the time scales for heat propagating into bath, heater and thermometer, respectively. As mentioned, $C_s \gg C_h$ and C_θ and, furthermore, with a good experimental design, k_h and $k_\theta \gg k_b$. Thus, $\tau_b \gg \tau_h$ and τ_θ. This means that heat is easier to thermalize between the heater, sample and thermometer than going to the bath.
c) ω is related to the frequency ($2\pi f$) which is an adjustable parameter in the measurements. In a proper setup, it is chosen such that $\omega < 1/\tau_h$ and $\omega < 1/\tau_\theta$. It means that there is a good thermal equilibrium among the sample, heater and thermometer as long as the frequency is not too high.

Based on the abovementioned assumptions, $1-\delta$ can be simplified to

$$1-\delta \cong \left[1+\frac{1}{\omega^2\tau_b^2}+\omega^2\left(\tau_h^2+\tau_\theta^2\right)\right]^{-1/2} \tag{3-13}$$

and the angle α

$$\alpha \cong arcsin\left[1+\left[\frac{1}{\omega\tau_b}-\omega(\tau_h+\tau_\theta)\right]^2\right]^{-1/2} \tag{3-14}$$

So far, this model only considers that the thermal conduction in the sample is perfect. If one take the finite thermal conductivity in the sample into account, the equation can be modified as follows:

$$1-\delta = \left[1+\frac{1}{\omega^2\tau_1^2}+\omega^2\tau_2^2+\frac{2k_b}{3k_s}\right]^{-1/2} \tag{3-15}$$

where k_s is the thermal conductance of the sample, $\tau_1 = \tau_b, \tau_2 = \tau_h + \tau_\theta + \tau_{int}$. τ_{int} is the heat propagating time within the sample and $\tau_{int} = C_s/k_s$. The thermal conductance of the sample itself is usually larger than that to the bath and thus the $2k_b/3k_s$ term can be neglected[2].

[2] In my setup k_s is an order of magnitude larger than k_b, there will be at most 5% correction on $1-\delta$, which would not affect the scientific conclusions in this thesis.

The temperature of the thermometer can be written as

$$T_\theta = T_b + T_{DC} + T_{ac}\cos(\omega t - \alpha) \tag{3-16}$$

$$T_{DC} = \frac{Q_0}{2k_b} \tag{3-17}$$

$$T_{ac} = \frac{Q_0}{2\omega C}F(\omega) \tag{3-18}$$

where $F(\omega)$ is a correction factor which has the form of

$$\left[1 + \frac{1}{\omega^2\tau_1^2} + \omega^2\tau_2^2\right]^{-1/2} \tag{3-19}$$

The temperature of the thermometer T_θ is equal to the bath temperature T_b plus a heating term T_{DC} and an oscillation term $T_{ac}\cos(\omega t - \alpha)$. The heating term and oscillation term can be understood as follows:

The heat input is in the form of

$$\dot{Q} = Q_0\left[\cos\left(\frac{1}{2}\omega t\right)\right]^2 = \frac{Q_0}{2} + \frac{Q_0\cos(\omega t)}{2} \tag{3-20}$$

Apparently, the heat input has two parts, the DC and ac parts. The first part is the average power $P = \langle\dot{Q}\rangle = Q_0/2$. It gives rise to a constant power dissipation in the sample and thus causes a constant heating

$$T_{DC} = \frac{Q_0}{2k_b} = \frac{P}{k_b} \tag{3-21}$$

The second part oscillates over time and leads to an oscillation in temperature $T_{ac}\cos(\omega t - \alpha)$. According to equation (3-18), heat capacity is in the denominator and it can be expressed as:

$$C = \frac{P}{\omega T_{ac}}F(\omega) \tag{3-22}$$

Power and frequency are set values and T_{ac} can be measured. However, there is a frequency dependent term $F(\omega)$.

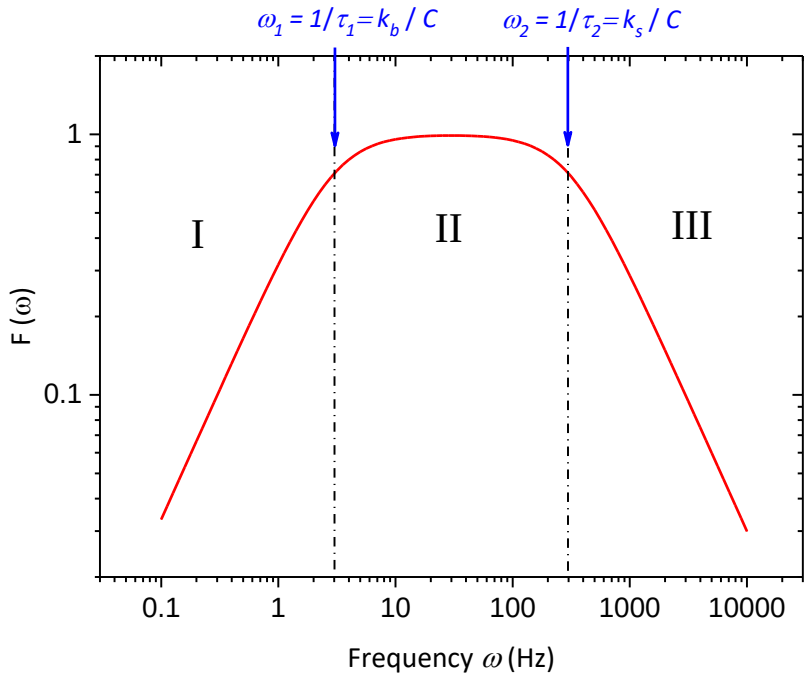

Figure 3.5: A schematic diagram for $F(\omega)$ against ω. The curve can be divided into three regions by ω_1 and ω_2.

Figure 3.5 shows the frequency dependence of $F(\omega)$. Clearly, it can be divided into three regions. In region I, the applied frequency is too low and most of the heat is lost to the bath. In region III, the frequency is too high and the heat does not have enough time to propagate to the thermometer. The best choice is region II. In this region, the frequency is low enough that there is enough time for the heater, sample and thermometer to thermalize and high enough that the signal can be decoupled from the bath. Consequently, the heat capacity can be measured and is proportional to $1/T_{ac}$.

This region is bounded by two cut-off frequency ω_1 and ω_2:

$$\omega_1 = \frac{1}{\tau_1} = \frac{k_b}{C} \tag{3-23}$$

$$\omega_2 = \frac{1}{\tau_2} \cong \frac{k_s}{C} \tag{3-24}$$

In equation (3-24), $\tau_2 = \tau_h + \tau_\theta + \tau_{int}$. Here, usually τ_{int} dominates because the heat capacity of the sample is greater than that of the heater and thermometer, $C_s \gg C_h$ and C_θ, and the thermal couplings of the heater and thermometer to the sample should be very good with a proper design and treatment. Therefore, $\tau_2 \cong \tau_{int} = C_s/k_s \cong C/k_s$.

In order to measure the heat capacity, one needs to make sure that there is a frequency window open which means $\omega_2 \gg \omega_1$. According to equation (3-23) and (3-24), the criterion becomes:

$$k_s \gg k_b \tag{3-25}$$

In this window, $F(\omega)$ serves as a correction factor. To reach 99% accuracy, there should be at least two orders of magnitude of frequency window open and the excitation frequency should be 10 times higher than the first cut-off frequency:

$$10\omega_1 < \omega < \frac{\omega_2}{10} \tag{3-26}$$

Therefore, $F(\omega)$ can be dropped and the heat capacity is

$$C = \frac{P}{\omega T_{ac}} \tag{3-27}$$

There is another physical quantity which can be determined in region I. If the excitation frequency is much lower than ω_1, $F(\omega)$ can be expressed as:

$$F(\omega) = \omega\tau_1 \tag{3-28}$$

and then T_{ac} can be expressed as:

$$T_{ac} = \frac{P}{\omega C} \times \omega\tau_1 = \frac{P}{\omega C} \times \omega \frac{C}{k_b} = \frac{P}{k_b} = T_{DC} \tag{3-29}$$

This result suggests that the heating term can be measured by the ac method with $\omega \ll \omega_1$. To reach 99% accuracy:

$$7\omega < \omega_1 < \omega_2 \tag{3-30}$$

and k_b can be calculated:

$$k_b = \frac{P}{T_{ac}} \tag{3-31}$$

The use of ac calorimetry brings several advantages.

First, the thermometer can be, for example, a thermocouple whose voltage V_{ac} can be read out by a lock-in amplifier which can average out the noise and pick-up the signal from a user-selected frequency and, thus, the signal-to-noise ratio can be easily enhanced.

Second, according to equation (3-18), the signal T_{ac} is inversely proportional to heat capacity C. Therefore, the smaller the sample, the larger the signal. In this method, a very small sample can be used.

Third, this method is suitable for measurements under non-adiabatic conditions. In practice, both the relaxation time and ac methods are non-adiabatic. τ_1 and τ_2 in the ac method and relaxation time method are actually the same. In relaxation time method, τ_1 is usually in the range of seconds to minutes in order to get a good temperature reading. However, if τ_1 is far smaller than 1s, namely the system is under strongly non-adiabatic conditions, only the ac method can measure heat capacity.

Fourth, the adiabatic method and relaxation time methods are both discrete measurements. Each measurement is done at a single value of a fixed parameter, e.g. temperature, magnetic field, etc. This is not suitable for measurements with small changes. However, with ac calorimetry, it is no problem to do measurements with continuous changes of parameters. Figure 3.6 shows heat capacity measurements of Beryllium under magnetic field. Quantum oscillations can be observed with an excellent signal-to-noise ratio.

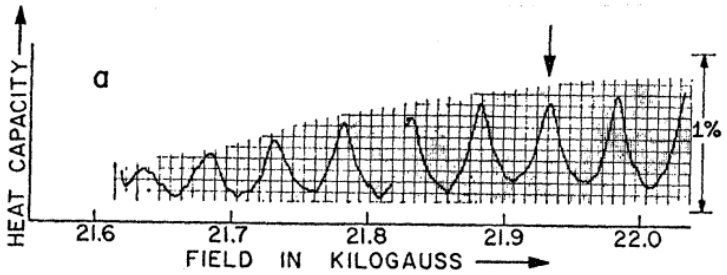

Figure 3.6: heat capacity measurement of Beryllium as function of magnetic field. Quantum oscillations can be measured by ac calorimetry. Reproduced from [65].

3.3 Design of the experimental setup and estimates of thermal conductance

To apply heat and measure temperature, a heater and a thermometer are needed. The thermometer in this study is a thermocouple which is made of Au and 0.07%Fe doped Au wires. They are both 25 μm in diameter, see Figure 3.7(a). The front ends are flattened to have a larger area. This makes it easier to spot-weld them together. The heater is made of resistive thin film on top of a silicon chip[3]. The dimensions of the heater are 0.5mm x 0.5mm x 0.25mm (1mm x 1mm x 0.25mm in the early test experiments), see Figure 3.7(b). Figure 3.8 shows a typical resistance of a heater in the range of 1 K to 4 K. The scale on the *y*-axis shows approximately 1% difference of the resistance value and the steps in the curve are the digitization from the lock-in. Both indicate that the change of the resistance over this temperature range is small. The mean value is 643.2 Ω and the systematic variation is about 0.5 Ω. To make a good thermal coupling between the sample, heater and thermocouple, silver epoxy is used. The one used in this study was DuPont 6838 single component epoxy (EPO-TEK® H20E, two-component silver epoxy, in the early test experiments). To fix the sample on the titanium plates and create thermal barriers, STYCAST® 2850 FT with Catalyst 23LV was used. It also serves as strain-transferring medium.

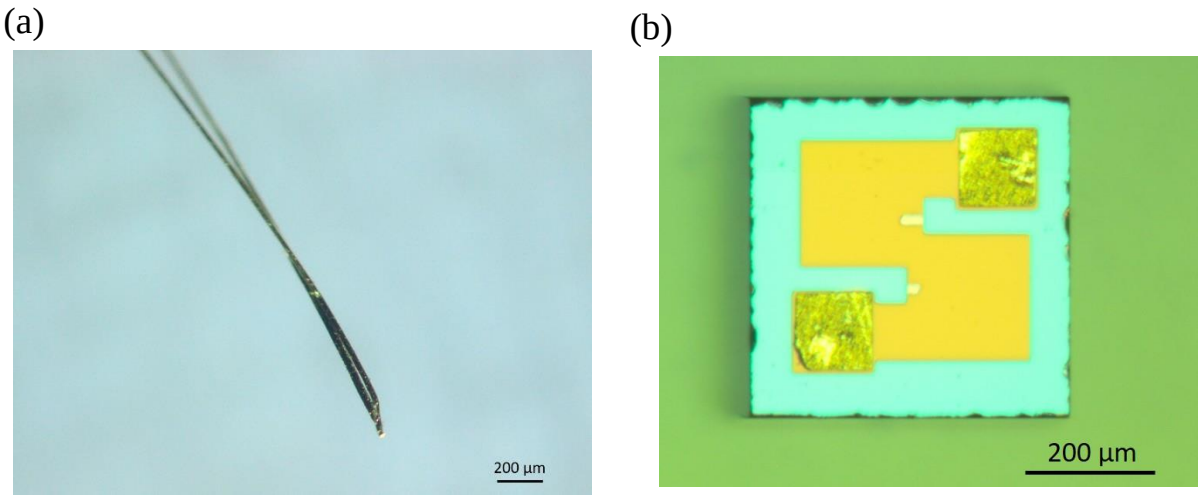

Figure 3.7: (a) A picture of a thermocouple, Au and 0.07%Fe-doped Au wires; (b) A picture of a resistive thin-film heater.

[3] State of the Art, Inc. Series number: S0202DS1001FKW.

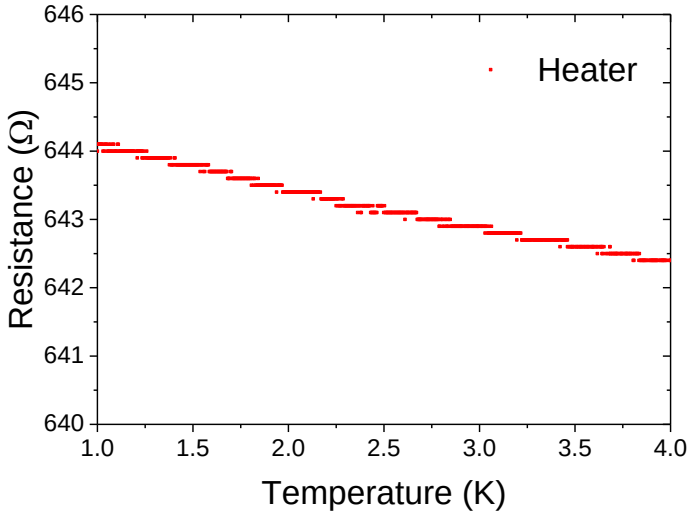

Figure 3.8: Resistance against temperature for a typical resistive heater.

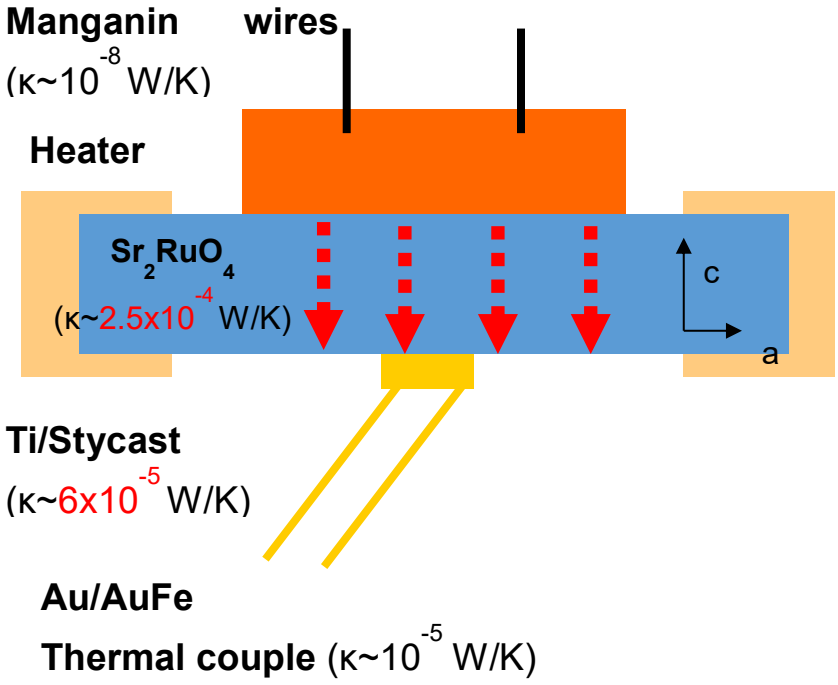

Figure 3.9: A schematic diagram of a sample setup. Estimates of individual thermal conductance are indicated.

Estimates of thermal conductance

According to equation (3-25), to ensure that there is a frequency window open for ac heat capacity measurements, the thermal conductance of the sample itself should be greater than that to the bath:

$$k_s > k_b$$

Figure 3.9 shows a schematic diagram of a sample setup. There are three channels that contribute to k_b, manganin wires, a thermocouple and Stycast/Ti plates. The thermal conductivity, κ, of manganin [66] and Stycast [67] can be described by

$$\kappa_{Manganin} = 9.5 \times 10^{-2}\, T^{1.19}\ \mathrm{W/mK}, \text{ for } T = 1 - 4\ \mathrm{K}$$
$$\kappa_{Stycast} = 9.2 \times 10^{-3}\, T^{2.65}\ \mathrm{W/mK}, \text{ for } T = 0.06 - 1\ \mathrm{K}$$

The thermal conductivity of the Au [68] at 1K is

$$\kappa_{Au}(1\mathrm{K}) = 546\ \mathrm{W/mK}$$

Thermal conductance is defined by

$$k = \kappa \frac{A}{l}, \tag{3-32}$$

where A is the area and l is the length. The dimensions of the manganin wires are 50 μm in diameter and 10 mm long. The Au wires are 25 μm in diameter and 20 mm long. The dimension of Stycast contact is 250 μm wide, 400 μm long and 15 μm thick. Thermal conductance of the elements at 1 K are:

$$k_{manganin}\,(1\mathrm{K}) \cong 3.8 \times 10^{-8}\ \mathrm{W/K}$$

$$k_{Au}(1\mathrm{K}) \cong 1.3 \times 10^{-5}\ \mathrm{W/K}$$

$$k_{Stycast}(1\mathrm{K}) \cong 6.1 \times 10^{-5}\ \mathrm{W/K}$$

Among these three channels, $k_{Stycast}$ dominates k_b.

Sr_2RuO_4 has a layered perovskite structure. The thermal conductivity in the in-plane, κ_{ab} is very different from that in the out-of-plane, κ_c. The thermal conductivities at 1 K are [69]:

$$\kappa_{ab}(1\mathrm{K}) \cong 10\ \mathrm{W/mK}$$

$$\kappa_c(1\mathrm{K}) \cong 0.1\ \mathrm{W/mK}$$

Therefore, there are two choices for k_s. A typical sample dimensions are 1 mm long, 250 μm wide and 100 μm thick. The thermal conductances of the sample are:

$$k_{ab}(1\text{K}) \cong 4 \times 10^{-3}\ \text{W/K}$$

$$k_c(1\text{K}) \cong 2.5 \times 10^{-4}\ \text{W/K}$$

Both of them are larger than $k_{Stycast}$

$$k_{ab}\ or\ k_c = k_s > k_b \cong k_{Stycast}$$

In this estimation, there is a frequency window open. However, the values are estimated at 1 K and they all vary with temperature. To be on the safe side and to ensure a wider frequency window, it is better to conduct heat in the in-plane. In addition, there is a more profound reason which will be mentioned later in the section 3.6.

Thermal relaxation time τ_1

Here I estimate the relaxation time τ_1 in this setup. The specific heat of Sr_2RuO_4 at 1 K is about 55 mJ/mol-K and the volume of a typical sample is 1 mm x 250 μm x 100 μm. The heat capacity of Sr_2RuO_4 at 1 K would be:

$$C_{Sr_2RuO_4}(1\text{K}) = 2.4 \times 10^{-8}\ \text{J/K}$$

and the relaxation time τ_1 would be:

$$\tau_1(1\text{K}) = \frac{C_{Sr_2RuO_4}}{k_b} = \frac{2.4 \times 10^{-8}}{6.1 \times 10^{-5}} \cong 0.4\ \text{ms}.$$

Signal size V_{ac}

Here I roughly estimate the size of the signal V_{ac} in the measurements.

$$V_{ac} = T_{ac} \times S. \qquad (3\text{-}33)$$

V_{ac} is the voltage difference across the thermocouple, T_{ac} is the amplitude of the temperature oscillation in the sample and S is the thermopower of the Au/0.07%Fe-doped Au thermocouple. At T = 1 K this is:

$$S(1\text{K}) = 4.62\ \mu\text{V/K}.$$

To measure heat capacity, $\omega > \omega_1$. The criterion I use here is $\omega = 5\omega_1$ and according to equation (3-27),

$$T_{ac} = \frac{P}{\omega C} = \frac{P}{5\omega_1 C} = \frac{1}{5}\frac{P}{(k_b/C)C} = \frac{1}{5}\frac{P}{k_b} = \frac{1}{5}T_{DC}$$

If 3% heating is applied at 1 K, $T_{DC} = 30$ mK and accordingly $T_{ac} = 6$ mK. The signal V_{ac} at 1K is:

$$V_{ac}(1\text{K}) = 6\ \text{mK} \times 4.62\ \mu\text{V/K} = 27.72\ \text{nV}$$

A typical lock-in has a noise level 2-5 $\text{nV}/\sqrt{\text{Hz}}$. Thus, it is possible in principle to pick up the signal and do measurements.

3.4 Test samples without applying strain (PPMS measurements)

3.4.1 Test sample #1

The first challenge of this type of measurement is to open a frequency window. To test the design, we started with a simpler configuration and measured it in a physical property measurement system (PPMS). Instead of using Ti plates, G10, a reinforced epoxy that has a relatively low thermal conductivity, was chosen to begin with.

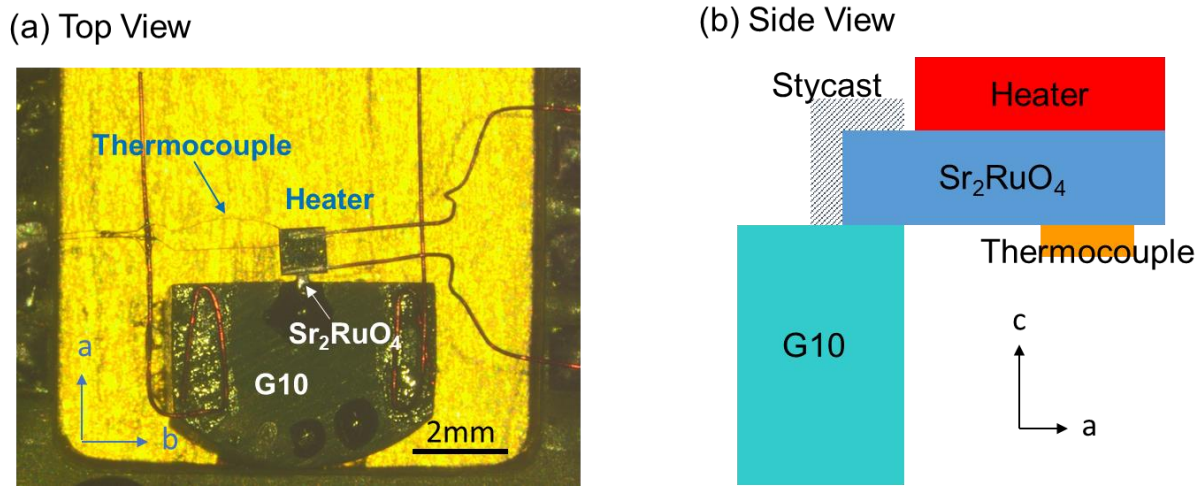

Figure 3.10: Test sample #1**.** (a) A picture of the sample setup on a PPMS puck (top view). (b) A schematic diagram showing the side view of the setup.

Figure 3.10(a) shows a picture of the sample setup for test sample #1 on a PPMS puck. One end of Sr_2RuO_4 is fixed on the edge of the G10 block with Stycast. A heater and a thermocouple are glued on the top and the bottom, respectively, of Sr_2RuO_4 with Ag epoxy H20E. The sample was annealed at 120°C for 30 minutes. Figure 3.10(b) shows a schematic diagram of the side view. In this setup, heat is conducted through the *c*-axis of Sr_2RuO_4 and, therefore, a smaller upper cut-off frequency, f_2, is expected.

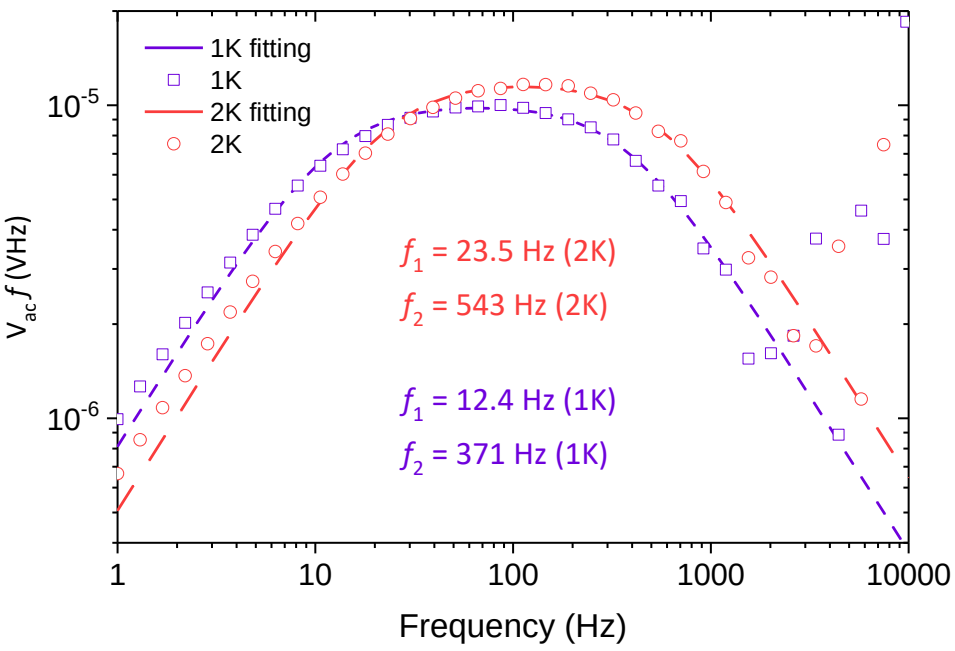

Figure 3.11: Frequency sweeps of the test sample #1 at T = 1 K (blue) and 2 K (red) with the fitting results for f_1 and f_2. The dashed lines are the fitting curves based on equation (3-19). The x-axis is the applied frequency in the heater (see text).

Figure 3.11 shows the frequency sweeps of the test sample #1 below (1 K) and above (2 K) $T_c \approx$ 1.5 K. The frequency on the *x*-axis is the applied frequency f on the heater and the oscillation in power is $2f$. The connection to ω in the ac calorimetry theory is:

$$\omega = 2\pi \times (2f) \tag{3-34}$$

From the experimental point of view, it is straightforward to plot the curve in terms of the applied frequency. Therefore, in the following frequency sweep curves, I will plot the signal as a function of the applied frequency. The frequency window shifts to higher frequency when the temperature rises. The dashed lines are the fitting curves based on the equation (3-19). The frequency windows are 12.4 Hz to 371 Hz at 1 K and 23.5 Hz to 543 Hz at 2 K obtained from the fitting results. In order to do heat capacity measurements in the temperature range of interest, the excitation frequency (f_{exc}) should always be in the frequency window and thus the valid frequency range in this sample is between 23.5 Hz and 371 Hz.

According to equation (3-31), the thermal conductance to the bath k_b, G10 in this case, can be estimated when $f_{exc} < f_1$. Here, I estimate k_b at 1 K with f_{exc}= 1 Hz:

$$k_b(1\text{K}) = \frac{P \times S}{V_{ac}} = \frac{2.98\ \mu\text{W} * 4.62\ \mu\text{V/K}}{933\ \text{nV} * \sqrt{2}} = 1.04 \times 10^{-5}\ \frac{\text{W}}{\text{K}}$$

According to equations (3-23) and (3-24), the thermal conductance of the sample along the *c*- axis at 1 K can be estimated as:

$$k_{s||c}(1\text{K}) = k_b \frac{f_2}{f_1} = 1.04 \times 10^{-5}\ \frac{\text{W}}{\text{K}} \times \frac{371\ \text{Hz}}{12.4\ \text{Hz}} = 3.12 \times 10^{-4}\ \frac{\text{W}}{\text{K}}$$

This is in good agreement with the estimated value in section 3.3.

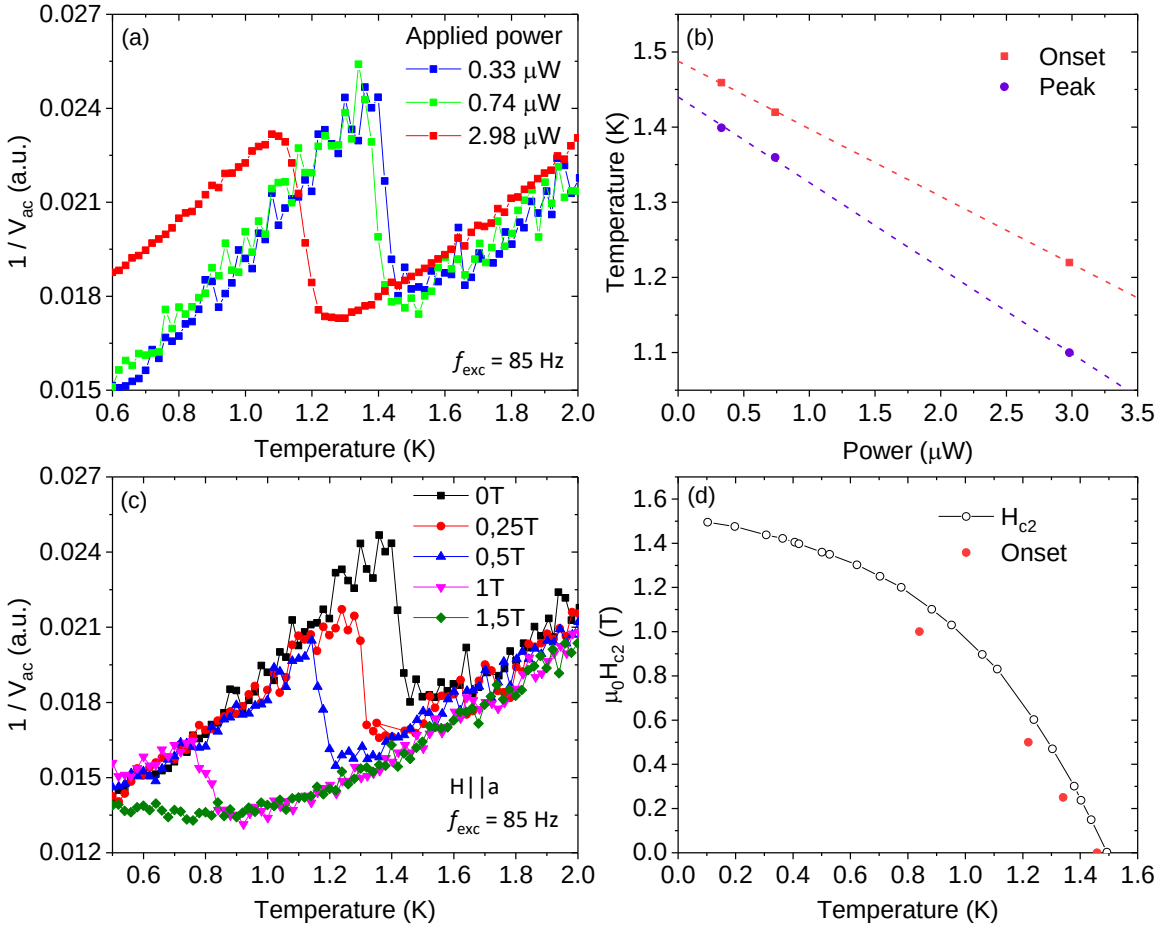

Figure 3.12: Test sample #1: (a) $1/V_{ac}$ against temperature with different applied powers. (b) T_c against power. The dashed lines are linear fits. (c) $1/V_{ac}$ against temperature with different fields $H_{||a}$. (d) $\mu_0 H_{c2}$ against temperature. The red points are the onset T_c*'s* from this sample and the black curve is H_{c2} from [70].

Figure 3.12(a) shows $1/V_{ac}$ against temperature for test sample #1 with different applied powers at 85Hz which is inside the frequency window at both 1 K and 2 K. The temperature on the *x*-axis is the temperature at the bath. $1/V_{ac}$ on the *y*-axis reflects the heat capacity signal according to equations (3-22) and (3-33). There is a superconducting transition and T_c shifts down to a lower temperature when the power is higher. According to equation (3-21), the heating T_{DC} is proportional to the applied power and thus the "real" T_c of the sample can be estimated as shown in Figure 3.12(b). The dashed lines are linear fits. The $T_{c,onset}$ and $T_{c,peak}$ are 1.49 K and 1.44 K, respectively. k_b can be determined from the slopes and they are 1.11×10^{-5} W/K and 0.88×10^{-5} W/K which agree well with the value determined by the ac method. The heat capacity jump $\Delta C/C$ is about 0.35. Comparing to the literature value which is about 0.7, there is 50% of signal coming from the addenda, e.g. wires, the heater chip, Stycast, G10, etc.. Figure 3.12(c) shows $1/V_{ac}$ against temperature under different magnetic fields along the *a*-axis. T_c is suppressed when the magnetic field is applied. Figure 3.12(d) shows H_{c2} against temperature. The black curve is H_{c2} from [70] and the red points are the data from this sample. The small deviation could come from the misalignment of the *a*-axis with respect to the direction of the applied field since the H_{c2} of Sr_2RuO_4 in *ab*-plane is known to be sensitive to the precise alignment [70].

Manipulating the frequency window

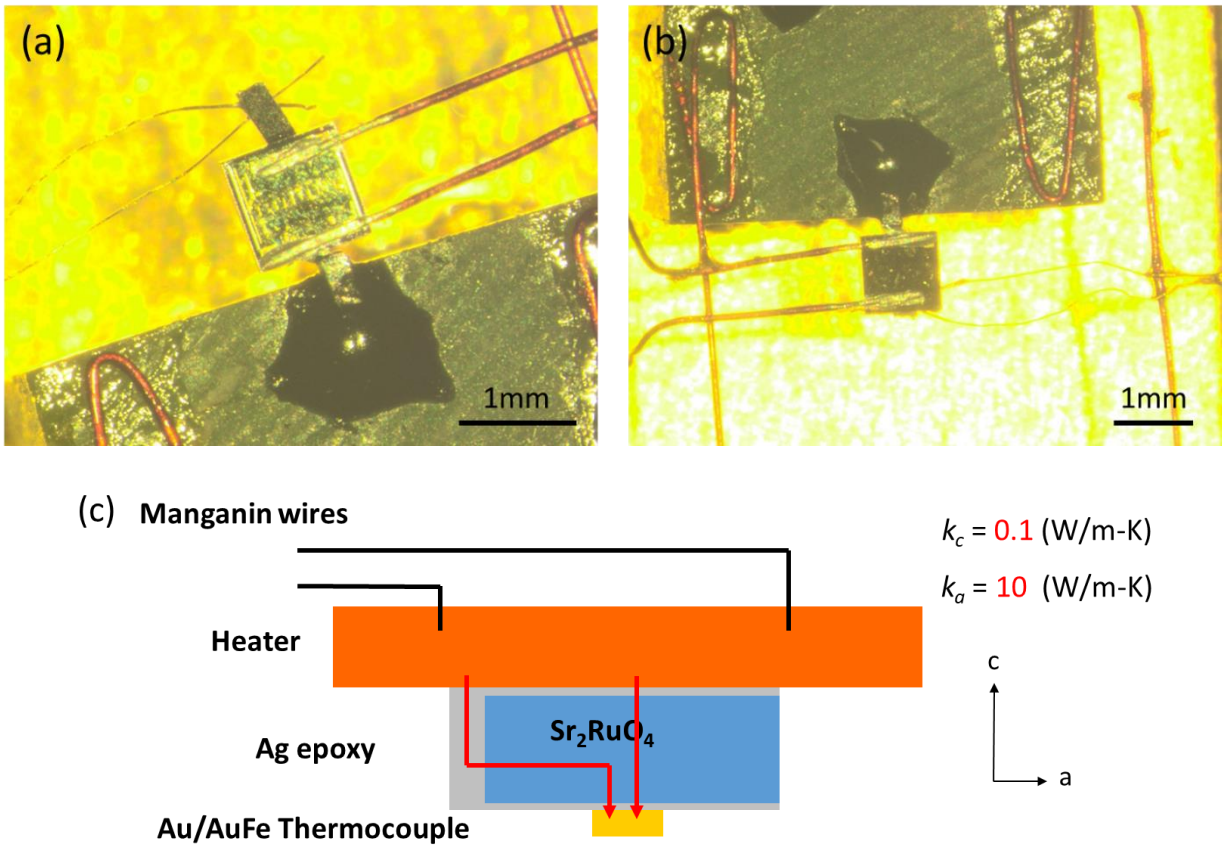

Figure 3.13: Pictures for test sample #1 (a) when it was broken and (b) when it was reassembled and Ag epoxy was applied to the edge of the Sr_2RuO_4 needle. (c) A schematic diagram of the setup from the front view.

The lower cut-off frequency f_1 is dominated by G10. By breaking the joint between G10 and Sr_2RuO_4, f_1 would be reduced. The upper cut-off frequency f_2 is determined by $k_{s||c}$. If the heat could be conducted along the *ab*-plane, f_2 would be increased. To do so, the joint was broken and Ag epoxy was applied to the edge of the Sr_2RuO_4 needle and annealed at 120°C.

Figure 3.13(a) shows a picture for test sample #1 after the joint was broken and (b) shows a picture when the sample was reassembled. The Ag epoxy was applied to the edge of the Sr_2RuO_4 needle as depicted in the Figure 3.13(c). The applied heat should now flow not only along the *c*-axis but also along the *ab*-plane.

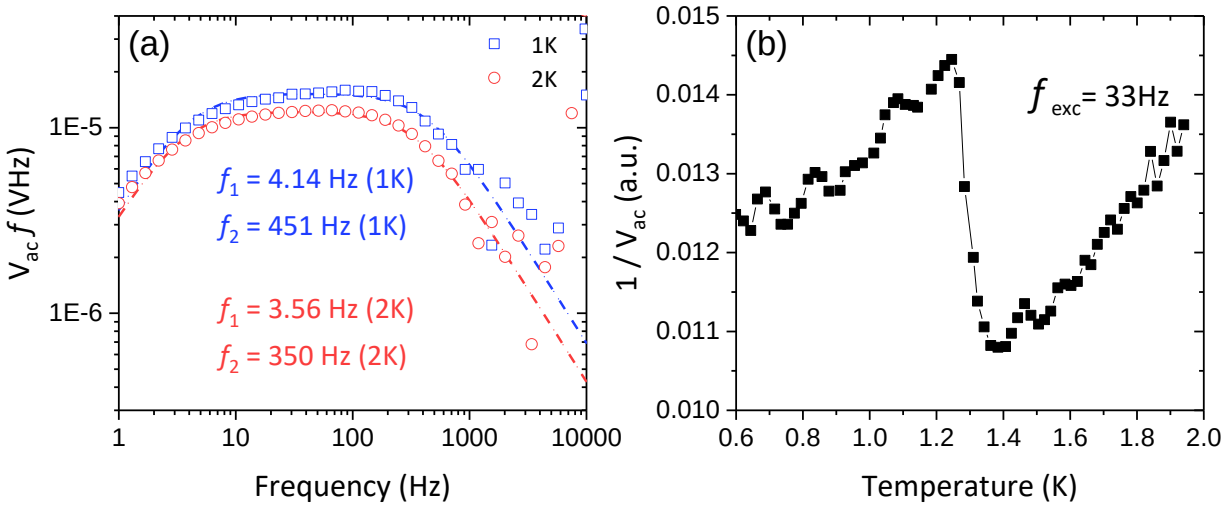

Figure 3.14: Test sample #1. (a) Frequency sweeps at T = 1 K (blue) and 2 K (red) with the fitting results for f_1 and f_2. The dashed lines are the fitting curves based on equation (3-19). (b) $1/V_{ac}$ against temperature with a different f_{exc}.

Figure 3.14(a) shows frequency sweeps at temperatures below (1 K) and above (2 K) the superconducting transition temperature (1.5 K). f_1 is reduced as expected and k_b can be estimated:

$$k_b(1K) = \frac{P \times S}{V_{ac}} = \frac{2.98\ \mu\text{W} * 4.62\ \mu\text{V/K}}{4475\ \text{nV} * \sqrt{2}} = 2.18 \times 10^{-6}\ \frac{\text{W}}{\text{K}}.$$

This value is consistent with the thermal conductance from the Au wires estimated in section 3.3. However, f_2 is not increased. This suggests that the heat propagation is still dominantly along the c-axis and that the Ag epoxy does not function properly. It indicates (a) the interface between the silver epoxy and Sr_2RuO_4 is poor and that (b) the thermal conductivity of the silver epoxy is low. Figure 3.14(b) shows $1/V_{ac}$ against temperature with a different excitation frequency f_{exc} = 33 Hz. A superconducting transition can still be observed.

3.4.2 Test sample #2

In this setup, Ti plates were used to mimic the real thermal properties in the final configuration. The estimates in section 3.3 suggest that k_b in this case would be comparable to $k_{s||c}$ and that the frequency window would be narrow or would not exist. To open this window, heat has to be conducted along the *ab*-plane. Two problems were raised by the test on sample #1: The interface between Ag epoxy and Sr_2RuO_4 was poor and the thermal conductivity of the Ag epoxy was too low. To solve these problems, Dupont 6838 (hereafter, 6838) which is another type of Ag epoxy having lower resistivity was used and the sample was annealed at 450°C for 1 hour to

(a) improve the interface between Ag and Sr_2RuO_4 because silver particles can diffuse across the surface layer of Sr_2RuO_4 and then make a good contact with the sample;

(b) help the grain-growth for silver particles to reduce its resistivity and thus increase its thermal conductivity.

Assembling procedure

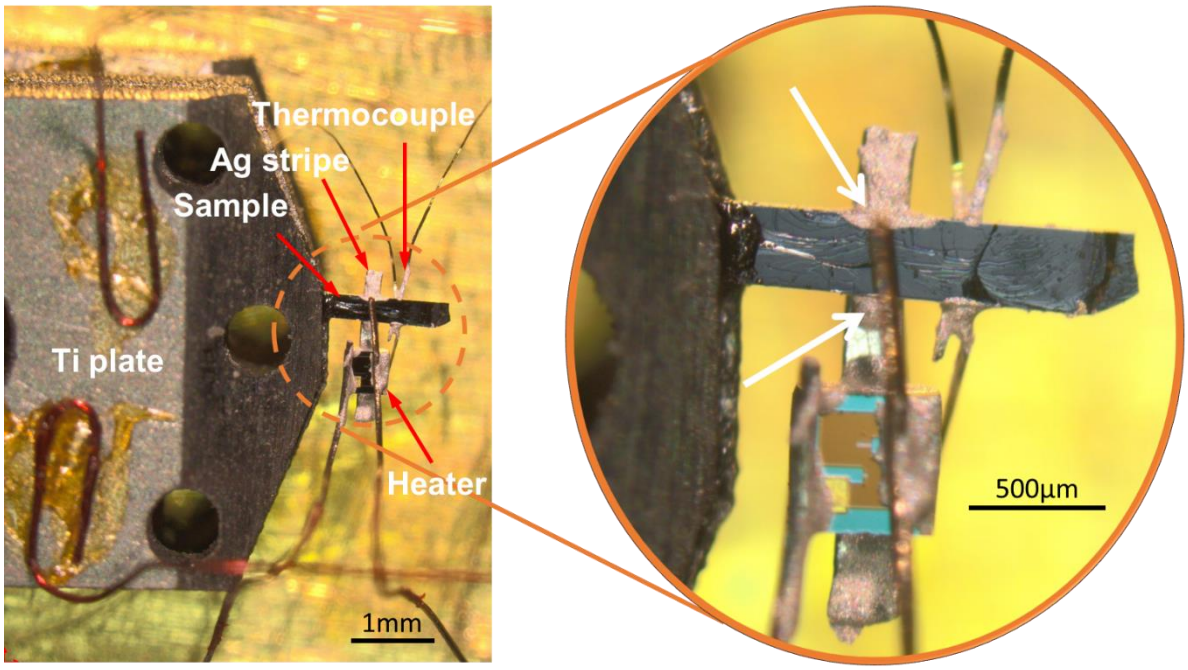

Figure 3.15: A photograph of the heat capacity setup for test sample #2 with the different elements indicated by the red arrows. Ag epoxy was applied to both edges of Sr_2RuO_4 as indicated by the white arrows.

Figure 3.15 shows a photograph of the heat capacity setup for test sample #2. The sample has gone through the following thermal preparation protocols:

(a) A silver stripe was attached to Sr_2RuO_4 with 6838;
(b) 6838 was applied to both edges of Sr_2RuO_4 as indicated by the white arrows in Figure 3.15;
(c) A thermocouple was attached to Sr_2RuO_4 with 6838;
(d) The whole sample was annealed at 450°C for 1 hour;
(e) A heater was placed on top of silver strip with 6838;
(f) The whole sample was annealed at 120°C for 1 hour;
(g) One end of Sr_2RuO_4 was attached to the Ti plate with Stycast;
(h) The whole sample was annealed at ~70°C overnight (>6 hours);
(i) The heater and thermocouple were wired up.

Steps (b) and (d) are the most important procedures for heat conduction. Step (b) guarantees that the applied heat conducts in the *ab*-plane and step (d) reduces the thermal barriers on the Ag/Sr_2RuO_4 interface and on the grain boundaries between the Ag particles. All the other steps are standard sample preparing procedures.

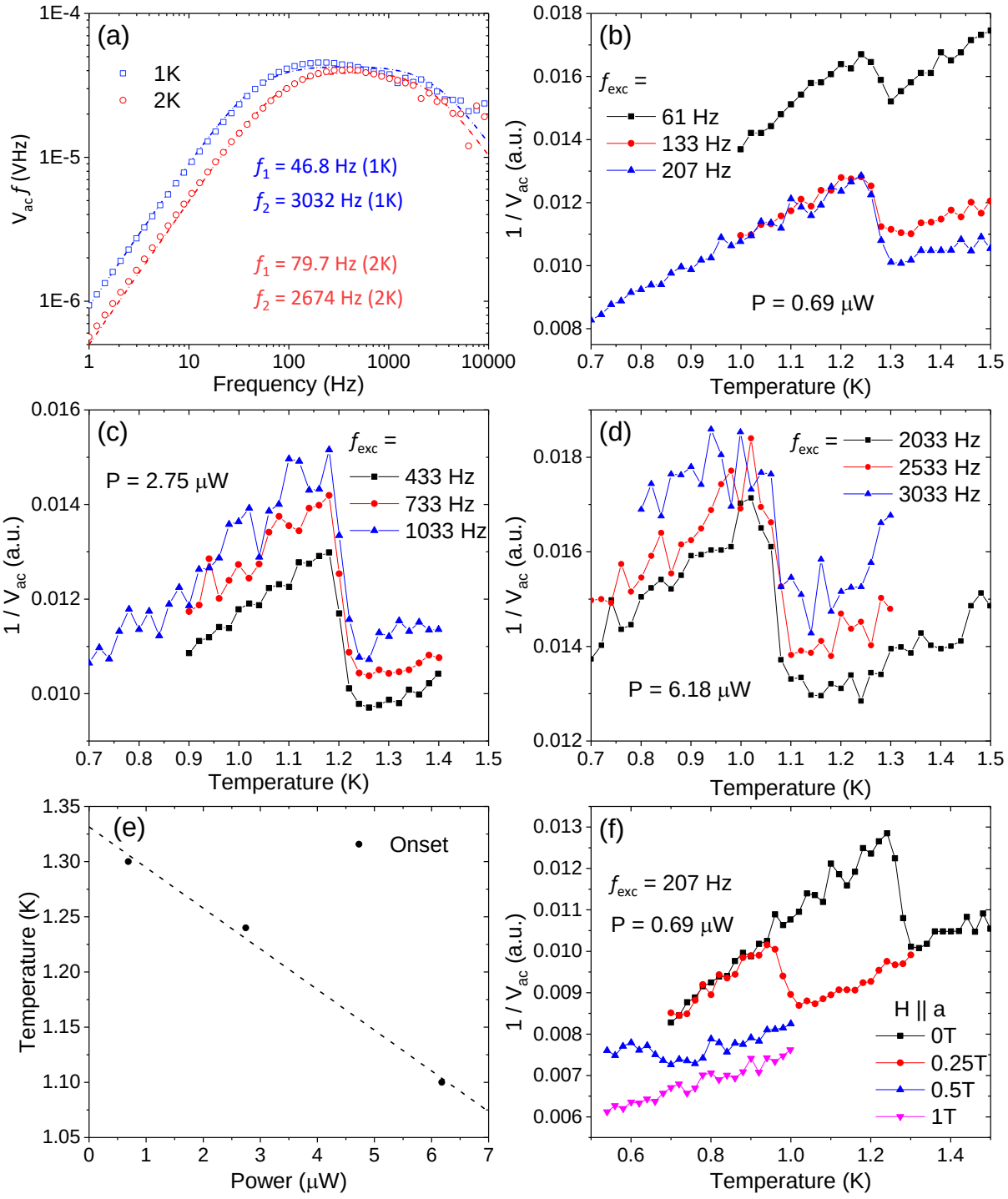

Figure 3.16: Results on the test sample #2. (a) Frequency sweeps at T = 1 K (blue) and 2 K (red) with the fitting results for f_1 and f_2. The dashed lines are the fitting curves based on equation (3-19). $1/V_{ac}$ against temperature with different frequencies and powers-- (b) low, (c) medium and (d) high powers. (e) T_c against power. Data points are onset T_c in the panel (b) to (d). The dashed line in panel (e) is a linear fit. (f) $1/V_{ac}$ against temperature with different fields applied parallel to the a-axis.

Figure 3.16(a) shows frequency sweeps below (1 K) and above (2 K) T_c. The frequency window is open and ranging from 46.8 Hz to 3032 Hz at 1 K and 79.7 Hz to 2674 Hz at 2 K. k_b and k_s at 1 K can be estimated with f_{exc} = 1 Hz:

$$k_b(1\text{K}) = \frac{P \times S}{V_{ac}} = \frac{6.18\ \mu\text{W} * 4.62\ \mu\text{V/K}}{936\ \text{nV} * \sqrt{2}} = 2.16 \times 10^{-5}\ \frac{\text{W}}{\text{K}}$$

and

$$k_s(1\text{K}) = k_b \frac{f_2}{f_1} = 2.16 * 10^{-5}\ \frac{\text{W}}{\text{K}} \times \frac{3032\ \text{Hz}}{46.8\ \text{Hz}} = 1.40 \times 10^{-3}\ \frac{\text{W}}{\text{K}}$$

k_b will be double in the real setup because both ends of the sample will be mounted on the Ti plates. The obtained value is comparable to but slightly smaller than the estimates in section 3.3. $k_s(1\text{ K})$ is in a good agreement with the estimated $k_{ab}(1\text{ K})$ in section 3.3. This result suggests that the annealing process is effective and heat conducts in the *ab*-plane.

Figure 3.16(b) shows $1/V_{ac}$ against temperature with low power and different frequencies. The heat capacity jump is smaller when f_{exc} is lower because the contribution of k_b is larger when f_{exc} is near f_1. To make the contribution of the heat capacity larger, a higher frequency is needed. The signal size with f_{exc} = 207 Hz and P = 0.69 μW is about 25 nV and the noise level from the lock-in output is about 2 nV/$\sqrt{\text{Hz}}$. A typical time constant in the measurement is 5 seconds and thus the noise is about 1nV. The noise is about 4% of the signal. Therefore, one is able to resolve approximately 20% of change in the measurements. The heat capacity jump in this case is about 35% which is near the limit of the current instrumentation. If the signal were smaller, the resolution would not be enough to resolve the transition. According to equation (3-27), the signal T_{ac} is proportional to the power P. To keep the signal-to-noise ratio when higher frequencies are used, the most effective way is to increase the power P but the consequence is that heating is larger according to equation (3-21). $1/V_{ac}$ against temperature with higher frequencies and powers are shown in Figure 3.16 (c) and (d). A superconducting transition is always observed and the transition happens at the same temperature independent of f_{exc} as long as the power remains the same. Figure 3.16 (e) shows T_c against power. The black points are the onset T_c determined from the data shown in panel (b) to (d). The dashed line is a linear fit and "real" T_c is about 1.33 K which agrees with the heat capacity measurement by the relaxation time method (see Figure 3.32, WDO3). k_b can be determined from the slope and it is 2.71×10^{-5} W/K which agrees with the value determined by the ac method, 2.16×10^{-5} W/K. Figure 3.16(f) shows $1/V_{ac}$ against temperature with different fields parallel to the *a*-axis. T_c is suppressed when the field is applied.

3.5 Introduction to the uniaxial stress technique

In this section, I will introduce the uniaxial stress apparatus used in this study before moving on to the heat capacity measurements under uniaxial stress. I will give a brief introduction to other uniaxial techniques and their applications and limitations. Subsequently, I will describe what has been improved in the current uniaxial stress apparatus and, most importantly, how to achieve homogeneous strain distribution in the strained samples.

3.5.1 Strain techniques

Anvil based uniaxial stress cell

An obvious way of applying uniaxial stress is to compress a sample with two anvils. When a sample is subject to a compressive force, it will compress along the force direction but expand transversely by the Poisson's ratio[4]. In this technique, the sample is usually held tight and locked by the frictional force on both ends. Therefore, the deformation on the sample is not distributed homogeneously across the ends, resulting in a transverse strain gradient even if both sample and anvil are carefully polished. Several configurations has been realized. The uniaxial stress can be achieved mechanically by torqueing a screw. In this method, the sample needs to be thermally cycled to adjust the applied stress because the torque can usually be applied only at room temperature. Heat capacity of UPt_3 under uniaxial [71] and biaxial[72] stress was studied using this methodology. An underdoped iron arsenide superconductor could also be detwinned by applying uniaxial stress [73] generated by a similar mechanism. Another way of applying uniaxial stress has been achieved by using He-activated bellow. The sample is held in one end and the other end is via a He-activated bellow with which the stress can be in situ adjusted by pressurizing the He gas. For example, heat capacity measurements of UBe_{13} [74], [75] and $CeIrIn_5$ [76] under uniaxial stress have been realized by this method.

[4] The transverse expansion corresponds to the material having a positive Poisson's ratio. Although positive Poisson's ratios exist for the huge majority of known materials, negative ones are also possible and in those very rare cases compression leads to transverse contraction.

Sample on a piezoelectric actuator

Uniaxial stress can be achieved by gluing a sample directly on top of a piezoelectric actuator. This use of the piezoelectric actuator provides a simple way to in situ adjust the strain. This technique was developed for modifying the electronic properties in semiconductors at low temperature [77]. Chu *et al.* [78] applied the technique to a correlated electron system.

In this technique, the sample needs to be prepared in the shape of a thin slab and glued on top of a piezoelectric lead zirconate titanate (PZT) stack. When a positive voltage is applied, PZT expands along the poling direction and the thin slab deforms accordingly. The applied strain in the sample can be measured by placing a resistive strain gauge on top of it. However, the maximum applied strain in this technique is limited by the maximum deformation, which is approximately 0.1% strain. In addition, the thermal expansion coefficient of PZT along the poling direction is about $-3 \times 10^{-6}\ \mathrm{K}^{-1}$ [79], i.e. PZT expands as it is cooled. In contrast, typical materials contracts about 0.1% to 0.5% as temperature decreases from room temperature to 4K. In this technique, therefore, differential thermal expansion tensions the sample when it cools down to 4K. If this tensile strain is fully transmitted, it is usually beyond the limit of PZT to bring the sample back to the zero strain.

Hicks *et al*. [80] designed a new strain apparatus based on PZT. In their design, they carefully null the differential thermal stress and the applied strain on the sample can be in principle as high as 1%. In my study, I use this type of strain apparatus. Therefore, I will introduce the principle of operation and related topics.

3.5.2 Strain apparatus

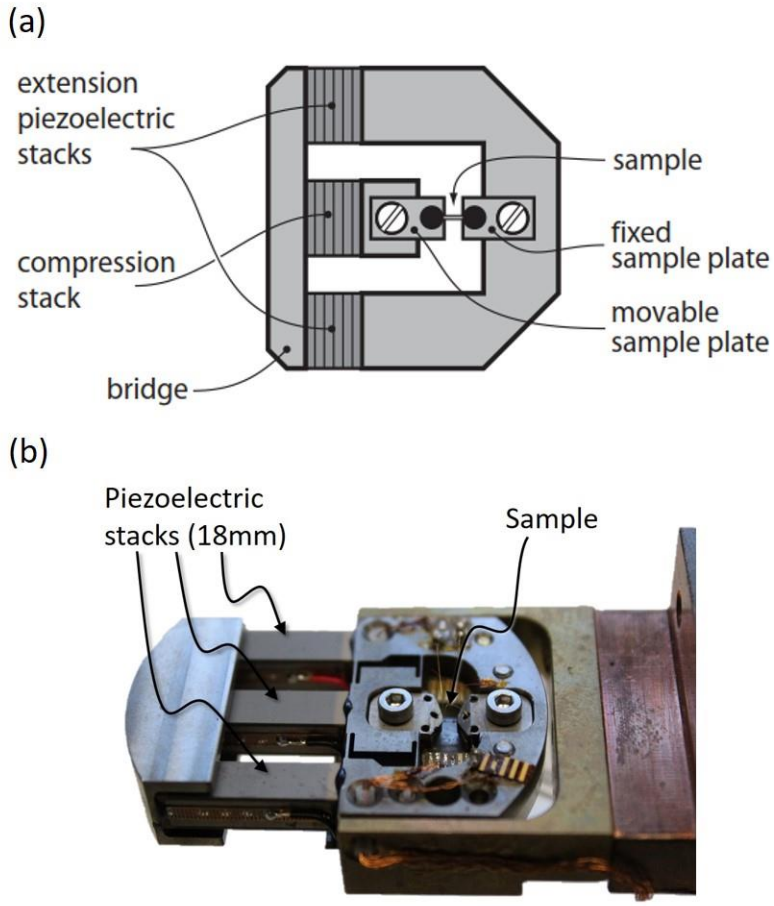

Figure 3.17: (a) A schematic diagram for a strain device. Reproduced from [80]. (b) A photograph of the strain apparatus.

Figure 3.17 shows a schematic diagram and a photograph for a strain apparatus. A sample sits across the gap between movable plates. Both compressive and tensile strains can be applied to the sample by manipulating the piezo stacks (PZSs). The sample is under compression (extension) when a positive (negative) voltage is applied on the compression stack (extension stacks) or vice versa.

There are several advantages in this design. The use of the PZS provides rapidly and in situ tunable strains. A large displacement can be imposed on a sample by using long PZSs, so the strain is amplified over that intrinsically achievable in the PZSs. The longest PZSs used in this study are 18mm long and a compressive strain approximately 0.7% was achieved in my study. Last but not

the least, the PZSs are arranged in such a way their thermal contraction largely cancels out. The entire strain apparatus can also be cooled down to cryogenic temperature, e.g. 100mK.

The displacement as a function of strain has a hysteresis loop on PZSs. To eliminate this hysteresis, a capacitor is used to monitor the displacement. The capacitor is composed of two parallel metal plates with area approximately 3 x 5 mm^2 and a separation of approximately 30 μm. One metal plate is fixed to the movable sample plate and the other is to fixed sample plate.

3.5.3 Stress and strain

Stress is a quantity describing how force is distributed and strain is a quantity describing how a sample deforms when it subjects to a force. The type of the stress and strain depends on the type of force inserted on a sample. Figure 3.18 shows the schematic diagram for (a) normal strain and stress and (b) shear stress and shear strain.

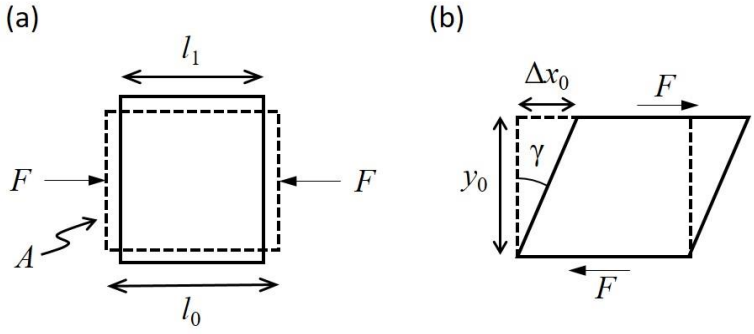

Figure 3.18: Schematic diagrams for (a) normal stress and normal strain, and (b) shear stress and shear strain. The dashed lines indicate the original shape.

When equal and opposite forces are applied normal to the opposite surfaces, the forces result in normal stress σ on the surfaces and normal strain ε on the sample, which are given by

$$\sigma = \frac{F}{A} \quad \text{and} \quad \varepsilon = \frac{l_0 - l_1}{l_0}. \tag{3-35}$$

In contrast, when a pair of equal and opposite forces are applied parallel to opposite surfaces, the forces results in shear stress τ on the surfaces and shear strain on the sample, which are given by

$$\tau = \frac{F}{A} \quad \text{and} \quad \gamma \cong \tan\gamma = \frac{\Delta x_0}{y_0} \tag{3-36}$$

At low strain where the responses are still elastic, the relation between stress and strain is given by Hooke's law:

$$\sigma = E \times \varepsilon \quad \text{and} \quad \tau = G \times \gamma \tag{3-37}$$

where E is the Young's modulus and G is the shear modulus.

Poisson's ratio

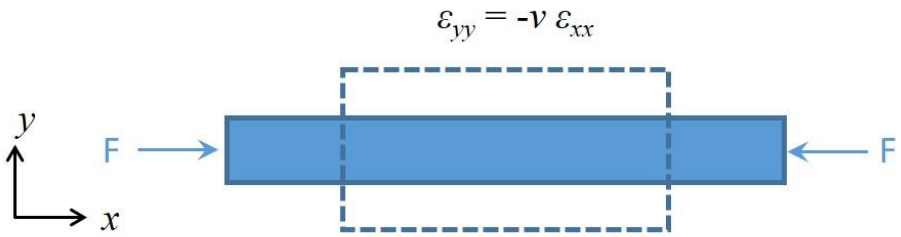

Figure 3.19: schematic diagram of a deformation of a sample under compression. The sample is compressed along the x-direction and expanded laterally according to its Poison ratio along y-direction.

Figure 3.19 shows the schematic diagram for the deformation of a sample under compression. When opposite forces F are applied to a sample along the axial direction $\hat{x}$, the sample is compressed along $\hat{x}$ and expanded transversely along $\hat{y}$. The amount of transverse strain is material-related and the relation between the axial strain ε_{axial} and the transverse strain ε_{trans} is defined as Poisson's ratio ν,

$$\nu = -\frac{\varepsilon_{trans}}{\varepsilon_{axial}}. \tag{3-38}$$

A sample can therefore have nonzero strain without any applied stress along the direction concerned.

Hooke's law for tetragonal lattice

To generalize the equation to three dimensional case, the displacement field $\boldsymbol{u}$ is often used, where $\boldsymbol{u}$ is a three dimensional vector field defining the displacement of a material at any point. The different components of the strain tensor ε_{ij} are defined by

$$\varepsilon_{ij} = \frac{1}{2}\left(\frac{\partial u_i}{\partial X_j} + \frac{\partial u_j}{\partial X_i}\right) \tag{3-39}$$

where X is the coordinate and the indices i and j label the direction of the principal axes. The full tensor $\boldsymbol{\varepsilon}$ has the following form:

$$\boldsymbol{\varepsilon} = \begin{pmatrix} \varepsilon_{xx} & \varepsilon_{xy} & \varepsilon_{xz} \\ \varepsilon_{yx} & \varepsilon_{yy} & \varepsilon_{yz} \\ \varepsilon_{zx} & \varepsilon_{zy} & \varepsilon_{zz} \end{pmatrix} = \begin{pmatrix} \varepsilon_{xx} & \frac{1}{2}\gamma_{xy} & \frac{1}{2}\gamma_{xz} \\ \frac{1}{2}\gamma_{yx} & \varepsilon_{yy} & \varepsilon_{yz} \\ \frac{1}{2}\gamma_{zx} & \frac{1}{2}\gamma_{zy} & \varepsilon_{zz} \end{pmatrix} \tag{3-40}$$

The diagonal elements represent the normal strains, whereas the off-diagonal elements represent the shear strains and $\gamma_{ij} = \gamma_{ji}$ by symmetry. The applied strain in this study is exclusively along the a-axis of Sr_2RuO_4. Therefore the notation ε_{xx} is used and $\varepsilon_{xx} > 0$ ($\varepsilon_{xx} < 0$) represents the sample is under tension (compression) along the *a*-direction.

Hooke's law can be generalized into three dimensions. In the general case, there will be 81 elements in the tensor. However, many elements can be simplified due to the symmetry of the material. In a system which has tetragonal symmetry, the tensor, which only has six independent parameters, can be expressed as:

$$\begin{pmatrix} \varepsilon_{xx} \\ \varepsilon_{yy} \\ \varepsilon_{zz} \\ 2\varepsilon_{yz} \\ 2\varepsilon_{zx} \\ 2\varepsilon_{xy} \end{pmatrix} = \begin{pmatrix} \frac{1}{E_x} & -\frac{\nu_{yx}}{E_x} & -\frac{\nu_{zx}}{E_z} & 0 & 0 & 0 \\ -\frac{\nu_{xy}}{E_x} & \frac{1}{E_x} & -\frac{\nu_{zy}}{E_z} & 0 & 0 & 0 \\ -\frac{\nu_{xz}}{E_x} & -\frac{\nu_{yz}}{E_x} & \frac{1}{E_z} & 0 & 0 & 0 \\ 0 & 0 & 0 & \frac{1}{G_{xz}} & 0 & 0 \\ 0 & 0 & 0 & 0 & \frac{1}{G_{xz}} & 0 \\ 0 & 0 & 0 & 0 & 0 & \frac{1}{G_{xy}} \end{pmatrix} \begin{pmatrix} \sigma_{xx} \\ \sigma_{yy} \\ \sigma_{zz} \\ \sigma_{yz} \\ \sigma_{zx} \\ \sigma_{xy} \end{pmatrix} \tag{3-41}$$

where E_i are the Young's moduli, ν_{ij} are the Poisson's ratios and G_{ij} are shear modulus. By symmetry, $\nu_{ij} = \nu_{ji}$. The elastic tensor or Sr_2RuO_4 has been measured at T = 300 K by resonance ultrasound spectroscopy [81]. By inverting the elastic tensor, $E_x = 175$ GPa, $E_z = 178$ GPa $\nu_{xy} = 0.394$, $\nu_{yz} = 0.207$, $G_{xz} = 65.7$ GPa and $G_{xy} = 61.2$ GPa.

In the strain apparatus, the stress is applied along the a-axis of the Sr_2RuO_4 sample and therefore only σ_{xx} is non-zero. To avoid confusion, I will explain the terminology used in the study, i.e. the difference between strain and uniaxial stress. The piezoelectric stacks generate displacements by the applied voltages and then push against the sample to deform it. It is clear from the tensor that when the stress is applied along x-direction, the sample deforms not only along the x-direction but also along the y- and z-directions. The amount of deformation in the x-direction can be measured by the capacitor but the strain on the sample is not uniaxial because sample expanded laterally according to its Poisson's ratio. In contrast, the stress on the sample is exclusively along x-direction so stress is the quantity that is uniaxial.

3.5.4 Sample mounting

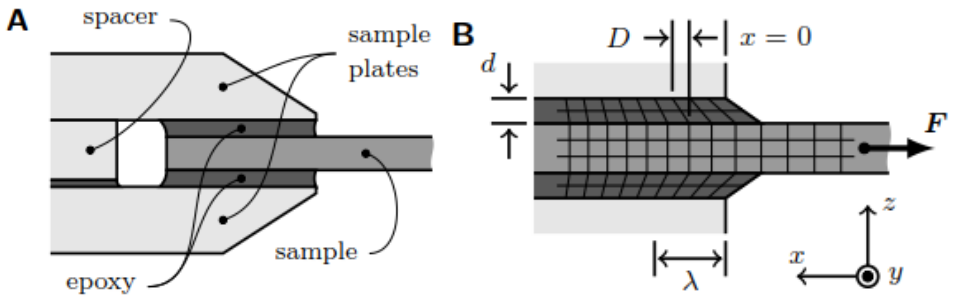

Figure 3.20: (a) A schematic diagram for the symmetric sample configuration. (b) Reproduced from [82].

The sample mounting proceeds as follows. A sample is sandwiched between the sample plates and fixed with epoxy layers in a symmetric way. When a force is applied to the sample, the load is transferred to the sample plates through the epoxy layers over a characteristic length scale λ. $D(x)$ is the displacement of sample with respect to its unloaded position and has the form [80]:

$$D(x) = D(0)e^{-x/\lambda}, \qquad \lambda = \sqrt{\frac{Etd}{2G}} \tag{3-42}$$

where E and t are the Young's modulus and thickness of the sample and G and d are the shear modulus and thickness of the epoxy respectively. The displacement $D(x)$ decays exponentially into the mounts.

Here I estimate a typical λ, using E = 175 GPa for Sr_2RuO_4, t = 150 μm, d = 15 μm, G = 6 GPa. In this case, λ = 180 μm. The overlap between the sample and the sample plates is greater than 400 μm and this amount of overlap provides enough epoxy length for most of the applied strain to be transmitted to the sample.

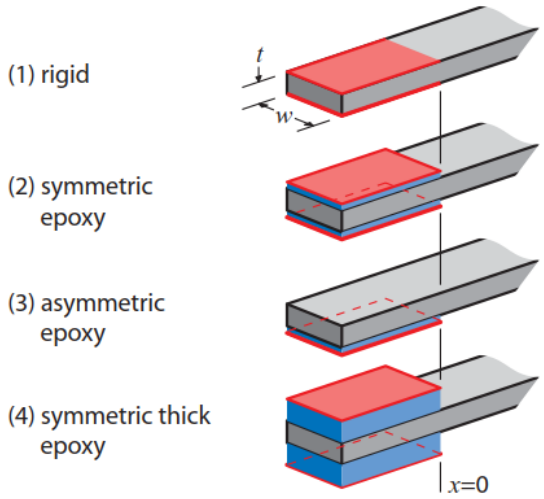

Figure 3.21: Schematic diagrams for the four different mounting models. The pink layers are constrained faces and the blue layers are the epoxy layers. Reproduced from [80].

Figure 3.21 shows schematic diagrams for the four different mounting models. The blue layers represent epoxy layers. The pink layers are constrained faces which represent the interface between sample plates and epoxy layers. A sample is fixed between the top and bottom sample plates and glued symmetrically with (1) hard epoxy layers, (2) soft and thin epoxy layers and (4) soft and thick epoxy layers. In model (3), the sample mounting is asymmetric and only the bottom surfaces are fixed to the sample plates with soft and thin epoxy layers.

M. Barber [82] used finite element analysis to simulate the strain ε_{xx} in different mounting models. The sample and epoxy were set to be isotropic with a Poisson's ratio of 0.3. The Young's modulus for the epoxy was set to be 1/10 of that of the sample. The sample has thickness t, width $3t$ and an exposed length $10.5t$. The thickness of the epoxy layers is $0.25t$ for the thin ones and t for the thick ones. The lengths embedded in the epoxy layers are much longer than the characteristic length λ to ensure that the load is fully transmitted. The differential thermal contraction is neglected in this simulation. The pink lines represent the constrained faces shown in Figure 3.21. The strain in all cases was set to be -0.1%, i.e. the constrained faces on both ends were moved toward to each other by 0.1% of the exposed length. The deformations are exaggerated by a factor of 200 for clarity.

Figure 3.22(a) shows ε_{xx} in the center *xz*-plane of the sample for models 1 to 3 and (b) shows ε_{xx} in the center *xy*-plane of the sample for model 2. In model 1, the strain is almost completely transmitted into the sample but high stress concentrates at the edge of the mounts. These points would increase the risk of a sample fracture. The stress concentration is less in model 2 and 3. The strain in the middle of the sample is less than 0.1% because of the soft epoxy layers. There is a strain gradient in the middle of the sample in model 3 because of the asymmetric mounting which leads to strain inhomogeneity. By contrast, the strain is homogeneous in model 2 as shown in Figure 3.22 (a) and (b).

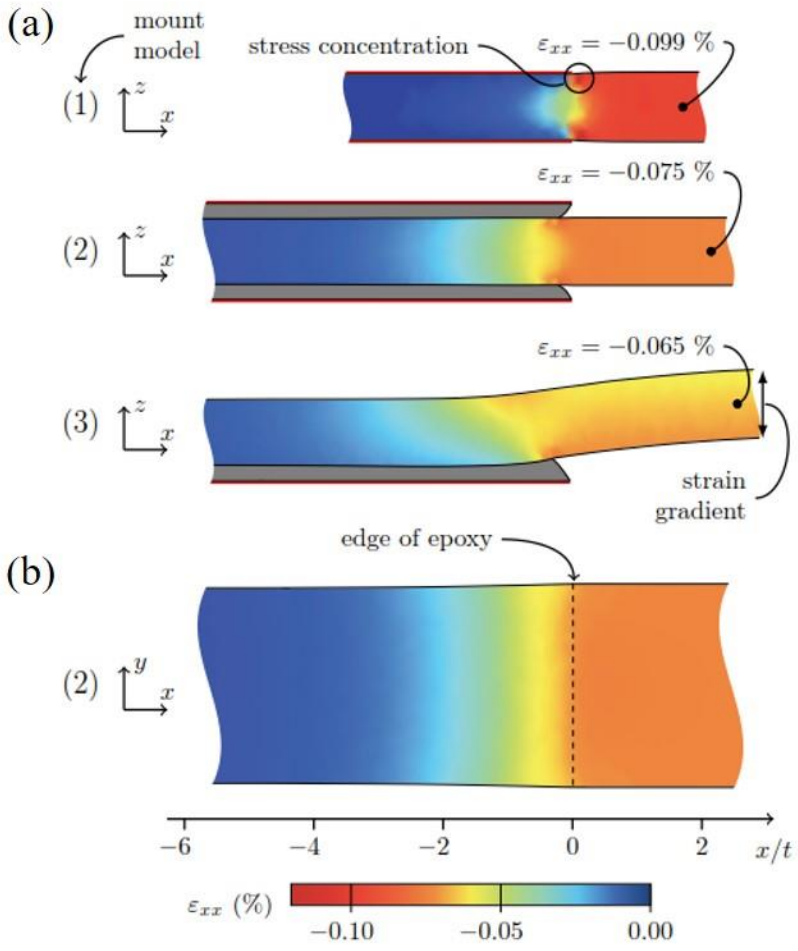

Figure 3.22: Finite element analysis for model 1 to 3. The pink lines represent constrained faces and grey layers represent epoxy layers. Sample plates were set to have displacement of $-0.1\% \times L$ in all cases. The deformations are exaggerated by a factor of 200. (a) Simulations on the center *xz*-plane. (b) A simulation for model 2 on the center *xy*-plane. Reproduced from [82].

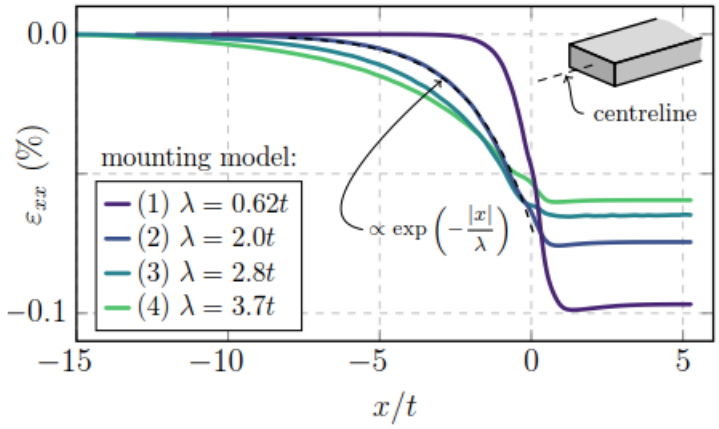

Figure 3.23: ε_{xx} profiles along the centerline of the sample for different mounting models. Reproduced from [82].

Figure 3.23 shows ε_{xx} profiles along the centerline of the sample for different mounting models. $x < 0$ represents the region where epoxy layers are. In all cases, ε_{xx} decays exponentially into the epoxy mounts. The dashed line is an exponential fit to model 2. The strain in the middle of the sample is smaller when λ is longer because the effective strained length is longer than the exposed length. One of the uncertainties in determining ε_{xx} in the middle of sample comes from λ because in practice the thickness of the epoxy layers are ill-defined.

Inhomogeneity	**Mounting model 1**	**Mounting model 2**	**Mounting model 4**
5%	0.5w	0.2w	0.1w
1%	0.9w	0.5w	0.4w

Table 3.1: The certain amount of ends needs to be exclude to reach a certain level of inhomogeneity in the center portion of the sample. Adapted from [82].

If the sample is mounted symmetrically, the strain distribution will be homogeneous in the center portion of the sample as shown in Figure 3.22(b). The inhomogeneity decays exponentially as shown in Figure 3.23. For the strain-related experiments, measurements should be carried out in the homogeneous region and exclude the signal from both ends near the mounts. Table 3.1 shows a guide for designing the experiments for different mounting models. It illustrates that how much of the ends needs to be excluded to reach a certain level of inhomogeneity in the center portion of the sample. For example, to reach 1% inhomogeneity with mounting model 2, the length that needs to be excluded on both ends is 0.5w. The best mounting model is the model 2, which can provide high and homogeneous strain in the center without high stress concentration at the edge of the mounts.

3.6 Samples with uniaxial stress apparatus in dilution refrigerator

In section 3.4, I demonstrated that heat capacity measurements under strongly non-adiabatic conditions are feasible. The test sample #2 which mimics the real configuration is able to show a superconducting transition at T_c. In section 3.5, I briefly introduce the uniaxial stress apparatus used in this study. The next step is to put samples on the uniaxial stress apparatus. In total, I performed heat capacity measurements under uniaxial stress on four different samples. In this section, I will use sample #3 to describe characteristic behaviors when a sample is under uniaxial stress.

3.6.1 Heat capacity measurements under uniaxial stress

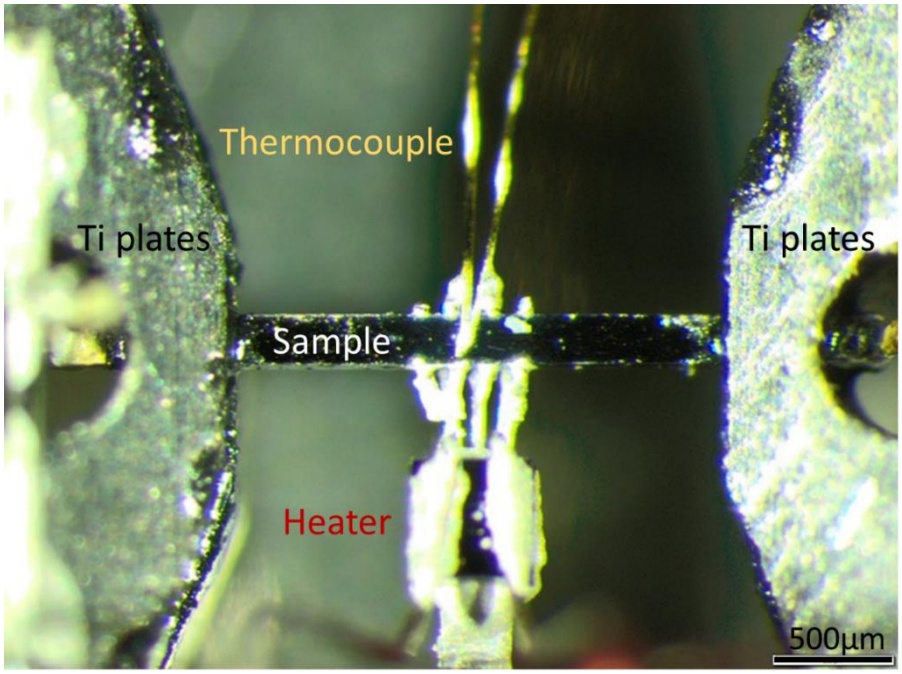

Figure 3.24: A photograph of the setup for heat capacity measurements of Sr_2RuO_4 under uniaxial stress.

Figure 3.24 shows a photograph of the setup for heat capacity measurements of Sr_2RuO_4 under uniaxial stress. A Sr_2RuO_4 crystal, previously cut to an appropriate size and aspect ratio, is placed

across the gap between Ti plates and fixed with Stycast. A heater and a thermocouple are thermally connected to the sample with silver wires and epoxy.

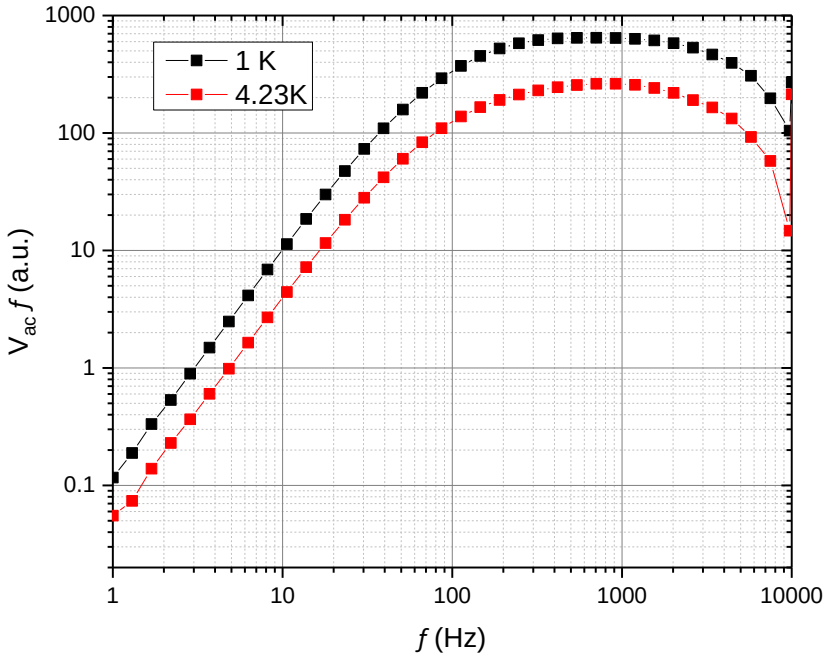

Figure 3.25: Frequency sweeps for sample #3 at T = 1 K and 4.23 K.

Figure 3.25 shows frequency sweeps at T = 1 K and 4.23 K. The frequency windows are open and remain more or less unchanged. This ensures that the heat capacity can be measured from T = 1 K to 4.23 K as long as f_{exc} is in this window which ranges from approximately 100 Hz to 5 kHz. k_b(1 K) cannot be estimated this time with f_{exc} = 1 Hz because the signal is cut by a low temperature transformer (see section 3.9.1 for details). However, it can be estimated by f_1. According to equation (3-23), $k_b = \omega_1 C$. The sample dimensions for the strained part are 2 mm long, 250 µm wide and 150 µm thick. The specific heat at T = 1 K is about 55 mJ/mol-K. Therefore,

$$k_b(1\text{K}) = \omega_1 C = 4\pi * 100\ \text{Hz} \times 5.74 * 10^{-8}\ \text{J/K} = 7.21 * 10^{-5}\ \text{W/K}$$

and, furthermore,

$$k_s(1\text{K}) = k_b \frac{f_2}{f_1} = 7.21 * 10^{-5}\ \text{W/K} \times \frac{5\ \text{kHz}}{100\ \text{Hz}} = 3.605 * 10^{-3}\ \text{W/K}.$$

Both values agree well with the estimates in section 3.3. That k_s(1K) agrees with k_{ab}(1K) indicates that heat conducts in the *ab*-plane. The next question is: Which frequency should be used in the measurements?

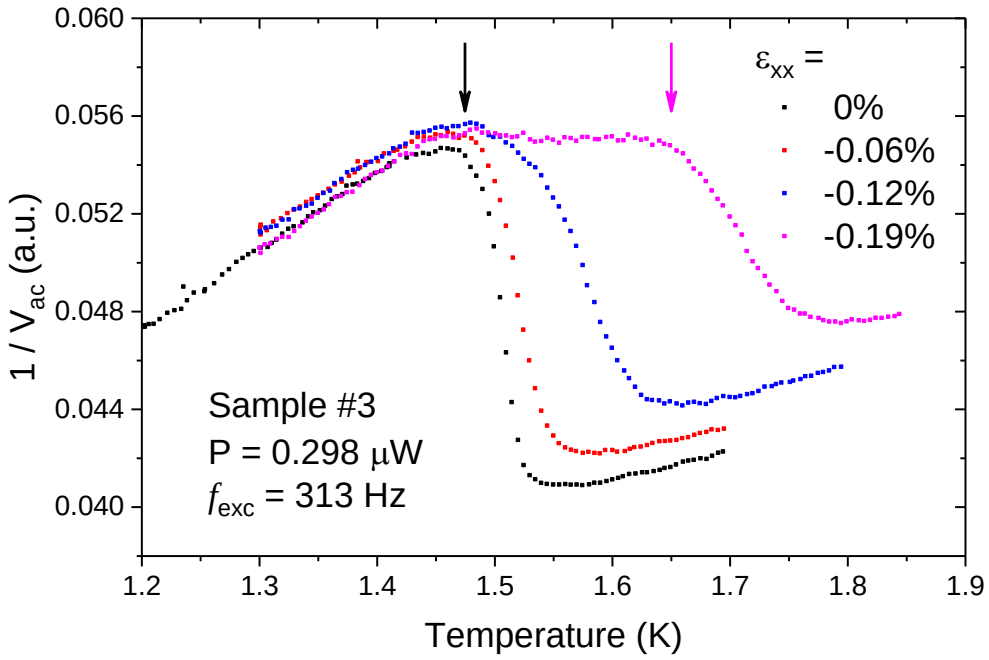

Figure 3.26: Heat capacity measurements for sample #3 at low f_{exc} with different strains. The black arrow indicates the unstrained T_c and the pink indicates the increase of T_c for ε_{xx} = -0.19%.

According to equation (3-27), a lower frequency gives a larger signal so a relatively low frequency was used to begin with. Figure 3.26 shows heat capacity measurements for sample #3 at different strains with a relatively low f_{exc} compared with the available frequency window. The black curve shows the measurement for ε_{xx} = 0%. There is a superconducting transition at T_c approximately 1.5 K. The transition temperature increases with increasing strain. The pink curve shows the measurement at ε_{xx} = -0.19%. The transition as indicated by the pink arrow goes up to 1.65 K but there is a second feature at 1.5 K as indicated by the black arrow. This 1.5 K kink is related to the unstrained T_c which indicates that there are signals coming from unstrained parts of the sample too, and that the measurement is sensitive to the strain profile of the sample mounted in the strain rig.

Frequency effect

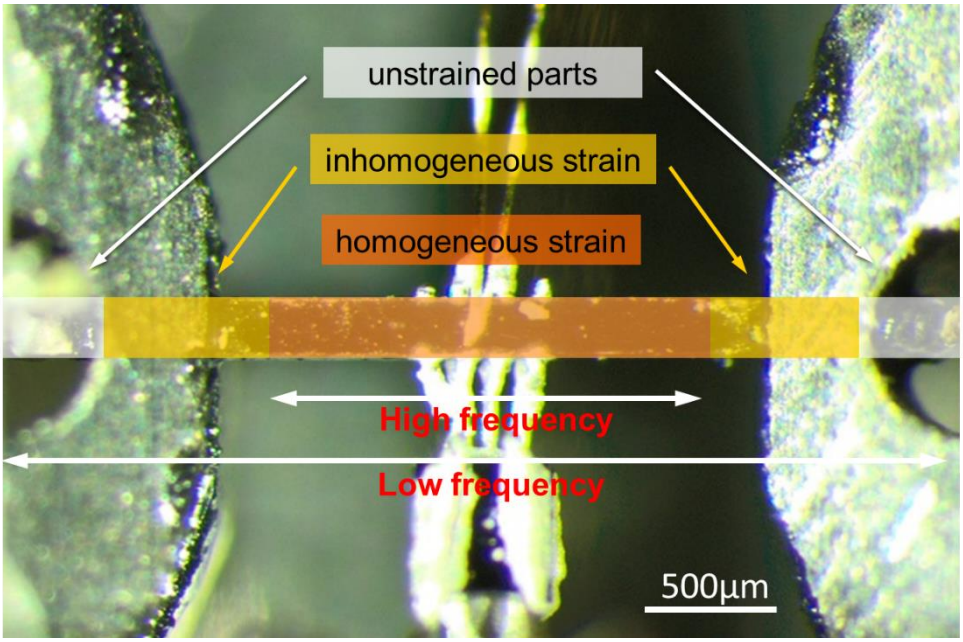

Figure 3.27: A photograph illustrating the inhomogeneity across the sample with different colored areas. High frequency is needed to probe the homogeneous part.

Figure 3.27 shows a photograph of the sample setup. The sample is fixed with Stycast on the Ti plates. When a strain is applied to the sample, the strain profile is very inhomogeneous across the sample. It can be divided into three regions. The white regions are the parts of sample without strain. In the yellow regions, the strain is very inhomogeneous and goes from zero to the applied strain. In the red region, the strain is almost homogeneous. This is the part of the sample that one needs to probe. This means that a high frequency should be used to do the measurements. Otherwise, the response from unstrained and inhomogeneous parts go into the measured signals. The next question is: What is the lowest frequency that can be used to ensure this and to obtain a signal as large as possible?

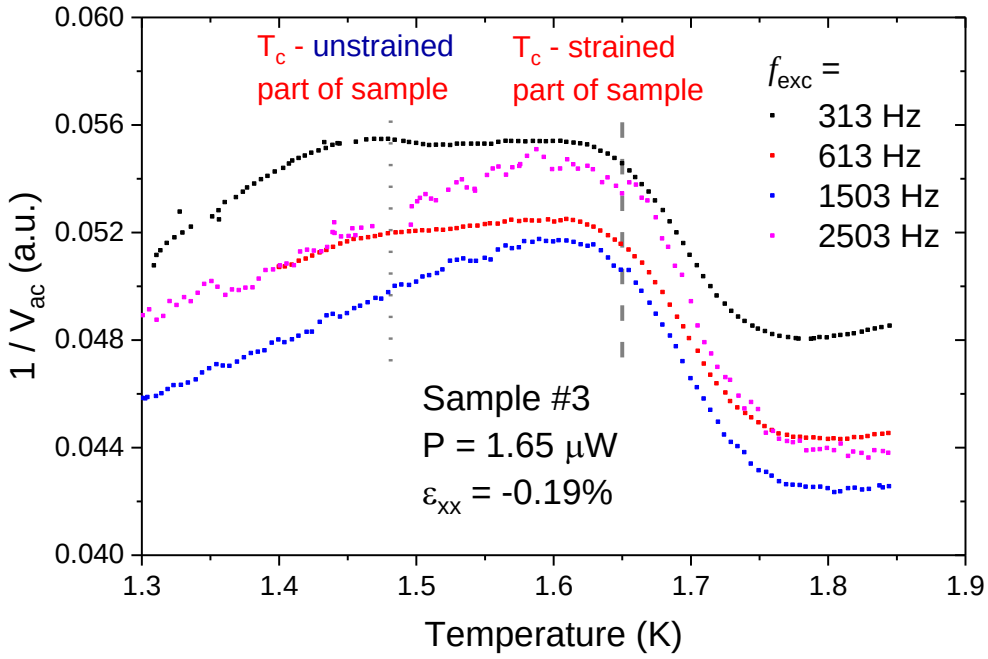

Figure 3.28: Frequency effect. Heat capacity measurements for sample #3 under compressive strain with different f_{exc}. The dotted (dashed) line indicates the T_c from unstrained (strained) part of the sample. The kink disappears with higher frequencies.

Figure 3.28 shows heat capacity measurements for sample #3 at ε_{xx} = -0.19% with different frequencies. There are two features in the graph, a heat capacity jump corresponding to the increase of T_c and a kink corresponding to the T_c from unstrained parts of sample. The size of the kink becomes smaller with increasing frequency f_{exc} = 613 Hz and vanishes with f_{exc} = 1503 Hz, whereas the size of the heat capacity jump remains unchanged. Therefore, the lowest frequency for probing the homogeneous part is approximately 1500Hz for sample #3.

3.6.2 Characteristic length

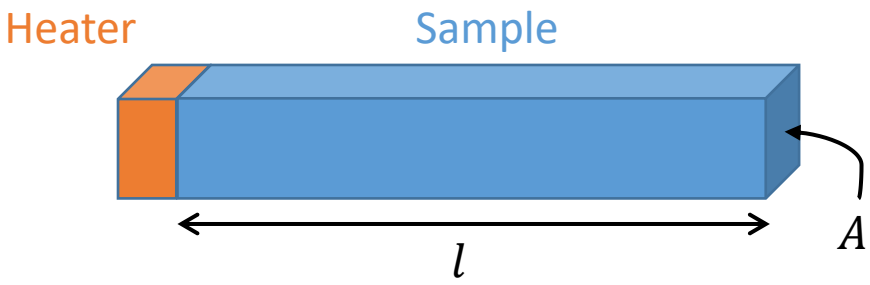

Figure 3.29: A schematic diagram for a long sample with a heater attached to one end.

The frequency effect indicates that there is a length scale related to f_{exc}. Figure 3.29 shows the concept of the characteristic length or probed length. A heater is attached to a long sample on its left end. For the heat propagating from the left to the right end, it takes the time

$$\tau = \frac{C}{k}, \tag{3-43}$$

where C is the heat capacity and k is the thermal conductance of the sample. C and k can be expressed as follow:

$$C = cAl \text{ and } k = \kappa A/l\,, \tag{3-44}$$

where c is the specific heat, κ is thermal conductivity, A is cross-sectional area and l is length. Therefore, $\tau = c\,l^2/\kappa$ or

$$l = \sqrt{\frac{\kappa}{\omega c}}, \tag{3-45}$$

where $\omega = 1/\tau$. l is called characteristic length or the probed length. It describes how far heat can propagate in the sample with the applied ω. The higher the frequency, the smaller the probed length. This illustrates the reason why the homogeneous region can be probed with high frequencies. Table 3.2 describes the length scales of several materials used in the measurements at T = 1 K with $2f_{exc} = \omega/2\pi = 4$ kHz.

Table 3.2 shows the estimates of characteristic length for different materials used in the heat capacity measurements. The characteristic length of Sr_2RuO_4 at T = 1 K with $2f_{exc}$ = 4 kHz is 0.64 mm, about half the length of the homogeneous part of a strained sample. The lowest frequency found to probe the homogenous part of sample #3 is about 1500 Hz, which is consistent with this estimate. In heat capacity measurements, heat is conducted via a silicon substrate and silver wires. The thickness of the substrate is about 0.25 mm and the length of silver wires is about 1 mm. Both

components have length scales far smaller than the corresponding characteristic lengths in Table 3.2. It suggests that heat is well thermalized in this setup even with a kHz excitation frequency.

	Specific heat [a] c (mJ/mol-K)	Thermal conductivity [b] κ (W/m-K)	Density d (g/cm^3)	Characteristic length l (mm)
Sr_2RuO_4 (*ab*)	55	10	5.92	0.64
Sr_2RuO_4 (*c*)	55	0.1	5.92	0.064
Silver	0.8	3940	10.49	44.9
Silicon	0.028	6.93	2.328	10.9
Gold	1	546	19.3	14.9

Table 3.2: Estimates of characteristic lengths at T = 1 K with $2f_{exc} = \omega/2\pi =$ 4 kHz for the materials used in heat capacity measurements. [a] Specific heat data: Silver and gold are from [83]; silicon is from [84]. [b] Thermal conductivity data: Sr_2RuO_4 is from [69]; silver, silicon and gold are from [68].

3.6.3 The direction of the heat flow

Figure 3.30: Schematic diagrams for heat flows (a) from *c*-axis and (b) from *b*-axis. The dashed lines indicate the homogeneous region of the sample.

To probe the homogeneous region, a high f_{exc} is needed. It is, therefore, important to conduct heat in the ab-plane and push f_2 to the higher frequency end of the available range. If the heat is conducted via the c-axis as shown in Figure 3.30(a), by the time heat reaches to the bottom, the heat on the top has already propagated to the inhomogeneous parts because $k_{ab} \gg k_c$ and thus $l_{ab} \gg l_c$ as shown in Table 3.2. It is almost impossible to probe the homogeneous region in the geometry. In contrast, if heat is conducted via the b-axis, the heat flow is evenly distributed and it is therefore possible to probe the homogeneous region with high f_{exc}.

3.6.4 The role of the annealing

As described in section 3.2.3, f_2 is determined by τ_h, τ_θ and τ_{int}, which are the thermalization time scales in the setup. Whichever has the largest value dominates f_2 and it is better to make all of them as small as possible. τ_{int} is an intrinsic value for the sample but τ_h and τ_θ strongly depend on the annealing process because it can dramatically change the thermal conductance k_h and k_θ.

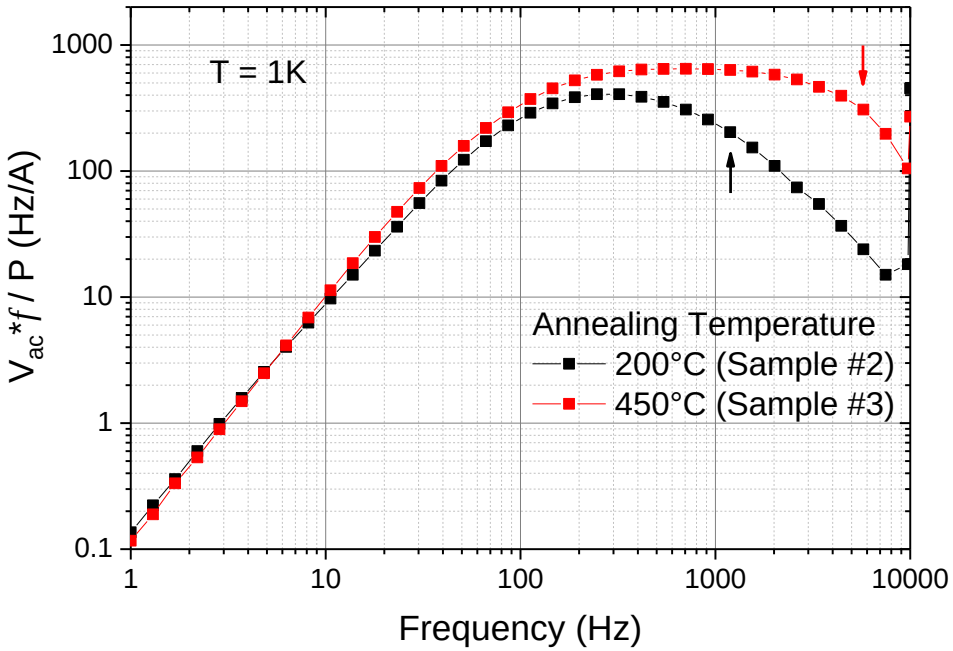

Figure 3.31: Frequency sweeps at T = 1 K for samples at different annealing temperatures. The arrows indicate the upper cut-off frequencies f_2.

Samples #2 and #3 have similar configurations but different annealing temperatures. Figure 3.31 shows the frequency sweeps for these two samples. There is a good agreement at low frequency, but huge difference at high frequencies. Sample #2 has a lower $f_2 \approx 1.2$ kHz as indicated by the black arrow and it is expected that τ_h and τ_θ limit the f_2 because of the low k_h and k_θ, which are likely dominated by the poor interfaces between sample and 6838. The silver particles do not have enough energy to diffuse into the sample at 200°C but do at 450°C. The diffusion process grows exponentially with the annealing temperature. It is reasonable that τ_h and τ_θ in sample #3 are at least an order of magnitude smaller than that in sample #2. f_2 in sample #3 would be greater than 12 kHz if f_2 were dominated by τ_h and τ_θ. The red arrow indicate f_2 in sample #3 which is about 5.5 kHz, suggesting that f_2 is dominated by τ_{int}. The calculated value in section 3.6.1 agrees with the estimates as well.

Although the lowest frequency to probe the homogeneous region in sample #2 is about 3 kHz, which is greater than its upper cut-off frequency f_2, it is still possible to probe the sample with high f_{exc} because there is still small amount of temperature oscillation on the sample, which reflects the heat capacity. However, this signal is small compared to that in sample #3. It is clear from Figure 3.31 that the signal with and without proper annealing can be an order of magnitude different and it is therefore important to anneal the sample properly to obtain a better signal size.

In short, the frequency effect in the ac-heat-capacity measurements makes use of the intrinsic properties of the material such that the homogeneous region can be probed. It is important that f_2 is tuned in such a way that it is dominated by the intrinsic properties of the sample as well. Otherwise, other factors come into play and signal size drops dramatically.

3.7 Smearing factors

In this section, I will discuss several factors that can smear the transition(s). They can be divided into two categories. The first one stems from the sample itself (intrinsic) and from the configuration (extrinsic) and the second one is from the measurement parameters. I will raise the issues in this section and then describe the parameters that have been achieved in practice, in section 3.8 for the sample part and in section 3.9 for the experimental part.

3.7.1 Sample quality

Several kinds of defects exist in Sr_2RuO_4 single crystals: point defects, dislocations, Ru inclusions, etc.. The T_c of Sr_2RuO_4 is highly dependent on the impurity concentration. The fewer impurities, the higher the T_c. The optimal T_c of Sr_2RuO_4 is about 1.5 K. Defect contributions affect heat capacity measurements because it is a bulk-sensitive probe. The transition width determines the quality of the sample and also sets experimental limits on resolving fine structures, e.g. two transitions with a small difference in T_c. Three batches of Sr_2RuO_4 single crystals were used in this study, from three different crystal growers with different sample naming conventions. Here, they are referred to as WDO3, C362 and Naoki3. Figure 3.32 shows heat capacity measurements on the three sample batches with the relaxation time method in the PPMS. The heat capacity results contain signals from electrons and phonons. The transition width for WDO3 is about 100 mK and those for C362 and Naoki3 are less than 100 mK.

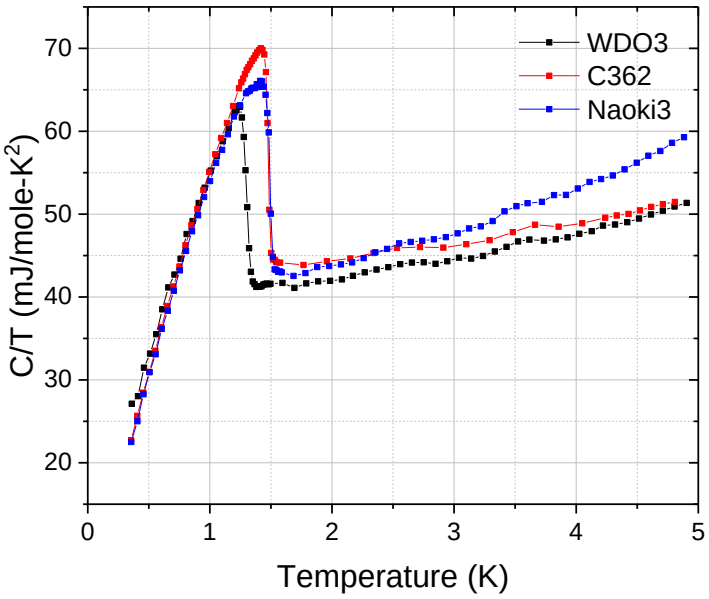

Figure 3.32: *C*/*T* against temperature for different Sr_2RuO_4 batches, measured with the relaxation time method. The heat capacity results contain signals from electrons and phonons.

3.7.2 The amplitude of T_{ac}

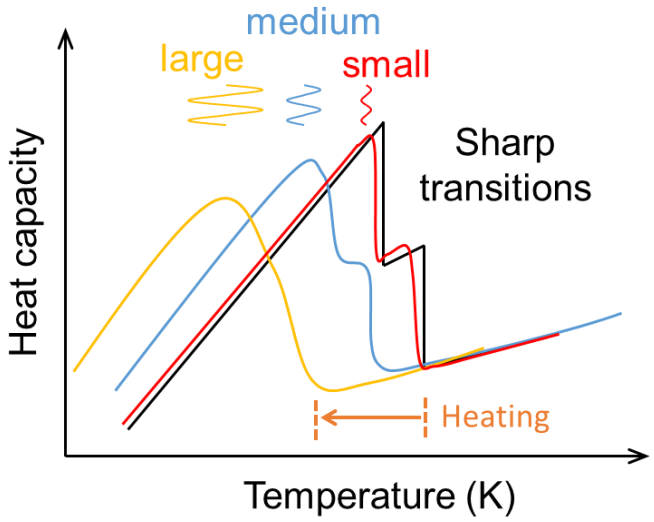

Figure 3.33: A schematic diagram demonstrating the results expected for heat capacity measurements with different amplitudes of T_{ac}, for a hypothetical sample whose sharp superconducting transition has been split, e.g. by the application of uniaxial pressure (black curve). A large T_{ac} will smear the transitions.

Figure 3.33 shows a schematic diagram for heat capacity measurements with different amplitudes of T_{ac}. The black curve has two sharp transitions with a small difference in T_c, one of the possibilities for strained Sr_2RuO_4. In order to measure this fine structure, a small T_{ac} should be used. Otherwise, the fine structure or transitions are rounded and the resolution is lost. According to equation (3-27), T_{ac} is proportional to P and the accompanying effect with large T_{ac} is sample heating as indicated by the arrow in Figure 3.33. There are two parameters that can tune T_{ac}: power P and frequency f_{exc} which are shown in Figure 3.12(a) and Figure 3.34, respectively.

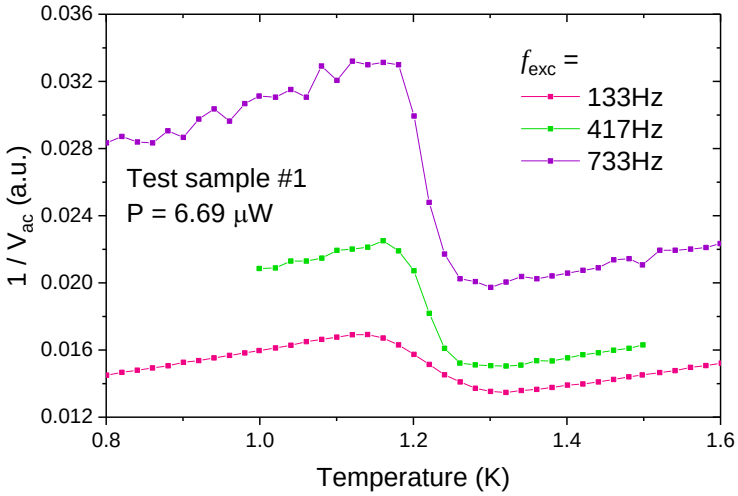

Figure 3.34: Smearing due to a large T_{ac}. Heat capacity measurements for test sample #1 with different f_{exc}.

Figure 3.12(a) shows heat capacity measurements for test sample #1 with the same frequency but different applied powers. The signal-to-noise (SN) ratio is higher with a larger applied power because T_{ac} is proportional to P. The red curve has better SN ratio but a more rounded transition than the others. T_{ac} in the blue and red curves are ≈ 3 mK and ≈ 6 mK. Compared to the superconducting transition width which is $\approx$50 mK, they are far smaller and thus the transition on both curves remains sharp. By contrast, T_{ac} in the red curve is $\approx$30 mK which is comparable to the transition width and therefore the transition is rounded and less steep than the others.

Figure 3.34 shows heat capacity measurements for test sample #1 with the same power but different f_{exc}. In order to do measurements with a higher f_{exc}, a higher power was used and to avoid large heating, k_b was increased by putting several coupling wires and $f_1 \approx 50$ Hz. T_c(midpoint) $\cong$1.22 K are the same but the transition width becomes broader with a lower f_{exc}. T_{ac} are about 6 mK, 15 mK and 55 mK for f_{exc} =733 Hz, 417 Hz and 133 Hz respectively. The curve with f_{exc} = 133 Hz has T_{ac} about 55 mK which is comparable to the transition width of the sample $\approx$50 mK and, therefore, the curve is more rounded than the others.

Based on the abovementioned considerations, in order to resolve a small structure in the measurements, T_{ac} smaller than the superconducting transition width is needed. This can be achieved by either reducing the power or increasing f_{exc}.

3.7.3 Temperature gradient on a sample

There is a constant heating power on the sample during the measurement. Most of the temperature gradient is dropped across the thermal barriers which are Stycast layers between sample and Ti plates. However, there is still a small amount of temperature gradient on the sample and this is a source of smearing on the transition(s). The ratio of the temperature drop is dependent on the ratio of the thermal conductance:

$$\frac{k_{sample}}{k_b} = \frac{k_{sample}}{C} \times \frac{C}{k_b} \cong \frac{f_{lowest}}{f_1}, \tag{3-46}$$

where f_{lowest} is the lowest frequency to probe the homogenous region which is roughly equal to the strained length. The heating in Figure 3.34 is T_{DC} ≈250 mK. Taking the parameters from sample #3 as an example, f_{lowest} is about 1500 Hz and f_1 is about 100 Hz. According to equation (3-46), the temperature gradient on the sample is:

$$T_{DC} \times \frac{f_1}{f_1 + f_{lowest}} = \frac{250\ \text{mK}}{16} \cong 16\ \text{mK}$$

This value is small but not far from the superconducting transition width of about 50 mK. It would be better to reduce the heating and increase the resolution for detecting fine structures.

3.7.4 Strain inhomogeneity

The strain profile will be very inhomogeneous when the sample is under strain. As described in section 3.6, the response can be confined to the homogeneous region by using a high f_{exc}. However, there are still several factors which cause small inhomogeneity in this "homogeneous" region due to sample preparation and mounting. Figure 3.35 shows a typical sample after wire-sawing and cleaving. There are terraces, rough edges and irregular shapes which would cause large inhomogeneities when it is under strain. To make it proper for strain measurements, it needs to be polished. Here, I describe two possible inhomogeneities in the polishing process and one in the sample assembling.

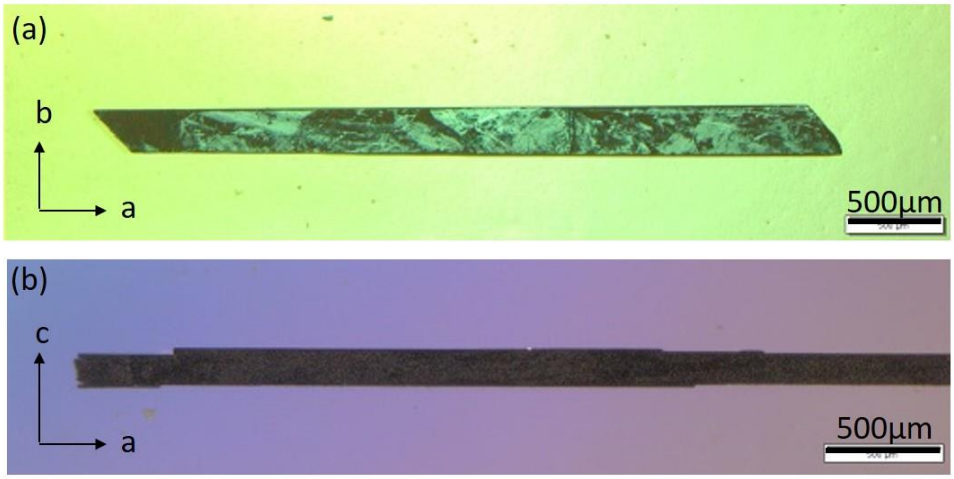

Figure 3.35: Photographs of a Sr_2RuO_4 sample after wire-sawing and cleaving. (a) the top view and (b) the side view.

Imperfect rectangular parallelepiped

An ideal sample would be a cuboid which means each surface is parallel to the opposite one. However, there are imperfections during sample preparation. Samples are sanded down to the dimensions which are suitable for measurements.

Figure 3.36: A schematic diagram for an imperfect rectangular parallelepiped.

Figure 3.36 shows a possible imperfection during the sanding process. The cross-section on the left is smaller than that on the right. Typical dimensions of a sample are 3 mm long, 200 µm wide and 150 µm thick. If there is a 5 µm difference between left and right end, the inhomogeneity would be 5 µm / 200 µm + 5 µm / 150 µm which amounts to about 6%. This kind of inhomogeneity can be reduced in the measurements by using a higher f_{exc} because the probed region becomes smaller. Usually, the probe length is less than 1.5 mm and the inhomogeneity is at least half of the value, in this case < 3%.

Surface roughness

Figure 3.37: A schematic diagram for surface roughness on a sample.

Figure 3.37 shows a schematic diagram for surface roughness. The surface roughness is determined by the particle size in the sand papers. The finest I used to polish is 1 μm diamond grit and thus the surface roughness is less than 1μm. The inhomogeneity is less than (1 μm / 200 μm + 1 μm / 150 μm) x 2 which is about 2.3%.

Sample Configurations

The strain inhomogeneity of two different types of sample configurations has been simulated by the Autodesk® Inventor®. The real configuration and the simulated results are shown in Figure 3.38. The Young's modulus of the sample was set to be 180 GPa and the Poisson's ratio was set to be 0.33. The sample has thickness 100 μm, width 300 μm and length 2 mm. One of the sample ends was set to be fixed and the other end was subjected to a pressure of 0.18 GPa, leading to $\varepsilon = 0.1\%$ if no silver contacts were made. Two types of the silver contacts were simulated. The silver and silver epoxy were set to have Poisson's ratio of 0.35. The Young's modulus for the silver epoxy was set to be 1/3 of that of the silver, which is 110 GPa. The color bar shows the strain scale, ranging from 0.07% to 0.13%. In Figure 3.38(b), one of the silver epoxy blocks was set to be invisible, as indicated by the dash-dot lines, such that the strain profile on the sample could be seen.

Figure 3.38(a) shows a photograph of sample #1. In order to conduct heat from the heater, a silver strip is glued to the sample with silver epoxy. Furthermore, to conduct heat in the *ab*-plane, sliver paste was painted on both edges. The contact length is about 300 μm and these contact areas create a large strain inhomogeneity on the sample because the Young's modulus of Sr_2RuO_4 and silver are very different. Figure 3.38(b) shows finite element simulation result based on this configuration. The strain inhomogeneity on the sample is greater than 80% in the center. It is not possible to resolve a small feature with this large inhomogeneity. In order to reduce this inhomogeneity, a new design has been developed and is shown in Figure 3.38(c). The difference is that the thermal contact is divided into four smaller areas instead of a large one. There are 8 50 μm-silver wires glued on both edges. The total contact area is almost the same but the inhomogeneity is reduced. Figure 3.38(d) shows the simulation based on the new configuration. There is still a large strain

inhomogeneity near the contact surfaces but it is reduced in the bulk. Since heat capacity is a bulk-sensitive measurement, the inhomogeneity near the surface is negligible. The strain inhomogeneity in this new configuration is ≈10%. Therefore, in the later samples, #2 to #4, this new configuration weas used (see Appendix A for detail).

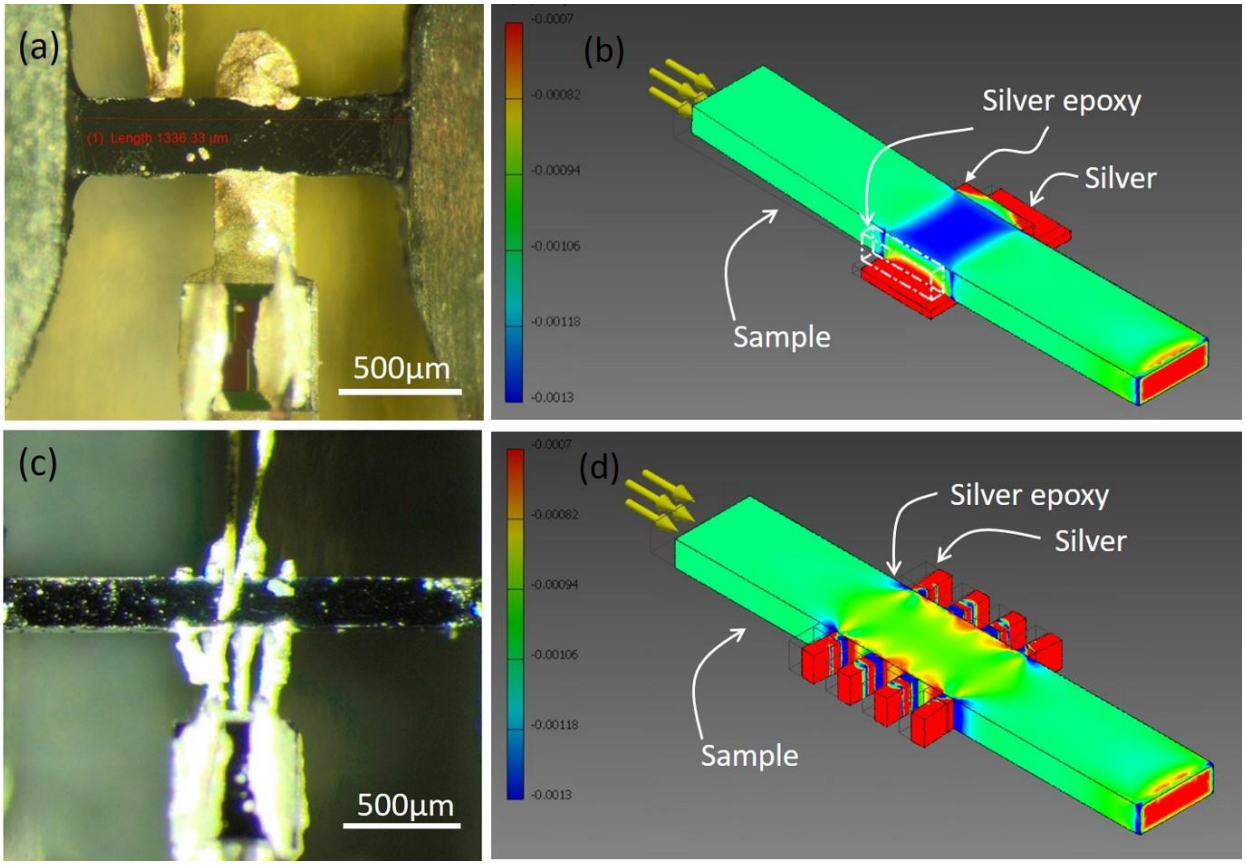

Figure 3.38: (a) A photograph of heat capacity measurement setup for sample #1. The silver contacts on the sample are large and create a large inhomogeneity in the center. (b) The simulation of the strain ε_{xx} pattern for sample #1. (c) A photograph of heat capacity measurement setup for sample #4. The silver contacts on the edges are small and the strain inhomogeneity is reduced in the center. (d) The simulation of the strain ε_{xx} pattern for sample #4.

Bending

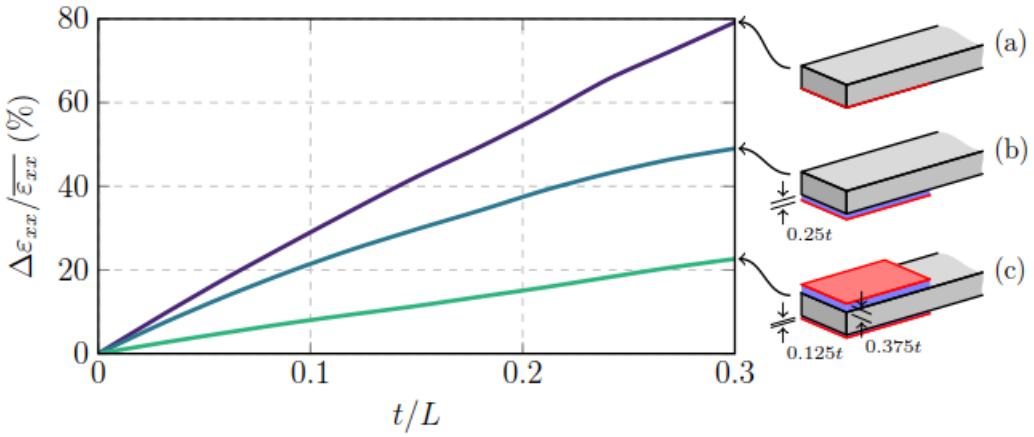

Figure 3.39: Strain inhomogeneity against sample aspect ratio with three mounting models: (a) a rigid epoxy layer and (b) a soft epoxy layer with thickness 0.25*t* holding only the bottom surface of the sample; (c) sample mounting with asymmetric epoxy layers holding both top and bottom surfaces. The sample is off center by 0.125*t* and the thickness between two plates is 1.5*t*. Strain inhomogeneity is defined by the difference of strain between the top and bottom of the bent sample divide by the average of the strain across the center plane of the sample. Reproduced from [82].

Asymmetric mounting of a sample leads to bending which has been simulated by M. Barber [82]. Figure 3.39 shows strain inhomogeneity against sample aspect ratio with three different mounting models. A sample mounted only on a single side with (a) a rigid epoxy layer or (b) a soft epoxy layer has inhomogeneity worse than that mounted between two plates glued with (c) asymmetric epoxy layers on the top and bottom surfaces. Models (a) and (b) still have inhomogeneity >10% with high aspect ratio $L/t = 20$. An ideal sample mounting would be that a sample mounted between two plates with symmetrical epoxy layers on both sides. However, the sample might end up with a small offset as illustrate in model (c). To reduce inhomogeneity to less than 10%, the design for the sample is aiming for the aspect ratio $L/t > 10$.

3.8 Sample preparation

Based on the above discussion, several conditions should be taken into account in order to perform good heat capacity measurements. I will describe how to achieve these conditions.

3.8.1 Dimension

Here, I take sample #4 as an example and show how to determine the size of the sample. According to DFT calculations [41], when the applied strain is near 0.75%, one of the Fermi sheets, the γ sheet, approaches the van Hove singularity. On the experimental side, there is a peak T_c when the applied strain is about 0.55% [41]. Hence, the sample should be prepared in a way that strain can reach up to 0.75% and beyond. The characteristic length of Sr_2RuO_4 at 1 K with f_{exc} =1 kHz is about 0.9 mm so the exposed length should be longer than 1.8 mm. On the other hand, there is a buckling limit on a strained sample [80]:

$$\frac{L}{t} = \frac{\pi}{\sqrt{3\varepsilon}}, \tag{3-47}$$

where L is the length of the sample (exposed length plus the length which the force is applied to), t is thickness of the sample and ε is the applied strain to the sample. To reach 1% strain and be suitable for probing the homogeneous part of sample, the exposed length is chosen to be 2 mm and L = 2 mm + 0.4 mm x 2. The estimated t is 150 μm and, therefore, the thickness of the sample is chosen to be 150 μm. The sample aspect ratio L/t is greater than 10. Stycast is used as force transfer medium. In order to reach high strain, there will be a high stress on Stycast and, eventually, this becomes a limiting factor. To reduce the stress, a wider sample is better and in this case the width of the sample is 200 μm.

3.8.2 Sample cutting and polishing

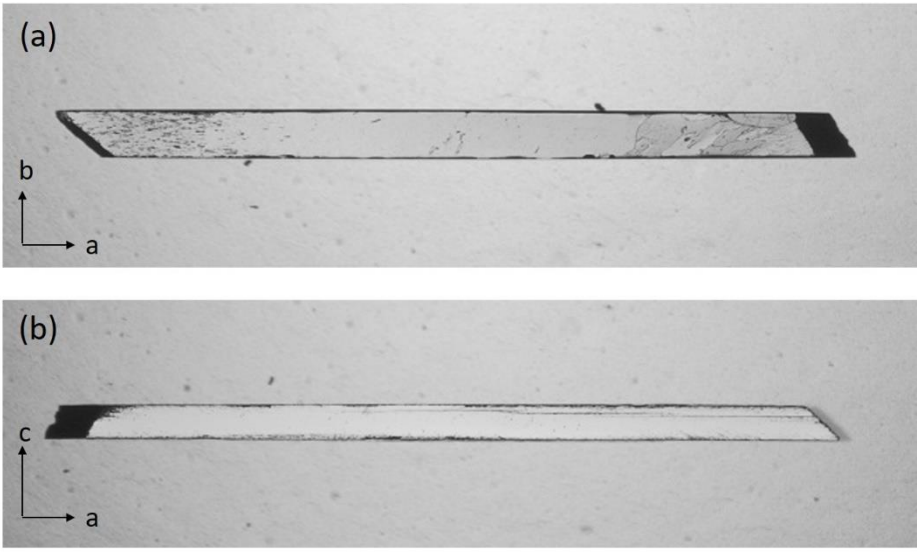

Figure 3.40: Photographs of sample #4 (a) top view and (b) side view after polishing and annealing.

A single crystal is placed on a goniometer and oriented in <100> by Laue x-ray diffraction. A slice is then cut out with a wire saw. During sawing, it typically breaks into several pieces of small slices or bars. Proper bars or slices were cleaved into several needles and then polished to the dimensions suitable for the measurements. To recover the defects induced during sawing and polishing procedures, the needles were annealed at 450°C for 24 hours. Figure 3.40 shows the photographs (a) top view and (b) side view for sample #4 after polishing and annealing. The sample dimensions are ≈3 mm long, 200 μm wide and 150 μm thick. Considerable effort was made to ensure that the surfaces were parallel to each other.

3.8.3 Sample assembling and mounting

To open a wider frequency window for the heat capacity measurements, heat has to conduct in the *ab*-plane. To reduce the strain inhomogeneity, the heater contacts on the sample should be small. To reduce bending induced inhomogeneity, a symmetric mounting model is needed. In this section, I will describe how to assemble and mount a sample to achieve these requirements.

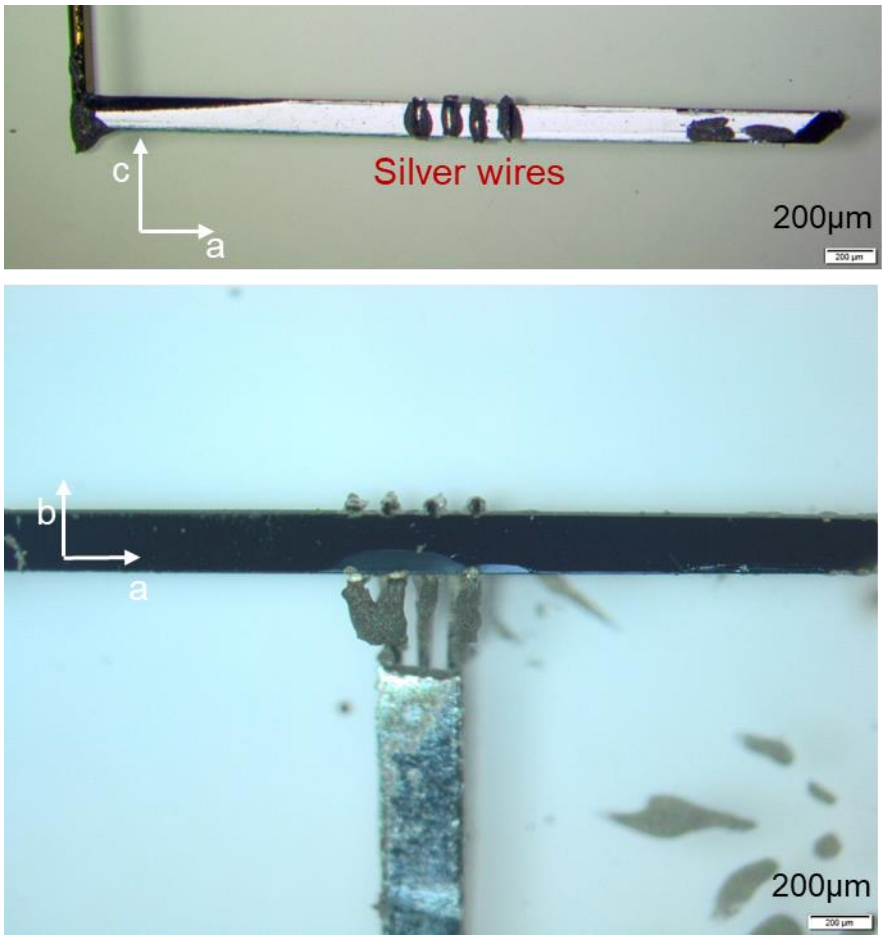

Figure 3.41: (a) A photograph for a long Sr_2RuO_4 sample with silver wires on the edge. (b) A photograph showing how sample is connected to silver fingers.

Figure 3.41 shows the pictures for the assembly. The configuration is complex and the sample went through different thermal treatments. Hence, I describe the procedures as follows:

(a) 4 silver wires (50 μm in diameter) were glued to one of the edges and a gold wire (100 μm in diameter) was glued to one of the ends with 6838 as shown in Figure 3.41(a). Subsequently, the sample was annealed at 120°C for 10 minutes to fix these wires.
(b) Repeat (a) on the other edge and end.
(c) Silver fingers with a platform were attached to the bottom of Sr_2RuO_4 with 6838
(d) 6838 was used to connect the silver fingers and wires on the edge of the sample as shown in Figure 3.41(b).
(e) A thermocouple Au/AuFe was glued to the other edge with 6838
(f) The whole sample was annealed at 450°C for 1 hour
(g) A heater was placed on top of the platform with 6838
(h) 6838 was applied to both edges of heater
(i) The whole sample was annealed at 120°C for 1 hour

The steps (a) and (b) are the most important because the silver wires conduct heat in the *ab*-plane and the strain inhomogeneity is reduced significantly with this geometry. The gold wires are used for resistivity measurements and heat coupling to the bath at low temperature. Step (d) is delicate. The volume of 6838 should be big enough such that thermal conductance is large enough to conduct heat to the sample. On the other hand, the shape of these parts need to be narrow otherwise all parts of silver glue stick together and create strain inhomogeneity on the sample. Step (f) reduces the thermal barriers which was described in section 3.4.2.

The mounting configuration used is the "symmetric epoxy" model shown in Figure 3.21. The sample is sandwiched between Ti plates and glued with Stycast layers as shown in Figure 3.24. The spacers are chosen to be 20 to 30 μm thicker than the sample thickness so the thickness of each Stycast layer would be around 15 μm. Compared to the thickness of the sample (150 μm for sample #4), the sample is expected to have less asymmetric Stycast layers than the one shown in Figure 3.39(c).

3.9 Experimental setup

3.9.1 Low temperature transformer

To probe the homogeneous region, high frequency excitation is needed, while to reduce heating, low power is needed. According to equation (3-18), low power and high frequency make the signal very small. A typical signal size from the thermocouple readout is 1 to 2 nV, whereas a typical noise level on a lock-in amplifier is 5 $\mathrm{nV}/\sqrt{\mathrm{Hz}}$. Therefore, it is almost impossible for a lock-in to pick up this tiny voltage if the signal is not amplified. One of the noise sources in this setup is Johnson noise, which is noise from resistors.

$$\text{Johnson noise} = \sqrt{4k_B RT}$$

The resistance of the thermocouple at 1 K is 0.1 Ω and the corresponding Johnson noise is 4 $\mathrm{pV}/\sqrt{\mathrm{Hz}}$. The signal size is 1 to 2 nV which is well above the Johnson noise. In principle, the signal from the thermocouple readout can be amplified to increase the signal to noise (SN) ratio. The signal is amplified by a low temperature transformer. This transformer is placed near the 1 K pot such that the signal is amplified before picking up additional thermal noise on the way up to room temperature. The amplification used in this study is 1:300 and thus the noise can be reduced down to about 20 $\mathrm{pV}/\sqrt{\mathrm{Hz}}$ which is already approaching the level of the Johnson noise. This transformer has different frequency responses with different input impedances as shown in Figure 3.42. The impedance of the thermocouple in this study is about 100 mΩ and the frequency response with 300 times amplification is shown in curve C. Typical f_{exc} in the measurements were between 1 kHz and 5 kHz which are in the operation window.

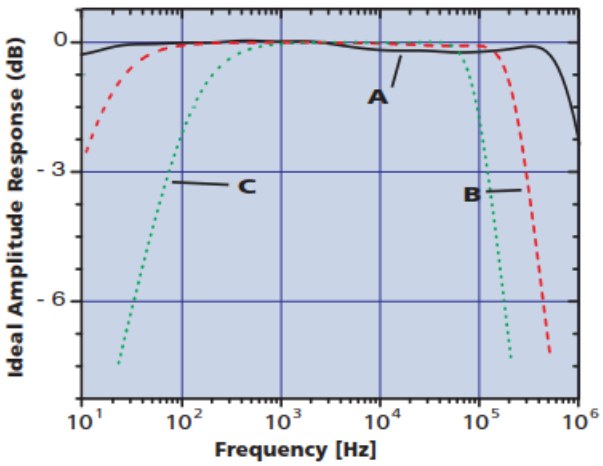

Right: *Frequency response of* ***LTT-h.***

	Frequency Response Curve	A	B	C	
	Matched Impedance	**$10^2\ \Omega$**	**$10^3\ \Omega$**	**$10^4\ \Omega$**	
P1	1:10	**1Ω**	**10Ω**	**100Ω**	**Bold indicates high frequency resonance has been completely eliminated**
P2	1:30	*100mΩ*	*1Ω*	**10Ω**	
P3	1:100	*10mΩ*	*100mΩ*	**1Ω**	
P4	1:300	*1mΩ*	*10mΩ*	*100mΩ*	*Italic indicates high frequency resonance can be controlled using matched damping element*
Primary	**Turns Ratio**	**Source Resistance**			

Figure 3.42: The frequency dependences of a low temperature transformer with different amplifications and input impedances. Reproduced from [85].

Input Impedance

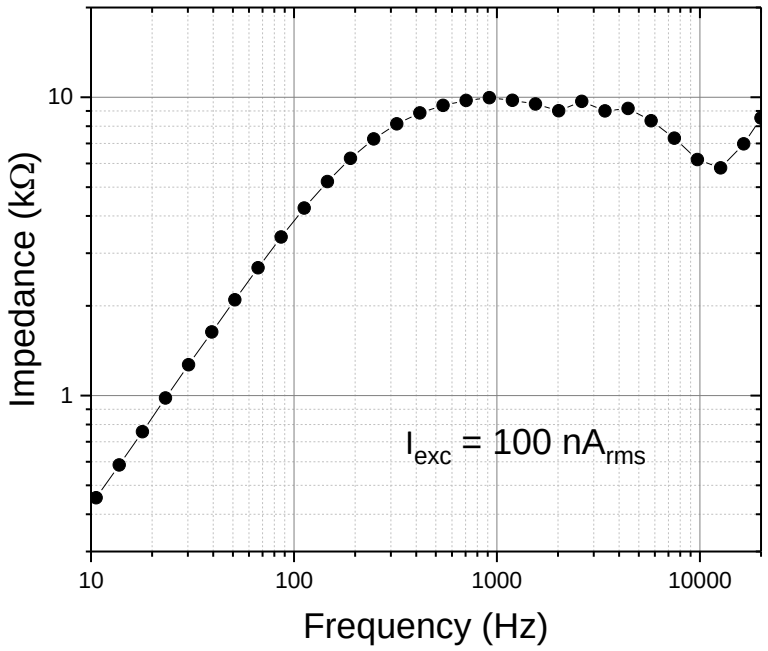

Figure 3.43: A frequency sweep of the impedance from the output of the transformer.

The frequency response of a transformer depends strongly on the input impedance. Practically, it is difficult to directly measure the resistance of the thermocouple and its wiring (the impedance should be dominated by these two elements). However, one can estimate the impedance, Z_{input}, from the transformer output, Z_{output}, because

$$Z_{output} = N^2 \times Z_{input}.$$

N is the transformer turns ratio. Figure 3.43 shows the impedance measurement from transformer output and the ratio N is 300. The input impedance

$$Z_{input} = \frac{10k\Omega}{300^2} = 0.11\Omega,$$

which is in agreement with curve C in Figure 3.42.

3.9.2 The size of T_{ac}

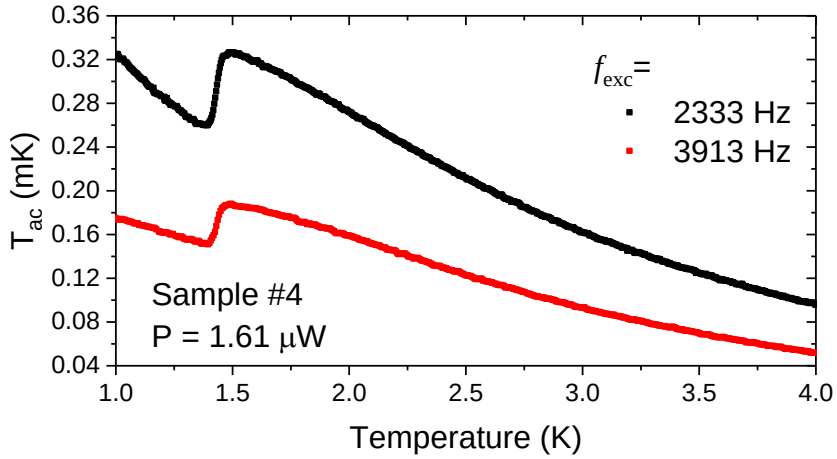

Figure 3.44: T_{ac} against temperature curves for sample #4 with different f_{exc}.

With the help of the low temperature transformer, low P for reducing heating and high f_{exc} for probing the homogeneous region with a high SN ratio are achievable and T_{ac} will be small. Figure 3.44 shows T_{ac} against temperature for sample #4 at ε_{xx} = 0% with different f_{exc}. T_{ac} < 1mK in the measurements and the transition with its width > 10 mK cab be resolved. The best samples in this study have transition width of about 50 mK. Hence, the smearing due to the size of T_{ac} is negligible.

3.9.3 Heating

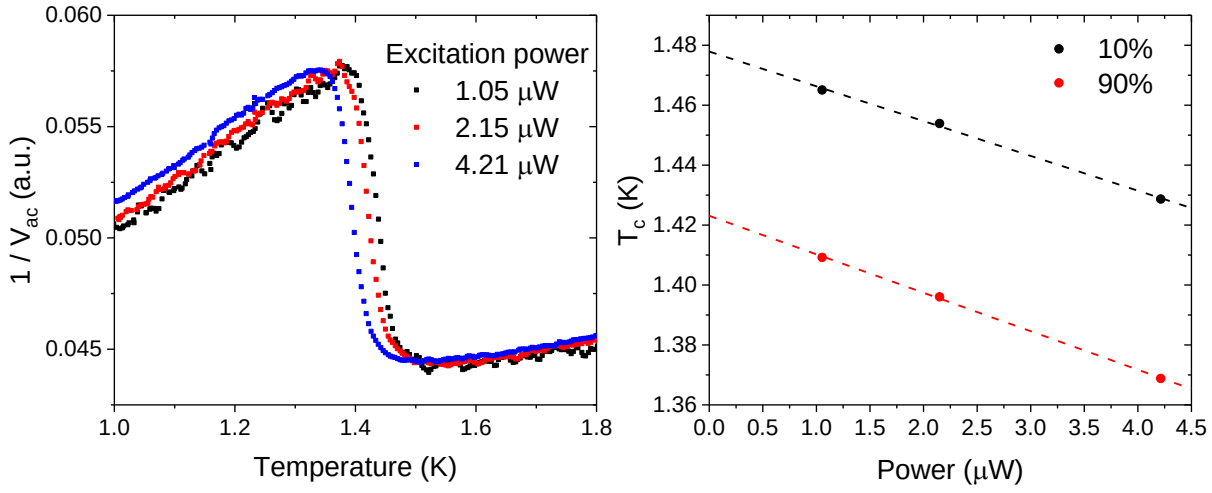

Figure 3.45: (a) $1/V_{ac}$ against temperature for sample #4 with different powers. (b) T_c against power for 10% and 90% of the transition levels.

Figure 3.45(a) shows heat capacity measurements for sample #4 with different applied powers. T_c moves to lower temperature with a higher power which indicates there are different amounts of heating depending on the excitation power in the measurements. Figure 3.45(b) shows two criteria for T_c with different powers. The dashed lines are linear fits and T_c taken at 10% of the transition level is about 1.48 K which agrees to the T_c determined by the relaxation time method (see Figure 3.32, Naoki3). k_b determined from the slopes are 8.61×10^{-5} W/K (10%) and 7.79×10^{-5} W/K (90%) which are consistence with the estimates in section 3.3.

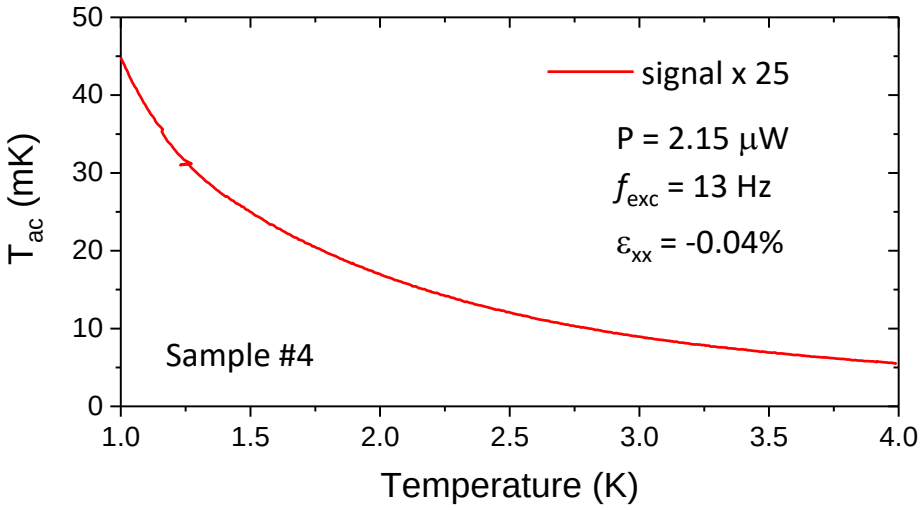

Figure 3.46: T_{ac} against temperature for sample #4 with f_{exc} lower than f_1 (≈100 Hz). The signal is multiplied by a factor of 25.

Figure 3.46 shows T_{ac} against temperature for sample #4 with $f_{exc} < f_1$. According to equations (3-29) and (3-30), if $7f_{exc} < f_1$, the signal T_{ac} is equal to T_{DC}. f_{exc} = 13 Hz which fulfills the criteria in equation (3-30) and thus the measurement shown in Figure 3.46 is a measurement of the heating T_{DC}. 13 Hz is not a proper working frequency as suggested in Figure 3.42, thus, certain amount of signal is cut. Based on the analysis in Figure 3.45(b), heating on the sample #4 at T = 1.45 K is about 25 mK with P = 2.15 μW. The reduced signal in Figure 3.46 at T = 1.45 K is about 1 mK which means there is ~96% of signal cut by the low temperature transformer. To estimate the heating on the sample, the signal is, therefore, multiplied by a factor of 25 as shown in Figure 3.46. This factor of 25 is reasonable compared to the frequency responses shown in Figure 3.42. In this thesis, the temperature on the x-axis is the temperature at the bath. The temperature difference between the sample and the bath is the heating T_{DC}, which is small compared to the bath temperature (1.7% at 1.5 K and 0.13% at 4 K). Therefore, sample temperature is roughly equal to the bath temperature. Throughout the thesis, the temperature given is the bath temperature.

The heating T_{DC} on sample #4 is < 50mK between T = 1 K and 4 K. The lowest frequency for probing the homogeneous region in sample #4 is about 2000 Hz. According to equation (3-38), the temperature gradient on the sample is less than:

$$T_{DC} \times \frac{f_1}{f_1 + f_{lowest}} = 50\ \text{mK} \times \frac{100\ \text{Hz}}{2000\ \text{Hz} + 100\ \text{Hz}} \cong 2.4\ \text{mK}$$

The value is far smaller than the superconducting transition width and, therefore, the smearing due to the temperature gradient on a sample is negligible.

3.9.4 Temperature hysteresis

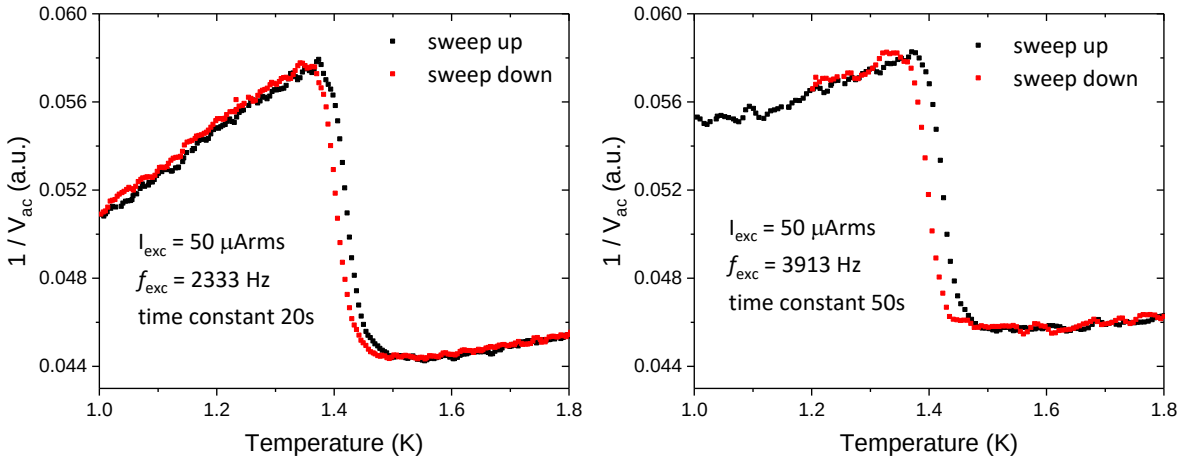

Figure 3.47: Hysteresis in temperature with different time constants used in the lock-in amplifier.

There is a small amount of temperature hysteresis in the experimental setup. The signal size fed into the lock-in amplifier is several hundred nV and the noise output from the lock-in amplifier is about 5 nV/$\sqrt{\text{Hz}}$. In order to obtain a better signal-to-noise ratio, long time constants were chosen to average the signal. Two typical time constant were used, 20 and 50 seconds for low and high f_{exc}, respectively. The SN ratio could reach 200 or higher. A data acquisition time smaller than the time constant is meaning less so the sampling was chosen to be either 20 or 50 seconds per data point. This leads to a hysteresis especially in case of a sharp transition. The superconducting transition width is about 50 mK. To resolve this transition and look for a splitting of the transition which might be small, the temperature interval between data points was chosen to be around 5 mK. The sampling rate and the temperature interval set the temperature sweeping rate. Table 3.3

summarizes parameters for the heat capacity measurements. Figure 3.47 shows the temperature hysteresis in the heat capacity measurements with different time constants used in the lock-in amplifier, (a) 20 seconds and (b) 50 seconds. The hysteresis is small compared to the superconducting transition width. Both up and down sweeps show a clear superconducting transition but it is easier to control temperature in the up-sweep mode. Therefore, most of data were taken with the temperature ramped up.

	f_{exc} (Hz)	Sweep rate (mK/min)	Time constant (s)	Temperature interval (mK)	Hysteresis (mK)
Protocol I	1503/2333	12	20	4	17
Protocol II	3913	7.2	50	6	25

Table 3.3: Parameters for the heat capacity measurements.

3.9.5 Temperature stability

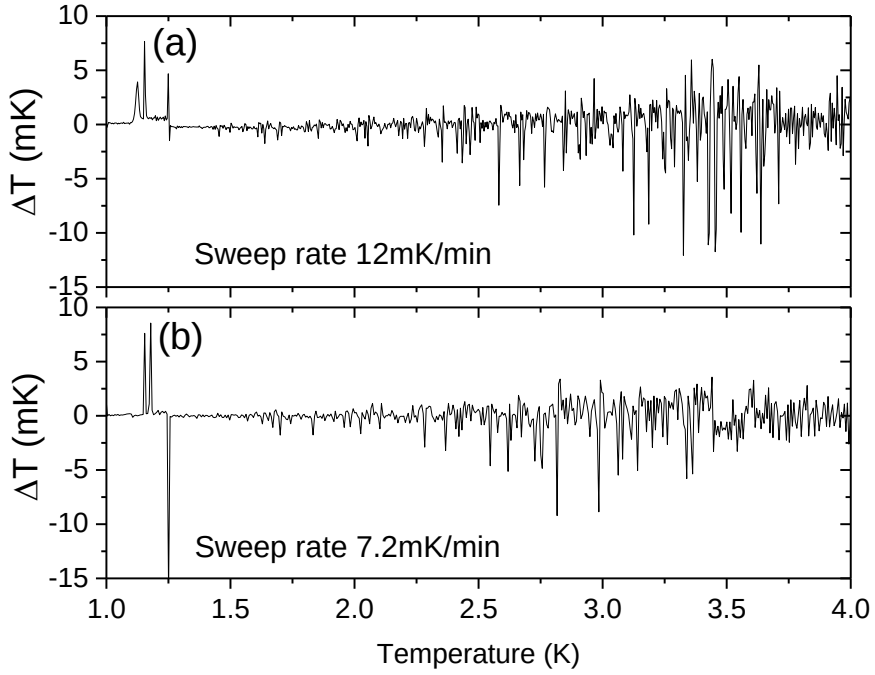

Figure 3.48: Temperature deviation as a function of temperature for different sweep rates.

Temperature stability is important for the heat capacity which is a function of temperature. Unstable temperatures would create additional noise in the signal. Figure 3.48 shows the temperature deviation as a function of temperature for different sweep rates. The temperature was ramped from 1 K to 4 K with PID control. The cooling power was generated by circulating a small amount of ^{3}He/^{4}He mixture. Hence, the temperature is stable near 1 K but fluctuates near 4 K. Even so, the temperature stability is still high near 4 K and $\Delta T/T < 0.5\%$. The spikes near 1.15 K are due to switching between the two temperature calibration functions and the spikes near 1.25 K are due to switching between heater ranges.

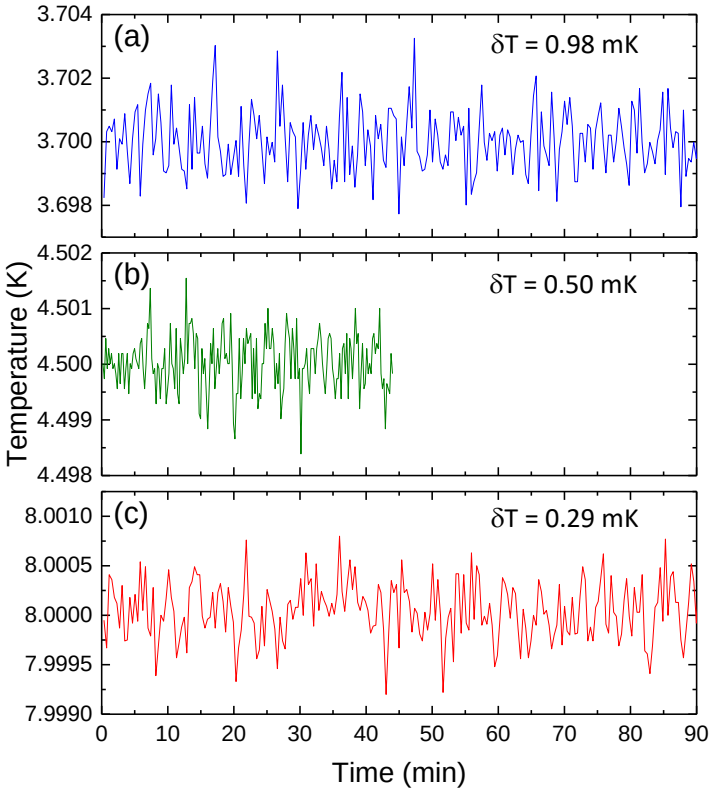

Figure 3.49: Temperature stability at different temperatures. δT stands for the temperature deviation.

A fixed temperature was needed in certain cases near or above 4K, e.g. the strain sweeps at the normal state. The change of the signal in some samples was only a few percentage and, therefore, a more stable temperature was needed near or above 4 K. In these cases, another set of PID parameters was employed. Figure 3.49 shows the temperature stability at different temperatures. The temperature is more stable than in the sweep mode even at higher temperatures. The temperature deviations δT in all cases are less than 1 mK.

3.9.6 Resonance peaks and noise under magnetic field

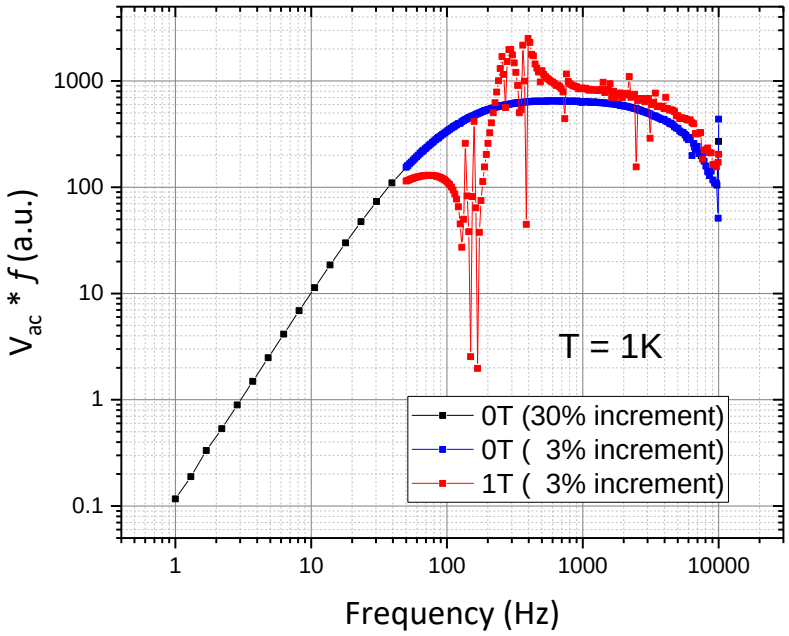

Figure 3.50: Frequency sweeps with and without magnetic field. There are resonance peaks and noise when magnetic field is applied.

When a magnetic field was applied, resonance peaks and noise appeared on the transformer output. Figure 3.50 shows $V_{ac}*f$ as a function of frequency with (red) and without (black and blue) magnetic field. A small increment (3%) of frequency was used to resolve these features (blue and red). The curve at $H = 0$ T is very smooth but noisy at $H = 1$ T. The resonance peaks and the noise are likely from wire vibrations. In order to obtain correct results in the field measurements, the excitation frequencies were chosen to be away from those peaks.

3.9.7 The anomaly in the low temperature

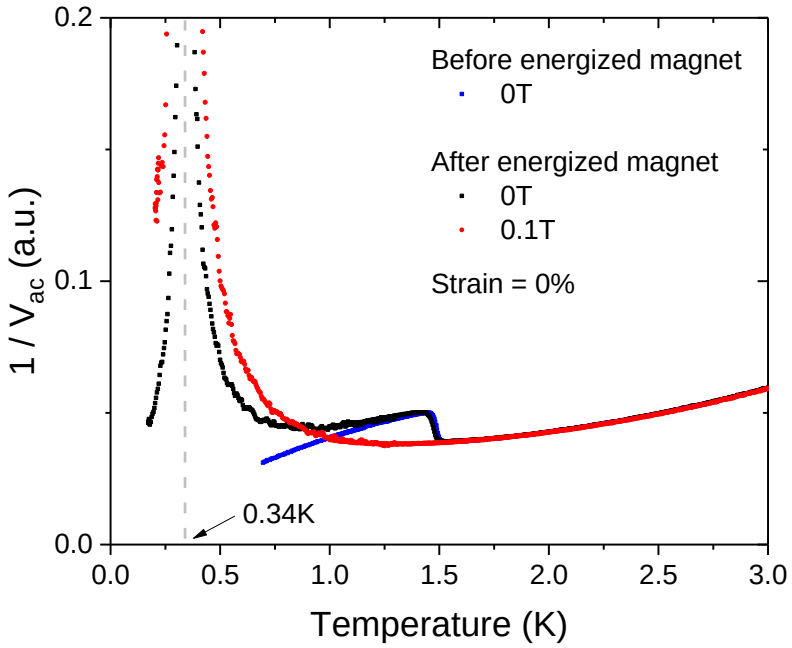

Figure 3.51: Heat capacity measurements for sample #3 before and after energizing the magnet. An anomaly appeared after the magnet was energized. The dashed line indicates the temperature at which peak of the anomaly locates. The red curve shows the measurement in the normal state.

An anomaly appeared in the heat capacity measurements after the magnet was energized. This anomaly is irreversible, namely the anomaly does not go away even if the applied magnetic field is reduced to zero again. Figure 3.51 shows the heat capacity measurements before (blue) and after (black and red) the magnet was energized. The black and blue curves are measurements at $H = 0$ T. The upper critical-field H_{c2} in Sr_2RuO_4 is about 75 mT and, thus, the red curve (0.1 T) is a measurement in the normal state. The dashed line indicates the temperature at which the peak of the anomaly locates. The anomaly sets in below T_c and it exists both in the normal state and in the superconducting state.

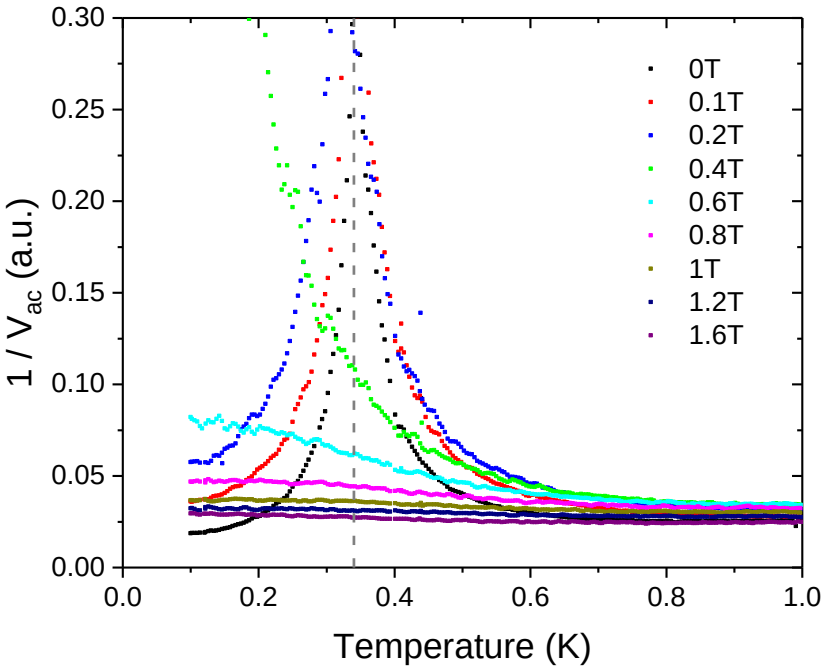

Figure 3.52: The anomaly for sample #3 with different fields.

Figure 3.52 shows the anomaly at ε_{xx} = 0.6% for sample #3 with different magnetic fields. The dashed line indicates the temperature 0.34 K. The position of the peak does not change significantly compared to that at ε_{xx} = 0%. Upon increasing magnetic field, the position of the peak moves to lower temperatures and its height is reduced.

If this anomaly is a Schottky anomaly, it suggests that there is a 2-level system whose energy scale is proportional to $k_B T_p$, where k_B is Boltzmann constant and T_p is the corresponding temperature at maximum heat capacity. The peak position decreases when the magnetic field is applied, suggesting that the gap between the levels is reduced with an increasing field. One can also speculate that it is from the sample setup.

3.10 Summary

My heat capacity measurements on a sample under uniaxial stress are strongly non-adiabatic. Heat pulse and relaxation time methods are not possible because the decay time from sample to the bath is about 1 ms which is too fast. Therefore, an ac method is employed in this study. In this ac method, it is essential to open a frequency window which is the valid region for heat capacity measurements. In section 3.4, I have demonstrated that it is possible to perform heat capacity measurements under strongly non-adiabatic conditions.

The strain distribution on a sample is highly inhomogeneous when a strain is applied. In section 3.6, I demonstrated that the homogeneous part of sample can be probed with a high excitation frequency (f_{exc}). Therefore, the requirement for opening a frequency window in this study is stricter because a high f_{exc} is needed. To meet this requirement, it is very important to conduct the heat in the *ab*-plane firstly because it can potentially tune the upper cut-off frequency (f_2) to the higher frequency end which is dominated by the intrinsic properties of the sample and secondly because the probed region can be well-controlled with f_{exc} in this configuration. The annealing process is important to push f_2 higher such that the signal will not be reduced due to the internal thermalization time between the heater, the thermocouple and the sample.

The frequency window and f_{exc} determine the correction factor $F(\omega)$ for the heat capacity measurements. The correction factor in the T_{ac} formula can reach 99% accuracy if f_{exc} meet the condition $10f_1 < f_{exc} < f_2/10$, where f_1 and f_2 are lower and upper cut-off frequencies, respectively. However, in my measurements, f_{exc} is going to be close to f_2 in order to probe the homogeneous region. Therefore, the correction factor, which is temperature dependent, is not negligible and the temperature dependence of T_{ac} comes from both heat capacity and correction factor.

Probing the homogeneous region requires high f_{exc} and reducing the heating effect on sample requires low power. Eventually, the signal size from the thermocouple readout is extremely small, about 1 to 2nV. With the help of the low temperature transformer it is then possible to pick up the signal with high signal-to-noise ratios using lock-in amplification techniques.

Inhomogeneities and measurement parameters can smear the sharp transition. Measurement parameters have little effect on smearing the transition because temperature gradients in the sample can be kept small compared to the width of the superconducting transition by using low temperature transformer, which can keep SN ratios high with a significantly reduced power. However, inhomogeneities coming from defects in the sample (intrinsic) and the measurement configuration (extrinsic) have the main effect. The best sample in this study has a transition width about 50 mK which is the limit for the resolution in temperature. To reduce inhomogeneities from the

measurement configuration, the sample needs to be polished into the shape of a rectangular parallelepiped and the heat contacts need to be small, about 50 μm in my case.

In short, heat capacity measurements of Sr_2RuO_4 under uniaxial stress are feasible. A number of efforts have been taken into account to look for the theoretically proposed splitting of the superconducting transition. Experimental results will be shown and discussed in the next Chapter.

Chapter 4
Experimental Results and Discussion

4.1 Introduction

The leading candidate of the order parameter for Sr_2RuO_4 is chiral *p*-wave. Investigating whether or not a split of the transition appears after the tetragonal lattice symmetry is lifted therefore becomes a very significant experiment. In this chapter, I will show the heat capacity measurements of Sr_2RuO_4 under uniaxial stress. I carefully reduced the smearing sources from sample configurations and measurement parameters. However, my data show null results even with high quality single crystals. I will discuss the experimental limits which set the upper limits for the second transition if it exists.

Heat capacity in my measurements is different from the conventional case because the probed volume changes as a function of temperature. Therefore, it is nontrivial to calculate the specific heat. In an ideal situation, there is a relation between the heat capacity and specific heat. I will discuss this relation and then analyze the specific jump $\Delta c/c$ at T_c. In my analysis the change of $\Delta c/c$ at the peak in T_c is not large.

The increase of T_c in strained Sr_2RuO_4 has been proposed to be related to the van Hove singularity. If so, an enhancement of the density of states is expected when the sample is under strain. To look for this signal, I performed strain sweeps in the normal state and observed an enhancement of heat capacity near the peak in T_c. In my analysis, there is an enhancement of the specific heat around the peak in T_c, suggesting the existence of the van Hove singularity. In addition, an unexpected dip located at the peak in T_c was observed in the better samples. The window for this dip structure is narrow and a slightly larger inhomogeneity in the sample can smear this structure.

Lastly, the pairing symmetry of 3.4K-Sr_2RuO_4 may be different from 1.5K-Sr_2RuO_4. Two approaches were used to investigate this issue. First, I performed heat capacity measurements at a series of small increments of strain. Second, I performed heat capacity measurements under magnetic fields at zero, medium strains and the peak in T_c. Unfortunately, they cannot give a clear and unambiguous answer to the question of a potential symmetry change. Nevertheless, the first approach suggests an enhancement of $\Delta c/c$ near the peak in T_c and the second approach suggests a strong increase of H_{c2} near the peak in T_c.

4.2 Sample configuration

Here I briefly describe the differences on the samples I used for my study. I performed the heat capacity measurements under uniaxial stress on four samples. Samples #1 and #2 are test samples whereas #3 and #4 are better samples. Three single crystals were used in my study. Samples #1 and #2 are from the same batch, whose T_c is approximately 1.35 K, whereas samples #3 and #4 are from the other two different batches, whose T_c are approximately 1.5 K. Samples #3 and #4 had less strain inhomogeneity in the homogeneous region because the heat contacts were smaller, see Chapter 3.7.4. In particularly for sample #4, all surfaces were polished and the shape was a rectangular parallelepiped as determined by inspection under a microscope. All samples except for sample #2 went through an annealing process at 450℃ for 1 hour so the signal was not cut by f_2, see Chapter 3.6.4. Samples #1 and #2 are short and wide, whereas samples #3 and #4 are long and narrow and thus are better for analysis (see section 4.6). In short, I made more and more improvements on the sample configuration and sample #4 was the best one for this study. The details of the sample configuration are summarized in Appendix A.

4.3 Heat capacity measurements

Samples #1 and #2 are my early samples for the purpose of testing. Several important features such as an increase of T_c and density of states can be already seen in these samples. However, they have larger inhomogeneity and modest sample quality. Therefore, I refer the interested reader to the Appendix B for their data. Samples #3 and #4 have high sample quality, less strain inhomogeneity and better signal-to-noise (SN) ratios and they are the main samples used for my study. The strains were applied not only up to the peak in T_c but also beyond. To confirm the results, two different excitation frequencies f_{exc} were used on both samples. Figure 4.1 and Figure 4.2 show C_{ac}/T against temperature for sample #3 with low and high f_{exc} respectively and so do Figure 4.3 and Figure 4.4 for sample #4. The black dashed lines in Figure 4.3(a) and Figure 4.4(a) are normal state curves which were measured at ε_{xx} = 0% with H = 0.1 T parallel to the c-axis[5]. The purple dashed lines in Figure 4.1(b) to Figure 4.4(b) are repeated curves at maximum T_c. The y-axis is plotted as C_{ac}/T and $C_{ac} = P/(\omega T_{ac})$, where P is the excitation power on the heater, $\omega = 2\pi \times (2f_{exc})$, and T_{ac} is the amplitude of the temperature oscillation. According to equation (3-22), heat capacity $C = F(\omega) \times P/(\omega T_{ac}) = F(\omega)C_{ac}$, where $F(\omega)$ is the correction factor. In an ideal case, $F(\omega) = 1$ and the measured signal C_{ac} is the heat capacity C. However, in my case, since the f_{exc} is close to the upper cut-off frequency f_2, $F(\omega)$ is not negligible and varies as a function of temperature. Therefore, C_{ac} is not only a function of heat capacity C but also a function of $F(\omega)$.

[5] Thermocouple was not calibrated under magnetic field. Here, I assume the thermopower $S(0.1\text{ T}) = S(0\text{ T})$.

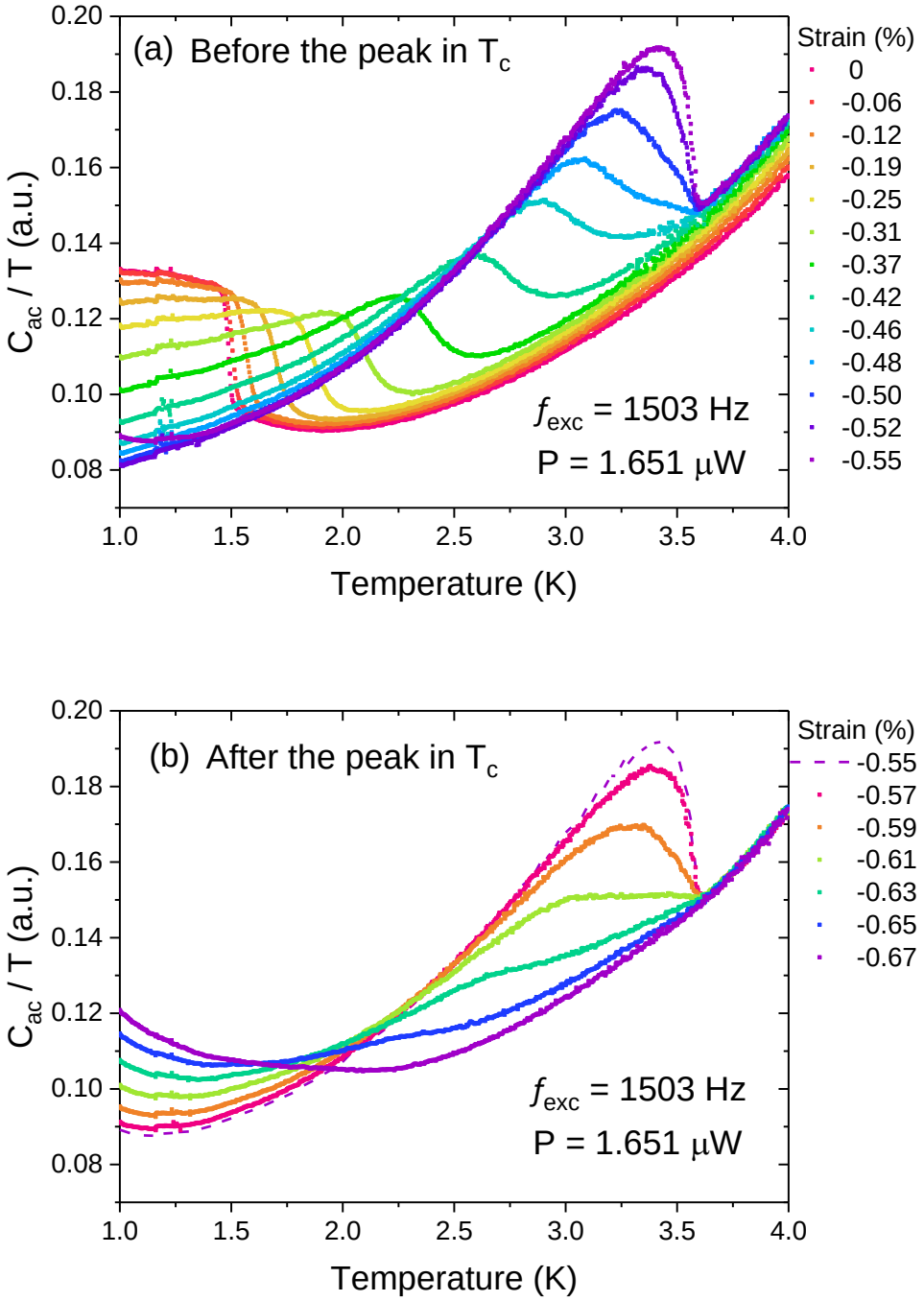

Figure 4.1: C_{ac}/T against temperature for sample #3 at a series of strains (a) before and (b) after the peak in T_c. The dashed line in panel (b) repeats the data at maximum T_c.

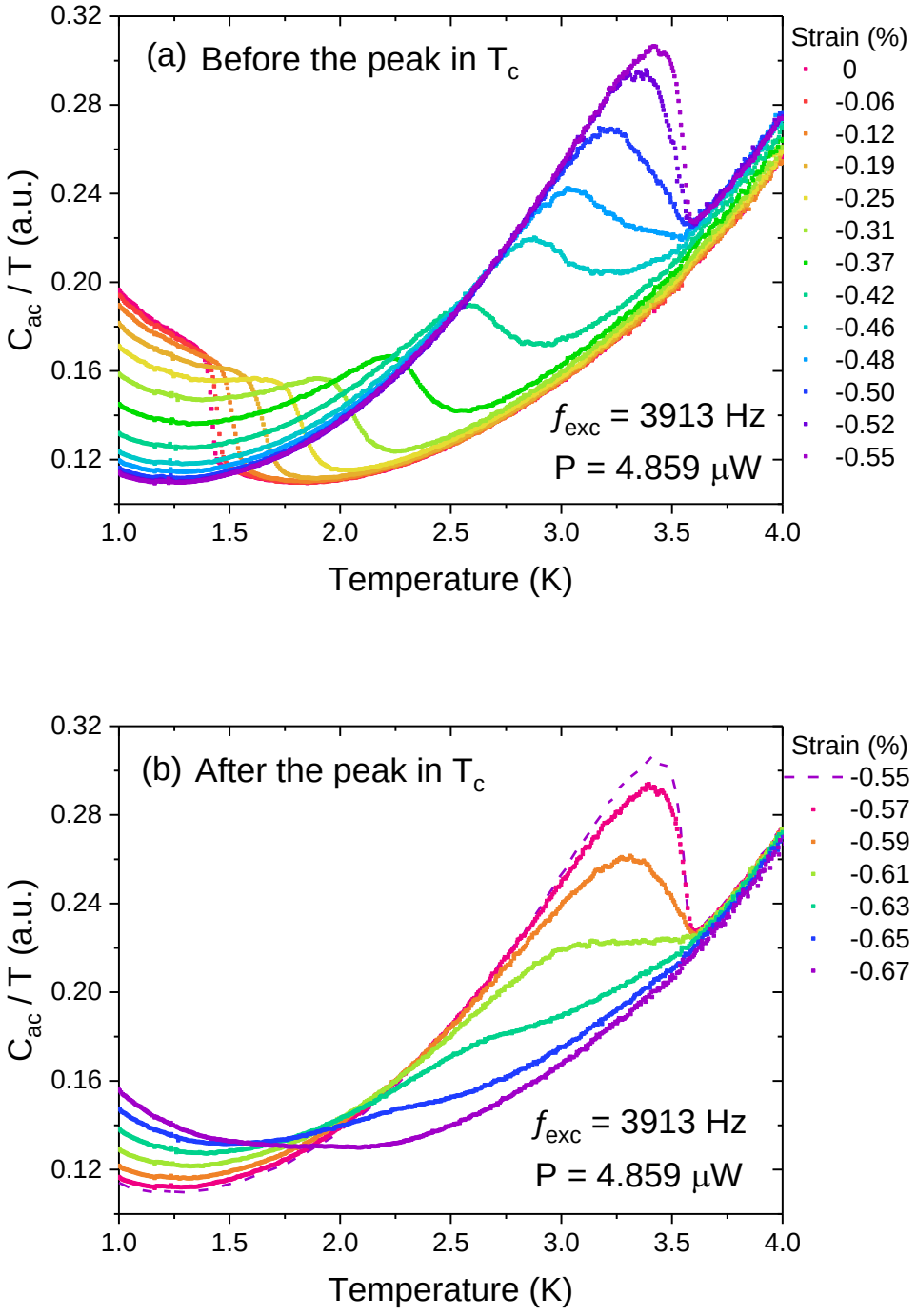

Figure 4.2: C_{ac}/T against temperature for sample #3 at a series of strains (a) before and (b) after the peak in T_c. The dashed line in panel (b) repeats the data at maximum T_c.

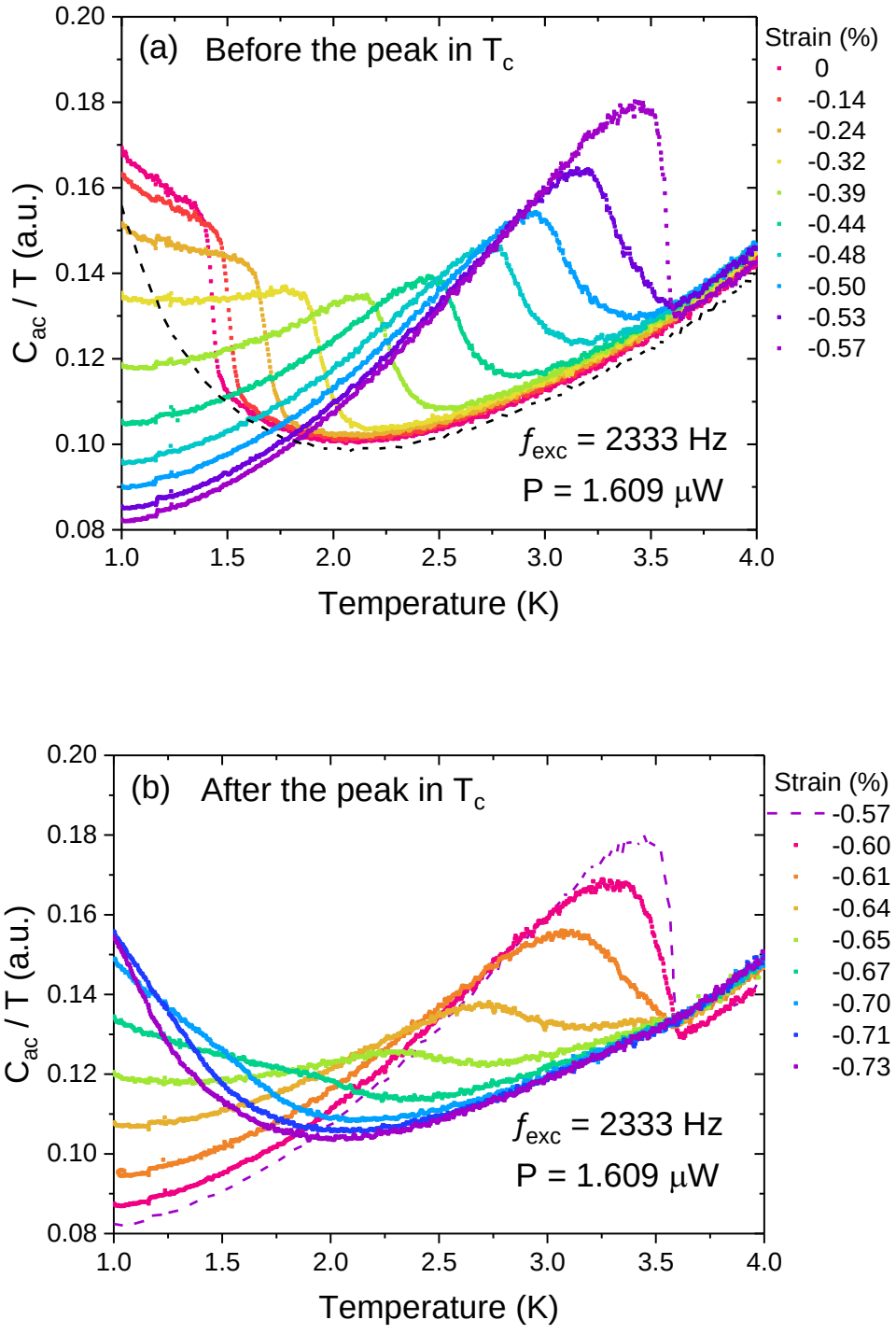

Figure 4.3: C_{ac}/T against temperature for sample #4 f_{exc} = 2333 Hz at a series of strains (a) before and (b) after the peak in T_c. The dashed line in panel (a) is the heat capacity measurement at ε_{xx} = 0% with $H_{||c}$ = 0.1 T. The dashed line in panel (b) repeats the data at maximum T_c.

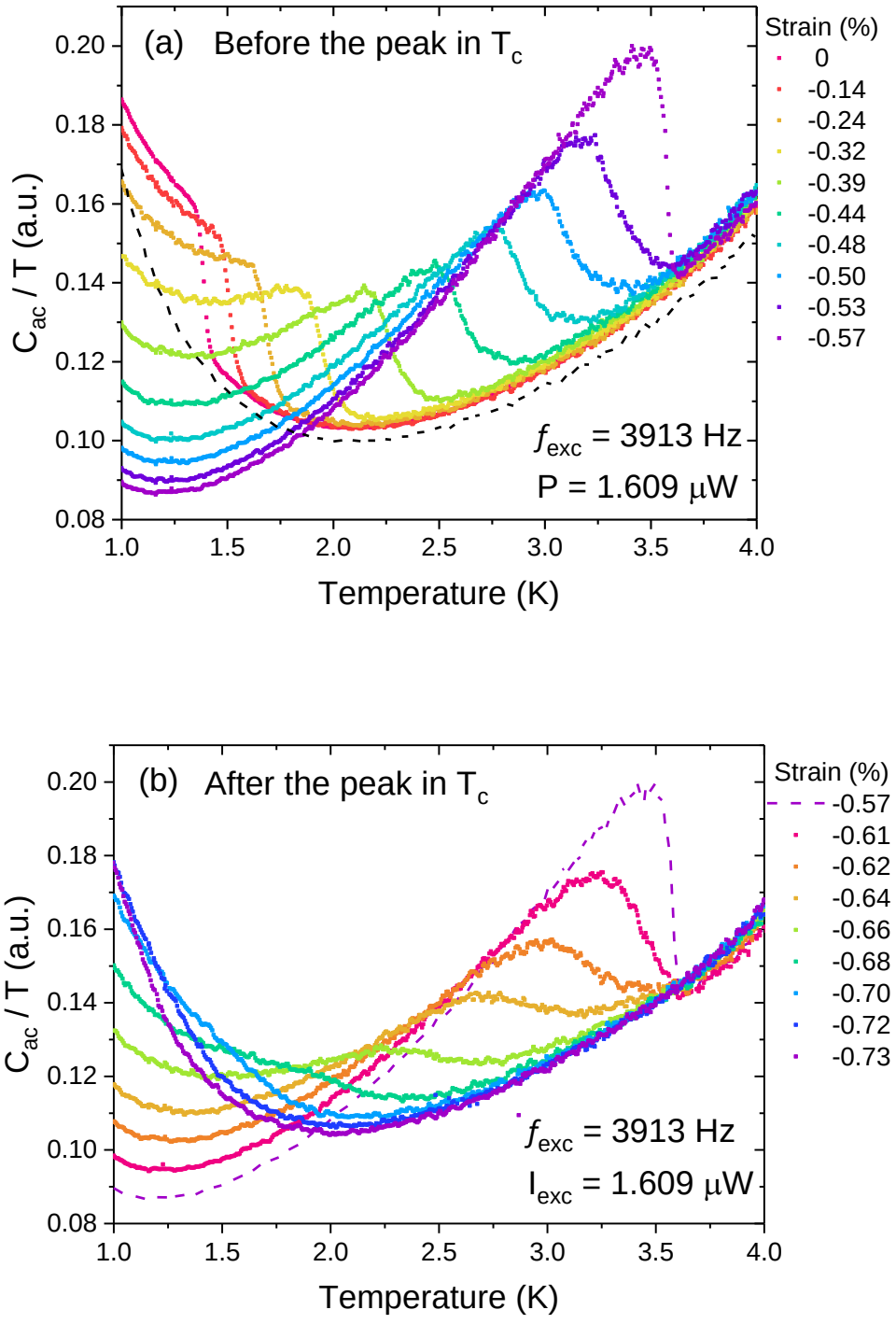

Figure 4.4: C_{ac}/T against temperature for sample #4 with f_{exc} = 3913 Hz at a series of strains (a) before and (b) after the peak in T_c. The dashed line in panel (a) is the heat capacity measurement at ε_{xx} = 0% with $H_{||c}$ = 0.1 T. The dashed line in panel (b) repeats the data at maximum T_c.

T_c increases when the strain is applied in all samples. The transitions are broad in the medium strain region, but they are sharp again when T_c reaches to the highest value-- 3.4 K for sample #1, 3.5 K for sample #2, and 3.6 K for sample #3 and #4. The ratio of maximum T_c to the unstrained T_c is approximately 2.4. Here I define the strain having the sharpest transition at peak T_c in the measurements as ε_{peakTc}. When the applied compression goes beyond ε_{peakTc}, T_c is suppressed rapidly. In sample #4, T_c even falls down below 1.5 K.

No obvious splitting of the transition was observed when the tetragonal lattice symmetry was lowered by applying the uniaxial stress. Although the transition is rounded at the medium strains, only a single transition can be identified. The rounded structure may be caused by inhomogeneity, which I will discuss in more detail in section 4.4. The results suggest the second transition would be difficult to detect if it does exist. I will discuss the detection limits in my experiments in section 4.5.

The heat capacity transitions are broader after the peak in T_c. Since T_c has a rapid decrease in the region, any small inhomogeneity will cause a large spreading of T_c's, leading to a rounded feature in the data. The transition in sample #4 after the peak in T_c is sharper than that in sample #3, indicating that sample #4 is less inhomogeneous. The inhomogeneity will be discussed in section 4.5.

The apparent heat capacity jump, $\Delta C_{ac}/\gamma T_c$, at zero strain on both samples #3 and #4 is between 0.3 and 0.4 which is smaller than the literature value of approximately 0.7. This difference is in a way unique in my measurements and is related to the changing probed length as the temperature varies. I will describe this issue in section 4.6.

An important quantity that can be extracted from the heat capacity measurements is the heat capacity jump as a function of strain. In sample #3 and #4, the heat capacity jump at ε_{peakTc} seems to be higher than that at zero strain. Details of the discussion will be shown in section 4.7.

The normal state heat capacity is enhanced with increasing strain on both samples #3 and #4. The effect is stronger in sample #3. In addition, an interesting feature occurs in sample#4 at ε_{peakTc}: There is a notably reduced normal state heat capacity. I will describe these features in more detail in section 4.8.

A number of features can be identified by comparisons and inspections. In the following, I will describe these issues in more detail.

The peak in T_c

To determine T_c, the curves are normalized to the background and the normal state value is set to be 0% of the transition and the peak in the superconducting state to be 100%. The midpoint is defined as 50% of the transition and the transition width is defined as the temperature difference between 20% to 80% levels.

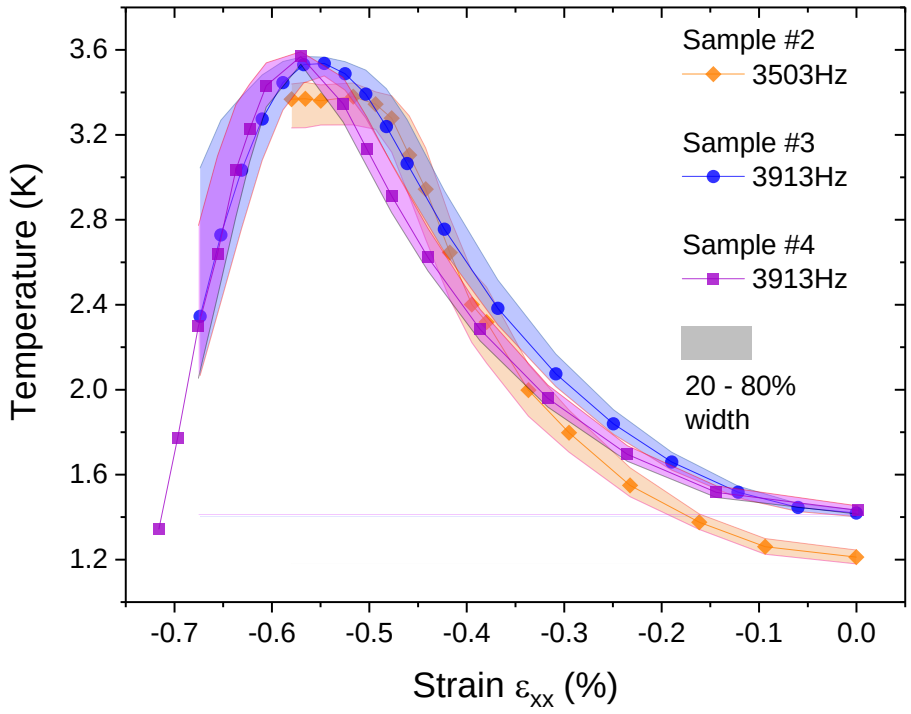

Figure 4.5: T_c against strain for sample #2, #3 and #4 taken with the similar frequencies. The solid points are the data at midpoints (50% levels of the transitions). The colored area represents the transitions from 20% to 80% levels.

Figure 4.5 shows T_c against strain for samples #2, #3 and #4 taken with similar f_{exc}. The results for sample #3 and #4 with a low f_{exc} behave similarly to the one with a high f_{exc} shown in the figure. The solid points are the data at midpoints and the colored areas are the transitions from 20% to 80% levels, which represent the transition width. It is clear that there is an enhancement of T_c around ε_{xx} = -0.55%. Since the heat capacity is a thermodynamic property and is sensitive to bulk, the enhancement of T_c in Sr_2RuO_4 under strain is a bulk property. This result is in a good agreement with the susceptibility measurement, which is, on the other hand, sensitive to the surface because that is where the screening currents flow at low applied fields [41].

Elastic response

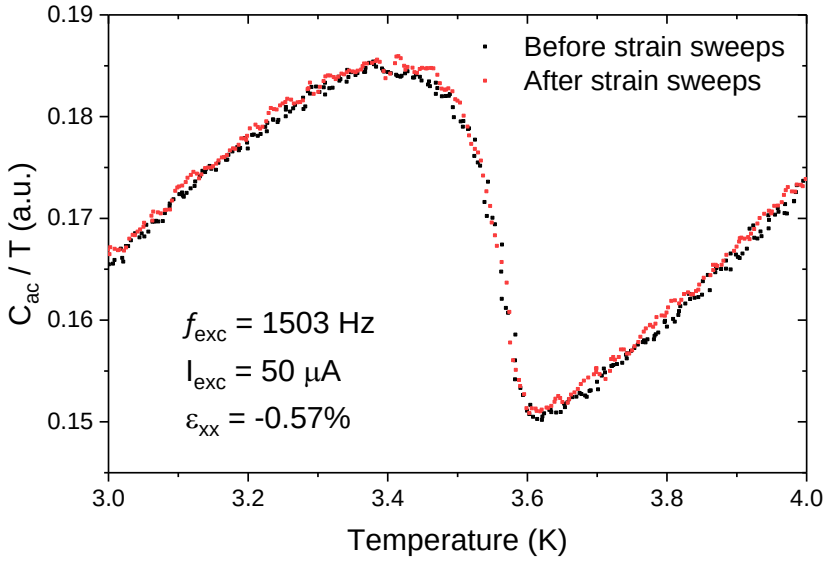

Figure 4.6: C_{ac}/T against temperature for sample #3 before and after strain sweeps.

Figure 4.6 shows C_{ac}/T against temperature for sample #3 at ε_{xx}=-0.57%, which is slightly beyond ε_{peakTc}, before and after strain sweeps. The sample went through several strain cycles from nearly 0% to the strain beyond ε_{peakTc}. No hysteresis is observed and both curves match well, proving that the response to the applied strain was elastic. Another evidence for elastic behavior is shown in strain sweeps (see section 4.8). The positions of the features such as dips, kinks and peaks, are independent of the sweep direction.

4.4 Heat capacity measurements with a higher f_{exc}

In Figure 4.1 to Figure 4.4, the transitions are broad and rounded at medium strains. Inhomogeneity such as imperfect parallel surfaces may be one of the reasons for smearing the transition. A rounded transition caused by this type of inhomogeneity can be sharpened by reducing the probed length, i.e. applying a higher f_{exc}. In the following, I will show measurements with higher f_{exc} to reduce the possible effect caused by this type of inhomogeneity. Figure 4.7 shows the measurements for sample #3 at ε_{xx} = -0.46% with f_{exc} up to 5513 Hz. The curves are normalized to 1 at 3.5 K. The probed length is reduced by nearly a factor of two from 1503 Hz to 5513 Hz. The heat capacity transition becomes sharper at f_{exc} = 3013 Hz, suggesting that this approach is effective, and the sharpness of the transition does not have a significant change at an even higher f_{exc}, suggesting that a frequency between 3013 Hz and 5513 Hz is a reasonable f_{exc} to exclude a minor inhomogeneity and to probe the very homogeneous part of sample. Figure 4.8 shows C_{ac}/T against temperature for sample #3 with f_{exc} = 5513 Hz from ε_{xx} = -0.42% to -0.52%, whereas Figure 4.9 shows C_{ac}/T against temperature for sample #4 with f_{exc} = 5513 Hz from ε_{xx} = 0% to -0.54%. Only a single transition has been observed in both samples.

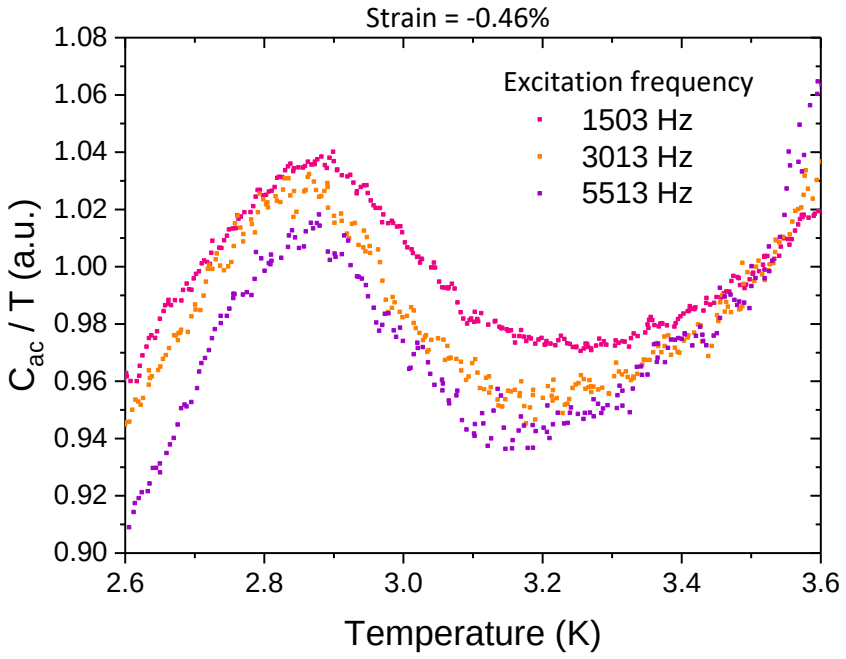

Figure 4.7: C_{ac}/T against temperature for sample #3 at ε_{xx} = -0.46% with different f_{exc}. The curves are normalized to the data at 3.5 K for comparison. The transition is sharper at higher frequencies.

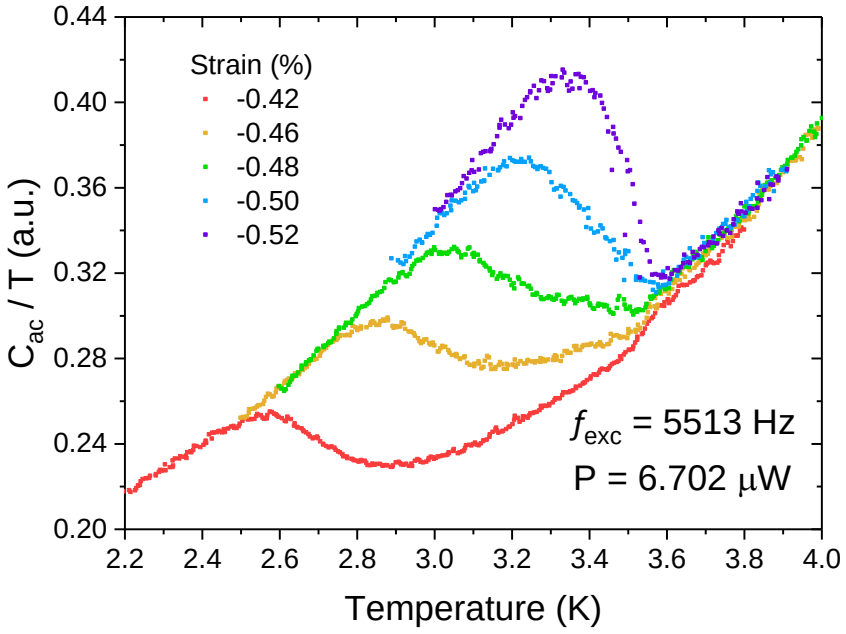

Figure 4.8: C_{ac}/T against temperature for sample #3 at various strains before the peak in T_c with high f_{exc} .

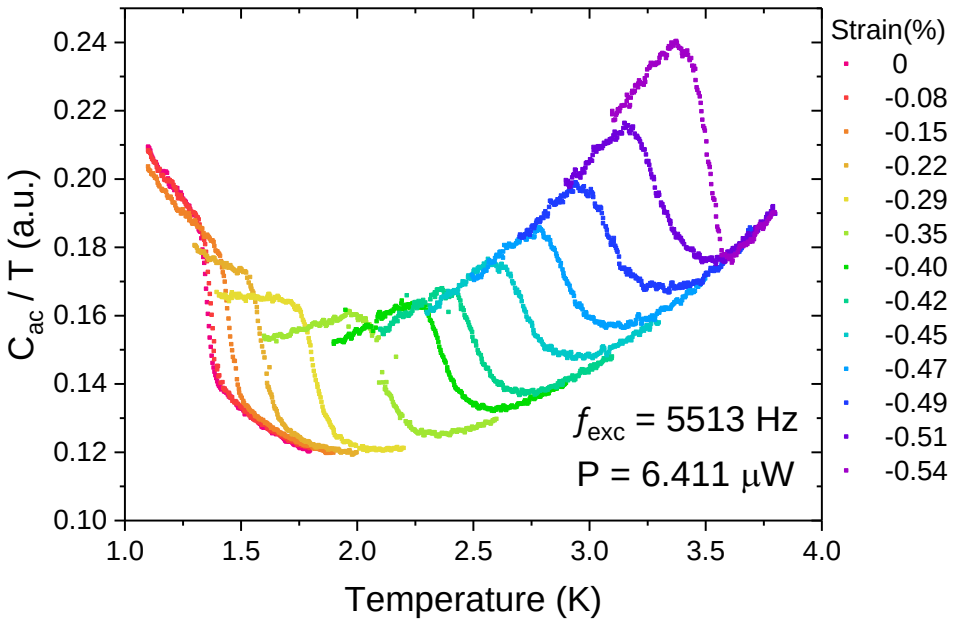

Figure 4.9: C_{ac}/T against temperature for sample #4 at various strains before the peak in T_c with high f_{exc}.

4.5 Limits on the detection of a possible second transition

The splitting of $p_x \pm ip_y$ is based on a symmetry argument which does not provide energy scales for the splitting, e.g. how much the splitting is and how large the jump sizes are. From the experimental point of view, there is noise in the signal and inhomogeneity from the sample (intrinsic) and the measurement configuration (extrinsic). Therefore, there are experimental limits on resolving small structures. Figure 4.10 shows a schematic diagram for a heat capacity measurement with two transitions with a small difference in T_c. The first transition has been observed with an approximately 30% change in $1/V_{ac}$ (or C_{ac}/T). Here, I estimate the experimental limits on detecting the second transition.

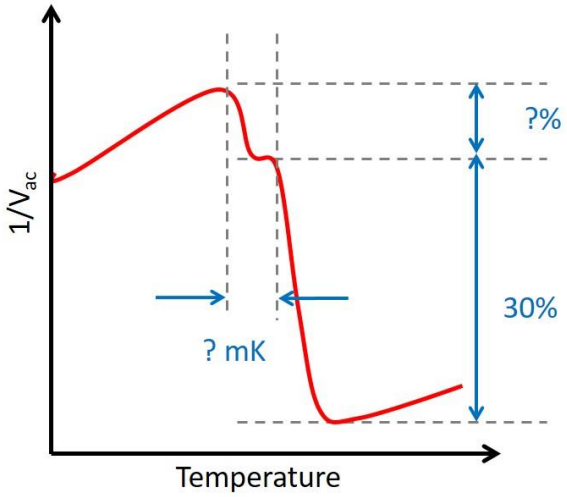

Figure 4.10: A schematic diagram for a heat capacity measurement with two phase transitions having a small difference in T_c. The observed first transition is 30% change in $1/V_{ac}$. There are experimental limits on detecting the size and the position of the second transition.

The limit on the size of the jump in V_{ac} at the second transition

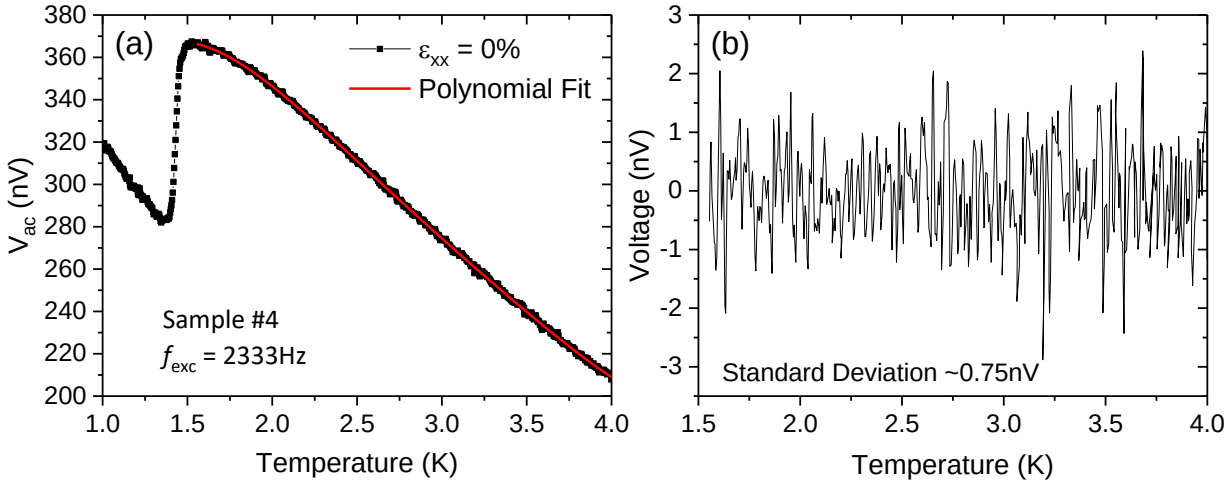

Figure 4.11: (a) The amplitude of the voltage V_{ac} against temperature at ε_{xx} = 0% for sample #4. The red line is a fitted curve on the normal state with a polynomial of degree 5. (b) The difference between the measured signal V_{ac} and the fitted curve. The standard deviation is 0.75nV.

The noise level determines the limit on detecting the second transition. Figure 4.11(a) shows the signal V_{ac} in the heat capacity measurement with a polynomial fit of degree 5 to the normal state. The noise can be derived by the subtraction as shown in Figure 4.11(b). The signal size at 1.6K is 366nV and the noise (standard deviation) is 0.75nV. The signal-to-noise ratio is 366nV/0.75nV = 488. In other words, the noise in the background is 1/488 which corresponds to 0.2%. To identify a small transition, the signal should be a factor of 10 larger than the background, i.e. larger than 2%. (see Figure 3.16(d) for example.) The ratio of the second to the first jump would be 2%/30% ≈7%. Hence, the experimental limit on detecting the second jump is about 7% of the first jump for sample #4 with f_{exc}=2333 Hz at temperature near 1.6 K. Table 4.1 estimates the experimental limits on detecting the second transition at 1.6 K and 3.6 K for sample #3 and #4 with different f_{exc} used in the measurements.

Sample, f_{exc}	V_{ac} (1.6 K)	V_{ac} (3.6 K)	Noise [A]	limits [B,C] (1.6 K, 3.6 K)
#3, 1503Hz	655nV	343nV	0.78nV	4%, 8%
#3, 3913Hz	630nV	257nV	0.90nV	5%, 12%
#4, 2333Hz	366nV	233nV	0.75nV	7%, 11%
#4, 3913Hz	211nV	130nV	0.63nV	10%, 16%

A: standard deviation; B: Limit with respect to the first transition; C: The estimates here are based on the raw signals.

Table 4.1: Estimates of the sizes of the experimental limits on the second transition for sample #3 and #4 at different temperatures.

The limit on determining the separation of two transitions

The width of the transition determines the detection limit for the separation of two transitions. A separation smaller than the width is unresolvable. Figure 4.12(a) and (b) show the first derivative of the measured curves with f_{exc} = 3913 Hz at strains before and after ε_{peak} for sample #3 and Figure 4.13(a) and (b) for sample #4. Here, I take the full width at half maximum (FWHM) as a criterion for the limit on determining the separation of transitions and the results are shown in Figure 4.12(c) and Figure 4.13(c). The FWHM goes from 33 mK at ε_{xx} = 0% to 500 mK at ε_{xx} = -0.55% for sample #3 and from 50 mK at ε_{xx} = 0% to 300 mK at ε_{xx} = -0.53% for sample #4. The behaviors with f_{exc} = 1503 Hz (2333 Hz) are similar to that with f_{exc} = 3913 Hz for sample #3 (sample #4).

Strain inhomogeneity

From the breadth of the transitions, the amount of the inhomogeneity can be estimated as follows:

$$\Delta T_c \cong \frac{dT_c(\varepsilon)}{d\varepsilon} \times \Delta\varepsilon = \frac{dT_c(\varepsilon)}{d\varepsilon} \times \frac{\Delta\varepsilon}{\varepsilon} \times \varepsilon \tag{4-1}$$

$\Delta T_{c,FWHM}$ can be determined from the dC_{ac}/dT curves and therefore:

$$\Delta T_{c,FWHM} = \left|\frac{dT_c(\varepsilon)}{d\varepsilon}\right| \times \frac{\Delta\varepsilon_{FWHM}}{|\varepsilon|} \times |\varepsilon| \tag{4-2}$$

The variation in T_c, $\Delta T_{c,FWHM}$, is related to the tangent slope on the $T_c(\varepsilon)$ curve$|dT_c(\varepsilon)/d\varepsilon|$, the strain inhomogeneity $\Delta\varepsilon_{FWHM}/|\varepsilon|$ and the applied strain $|\varepsilon|$. It is inevitable to have a certain amount of strain inhomogeneity in a sample and, therefore, the higher the applied strain, the larger the variation in T_c. The variation is even larger when the applied strain goes beyond ε_{peak} because the tangent slope is steeper. Here I use the $T_c(\varepsilon)$ determined at 50% of the transitions to simulate $\Delta T_{c,FWHM}$ with various amounts of inhomogeneity as shown in Figure 4.12(c) and Figure 4.13(c). The value $\Delta T_{c,FWHM}$ near ε_{xx} = 0% are different from the simulations because there is finite transition width at ε_{xx} = 0% which is intrinsic to the sample. The strain inhomogeneity plays a significant role when the applied strain is large. Hence, the inhomogeneity is determined primarily by matching to the data for $\varepsilon_{xx} \geq 0.55\%$. The simulations suggest that there is approximately 13% inhomogeneity in sample #3 and approximately 8% inhomogeneity in sample #4.

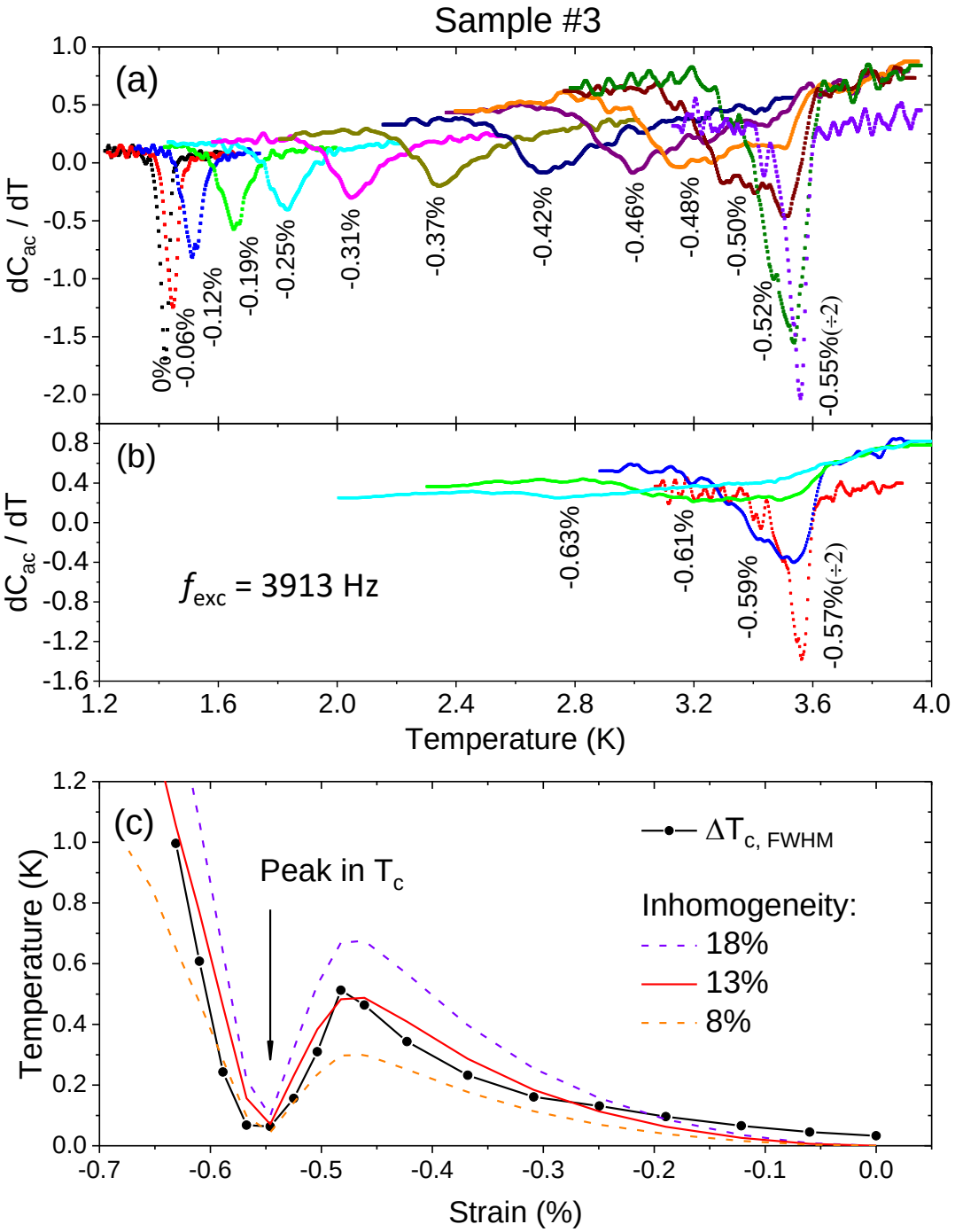

Figure 4.12: The first derivative of C_{ac} with respect to temperature for sample #3 at different strains (a) before the peak in T_c and (b) after the peak. The curve at -0.55% in panel (a) and -0.57% in panel (b) are reduced by a factor of 2. (c) The transition width against strain. The solid points are the FWHM derived from the results in (a) and (b). Three simulation curves (see text) with different inhomogeneities are shown for comparison. The arrow marks the position of the peak in T_c. Further explanation is given in the text.

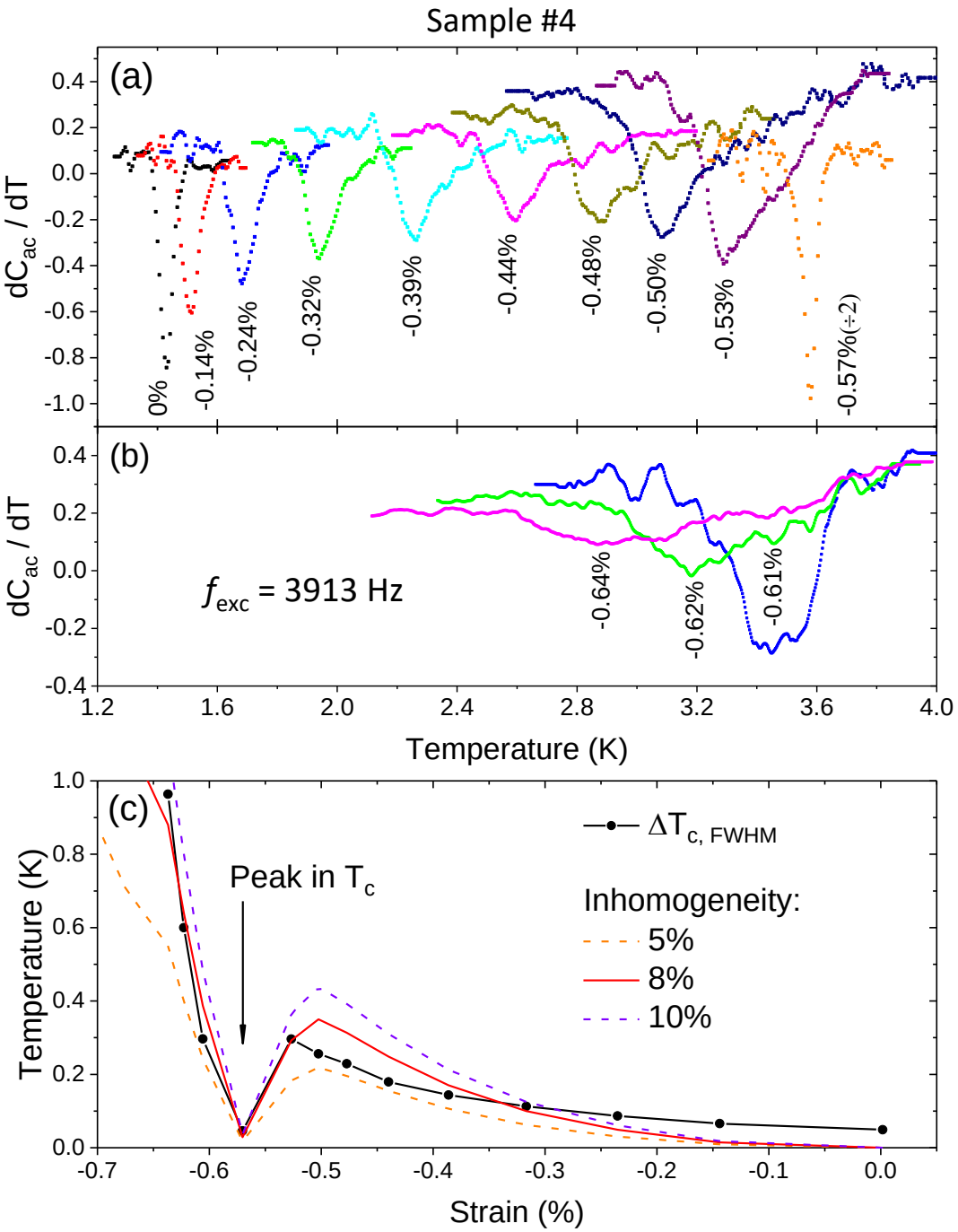

Figure 4.13: The first derivative of C_{ac} with respect to temperature for sample #4 at different strains (a) before the peak in T_c and (b) after the peak. The curve at -0.57% in panel (a) is reduced by a factor of 2. (c) The transition width against strain. The solid points are the FWHM derived from the results in (a) and (b). Three simulation curves (see text) with different inhomogeneities are shown for comparison. The arrow marks the position of the peak in T_c. Further explanation is given in the text.

Higher quality heat capacity measurements near zero strain

In the previous discussions, the experimental limit on detecting the second jump for sample #4 around T = 1.6 K was found to be about 7%. Here I present a set of the higher quality heat capacity measurements near ε_{xx} = 0% to set another limit near 1.6 K. The second transition is expected to happen at temperature lower than the first one. Hence, the measurements were performed between 1 K and 1.5 K.

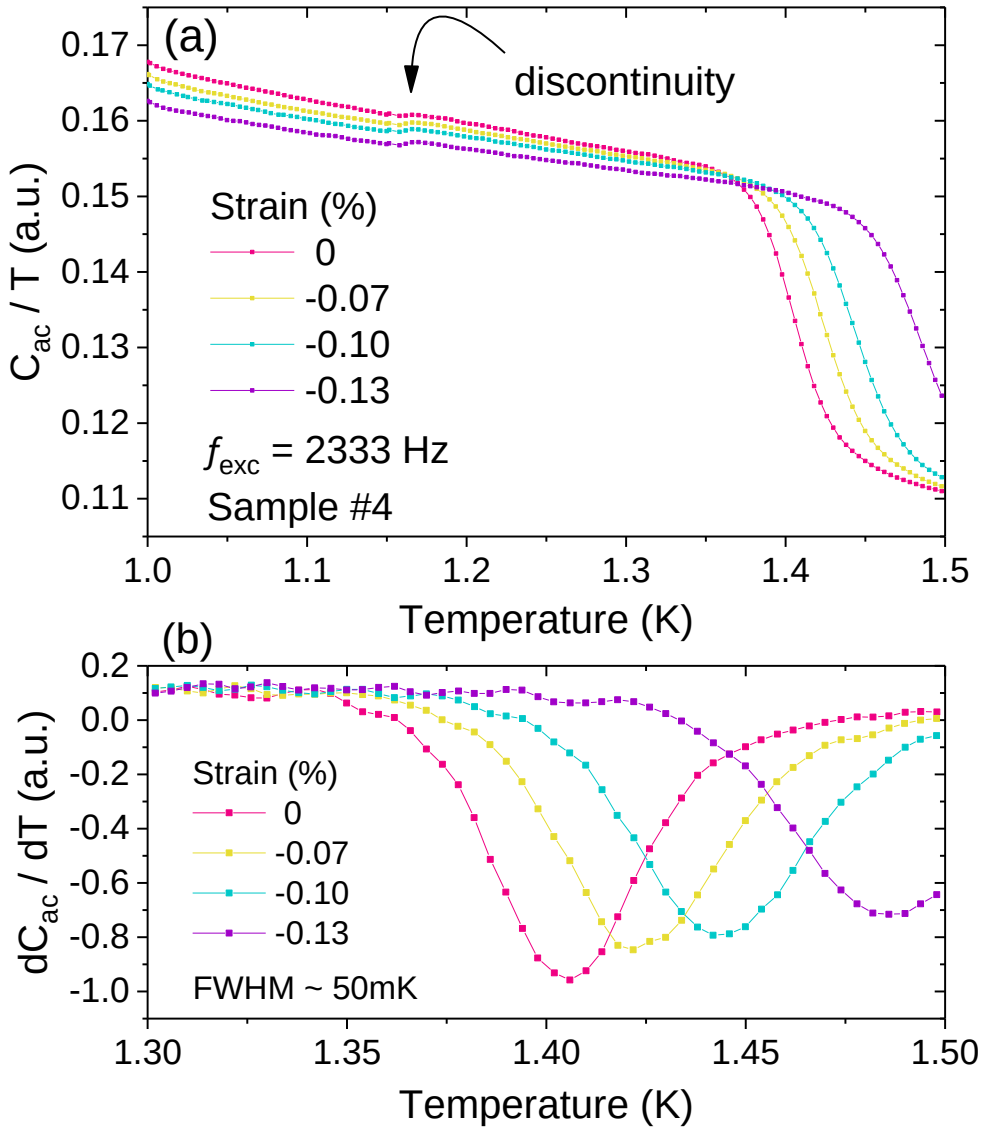

Figure 4.14: (a) High quality heat capacity measurements for sample #4 near ε_{xx} = 0%. (b) dC_{ac}/dT against temperature near T_c.

Figure 4.14(a) shows high quality heat capacity measurements for sample #4 at different strains. The existence of the second jump might be small. To achieve a better signal-so-noise ratio, the measurements were repeated several times at each strain— 20, 34, 18 and 20 times for the 0%, -0.07%, -0.1% and -0.13% curves, respectively. The curves shown in the figure are results after the averaging. The curves are smooth below T_c except for the discontinuities around 1.15 K indicated by the arrow. This is an artifact, due to the calibration ranges of the thermometer used in the measurements. The calibration functions switch at T = 1.15 K, causing the small discontinuity. The purpose of showing this discontinuity is to demonstrate that the signal-to-noise ratio in these measurements is high enough to see a very small change. This discontinuity is about 0.5% of the signal which means a jump as small as 0.5% can be resolved in the measurements. Therefore, a stricter limit for the ratio of the second to the first jump is 0.5% / 30% which is about 2%. Figure 4.14(b) shows the first derivative of the curves near T_c in (a) and FWHMs are about 50 mK.

Heat capacity measurements near zero strain

The splitting of $p_x \pm ip_y$ in principle should lead to a cusp around ε_{xx} = 0%. Figure 4.15(a) and (b) show C_{ac}/T against temperature for sample #4 under compressive strain and tensile strain respectively. Figure 4.15(c) shows T_c against strain for sample #4. The points represent the 50% levels of the transitions and the colored area shows the range between the 20% to 80% levels. There is no convincing evidence for a cusp. The 50% criterion data can be fitted by a quadratic polynomial, $T_c = 1.405\ \mathrm{K} + 5.218\ \mathrm{K}/\%^2 \times \varepsilon^2$, with no linear cusp, in agreement with the results reported in Ref. [60]. T. Scaffidi and colleagues predicted that the cusp linear term at low strain is $0.3\ \mathrm{K}/\%$ [41]. The dashed line shows a fit with a $0.3\ \mathrm{K}/\%$ cusp imposed on the model: $T_c = a + 0.3 * |\varepsilon| + c * \varepsilon^2$. The fitted results are $a = 1.399\ \mathrm{K}$ and $c = 2.476\ \mathrm{K}/\%^2$. Clearly, the dashed line does not fit to the data, indicating the linear cusp is smaller than the prediction. This result rule out the cusp at level of $0.3\ \mathrm{K}/\%$ and imposes a constraint on calculations.

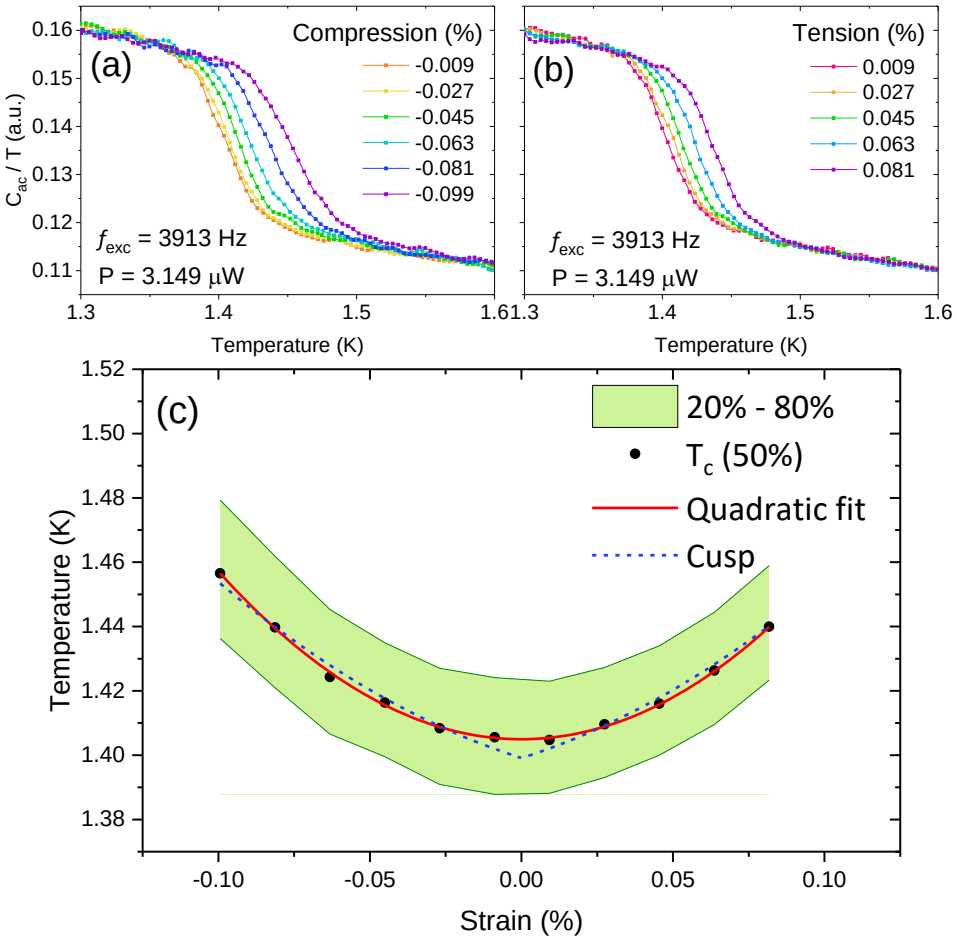

Figure 4.15: C_{ac}/T against temperature under (a) compression and (b) tension for sample #4. (c) T_c against strain near zero strain. The colored area is the transitions from 20% to 80%. The points are transitions at 50%. The red curve is a quadratic fit to T_c (50%). The dashed line is a fit with a linear cusp, $0.3\ \mathrm{K}/\% * |\varepsilon|$ (see main text for detail).

4.6 The relation between the heat capacity and the specific heat in the measurements

Heat capacity in my measurements is different from the convention. In conventional cases, heat capacity measurements are performed with a constant volume or mass. However, in my case, the probed length is changing because both thermal conductivity and specific heat are functions of temperature. Therefore, it is not trivial to convert heat capacity into specific heat. I will explain how the specific heat and the measured heat capacity are related.

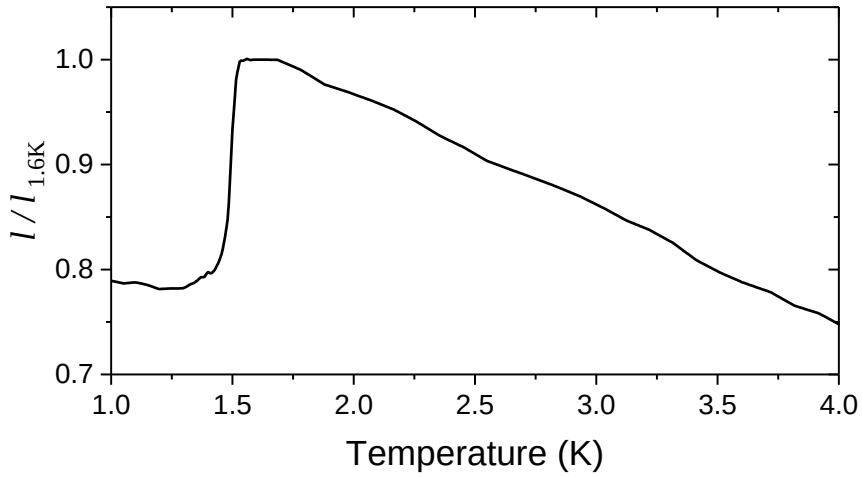

Figure 4.16: Normalized probed length $l/l_{1.6\mathrm{K}}$ against temperature.

According to equation (3-45), the probed length l is temperature dependent and determined by the thermal conductivity $\kappa(T)$, specific heat $c(T)$ and excitation frequency ω.

$$l(T) = \sqrt{\frac{\kappa(T)}{\omega \times c(T)}} \tag{4-3}$$

The probed length varies with temperature and the probed volume is therefore not a constant. Figure 4.16 shows the probed length l as a function of temperature. l is normalized to $l(1.6\ \mathrm{K})$ and there is a sharp change across T_c duo to the specific heat jump. The specific heat data is taken from the curve "Naoki3" in Figure 3.32 and the thermal conductivity data is from E. Hassinger *et al.*[48].

Here I start with an ideal case to demonstrate the relation between the heat capacity and the specific heat in this type of measurements. Suppose that $F(\omega) = 1$, the heater is a point-like contact on the sample and heat flow is one dimensional. The measured signal C_{ac} in ac calorimetry is equal to the

heat capacity C, which is equal to the specific heat c_V times the probed volume V. The probed volume is $V = l \times A$ where l is the probed length and A is the cross-sectional area.

$$C_{ac}(T) = C = c_V \times V = c_V \times \sqrt{\frac{\kappa}{\omega c}} \times A = \frac{A}{\sqrt{\omega}}\sqrt{\kappa(T)c(T)} \qquad (4\text{-}4)$$

C_{ac} is therefore not only related to the specific heat $c(T)$ but also related to the thermal conductivity $\kappa(T)$ because of the changing probed length as a function of temperature[6].

In a real situation, since f_{exc} is not far from f_2, $F(\omega) < 1$ and $C_{ac} = C/F(\omega)$. To eliminate $F(\omega)$, I assume that $F(\omega)$ in superconducting and normal state are the same and according to equation (4-4),

$$\frac{C_s}{C_n} = \frac{C_{ac,s}}{C_{ac,n}} = \frac{T_{ac,n}}{T_{ac,s}} = \sqrt{\frac{\kappa_s c_s}{\kappa_n c_n}} \qquad (4\text{-}5)$$

$\kappa_s(T)$, $\kappa_n(T), c_s(T)\ and\ c_n(T)$ at ε_{xx} = 0% are known curves and $C_{ac,s}\ and\ C_{ac,n}$ are the measured data. Therefore, the measured data at ε_{xx} = 0% can be compared with the model based on the equation (4-5).

[6] One of the important thermodynamic quantities is entropy. Since the probed length changes over temperature, it is not possible to obtain this quantity from the measurements.

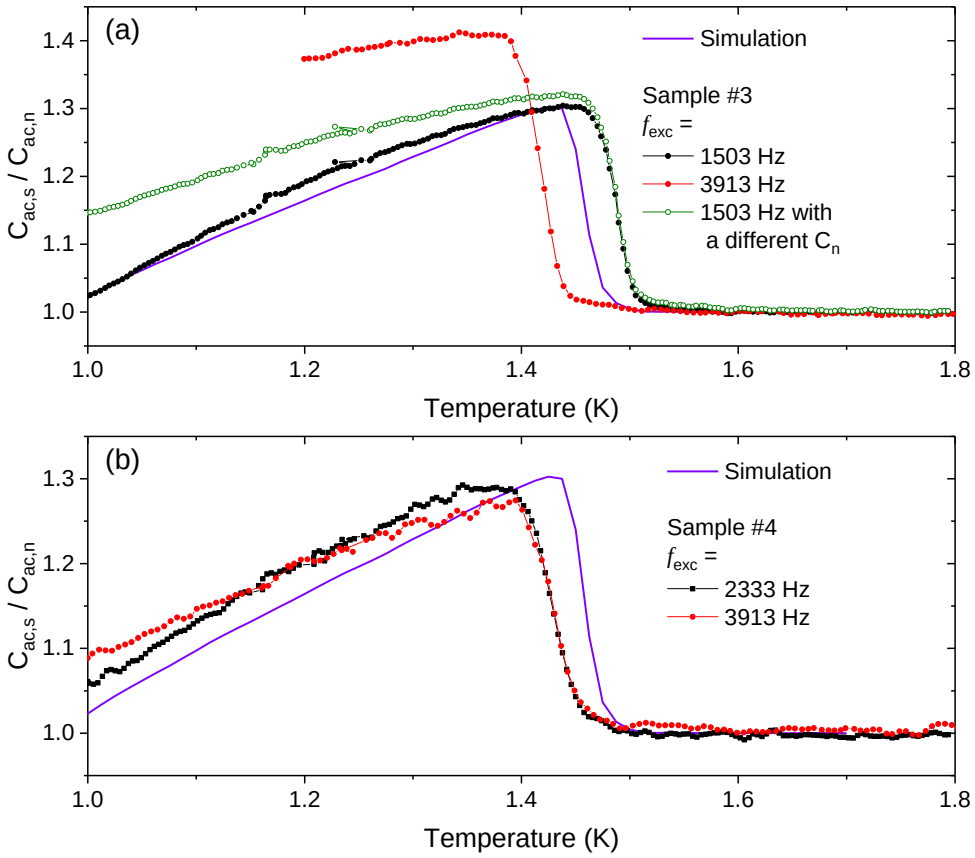

Figure 4.17: $C_{ac,s}/C_{ac,n}$ against temperature for (a) sample #3 and (b) sample #4 at ε_{xx} = 0% with different f_{exc}. The solid lines in panel (a) and (b) are simulations based on the equation (4-5). The green curve in panel (a) has a different $C_{ac,n}$, see text for details.

Figure 4.17 shows the comparisons at ε_{xx} = 0% between the measured curves[7] and the simulation curves based on the point-like contact model. $C_{ac,s}$ are measurements at H = 0 T and $C_{ac,n}$ are measurements at H = 0.1 T except for the green curve in panel (a). The solid lines are the simulation curves. The specific heat data are taken from Deguchi *et al*. [86]. The thermal conductivity data are taken from E. Hassinger *et al*.[48]. T_c is scaled to be 1.45 K to match the specific heat data. The red curve in panel (a) has a lower T_c because the applied power for the measurement is higher, leading to a large T_{DC} offset.

[7] The normal state of $T_{ac,n}/T_{ac,s}$ are slightly greater than 1 and it is likely due to a slightly different response of the thermocouple under magnetic field. To eliminate this offset, $T_{ac,n}/T_{ac,s}$ were normalized such that the normal state is 1.

The sizes of the heat capacity jumps, $\Delta C/C = \Delta C_{ac}/C_{ac}$, in Figure 4.17(b) are comparable to the simulation but in Figure 4.17(a) only the one with a lower f_{exc} matches the simulation. The $\Delta C_{ac}/C_{ac}$ for sample #3 with a higher f_{exc} is larger than the simulation. A higher f_{exc} means a shorter probed length for the sample. When the probed length is not much longer than the width of the sample or the region of the heater contacts, the assumptions of point-like contact and 1D heat flow break down. The difference between sample #3 and #4 is the width. Sample #3 is 50 μm wider than sample #4 and, therefore, sample #4 is less sensitive to the dimensionality of the heat flow. The results in Figure 4.17(a) suggest that the dimensionality plays a significant role for sample #3.

Figure 4.17(a) shows $C_{ac,s}/C_{ac,n}$ against temperature for sample #3. The black curves in both panels and the red curve in panel (b) seem to more or less fit the simulation curves. However, an anomaly is induced when the magnetic field is applied and there is an additional signal in $C_{ac,n}$ as described in Chapter 3.9.7. Hence, the $C_{ac,s}/C_{ac,n}$ curves need to be modified. Here I use sample #3 as an example. The green and black curves in Figure 4.17(a) are the $C_{ac,s}/C_{ac,n}$ curve with and without the modification due to the anomaly at low temperatures. The green curve deviates from the simulation below T_c. Several factors can contribute to this deviation: (a) The heat flow is far from perfectly 1D; (b) The specific heat and thermal conductivity of Sr_2RuO_4 are sample-dependent; (c) There are small addenda contributions to the measurements. Although the experimental curves do not perfectly fit to the simulation, $C_{ac} \propto \sqrt{\kappa c}$ is still a good approximation with which to interpret the heat capacity measurements.

Here, I estimate the addenda for sample #3. The addenda are dominated by silver and the silicon substrate for heater. There are 10 small silver wires (150 μm long and 50 μm in diameter) on both edges of the sample, 3 silver wires (1 mm long and 50 μm in diameter) and a silver stripe (1 mm x 300 μm x 10 μm) for the heater platform. The specific heat for silver at 1 K is about 0.8 mJ/mol-K, density $\rho_{Ag} = 10.49\ \mathrm{g/cm^3}$ and molar mass $M_{Ag} = 108\ \mathrm{g/mol}$. Together with the silver epoxy, the heat capacity from silver at 1 K is about 2×10^{-9} J/K. The substrate of the heater has dimensions 500 μm x 500 μm x 250 μm. The specific heat for silicon at 1 K is about $c_{Si} = 0.028$ mJ/mol-K, density $\rho_{Si} = 2.329$ g/cm^3 and molar mass $M_{Si} = 28$ g/mol, so the Si heat capacity is approximately 1.46×10^{-10} J/K. The total addenda heat capacity is about 2.2×10^{-9} J/K. The exposed sample has dimensions 2 mm x 250 μm x 150 μm. The specific heat for Sr_2RuO_4 at 1 K is about $C_{Sr_2RuO_4} = 55$ mJ/mol-K, density $\rho_{Sr_2RuO_4} = 5.92$ g/cm^3 and molar mass $M_{Sr_2RuO_4} = 340.31$ g/mol. The heat capacity of the exposed sample at 1 K is about 7.2×10^{-8} J/K. In the measurements, the probed length is smaller than the exposed length and, therefore, the addenda contributes approximately 5% of the total heat capacity.

4.7 Estimates for $\Delta c/c$

One of the important quantities that can be retrieved from heat capacity measurements is the electronic specific heat jump $\Delta c_e/c_e$. It is 1.43 for a superconductor with a full, isotropic gap on a spherical or cylindrical Fermi surface (s-wave or a fully-gapped p-wave state), 0.95 for a superconductor whose gap has vertical nodes on a cylindrical Fermi surface (d-wave) and 0.74 for the multi-band Sr_2RuO_4 [27]. However, the contributions from the addenda and phonon are not removable in this measurement approach. Therefore, in the following, I estimate $\Delta c/c$ for sample #3.

According to equation (4-5), the specific heat ratio c_s/c_n cab be expressed as follow:

$$\frac{c_s}{c_n} = \frac{\kappa_n}{\kappa_s}\left(\frac{T_{ac,n}}{T_{ac,s}}\right)^2 \tag{4-6}$$

where $T_{ac,s}$ and $T_{ac,n}$ are the amplitudes of the temperature oscillations in the superconducting state and in the normal state, respectively and κ_s and κ_n are thermal conductivity in the superconducting state and in the normal state, respectively. The relation between c_s/c_n and $\Delta c/c$ is:

$$\frac{\Delta c}{c} = \frac{c_s}{c_n} - 1. \tag{4-7}$$

The difference between κ_s and κ_n is small in the vicinity of T_c and, therefore,

$$\frac{c_s}{c_n} \cong \left(\frac{T_{ac,n}}{T_{ac,s}}\right)^2 \text{ near } T_c. \tag{4-8}$$

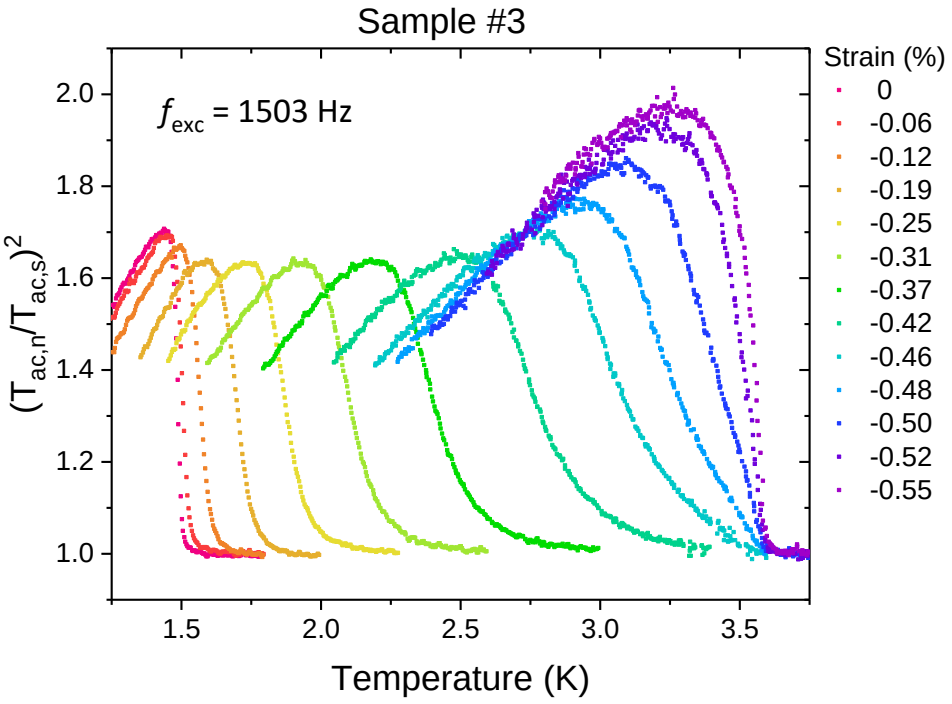

Figure 4.18: $(T_{ac,n}/T_{ac,s})^2$ against temperature for sample #3 at a series of compressive strains before the peak in T_c.

Figure 4.18 shows the results of $(T_{ac,n}/T_{ac,s})^2$ against temperature for sample #3 with f_{exc} = 1503 Hz from ε_{xx} = 0% to ε_{peak} = -0.55% [8]. The height of the transition drops a little bit when the strain is applied and stays at ≈1.65 until ε_{xx} = -0.37%. When a higher strain is applied, there is an increase of the height, reaching its maximum value of ≈1.95 at ε_{peak}. There is an enhancement of c_s/c_n from this analysis. However, in the original data, $T_{ac,n}/T_{ac,s}$ go from $\sqrt{1.65}$ to $\sqrt{1.95}$ which is about a 10% change. This change is small and thus a more careful analysis has to be taken into account to interpret this result. The assumption here is based on $C_{ac}\sim\sqrt{\kappa c}$ which is valid for a point-like heater contact in 1D. In real setups, heater and sample have finite widths, and the probed length is not much longer than these two widths. Hence, the dimensionality will play a role and $\sqrt{\kappa c}$ is only an approximation valid in limited cases. In the following, I will discuss this issue.

[8] The normal state values of $T_{ac,n}/T_{ac,s}$ are greater than 1, an effect that is dominantly due to different normal state values at different strains. To eliminate this offset, $T_{ac,n}/T_{ac,s}$ were normalized such that the normal state value is 1.

Resistivity and thermal conductivity

The Wiedemann-Franz law describes the relation of the thermal conductivity κ and electrical conductivity σ in a metal if electrons play the dominate role on the heat and electric transport:

$$\frac{\kappa}{\sigma} = LT, \tag{4-9}$$

where T is temperature and L is the Lorenz number $L = \pi^2(k_B/e)^2/3 = 2.44 \times 10^{-8}\ \mathrm{W\Omega K^{-2}}$. Sr_2RuO_4 is known to follow the Wiedemann-Franz law well at low temperature [48].

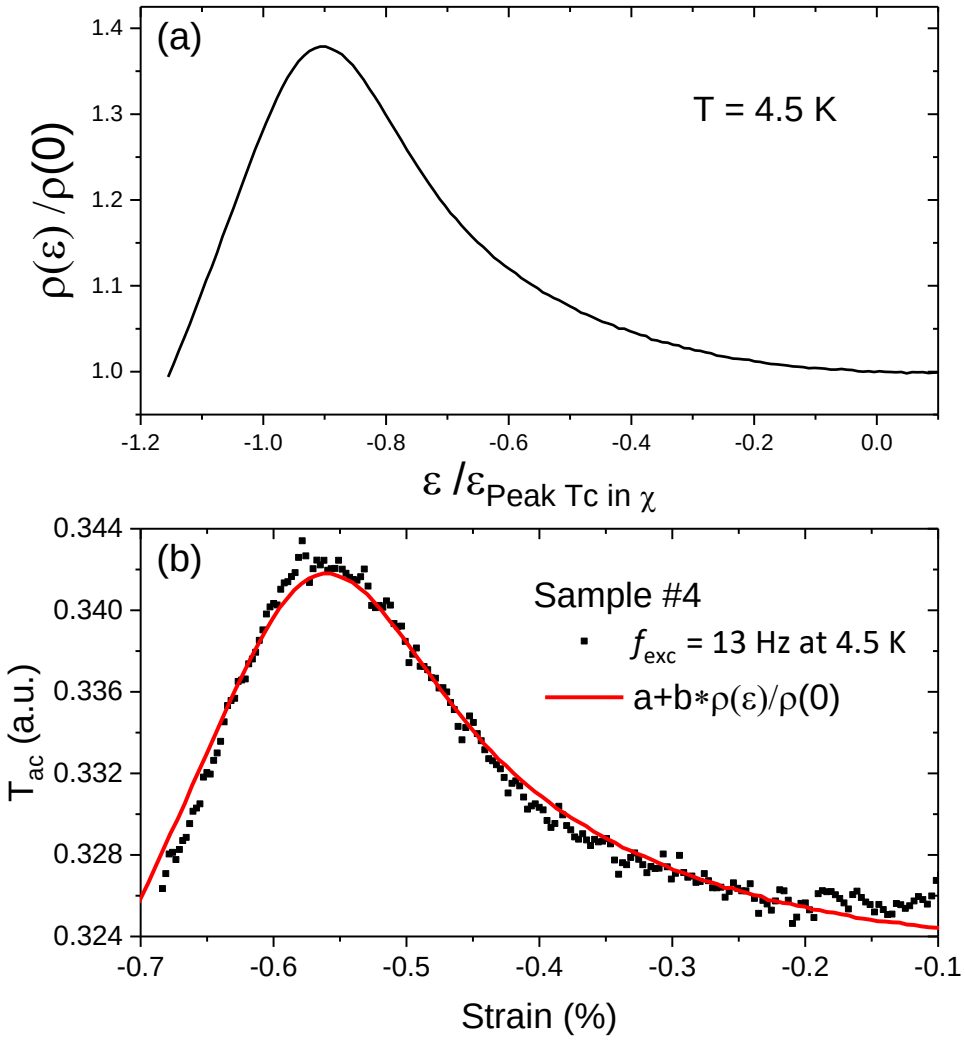

Figure 4.19: (a) Normalized resistivity *ρ(ε)/ρ(0)* against normalized strain *ε/ε(*peak T_c in *χ)* at T = 4.5 K from M. Barber *et al*. [87]. (b) T_{ac} against strain for sample #4 at 4.5K with f_{exc} = 13 Hz. The red line is a fitting curve based on the model *a + b*ρ(ε)/ρ(0)*. The details are described in the text.

Figure 4.19(a) shows the resistivity against strain at 4.5 K from M. Barber *et al*. [87]. The *x*-axis is normalized to the peak T_c in susceptibility χ measurements. $\rho(\varepsilon)$ is enhanced by 40% around the strain at which the peak T_c is seen in χ. The enhancement of the resistivity suggests that there is a reduction of the thermal conductivity according to the Wiedemann-Franz law.

According to equation (3-31), T_{ac} is a measurement of the thermal conductance to the bath k_b when $f_{exc} < f_1$. The heater is placed in the middle of the sample and the heat flow goes from sample to the Stycast and then to the bath. Therefore, k_b as a function of strain ε contains contributions from not only the Stycast but also the sample:

$$\frac{1}{k_b(\varepsilon)} = \frac{1}{k_{sty}} + \frac{1}{k_s(\varepsilon)} \tag{4-10}$$

Since Stycast is an amorphous material and the changes of the geometry in Stycast layers are negligible, its thermal conductivity is assumed to be independent of strain. Therefore, the change in $k_b(\varepsilon)$ is due to the change in $k_s(\varepsilon)$, the response of which can be replaced according to the Wiedemann-Franz law:

$$k_s(\varepsilon) = k_s(0) \times \frac{k_s(\varepsilon)}{k_s(0)} = k_s(0) \times \frac{\rho(0)}{\rho(\varepsilon)} \tag{4-11}$$

Figure 4.19(b) shows T_{ac} against strain for sample #4 at T = 4.5 K at which the resistivity data is reported. (Sample #3 broke on cooling so here I demonstrate the concept on the data from sample #4.) To reach 99% accuracy according to equation (3-30), f_{exc} = 13 Hz was used. There is a peak in T_{ac} and the position of this peak, within experimental error, is the same as the peak in T_c determined by the heat capacity measurements (see section 4.8). Therefore, the peak in resistivity is set to be equal to ε_{peakTc} in the fitting model.

According to equations (3-31), (4-10) and (4-11),

$$T_{ac}(\varepsilon) = \frac{P}{k_b(\varepsilon)} = \frac{P}{k_{sty}} + \frac{P}{k_s(\varepsilon)} = \frac{P}{k_{sty}} + \frac{P}{k_s(0)} \times \frac{\rho(\varepsilon)}{\rho(0)} \tag{4-12}$$

The fitting model is, therefore, $a + b*\rho(\varepsilon)/\rho(0)$. The result is shown in Figure 4.19(b) with the red line. The fitting curve is not perfect but it matches the data fairly well which suggests this fit already captures the essential features. One of the possible reasons for the deviation is from the $\rho(\varepsilon)/\rho(0)$ curve because the authors in Ref. [87] show that it is sample dependent. The fitting results are a = 0.277 and b = 0.0469. k_{sty} and $k_s(0)$ can, in principle, be estimated from a and b but the signal T_{ac} has been reduced since f_{exc} is low and not working in a proper frequency range for the low temperature transformer. In summary, the results suggest that there is a reduction of thermal conductivity to 70% at ε_{peak}.

The reduction of the probed length

Here I discuss two factors that can shorten the probed length at ε_{peakTc} at T = 3.5 K. The first one is the difference in temperature as shown in Figure 4.16. The probed length is reduced to ≈80% at T = 3.5 K. The second one is the change of the thermal conductivity κ and specific heat c at ε_{peakTc}. As discussed above, $\kappa(\varepsilon = \varepsilon_{peakTc})$ is reduced to 70% of its value at zero strain. From the strain sweep data (see section…), the signal $1/V_{ac}$ remains more or less the same in the entire strain range and increases by only a few percent around ε_{peakTc}. This suggests that there is a ≈40% increase of specific heat at ε_{peakTc} based on the relation $C_{ac} \propto \sqrt{\kappa c}$. Therefore, the probed length at ε_{peakTc} is reduced to 70% of that at zero strain:

$$l_{peakTc} = \sqrt{\frac{\kappa(\varepsilon_{peakTc})}{\omega c(\varepsilon_{peakTc})}} = \sqrt{\frac{0.7\kappa(0\%)}{\omega \times 1.4c(0\%)}} = 0.7 l_{0\%}$$

The lowest frequency to probe the homogeneous part for sample #3 is about 1500 Hz which is determined around T = 1.5 K at low strain. When the strain is applied up to ε_{peakTc}, the probed length around T = 3.5 K is reduced to ≈55% in total and the length scale is comparable to the widths of the heater and the sample. The heat flow is more toward to 2D instead of 1D and $\sqrt{\kappa c}$ is not a good approximation for the heat capacity.

Heat capacity measurements at the peak in T_c with different f_{exc}

The second effect discussed above suggests that the lowest frequency at ε_{peakTc} is lower than 1500 Hz because the thermal conductivity at ε_{peakTc} is lower than that at zero strain and the specific heat is higher. To verify this argument, I performed heat capacity measurements with different f_{exc} to find out if the lowest f_{exc} at ε_{peakTc} is lower than 1500 Hz.

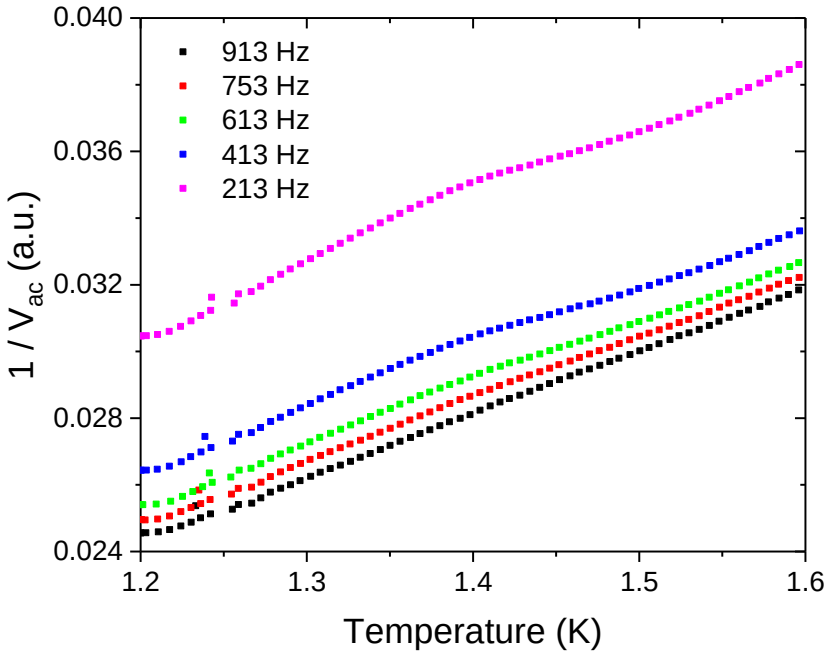

Figure 4.20: Heat capacity measurements for sample #3 with different f_{exc} at ε_{peakTc}.

Figure 4.20 shows the heat capacity measurements as function of temperature from 1.2 K to 1.6 K for sample #3 at $\varepsilon_{\text{peak Tc}}$ with different f_{exc}. There is a kink related to the unstrained T_c at lower f_{exc}. When the f_{exc} is increased, the size of the kink is reduced. It disappears when f_{exc} goes beyond 753 Hz. In other words, to probe the homogenous region at $\varepsilon_{\text{peak Tc}}$, the lowest frequency is 753 Hz. This frequency is half as much as the one determined at low strain, 1503 Hz. It indicates that the probed length at $\varepsilon_{\text{peak Tc}}$ is 70% of the one determined at low strain and supports the second reason for the reduction of the probed length.

The probed length at high f_{exc} is short and comparable to the width of the sample and the heater. The heat flow becomes more 2D-like and $\sqrt{\kappa c}$ is no longer a good approximation for the heat capacity. To reduce this 2D effect and obtain a qualitative comparison of c_s/c_n between ε_{xx}= 0% and ε_{peakTc}, a series of lower frequencies were used to measure the heat capacity for sample #3 at ε_{peakTc}.

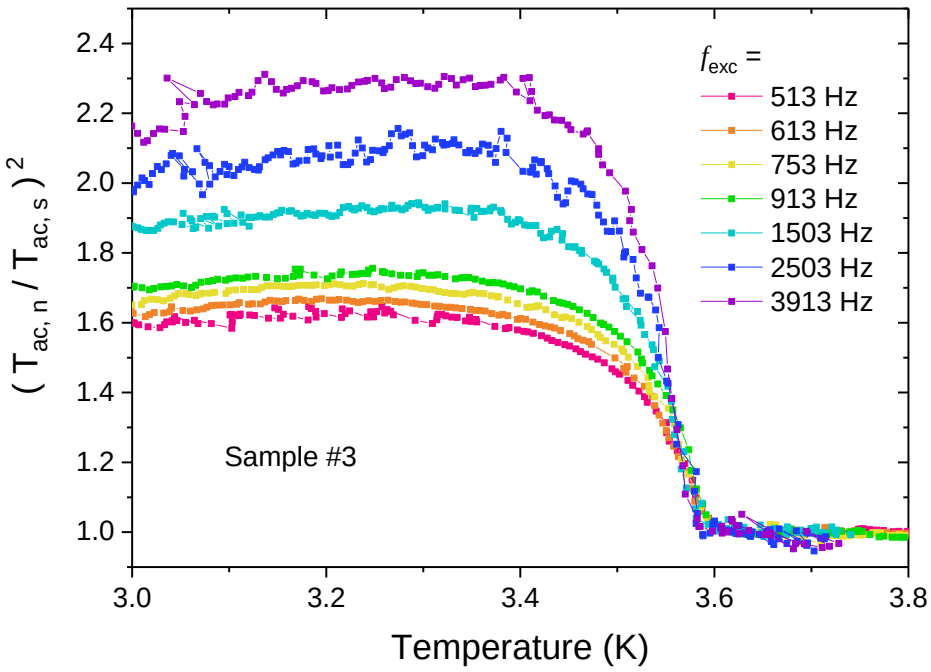

Figure 4.21: $(T_{ac,n}/T_{ac,s})^2$ against temperature for sample #3 with different f_{exc}.

Figure 4.21 shows $(T_{ac,n}/T_{ac,s})^2$ against temperature with f_{exc} from 513 Hz to 3913 Hz[9]. $T_{ac,n}$ and $T_{ac,s}$ are the temperature oscillations in the normal state (H = 0.2 T) and the superconducting state (H = 0 T). The transition height reduces when f_{exc} decreases. The heights are ≈2.3 at 3913 Hz, the highest frequency in the measurements, ≈1.9 at 1503 Hz, the lowest frequency determined near 1.5 K with a low strain, and ≈1.7 at 753 Hz, the lowest frequency determined near 1.5 K with $\varepsilon_{xx} = \varepsilon_{peakTc}$. Since these are measurements around 3.5 K, the probed length is reduced to 80%. It suggests that the lowest frequency to probe the homogeneous region near 3.5 K is 753 Hz × $(80\%)^2$ ≈ 480 Hz. The lowest f_{exc} in Figure 4.21 is 513 Hz, which is greater than 480 Hz, and the transition height goes down to ≈1.6. Qualitatively speaking, this indicates that the evolution of $\Delta c/c$ from zero strain to $\varepsilon_{peak\ Tc}$is not very large.

[9] The normal state values of $T_{ac,n}/T_{ac,s}$ are slightly greater than 1 and it is likely due to a slightly different response of the thermocouple under magnetic field. To eliminate this offset, $T_{ac,n}/T_{ac,s}$ were normalized such that the value in the normal state is 1.

4.8 Strain sweeps in the normal state

Experimentally, it is clear from Figure 4.1 to Figure 4.4 that the value of C_{ac}/T in the normal state is enhanced when a compressive strain is applied. In sample #4, C_{ac}/T is reduced around ε_{peakTc}. Theoretically, A. Steppke *et al.* [41] suggest that the γ-sheet approaches the vHS under strain and, thus, there is an increase of DoS around vHS. Therefore, I carried out strain sweeps to determine C_{ac} as a function of strain at constant temperature. I performed the measurements on all samples and studied sample #3 and #4 in detail.

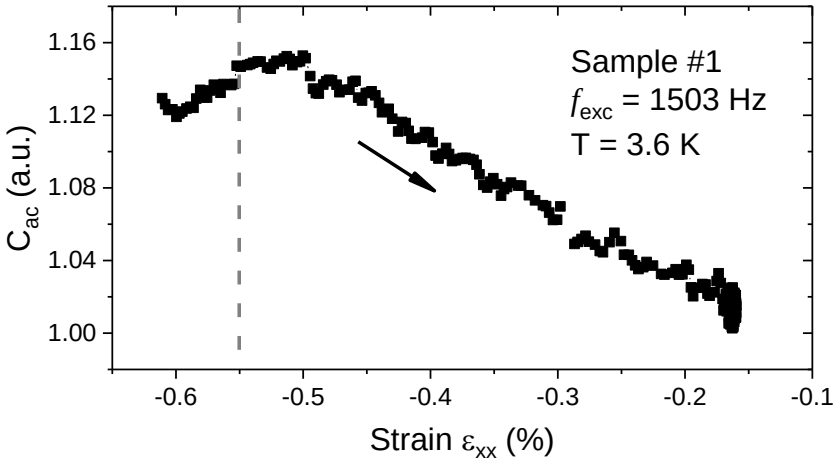

Figure 4.22: C_{ac} against strain in the normal state for sample #1. The arrow indicates the direction of the sweep. The dashed line indicates ε_{peakTc}.

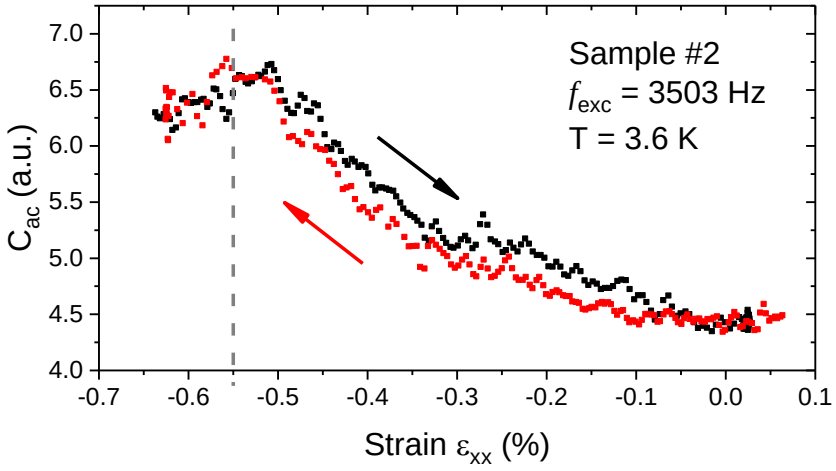

Figure 4.23: C_{ac} against strain in the normal state for sample #2. The arrows indicate the directions of the sweeps. The dashed line indicates ε_{peakTc}.

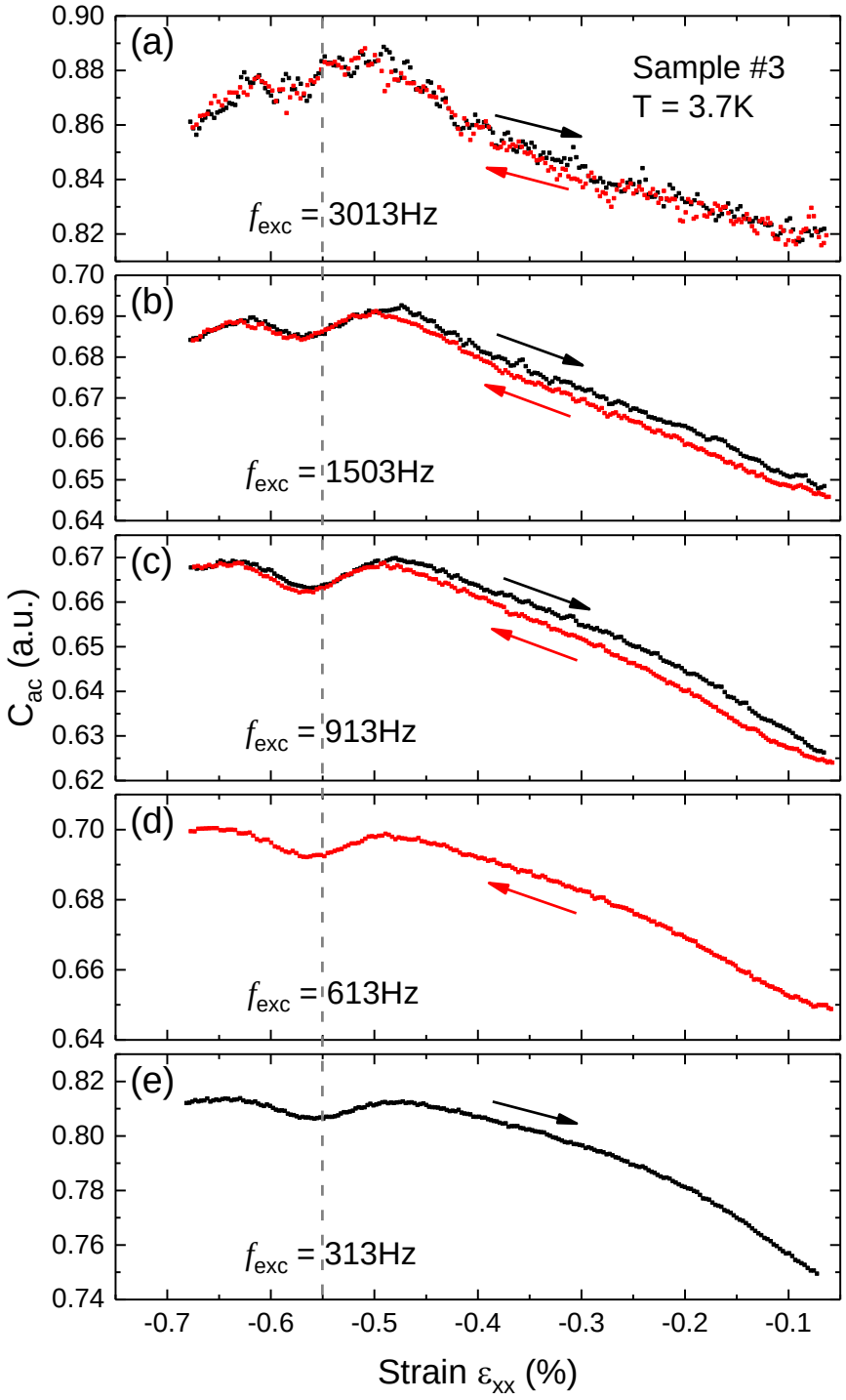

Figure 4.24: C_{ac} against strain in the normal state for sample #3 with different f_{exc}. The arrows indicate the directions of the sweeps. The dashed line indicates ε_{peakTc}.

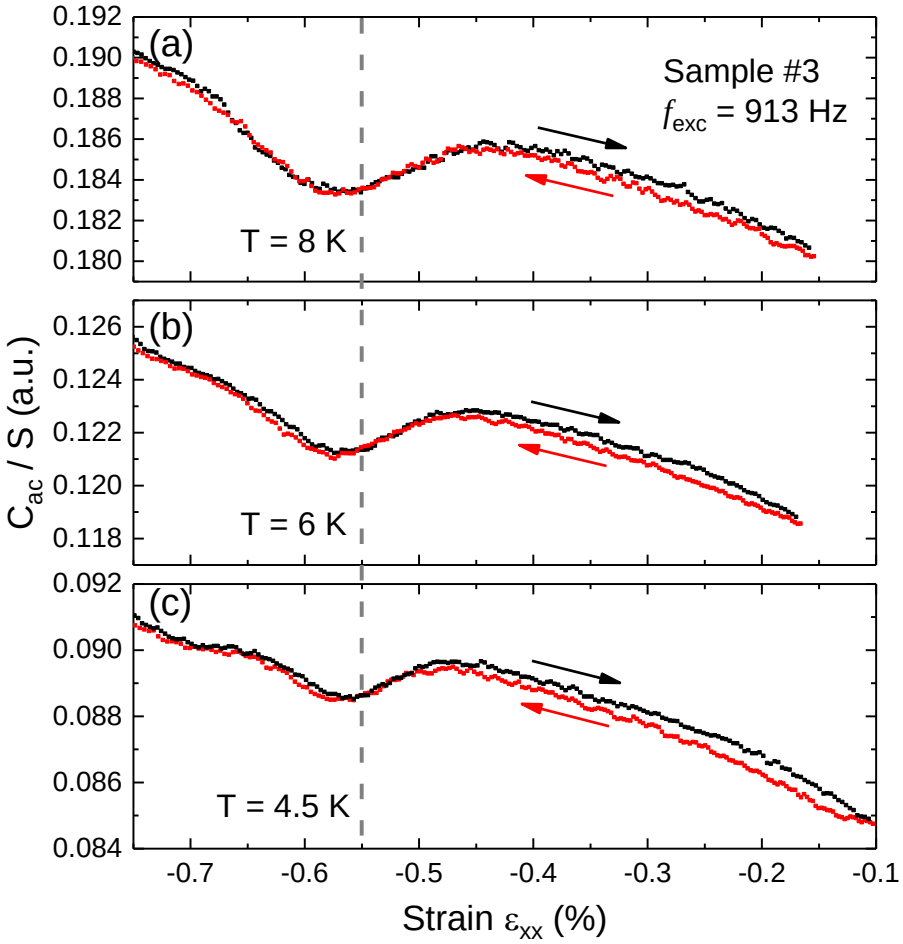

Figure 4.25: C_{ac}/S against strain in the normal state for sample #3 at different temperatures. Here S is the thermopower, used for normalization to allow comparison of data outside the calibrated range of the thermocouple (see main text and footnote for explanation).The arrows indicate the directions of the sweeps. The dashed line indicates ε_{peakTc}.

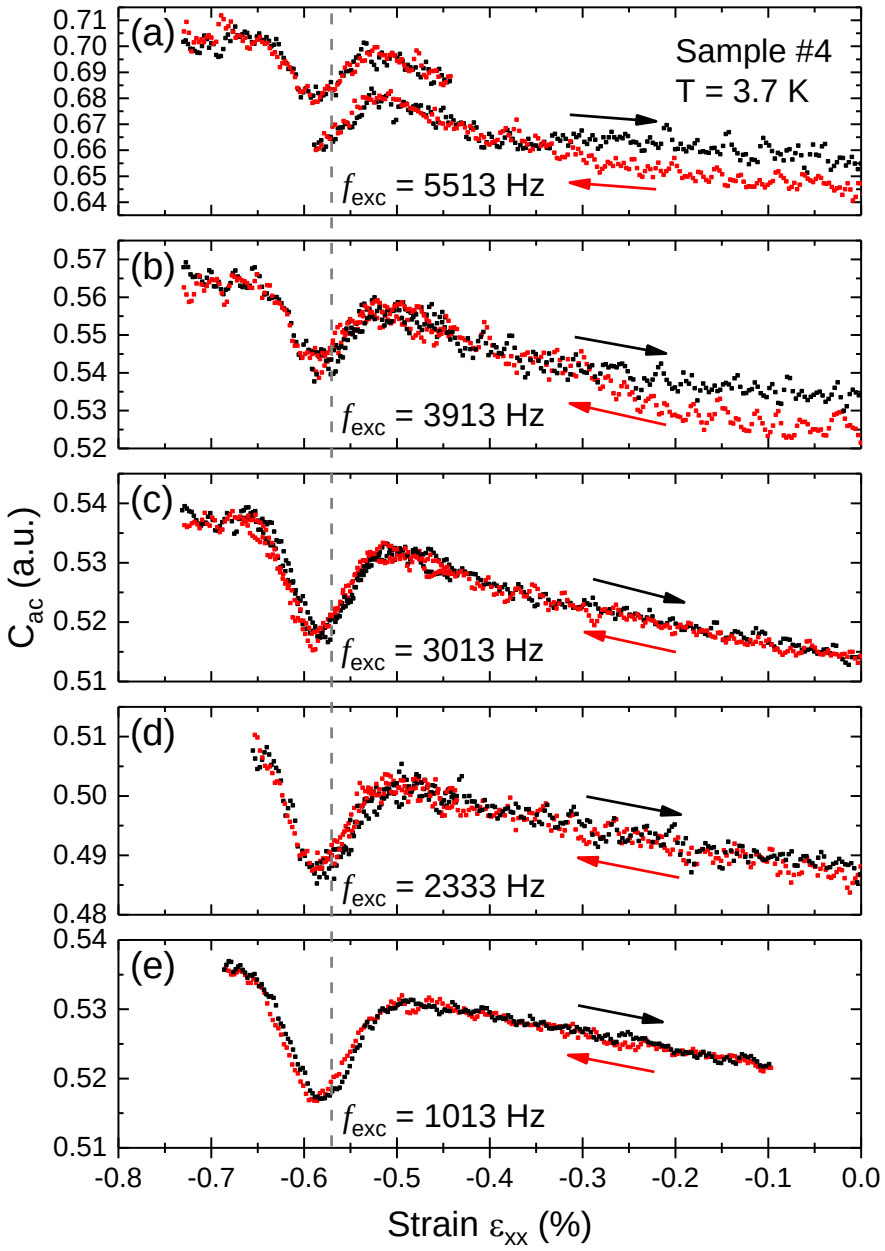

Figure 4.26: C_{ac} against strain in the normal state for sample #4 with different f_{exc}. The arrows indicate the directions of the sweeps. The dashed line indicates ε_{peakTc}.

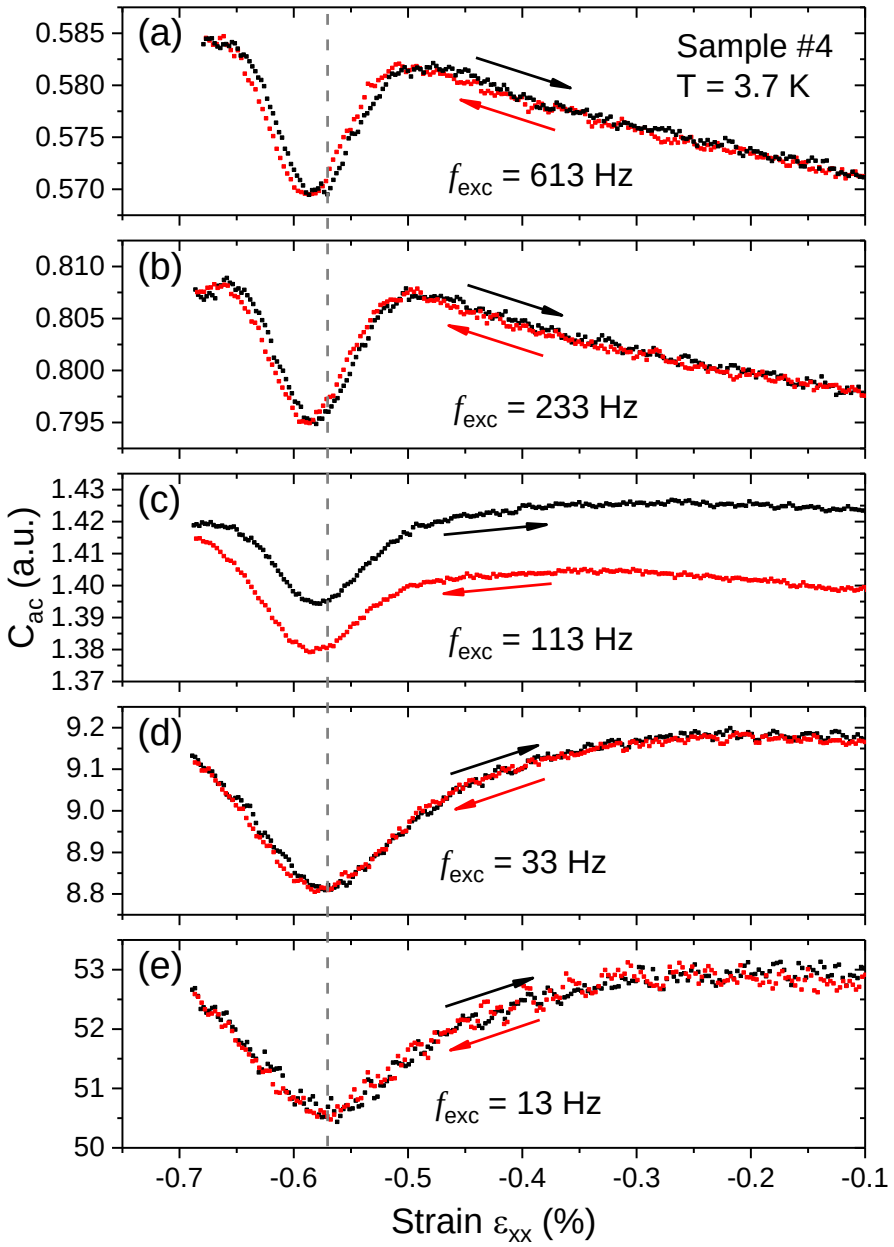

Figure 4.27: C_{ac} against strain in the normal state for sample #4 with different f_{exc}. The arrows indicate the directions of the sweeps. The dashed line indicates ε_{peakTc}.

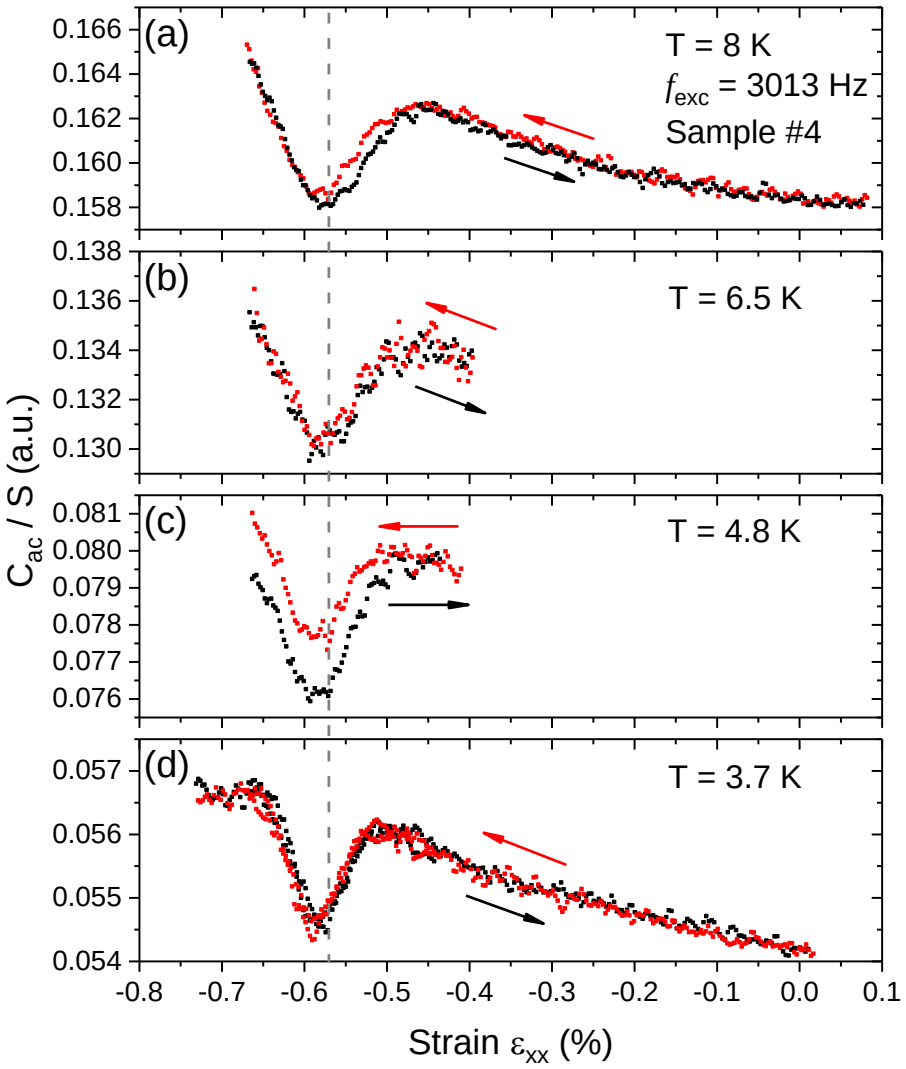

Figure 4.28: C_{ac}/S against strain in the normal state for sample #4 at different temperatures. The arrows indicate the directions of the sweeps. The dashed line indicates ε_{peakTc}.

Figure 4.22 and Figure 4.23 show C_{ac} against strain in the normal state for sample #1 and #2. The arrows indicate the directions of the sweeps and the dashed lines indicate ε_{peakTc}. C_{ac} increases when strain is applied and reaches to its maximum around ε_{peakTc} for both samples. The increase of C_{ac} in sample #1 is greater than 15% and in sample #2 is about 45%.

Sample #4 remained intact during the cool-down (see Appendix A) so here I begin with sample #4. Figure 4.26 and Figure 4.27 show C_{ac} against strain in the normal state for sample #4 with different f_{exc}. The lower cut-off frequency f_1 is about 100 Hz. In Figure 4.26 and Figure 4.27 (a)-(b), because $f_{exc} > f_1$, they are measurements of the heat capacity. C_{ac} is enhanced when ε_{xx} approaches ε_{peakTc} but the enhancement is small (about 3%) compared to that in sample #1 and #2. However, a remarkable feature appears at ε_{peakTc}. There is a rapid decrease of C_{ac} around ε_{peakTc}. This dip structure is repeatable for $f_{exc} > f_1$ and for both sweeping directions. Its size is about 3% of the total signal for $f_{exc} > 1000$ Hz. In Figure 4.27 (d) and (e), because $f_{exc} < f_1$, the measurements correspond to the thermal conductance to the bath k_b as described in section 4.7. The dip at ε_{peakTc} indicates a reduction of the thermal conductivity of the sample and is consistence with the resistivity data based on the Wiedemann-Franz law. In Figure 4.27 (c), the measurements are a combination of heat capacity and thermal conductance because $f_{exc} \cong f_1$. The curves have the shape of k_b but tend to form a kink around ε_{xx} = -0.5%. Figure 4.28 shows C_{ac}/S against strain in the normal state for sample #4 at different temperatures, where S is the thermopower of the Au/AuFe thermocouple[10]. The dip persists up to 8 K and its location is temperature independent.

Similar measurements were done on sample #3[11]. Figure 4.24 shows C_{ac} against strain in the normal state for sample #3 with different f_{exc}. C_{ac} is enhanced by more than 7% near ε_{peakTc} and a dip is located at ε_{peakTc}. The dip is repeatable as well at different f_{exc}. However, its shape is rounded and its size is about 1% of the total signal. Figure 4.25 shows show C_{ac}/S against strain in the normal state for sample #3 at different temperatures. The dip persists up to 8 K and its location is temperature independent.

The dip structure appears on both sample #3 and #4. The shape in sample #3 is more rounded than that in sample #4, and the size in sample #3 is smaller than that in sample #4. The difference between sample #3 and #4 is the inhomogeneity. Sample #3 is less homogeneous than sample #4 and according to the simulations, the inhomogeneity is 13% for sample #3 and 8% for sample #4. The inhomogeneity smears the features in the measurements, so it is reasonable that the dip in sample #3 is rounded and smaller. Besides, samples #1 and #2 are more inhomogeneous than sample #3 so it is reasonable as well that they are featureless at ε_{peakTc}. The picture of the

[10] The calibration of the thermocouple was carried out up to 4.5 K. The voltage response could therefore not be used to convert to the temperature on the thermocouple above 4.5 K. Therefore, the y-axis is plotted as C_{ac}/S for comparison.

[11] The data shown here were taken at a different run. Hence, the normal state C_{ac} is slightly different from the value shown in section 4.3. I refer the interested reader to the Appendix C for their difference.

inhomogeneity can explain the shape of the dip in all samples. It is then expected that the dip structure will be sharper and deeper with a less inhomogeneous sample.

The overall rise from low strain to the peak in T_c is 15% for sample #1, 45% for sample #2, 7% for sample #3 and 3% for sample #4. Samples #1 and #2 are different from #3 and #4 because the aspect ratios of the samples' geometry are significantly different. Samples #1 and #2 are short and wide whereas #3 and #4 are long and narrow. The homogeneous region in samples #1 and #2 is comparable to the heater contacts and their widths so the signal is sensitive to the change of the probed length, causing a larger overall rise than that in samples #3 and #4. For samples #3 and #4, the differences come from the effective thermal conductance of the sample. Sample #4 remained intact during the cool-down process whereas sample #3 broke. Figure 4.29 shows T_{ac} as a function of strain for sample #3 at T = 4.5 K. Since $f_{exc} < f_1$, T_{ac} is inversely proportional to the thermal conductance of the sample. The inset shows T_{ac} near zero strain. The large step around zero strain evidences that the sample is broken. The red line is a fit described in section 4.7 and whose parameters are obtained based on the data $\varepsilon > 0.45\%$. The large difference between the red line and the measured data at low strains indicates that the thermal conductance is still dominated by the interface between the broken pieces even though the sample is reengaged at low strains. Hence, the effective thermal conductivity tends to be smaller at low strain, causing a smaller C_{ac} in the strain sweeps for sample #3 near zero strain. A downward curve can be observed especially at lower f_{exc}.

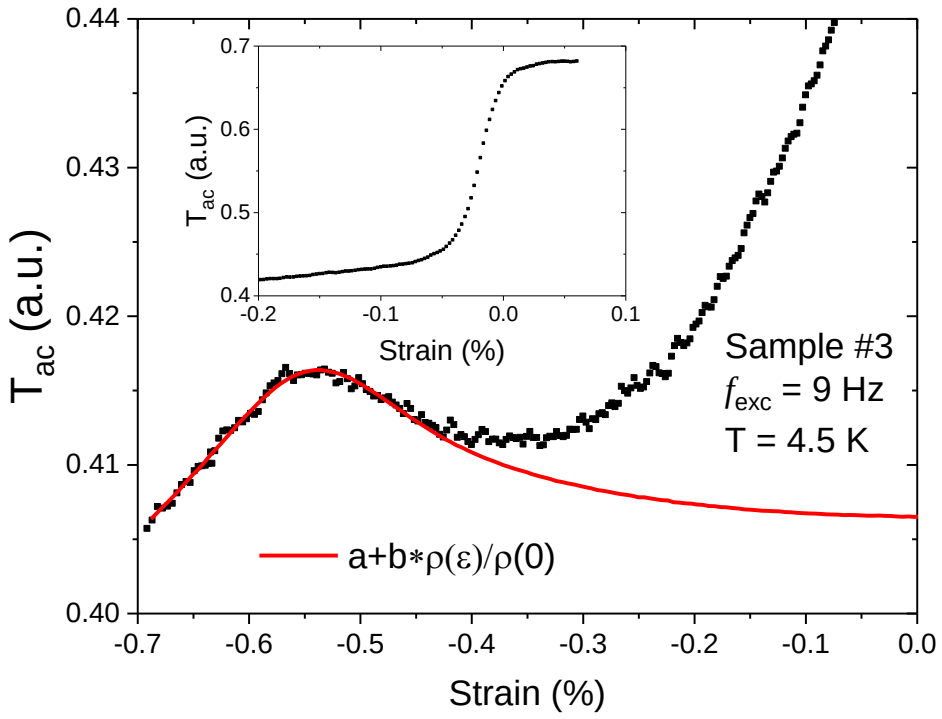

Figure 4.29: T_{ac} as a function of strain for sample #3 with $f_{exc} < f_1$. The red line is a fitting curve based on the model $a + b*\rho(\varepsilon)/\rho(0)$ described in section 4.7. The inset shows the strain sweep around zero strain.

T_c and C_{ac} against strain

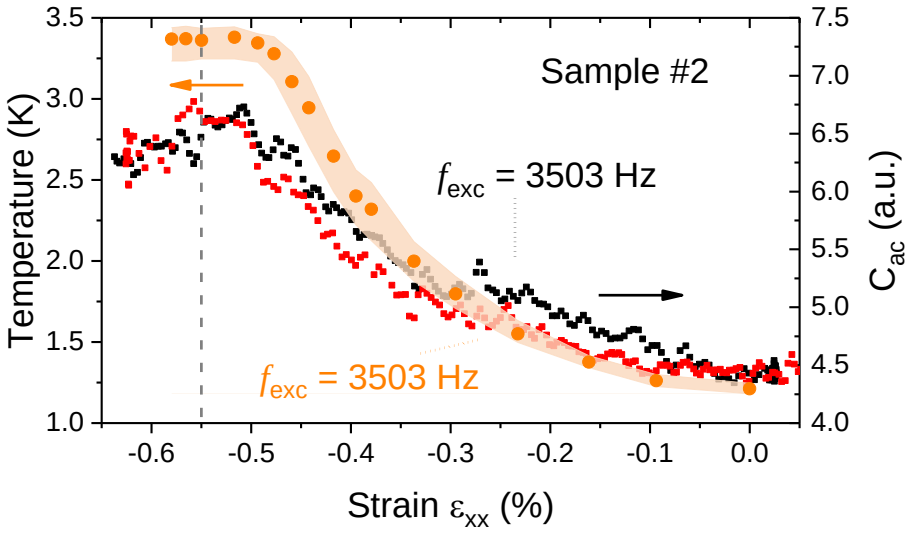

Figure 4.30: T_c and C_{ac} against strain for sample #2. The dashed line indicates the position of ε_{peakTc}.

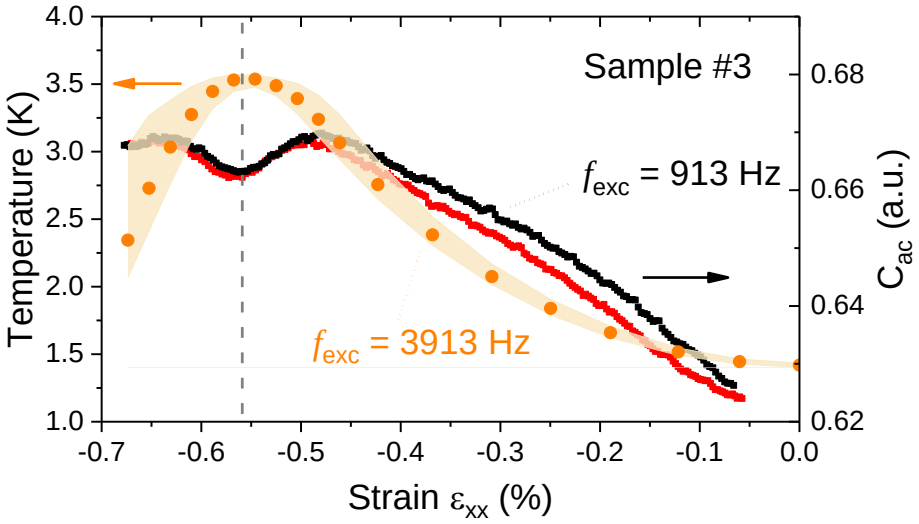

Figure 4.31: T_c and C_{ac} against strain for sample #3. The dashed line indicates the position of the dip minimum in the strain sweeps.

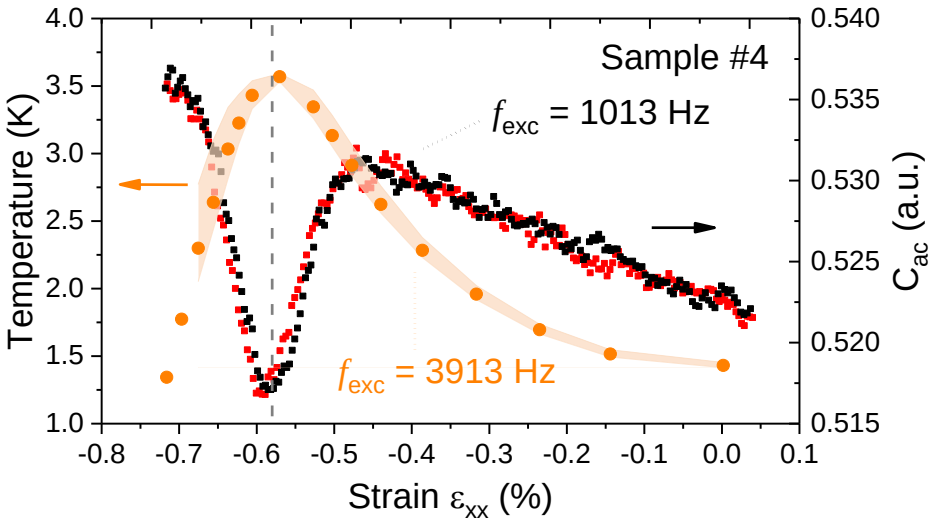

Figure 4.32: T_c and C_{ac} against strain for sample #4. The dashed line indicates the position of the dip minimum in the strain sweeps.

Figure 4.30 to Figure 4.32 show both T_c and C_{ac} as a function of strain for sample #2 to #4. The strain sweeps in sample #2 are featureless because of strain inhomogeneities but sample #3 and #4 both have a dip in the strain sweeps. Remarkably the peak in T_c lays inside the dip in the strain sweeps. Here I first discuss the sample #4 since the dip is more obvious.

In Figure 4.32, the T_c curve is determined at f_{exc} = 3913 Hz and the strain sweeps are at f_{exc} = 1013 Hz. The dashed line indicates the position of the dip minimum, ε_{dip}, in the strain sweeps. The difference between ε_{dip} and ε_{peakTc} is ≈0.01%. In the T_c curve, there is no corresponding point at ε_{dip} and the data for strain sweeps at ε_{peakTc} are near the dip minimum with the difference in the noise level. Hence, within experimental resolution, the position of the peak in T_c is indistinguishable from the position of the dip minimum in strain sweeps. Similarly, although the dip is smaller and rounded in sample #3, its peak in T_c peaks inside the dip and $\varepsilon_{peakTc} \approx \varepsilon_{dip}$ within the experimental resolutions.

Specific heat as a function of strain

The reduced thermal conductivity at ε_{peakTc} suggests a reduced probed length in the measurements. Assuming that the specific heat remains constant, C_{ac} would decrease as function of strain due to the reduction of the probed volume. However, the measured C_{ac} in all samples has at least a few percent of enhancement around ε_{peakTc}. This suggests that there is an increase of the specific heat around ε_{peakTc}. The measured C_{ac} is approximately proportional to $\sqrt{\kappa c}$, if the probed length is longer than the width of the sample and the length of the heater contacts on the sample. Since sample #4 has the narrowest width and longest exposed length among the samples, I use it to simulate the specific heat.

According to equation (4-4),

$$C_{ac} \propto \sqrt{\kappa c}$$

By applying the Wiedemann-Franz law, the specific heat c as function of strain can be estimated:

$$c(\varepsilon) \propto \frac{C_{ac}^2(\varepsilon)}{\kappa(\varepsilon)} \propto \rho(\varepsilon) \times C_{ac}^2(\varepsilon) \qquad (4\text{-}13)$$

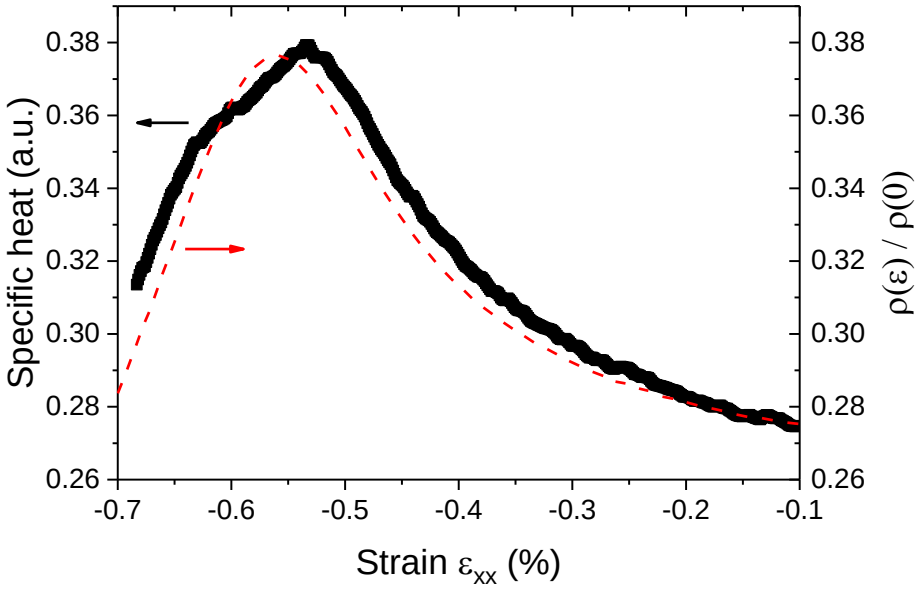

Figure 4.33: The calculated specific heat against strain for sample #4. The dashed line indicates $\rho(\varepsilon)/\rho(0)$ scaled by a factor of 0.273.

Figure 4.33 shows the calculated specific heat as a function of the applied strain. The specific heat is enhanced around ε_{peakTc}. $C_{ac}(\varepsilon)$ is from the measurements at f_{exc} = 1013 Hz and $\rho(\varepsilon)$ is from M. Barber *et al*.[87] as shown in Figure 4.19(a). The dashed line indicates $\rho(\varepsilon)/\rho(0)$ scaled by a factor of 0.273. The change in C_{ac} is small in all cases, see Figure 4.26 and Figure 4.27. The specific heat is dominated by $\rho(\varepsilon)$ and has little dependence on C_{ac} at different f_{exc}. The signal $C_{ac}(\varepsilon)$ includes the addenda. A constant background is expected so the shape of the specific heat curve will not change and the enhancement of the specific heat around ε_{peakTc} is robust. The enhancement of the specific heat around ε_{peakTc} is more than 35% and it will be larger if the addenda contribution is removed.

The next thing that needs to be considered is the temperature dependence of the specific heat as a function of strain. It has been shown that the dip structure in the strain sweeps for both sample #3 and #4 persists up to 8K with its location unchanged, suggesting that it is related to the band structure, which is believed to be temperature independent. Besides, the peak position in the resistivity measurements [87] remains the same up to 15 K. Both evidences suggests that the enhancement of calculated specific heat around ε_{peakTc} is related to the band structure.

All in all, the enhancement of specific heat around ε_{peakTc} is related to the band structure and suggests the existence of vHS. For comparisons, DFT calculations [41] suggests a $\approx 25\%$ enhancement of DoS at vHS.

The strong increase of T_c under strain can be understood as an increase of the DoS when the γ-sheet approaches the vHS. The result from the calculated specific heat shows an enhancement around ε_{peakTc} and suggests the existence of the vHS. However, the existence of the dip in the strain sweeps at ε_{peakTc} is unexpected from the picture of the vHS. Another possible scenario is that the peak in T_c comes from the formation of a strain-induced phase which reduces T_c. Y.-C. Liu *et al*. [88] predicted the formation of spin density wave (SDW) for uniaxial pressured Sr_2RuO_4 based on the functional renormalization group calculations. However, M. Barber *et al*. [87] point out that a SDW should open a magnetic gap at low temperatures and, in principle, should cause an increase in resistivity. Their resistivity data show no signature of an ordering transition and does not support the picture of the appearance of a SDW under strain. The presence of this dip at ε_{peakTc} in the strain sweeps is a puzzle. Its existence can be explained by several possibilities (a decrease of thermal conductivity, a decrease of specific heat or others) and is worthy of further study.

4.9 Heat capacity measurements at a series of small increments of compressive strains

A. Steppke *et al.*[41] suggest that the pairing symmetry in 3.4K-Sr_2RuO_4 might be different from that in 1.5K-Sr_2RuO_4. That the hysteresis in $H_{c2||a}$ against temperature for 3.4K-Sr_2RuO_4 and the size of $H_{c2||a}(0)$ are consistent with the Pauli limit suggests that the pairing in 3.4K-Sr_2RuO_4 is spin-singlet and that there is a pairing symmetry change somewhere between $\varepsilon_{xx} = 0\%$ and ε_{peakTc}. If this is the case, it is expected that there should be a change in the heat capacity as well. To search for this possibility, heat capacity measurements at a series of small increments of compressive strains were done for sample #2 to #4.

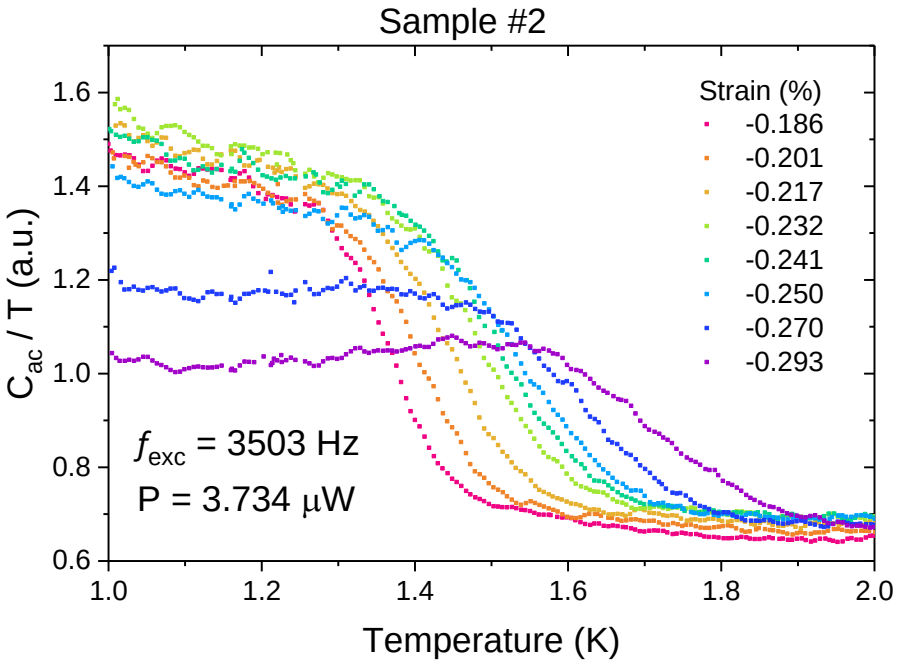

Figure 4.34: C_{ac}/T against temperature for sample #2 at a series of small increments of compressive strains.

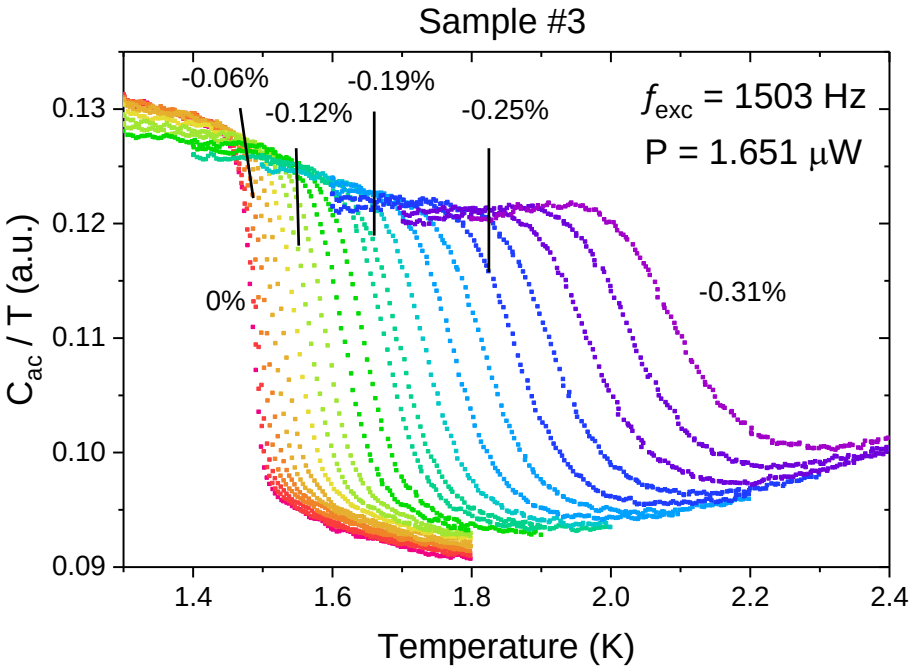

Figure 4.35: C_{ac}/T against temperature for sample #3 at a series of small increments of compressive strains with f_{exc} = 1503 Hz.

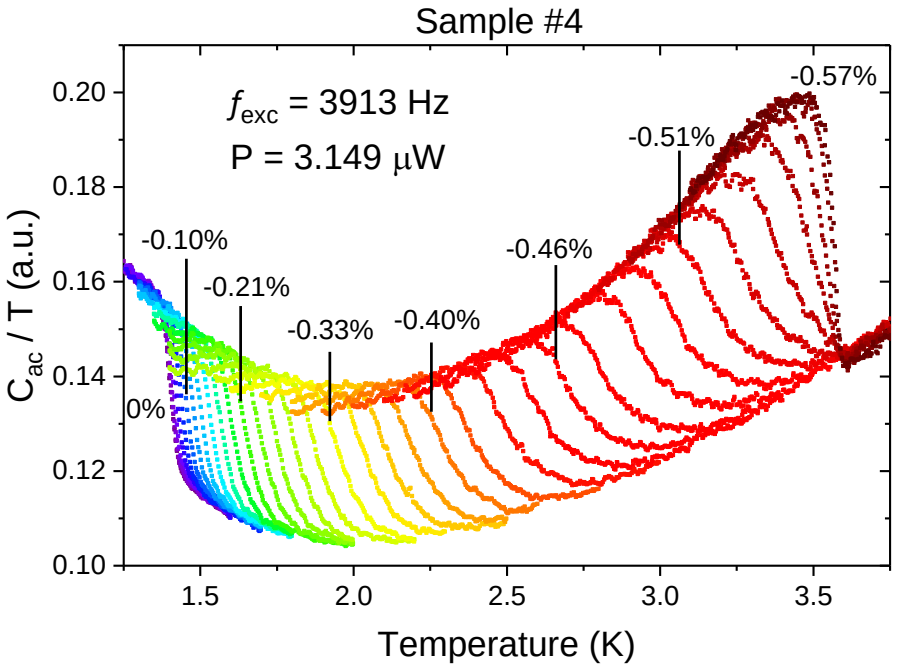

Figure 4.36: C_{ac}/T against temperature for sample #4 at a series of small increments of compressive strains with f_{exc} = 3913 Hz.

In sample #2 (see Figure B.2 in Appendix B), the evolution of C_{ac}/T curves has an anomaly at ε_{xx} = -0.23%. T_c increases continuously but the size of the heat capacity jump stays roughly the same at ε_{xx} = -0.16% and -0.23% and reduces significantly at the next strain ε_{xx} = -0.29%. To study this anomaly, more measurements were done in these strain intervals. Figure 4.34 shows C_{ac}/T against temperature for sample #2 at a series of small increments of compressive strains around ε_{xx} = -0.23%. In addition to the increase of T_c, the heat capacity jump reaches to its maximum at ε_{xx} = -0.232% and then decreases rapidly at ε_{xx} > -0.232%. Since this anomaly is an interesting feature, similar measurements were done on sample #3 and #4. Figure 4.35 shows C_{ac}/T against temperature for sample #3 at a series of small increments of compressive strains up to -0.31% and Figure 4.36 for sample #4 up to ε_{peakTc}. The evolution of T_c and the size of heat capacity jump are smooth and there is no such an anomaly on both sample #3 and #4. Since this anomaly is not repeatable, it might be an experimental artefact due to the sample configuration. Apart from this, there is no significant change in heat capacity measurements.

Another sign of pairing symmetry change might be the specific heat jump $\Delta c/c$. If the specific heat jump is purely from the electronic contribution, i.e. $\Delta c_e/c_e$, where c_e is the electronic specific heat, $\Delta c_e/c_e$ for Sr_2RuO_4 is 0.74 [27], for an isotropic gap[12], s-wave, is 1.43 and for vertical line-nodes gap, d-wave, on a cylindrical Fermi surface is 0.95 [27]. The corresponding electronic "heat capacity" ratio $C_{e,s}/C_{e,n}$ in our measurements would be $\sqrt{1+0.74} \cong 1.319$ for Sr_2RuO_4, $\sqrt{1+1.43} \cong 1.559$ for s-wave and $\sqrt{1+0.95} \cong 1.396$ for d-wave. However, the presence of the addenda and phonon contributions reduces these values.

Section 4.7 describes the evolution of $\Delta c/c$. The specific heat jump seems to be larger and comparable to 1.43 at ε_{peakTc} but it is strongly affected by the f_{exc}. c_s/c_n at ε_{peakTc} with lower f_{exc} is close to the value at zero strain for sample #3. Hence, the possibility of a large change in c_s/c_n can be ruled out. The next step is to analyze how it evolves qualitatively. Since the difference in c_s/c_n between ε_{peakTc} and $\varepsilon_{xx} = 0\%$ is small and comparable to the addenda (about 5%) and phonon contribution (about 10% in unstrained Sr_2RuO_4), it is difficult to distinguish if there is an enhancement at ε_{peakTc} or not in this approach. Hence, I will use another approach to discuss this issue.

c_s and c_n are the specific heat values below and above T_c. The evolution of c_s/c_n can be determined by the evolutions of c_s and c_n[13]. According to equation (4-8), c_s and c_n are related to $1/T_{ac,s}$ and $1/T_{ac,n}$. Figure 4.1(a) and Figure 4.2(a) show C_{ac}/T against temperature for sample #3. Both the peak of superconducting transition and normal state evolves smoothly. Although $\left(T_{ac,n}/T_{ac,s}\right)^2$ is larger at ε_{peakTc}, it has been demonstrated that it is difficult to use this smooth

[12] In addition to s-wave, $p_x \pm ip_y$ and $d_{x^2-y^2} \pm id_{xy}$ on a simple circular Fermi surface can also give an isotropic gap.

[13] c_n as a function of strain can be simulated as shown in section 4.8 but c_s cannot because the peak in heat capacity varies as a function of temperature when the strain is applied. In the main text, I provide a different approach.

change to determine the evolution of c_s/c_n. This is, however, different in the sample #4 as shown in Figure 4.36. The peak of the superconducting transition evolves smoothly up to ε_{peakTc} but there is a rapid decrease in the normal state near ε_{peakTc}. This decrease is clearer in the strain sweeps as shown in Figure 4.26 to Figure 4.28. There is a dip at ε_{peakTc} and its size is about 3% of the total signal at f_{exc} > 1 kHz for sample #4. The rapid decrease near ε_{peakTc} is unlikely from the addenda and phonon contribution because they are simply constant or slowly varying backgrounds in the strain sweeps. Therefore, the rapid decrease in the normal state specific heat suggests an enhancement of c_s/c_n around ε_{peakTc} for sample #4.

The difference between sample #3 and #4 is the inhomogeneity as described in section 4.8. The strain sweeps on both samples show similar behaviors. They both have a dip at ε_{peakTc} but the size in sample #3, about 1%, is smaller because it is more inhomogeneous than sample #4. The 1% dip in the strain sweeps for sample #3 explains the reason why it remains ambiguous for determining the evolution of c_s/c_n in section 4.7. Sample #4 which has less inhomogeneity gives a 3% change at ε_{peakTc}. It is then expected that the dip will be deeper in a homogeneous sample. In addition to a reduced value for c_n around ε_{peakTc}, it is expected that there will be a larger value for c_s in a less inhomogeneous sample because inhomogeneities smear the transition as discussed in Chapter 3.7.4. It is difficult to estimate the increase of c_s but the decrease of c_n is 3% for sample #4. Therefore, the enhancement of c_s/c_n at ε_{peakTc} in a homogeneous sample is likely to be $> 6\%$. Moreover, the addenda and phonon contributions are included in the estimate so it is expected that removing these backgrounds will give an even larger c_s/c_n.

A. Steppke *et al.*[41] suggest that there might be a *p*- to *d*-wave pairing symmetry change before the peak in T_c. Here I first discuss a hypothetical case. Supposed that there were only a single Fermi surface in 3.4K-Sr_2RuO_4, which is unlikely, based on the results of DFT calculations. The enhancement in $T_{ac,n}/T_{ac,s}$ from the 1.5K-Sr_2RuO_4 to the *d*-wave living on a simple circular Fermi surface would be $\sqrt{1.95/1.74} - 1 \approx 5.9\%$. From the previous discussions, there is about 10% inhomogeneity in the sample which would smear the transition. Besides, there is approximately a 5% addenda contribution, which raises the uncertainty in the measurements. These two factors would reduce the resolution for the 5.9% enhancement. Secondly, there are three Fermi sheets in Sr_2RuO_4. The order parameter can live in one of the sheets and induce superconductivity on the others. Figure 4.37 shows results from the weak coupling calculations. The superconducting gap, which is proportional to the width of the traces, opens on all Fermi sheets. The $\Delta c/c$ at ε_{xx} = 0% is about 0.7 in both parities. Although the superconducting gap redistributes at the peak in T_c, a large change in $\Delta c/c$ is unlikely.

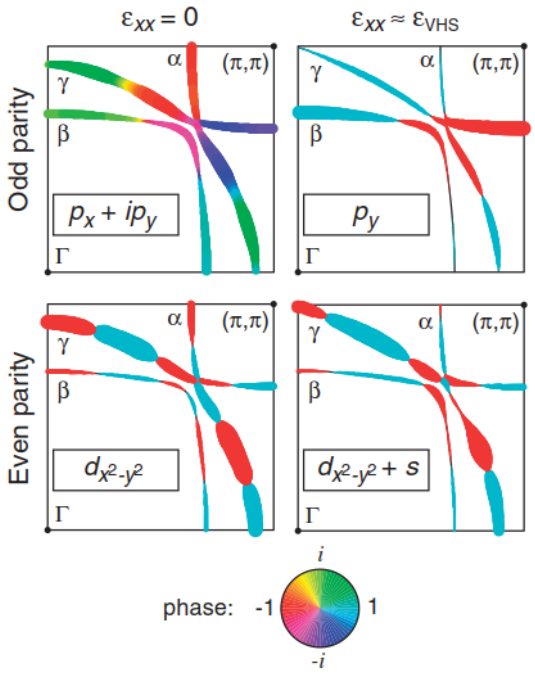

Figure 4.37: Weak coupling calculations for different parities, from ref. [41]. The width of the traces is proportional to the magnitude of the superconducting gap and the color indicates the phase.

The amount of the enhancement of $\Delta c/c$ from the experimental observation is not large and consistent to the scenario of the p- to d-wave symmetry change. In the strain sweeps, a kink nearly at ε_{xx} = -0.5% marks the onset of the dip formation. It is tempting to associate this kink and the enhancement of $\Delta c/c$ with the change of the pairing symmetry. However, the current experimental result is not sufficient to support this comment because it is not a direct evidence for such pairing symmetry change. A strong evidence would be measurements of nuclear magnetic resonance (NMR) Knight shift to see if the susceptibility is reduced or not when 3.4K-Sr_2RuO_4 goes into the superconducting state. At time of writing, such experiments are underway on strained Sr_2RuO_4 in the group of Prof. Stuart Brown at the University of California Los Angeles, and it will be very interesting to see what they observe.

In summary, the anomaly shown in the sample #2 is not repeatable in sample #3 and #4 which are considered as better samples. It is likely an artefact due to sample configurations. In sample #4, the rapid decrease of the normal state specific heat suggests an enhancement of c_s/c_n at ε_{peakTc}. This decrease is more obvious in the strain sweeps: A dip is located at ε_{peakTc}. The sizes are 1% for sample #3 and 3% for sample #4. For a less inhomogeneous sample, it is expected to have a deeper dip. Also, the superconducting transition will be sharper and will increase the value of c_s. That the increase of c_s and decrease of c_n gives an enhancement of c_s/c_n around ε_{peakTc}. Besides, the addenda and phonon contribution are included in the measurements and removing these

backgrounds will give a larger c_s/c_n. Since there is a decrease of $1/T_{ac,n}$ about 3% for sample #4, a conservative estimate for the enhancement of c_s/c_n at ε_{peakTc} is more than 6%. The amount of enhancement is not large and consistent to the scenario of a p-to-d pairing symmetry change proposed by A. Steppke *et al*.[41].However, my results are not sufficient to give clear and unambiguous support for this scenario. A further study with NMR Knight shift would be helpful to resolve if there is a triplet-to-singlet pairing symmetry change near the peak in T_c.

4.10 Heat capacity measurements under magnetic field

In this section, I will first present the heat capacity measurements at the peak in T_c for samples #2 to #4. Measurements of H_{c2} have been proposed to be an approach to distinguish the even or odd pairing symmetry for Sr_2RuO_4 under uniaxial stress [41]. To investigate this, measurements at two medium strains and at zero strain have been done on sample #3. I will show this data set and discuss the results.

4.10.1 Measurements at peak in T_c

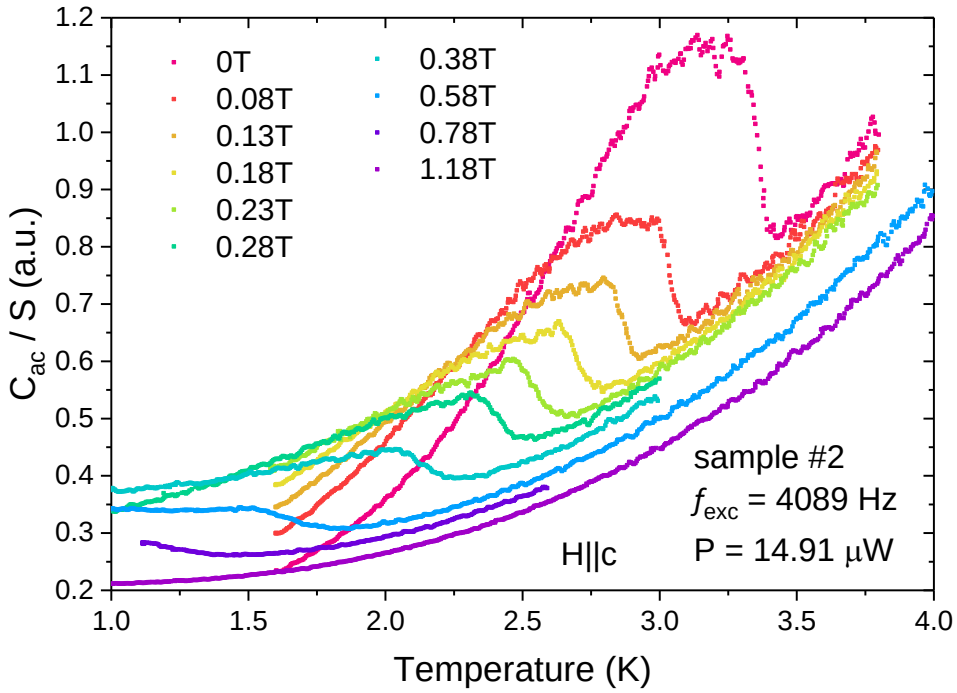

Figure 4.38: C_{ac}/S against temperature for sample #2 at ε_{xx} = -0.55% under different magnetic fields parallel to the *c*-axis.

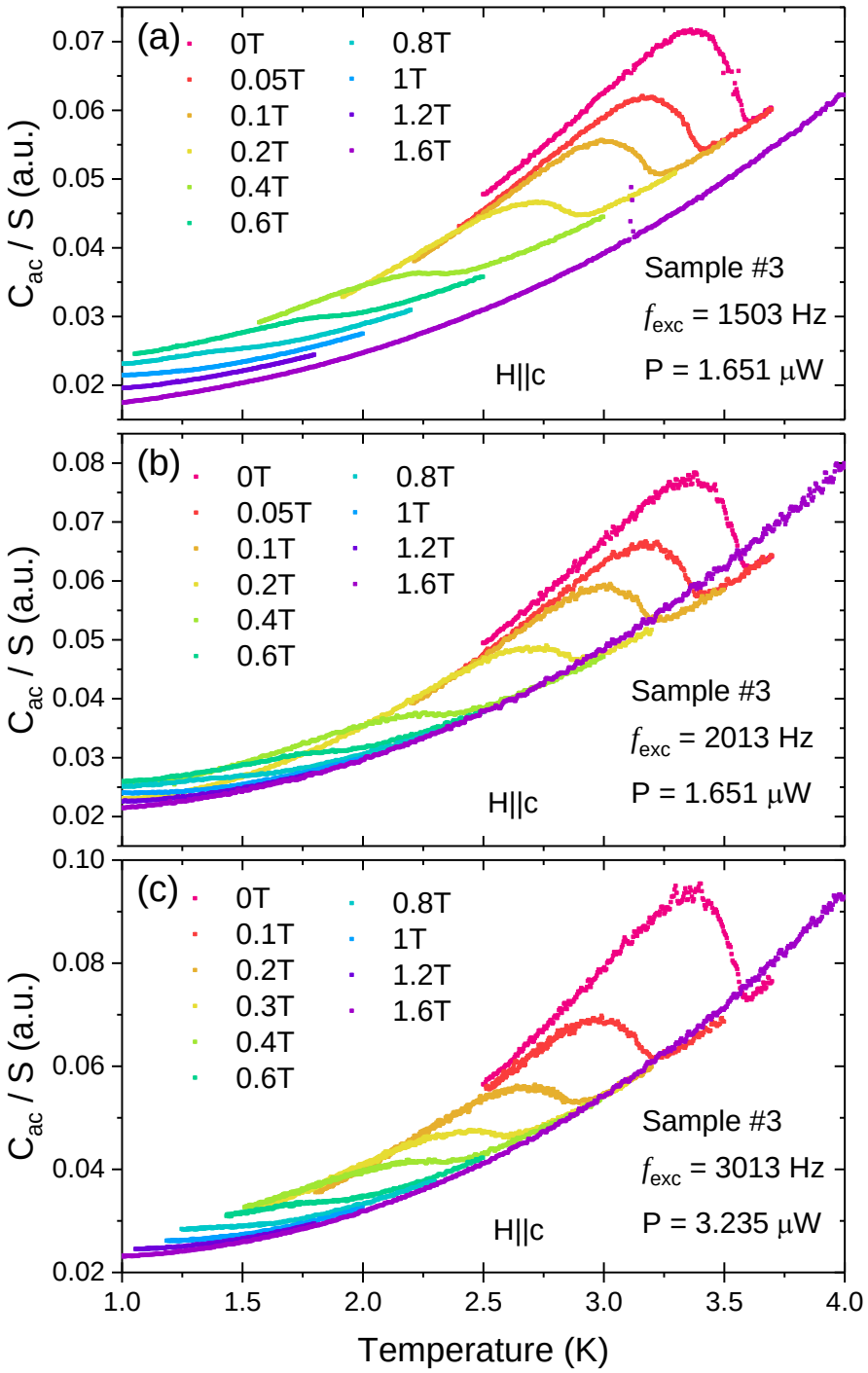

Figure 4.39: C_{ac}/S against temperature for sample #3 at ε_{xx} = -0.52% under different magnetic fields parallel to the *c*-axis with different f_{exc}.

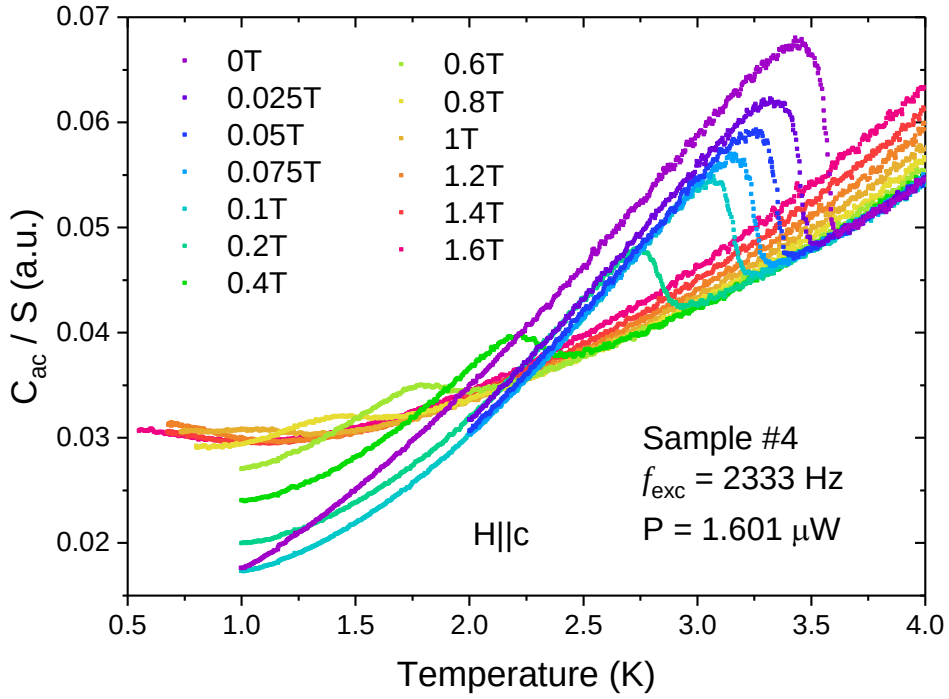

Figure 4.40: C_{ac}/S against temperature for sample #4 at ε_{xx} = -0.57% under different magnetic fields parallel to the *c*-axis.

The thermocouple Au/AuFe has not been calibrated under magnetic field, so data shown here are C_{ac} divided by the thermopower S of the thermocouple. Figure 4.38 to Figure 4.40 show C_{ac}/S against temperature for sample #2 to sample #4 under fields parallel to the *c*-axis. For sample #2 and sample #4 the measurements are at $\varepsilon = \varepsilon_{peakTc}$ whereas for sample #3 the measurements were at slightly lower strain. As the magnetic field was switched on, resonance peaks and noise spikes appeared in the frequency sweep, see Chapter 3.9.6. To ensure that the measured results were not subject to these experimental artefacts, f_{exc} was carefully chosen to lie away from these peaks and spikes. In particularly for sample #3, data was recorded with different f_{exc} and. All results have been consistent.

In all cases, T_c is suppressed with an increasing magnetic field and so is the size of the heat capacity jump. The transition becomes broader and smaller in higher fields and it is difficult to distinguish a transition for $H > 1$ T. In magnetic field, the values of C_{ac}/S increase in the normal state, which is not expected. This could be due to a decrease of S or an increase of C_{ac} under magnetic field. There is a suddenly reduced heat capacity jump at $H \leq 0.05T$ in both samples #3 and #4. This anomaly can be observed at zero strain as well, see Figure 4.44. The zero strain heat capacity of Sr_2RuO_4 has been studied very well. To my knowledge, no such an anomaly has been reported in the literature. Therefore, the anomaly could be an experimental artefact and should not be overinterpreted unless new evidence is found.

To determine T_c, the measured curves were normalized to the background. The normal state is set to be 0% of the transition whereas the peak of the heat capacity is set to be 100%. The midpoint is defined as 50% of the transition. Figure 4.41 shows H_{c2} as a function of temperature for samples #2 to #4 using the midpoint criterion. The stars represent the data from susceptibility measurements [41]. Since the transition is broader and smaller at higher field, the data cannot be extended to higher fields. Nevertheless, the heat capacity data closely resemble to the susceptibility data.

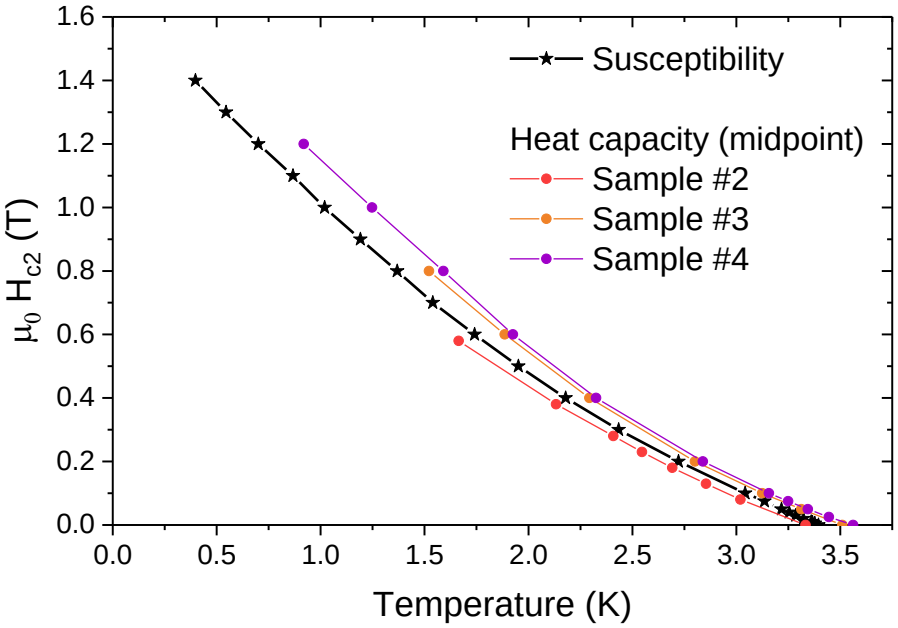

Figure 4.41: The H_{c2}-T Phase diagrams for different samples at/near the peak in T_c. The stars represent the data from the susceptibility measurements [41]. The lines serve as a guide to the eye.

4.10.2 Measurements at medium strains and zero strain

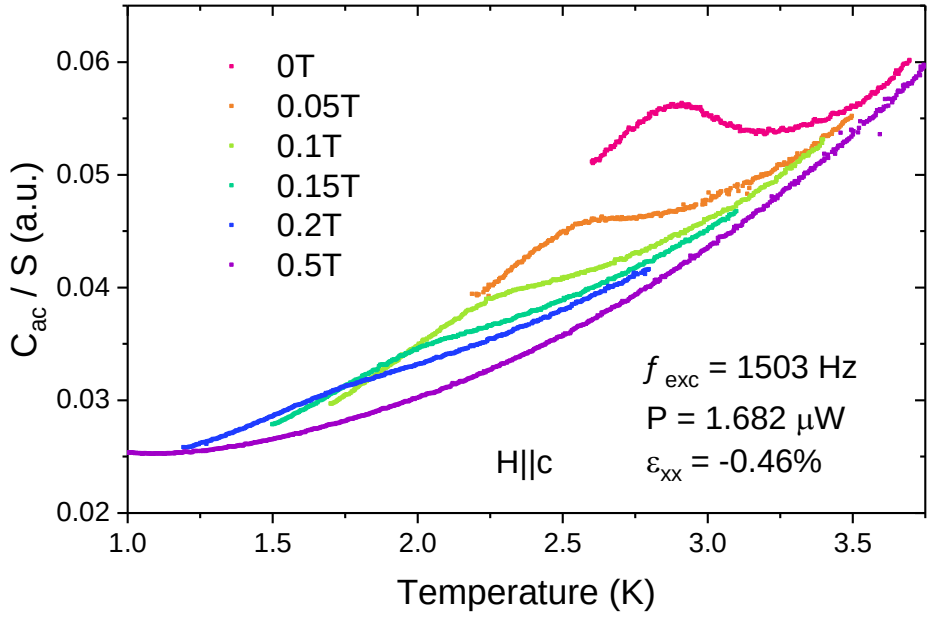

Figure 4.42: C_{ac}/S against temperature for sample #3 at ε_{xx} = -0.46% under different magnetic fields parallel to the *c*-axis.

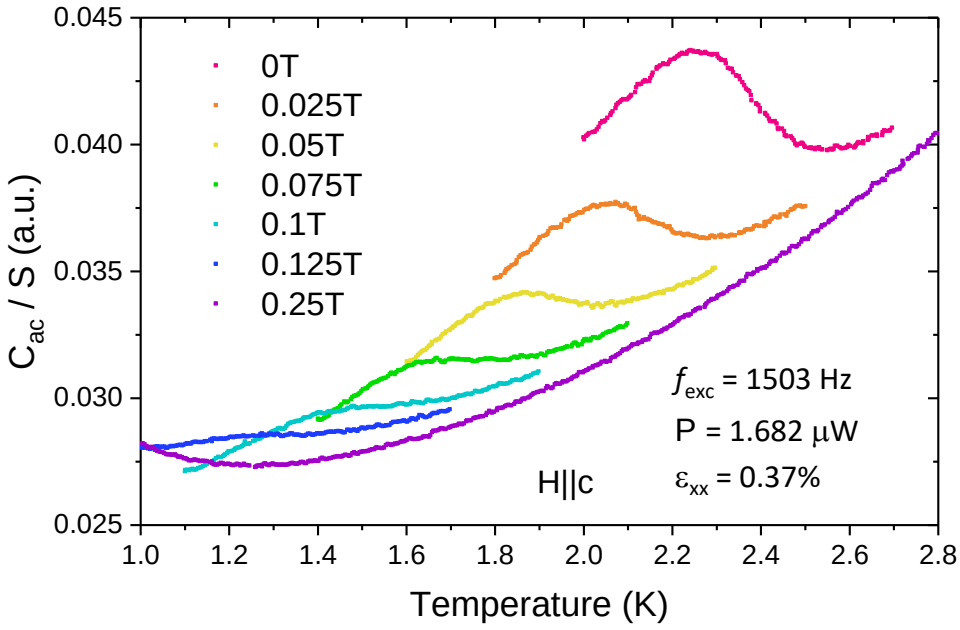

Figure 4.43: C_{ac}/S against temperature for sample #3 at ε_{xx} = -0.37% under different magnetic fields parallel to the *c*-axis.

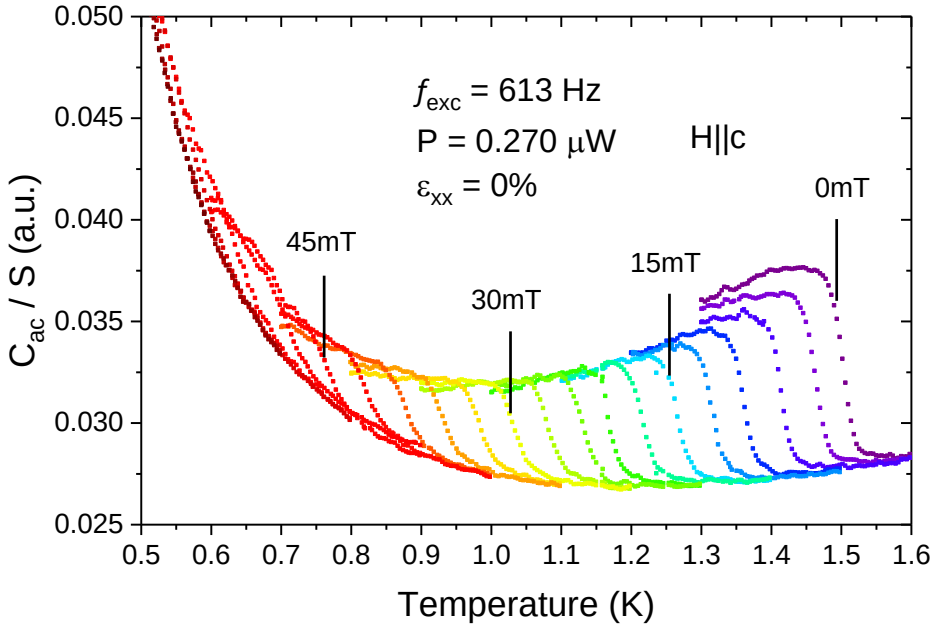

Figure 4.44: C_{ac}/S against temperature for sample #3 at ε_{xx} = 0% at fields in 3mT increments between 0 and 63 mT parallel to the *c*-axis.

Figure 4.42 to Figure 4.44 show C_{ac}/S against temperature for sample #3 at ε_{xx} = -0.46%, -0.37% and 0% with different magnetic fields applied parallel to the *c*-axis. As the magnetic field was applied, an anomaly appeared at the low temperature, see Chapter 3.9.7. This anomaly can be observed in the measurements especially in Figure 4.44. T_c in all cases is suppressed with an increasing field. The transitions at medium strains are already broad without applied field and become broader and smaller with applied field. Therefore, it is difficult to experimentally observe a sizeable and distinguishable transition near the critical field $H_{c2}(0)$ with the heat capacity approach. In contrast, the transition at zero strain is sharp in zero applied field, but the strong upturn in the background signal at low temperature makes the transitions hard to distinguish near $H_{c2}(0)$ as well.

T_cs were determined by the same procedure as that mentioned above. Figure 4.45 shows the H_{c2}-T phase diagrams for sample #3 at different strains. The colored areas represent the transitions between the 20% and 80% levels and the square (circle) points represent the data determined at 20% (80%) level. The transition width in the case of ε_{xx} = -0.46% is wider and the data at 80% level still follow the behavior at the peak T_c, indicating that part of the sample still has strains near the peak in T_c , i.e. that the strain is inhomogeneous.

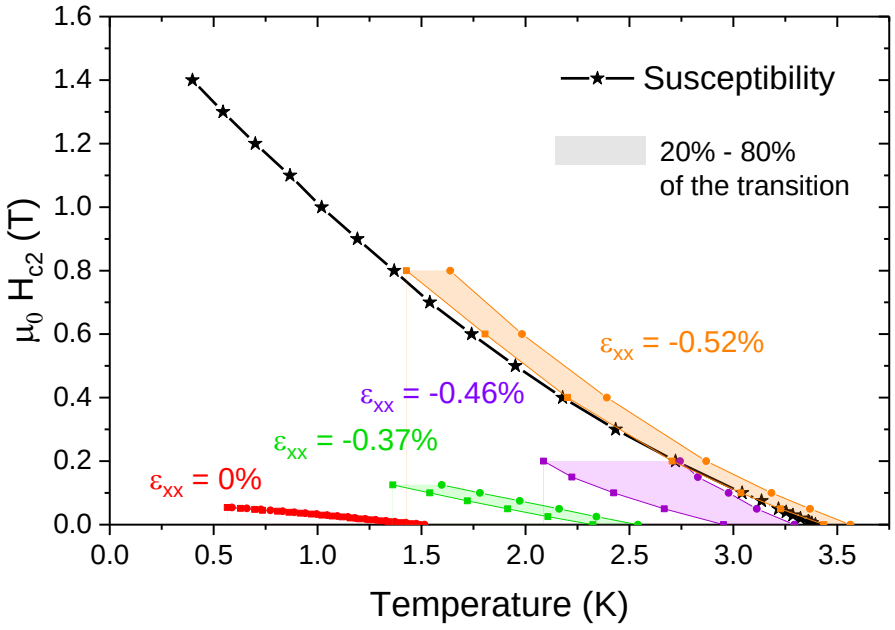

Figure 4.45: The H_{c2}-T phase diagram for sample #3 at different strains. The stars represent the data from susceptibility measurements [41]. The colored areas represent the transitions between 20% to 80% levels for my heat capacity measurements. The squares (circles) represent the data at the level of 20% (80%).

Discussion

$H_{c2}(0)$ has been proposed to be an approach to distinguish the even or odd pairing symmetry for Sr_2RuO_4 under uniaxial stress [41]. $H_{c2}(0)$ would increase more than linearly in T_c^2 for even parity pairing symmetry and less for odd parity. In the following, I will estimate $H_{c2}(0)$ at different strains.

In all cases, H_{c2} near T = 0 K is not measureable by the heat capacity approach but H_{c2} data near T_c are experimentally available. Therefore, the Werthamer-Helfand-Hohenberg (WHH) formula [89] is used to estimate H_{c2} at different strains:

$$H_{c2}(T=0K) = -0.7 \left.\frac{dH_{c2}}{dT}\right|_{T\to T_c} \times T_c. \qquad (4\text{-}14)$$

The slope changes significantly in Figure 4.45, indicating there is a strong enhancement of H_{c2} near the peak in T_c. Figure 4.46 (a) shows $H_{c2}(0)$ determined by WHH formula for different cases and (b) shows the calculated $H_{c2}(0)/T_c^2$ at different strains. The end points on the line segments represent the data determined by the 20% and 80% criteria. The large separation at ε_{xx} = -0.46% results from the inhomogeneity in the sample. Although $H_{c2}(0)$ at the peak in T_c, about 1.5 T, is

underestimated by the WHH formula, it is clear that both $H_{c2}(0)$ and$H_{c2}(0)/T_c^2$ are enhanced near the peak in T_c.

The data set presented in Figure 4.46 is estimated from the WHH formula, which is an indirect approach to determine $H_{c2}(0)$. It would be very interesting to directly measurement the $H_{c2}(T \to 0)$ at strains between ε_{xx} = -0.37% and 0% to see whether or not $H_{c2}(0)/T_c^2$ goes below the zero strain value. The heat capacity approach is difficult because the transition near $H_{c2}(0)$ is unresolvable but other approaches such as resistivity or (probably better) susceptibility would be helpful. At the time of writing, my colleagues Fabian Jerzembeck and Clifford Hicks focus on the susceptibility measurements on Sr_2RuO_4 under uniaxial stress at the lowest achievable temperature and try to obtain the $H_{c2}(T \to 0)$ as a function of strain. It would be interesting to see what they observe.

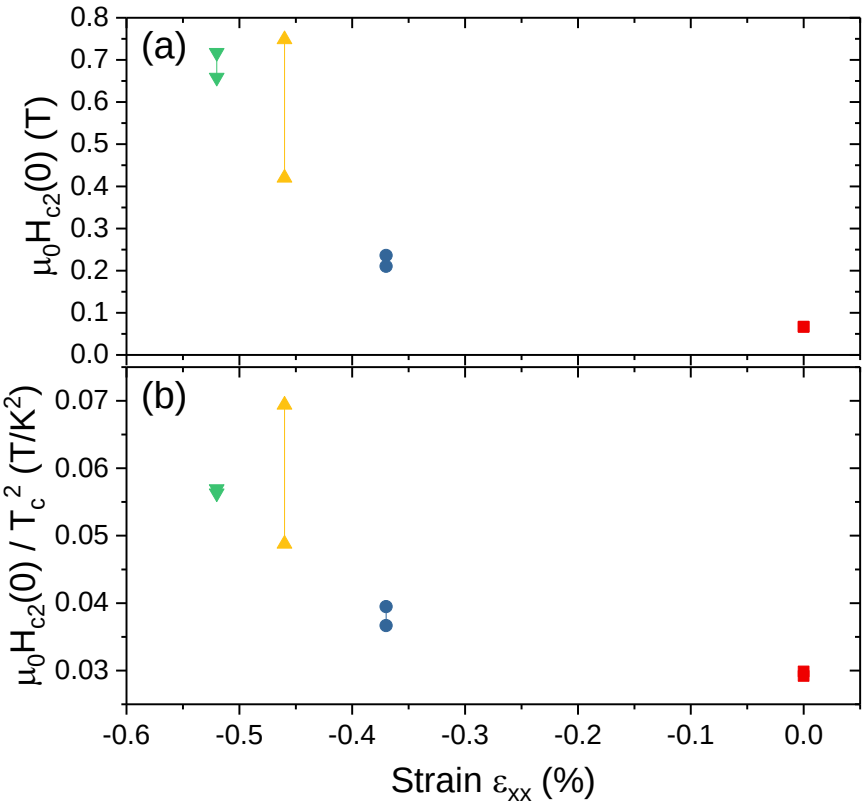

Figure 4.46: (a) The upper critical field based on the WHH formula as a function of strain. (b) $\mu_0 H_{c2}(0)/T_c^2$ as a function of strain. The end points on the line segments represents the data determined by the 20% and 80% criteria.

4.11 Summary

I measured the heat capacity of Sr_2RuO_4 under uniaxial stress. T_c is enhanced with increasing strain. A strong peak in T_c was observed and located at approximately $\varepsilon_{xx} = -0.55\%$ and T_c is then suppressed rapidly with further compression. My measurements provide the first thermodynamic evidence of the increase of T_c in Sr_2RuO_4 under uniaxial stress. In contrast to susceptibility measurements, heat capacity is a bulk-sensitive approach for determining T_c. Therefore, the increase of T_c is not related to the surface but is a bulk property.

Significant improvements have been made to reduce the inhomogeneity on the sample and to increase the signal-to-noise ratio. The strain inhomogeneity in the part of the sample probed by my measurements is approximately 10%. The temperature resolution (the temperature oscillation T_{ac}) is less than 1mK. The noise readout from the thermocouple is approximately 20 $\mathrm{pV}/\sqrt{\mathrm{Hz}}$ (or 4 $\mu\mathrm{K}/\sqrt{\mathrm{Hz}}$ at T = 1 K). Within my experimental resolution, only a single superconducting transition was observed. In addition, a cusp can be barely observed around the zero strain. My results put strong constraints on the existence of a second transition. If the second transition exists, its signature in specific heat would have to be small, or its T_c would have to be be very close to that of the first transition.

Heat capacity C_{ac} in my measurements is not only related to the specific heat c but also to the thermal conductivity κ because the probed volume varies as a function of temperature. In an ideal case where the heat flow is one-dimensional, the heater is a point-like contact on the sample and the upper cut-off frequency is far away from the excitation frequency, the relation is $C_{ac} \propto \sqrt{\kappa c}$. In reality, none of these conditions is perfectly met and the relation serves as an approximation.

The heat capacity jump at T_c strongly depends on the excitation frequency f_{exc}. To determine the magnitude of the jump at T_c in my measurements is not a trivial task. In my analysis, the change of the specific heat jump between unstrained samples and samples near the peak in T_c is not large, approximately 10%.

One of the possible reasons for an increase of T_c for Sr_2RuO_4 under strain is that the γ sheet approaches the van Hove singularity (vHS), causing an increase of the density of states. I performed the heat capacity C_{ac} measurements as a function of strain. With the knowledge of the relation, $C_{ac} \propto \sqrt{\kappa c}$, it was possible to calculate the specific heat as a function of strain. The calculation strongly suggests that there is an enhancement of the specific heat around the peak in T_c, evidencing the existence of the vHS.

I also investigated the possibility of a strain-dependent pairing symmetry change with the heat capacity approach. However, a change of the gap symmetry on the Fermi surfaces is unlikely to give a large change in the heat capacity jump. Hence, the heat capacity approach cannot give a

strong and unambiguous answer to whether such a symmetry change is taking place or not. In addition, I performed heat capacity measurements at different strains under magnetic field and extracted T_c for the *H*-*T* phase diagrams. It is difficult to determine T_c near the critical field $H_{c2}(0)$ because the transitions are smeared before reaching $H_{c2}(0)$. An alternative method, the Werthamer-Helfand-Hohenberg (WHH) formula was then used to estimate the $H_{c2}(0)$. $H_{c2}(0)$ is enhanced near the peak in T_c, and so is $H_{c2}(0)/T_c^2$. $H_{c2}(0)$ determined by WHH formula is an indirect approach so the calculated $H_{c2}(0)/T_c^2$ would be less significant. It will be interesting to directly measure $H_{c2}(T \to 0)$ by means of resistivity or susceptibility and to see if the $H_{c2}(0)/T_c^2$ value is reduced near zero strain. Therefore, a conclusive statement on whether or not the order parameter changes parity in Sr_2RuO_4 under uniaxial stress is not yet possible.

Chapter 5
Conclusions and Outlook

In this thesis, I demonstrated that I realized heat capacity measurements under uniaxial stress and presented the measured results on Sr_2RuO_4. To apply the uniaxial stress, the sample was thermally anchored with anvil blocks, leading to strongly non-adiabatic conditions for heat capacity measurements. The pulse and relaxation time methods could not be used in this case, because the relaxation time is too fast, about 1 millisecond. Instead, an ac heat capacity method was employed. An important achievement in my setup is that the probed region can be controlled by the excitation frequency. Despite of a highly inhomogeneous strain profile distribution across the sample, the central homogeneous part of the sample can still be probed by using high excitation frequencies. Great care was taken to improve the experimental resolution. The inhomogeneity, which is a source of smearing of sharp features, can be reduced to approximately 10% in the homogeneous region. In the optimized setup, the amplitude of the temperature oscillation can be less than 1 mK with a signal-to-noise ratio larger than 200, meaning that small features and small changes in the heat capacity are resolvable.

The main purpose of developing this challenging technique was to apply a symmetry-breaking field on Sr_2RuO_4 and to investigate its thermodynamic behavior. For the detailed conclusions of the experimental study on Sr_2RuO_4, I refer the reader to the summary of the experimental results (Chapter 4.11). In the following, I would like to highlight several points which are important for future experiments and developments.

The most-discussed pairing symmetry in Sr_2RuO_4 is chiral *p*-wave. The degeneracy that produces such an order parameter would be lifted when the lattice symmetry is lowered, leading to two separate phase transitions which would be visible in the heat capacity measurements under uniaxial stress. However, within my experimental resolution, only a single transition could be identified. My results put strong constraints on the second transition. Its specific heat jump would have to be small or its T_c would have to be close to that of the first transition. To further investigate whether or not the splitting of the transition exists, other approaches are needed. Below the second transition, the superconducting state has the property of breaking time reversal symmetry. Even if the heat capacity jump is small, measurements such as muon spin relaxation[14] or Kerr rotation should be able to detect such a time reversal symmetry broken state. It will be interesting to see

[14] This is currently investigated by Shreenanda Ghosh and Prof. Dr. Hans-Henning Klauss at TU Dresden and Dr. Clifford Hicks at the Max Planck Institute for Chemical Physics of Solids, Dresden.

whether or not the T_c determined by muon spin relaxation or Kerr rotation is below the T_c determined by heat capacity or susceptibility.

The strong peak in T_c of Sr_2RuO_4 under uniaxial stress has been proposed to be associated with an increase of the density of states around the van Hove singularity. My analysis strongly suggests an enhancement of the specific heat around the peak in T_c, evidencing the existence of the van Hove singularity. The next step would be to perform experiments which are directly sensitive to the Fermi surface topology. Quantum oscillation measurements and angle-resolved photoemission spectroscopy are two common approaches. Successful experiments would be able to directly observe whether the Fermi level of Sr_2RuO_4 approaches the van Hove singularity under uniaxial stress as theoretically predicted and as suggested by my specific-heat data.

Sr_2RuO_4 under uniaxial stress at the maximum T_c may be an even parity superconductor. One of the consequences might be that there is an odd-to-even parity change at medium strains. My heat capacity approach could not give a strong and unambiguous evidence about this because it might not be sensitive to this change. A more direct probe would be the nuclear magnetic resonance Knight shift[15]. Another proposed method is to measure the upper critical field H_{c2}. The heat capacity approach was not successful because the transitions became too broad to resolve unambiguously before $H_{c2}(0)$ was reached. More suitable approaches will be resistivity and susceptibility[16] measurements.

In the current setup, the heat capacity is entangled with the thermal conductivity in the raw experimental signal. As a result, the probed volume is a function of temperature. This setup is useful to observe an increase of T_c and the existence of the superconducting phase transition. However, other behaviors such as the temperature dependence of the specific heat at very low temperature and the specific heat jump at T_c would be nontrivial or difficult to determine. The next stage of the technical development, in an ideal world, would be heat capacity measurements *without* a changing volume. It remains to be seen, however, whether such a technique can be realized.

Thermal conductivity measurements can also give us a valuable information about the pairing symmetry. In Chapter 4.7, the analysis of the thermal coupling between the system and the environment suggests that measurements of the thermal conductance of Sr_2RuO_4 could be performed in a setup like this, with low excitation frequencies. In principle, in addition to DC and 3ω methods [90], this 2ω method would be able to measure thermal conductivity of the sample by placing another thermocouple near one of the sample ends. In contrast to a DC method, the ac method provides an opportunity for a better signal read out by lock-in amplifier in combination with a low temperature transformer, taking advantage of its extremely low-noise amplification.

[15] This is underway in the group of Prof. Stuart Brown at the University of California Los Angeles.
[16] This is currently investigated by my colleagues Fabian Jerzembeck and Dr. Clifford Hicks.

Once the technical developments for heat capacity and thermal conductivity measurements under uniaxial stress are mature, measurements such as angle-resolved heat capacity and angle-resolved thermal conductivity should also be possible. They are powerful measurements to detail the symmetry of the superconducting gap structures.

The successful developments of the techniques could be used for investigating other interesting materials as well. $PrOs_4Sb_{12}$ is known material whose T_c is about 1.8 K and whose superconducting state breaks time reversal symmetry [91]. In principle, heat capacity measurements under uniaxial stress can be applied to lower the lattice symmetry and to look for signatures of splitting[17]. UBe_{13} has been studied by other uniaxial stress techniques but no splitting was observed within their experimental resolution. Nevertheless, it might be still worthy to reinvestigate this material with the current technique because the applied strain can reach at least 0.7% with a highly homogeneous strain distribution and the homogeneous region can be probed by tuning the excitation frequency.

The above mentioned projects mainly focus on the superconductors which break time reversal symmetry. There are more opportunities beyond this scope. Since the top surface of the sample is exposed, other probes such as scanning tunneling microscopy, optical measurements, etc. are also possible. In combination with many other interesting materials, e.g. unconventional superconductors, topological insulators, etc., there are still plenty of possibilities for new experiments and exciting results to come.

[17] This is currently investigated by my colleagues Janas Kunnelakat John and Dr. Michael Nicklas and I.

Appendix

A. Sample configuration

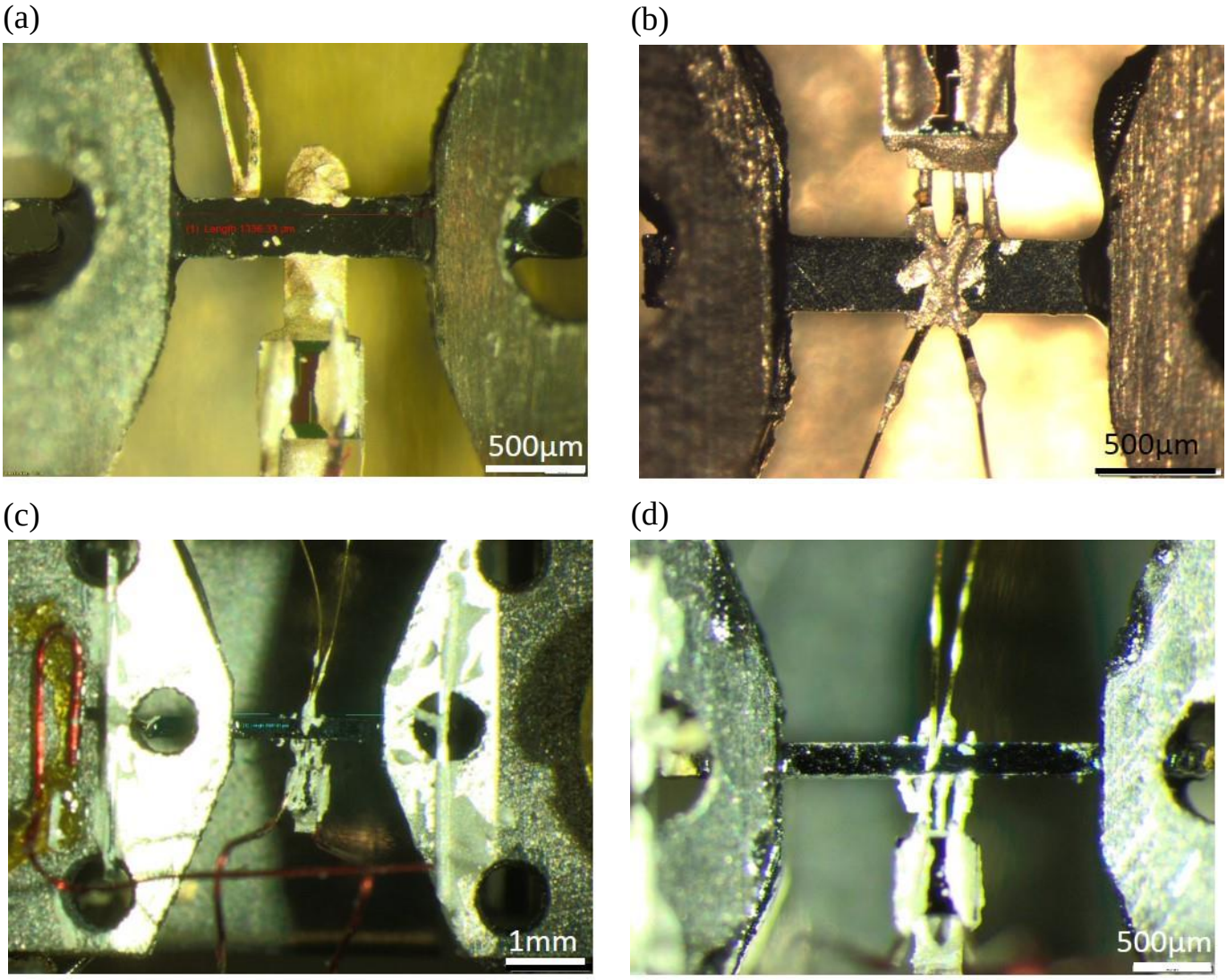

Figure A.1: Photographs of the heat capacity setups for experiments under uni-axial stress for (a) sample #1, (b) sample #2, (c) sample #3 and (d) sample #4. Further details are described in the text.

Figure A.1 shows pictures of the setup for the heat capacity measurements under uniaxial stress from samples #1 to #4. Sample #1 is the first sample and sample #4 is the last. In sample#1, a silver strip was used to conduct the heat from the heater to the sample. The contact length is about 300 μm and the strain inhomogeneity is large in this region because the Young's modulus of silver is different from that of Sr_2RuO_4 (see Chapter 3.7.4). To reduce the strain inhomogeneity, three 50 μm-silver fingers were used to conduct heat for samples #2 to #4. The thermal conductance from the silver fingers to the sample depends on the contact area on both the silver fingers and the sample. In the sample #2, only silver epoxy was used and the contact area on the silver finger is small. To increase this area, silver dots (50 μm in diameter and ≈200 μm in length) were used to decorate on both sides of the sample, see samples #3 and #4, and they were then thermally contacted to the silver fingers by silver epoxy. Another benefit of doing this decoration is that the contact dimensions are well defined. The contact widths on sample #2 vary (>50 μm) because silver epoxy spread on the edge of the sample and increased the inhomogeneity. By contrast, the contacts on samples #3 and #4 are well defined, ≈50 μm, and reduce the inhomogeneity.

The position of the thermocouple determines the upper cutoff frequency f_2. In sample #1, it was placed next to the heater and the distance is ≈300 μm. To make the distance shorter and make the setup more symmetric (samples #2 to #4), the thermocouple was placed on the side opposite to the heater and its junction was glued on top of the sample surface.

The probed length $l_{probe} = \sqrt{\kappa/c\omega}$ is associated with the exposed length, see Chapter 3.6.2. Besides, the lower the excitation frequency, the larger the signal. To obtain a better SN ratio, a longer sample is needed. In samples #1 and #2, the exposed lengths are ≈1.3 mm and in the samples #3 and #4, they are ≈2 mm. Another reason for a longer exposed length is because of the thermal conductivity. Samples #1 and #2 have T_c ≈1.35 K and samples #3 and #4 have T_c ≈ 1.5 K. It is expected that samples #3 and #4 have the higher thermal conductivity and, therefore, a longer probed length.

The thickness of the sample is ultimately determined by the buckling limit, see Chapter 3.8.1. To keep this limit, the longer the strained length, the thicker the thickness. In samples #1 and #2, the thicknesses are ≈100 μm and in samples #3 and #4, they are ≈150 μm.

The width of the sample can determine the upper cutoff frequency (as mentioned above) and the size of the homogeneous region (see Chapter 3.5.4). Assuming the sample is a perfect rectangular parallelepiped without bending induced inhomogeneity, according to Table 3.1, the part that should be excluded at the both ends to reach 1% inhomogeneity is 0.5*w*. To obtain a large homogeneous region in the exposed sample, the sample needs to be long and narrow. The widths of samples #1 to #4 are 300 μm, 300 μm, 256 μm and 207 μm, respectively. Samples #3 and #4 are longer and narrower than samples #1 and #2.

Surface roughness and an imperfect shape of the rectangular parallelepiped will be a source of inhomogeneity (see Chapter 3.7.4). Table A.1 describes the polishing process and results on each sample. After the polishing process, sample #2 to #4 were annealed at 450°C for 24 hours whereas the sample #1 was not.

	Polishing process and results
Sample #1	Only the bottom surface was polished
Sample #2	4 surfaces were polished
Sample #3	The top and one side of surfaces were polished carefully with diamond grits down to 1 μm hence the roughness is smaller than 1μm. The bottom and another side of surface were not polished.
Sample #4	4 surfaces were polished carefully with diamond grits down to 1μm and hence the roughness is smaller than 1μm. During the polishing process the crystal was aligned carefully. The top and the bottom are parallel and the two side surfaces are parallel as well, as determined by inspection under a microscope.

Table A.1: The polishing process and results on the sample #1 to #4.

The thermal conductivity of the silver epoxy and the interface resistance between the silver epoxy and the sample determine the values of k_θ and k_h (see Chapter 3.6.4). Most likely the interface resistance plays the dominant role. To increase both k_θ and k_h, a high temperature heat treatment was introduced. Samples #1, #3 and #4 were annealed at 450°C for 1 hour, whereas sample #2 was annealed at 200°C for 1 hour.

When a sample is cooled down, it is, empirically, easier to break when the sample is pulled due to thermal contractions between different elements. Even if the sample is broken upon cooling, it is still able to apply compression as soon as the sample is reengaged. Sample #1 and #3 broke during the cooling process. Sample #2 remained intact but broke when it was under a small tensile strain. Sample #4 did not break during the cooling process and remained intact during the entire set of measurements.

Sample #1 was the first sample used to test the concept of heat capacity measurements under uniaxial stress. Later, more and more considerations were taken into account. Sample #4 is the latest and the best sample in this study. Table A.2 summarizes the information for the 4 samples.

	Sample #1	Sample #2	Sample #3	Sample #4
Sample batch	WDO3	WDO3	C362	Naoki3
Exposed length, *L*	1.37 mm	1.34 mm	2 mm	2.07 mm
Width	300 μm	300 μm	256 μm	207 μm
Thickness, *t*	100 μm	100 μm	147 μm	150 μm
t*/*L	0.073	0.075	0.074	0.072
T_c	1.35 K	1.35 K	1.5 K	1.5 K
Polishing	Bottom surface	4 surfaces	Top and 1 side surfaces, carefully	4 surfaces, carefully
Annealing after the polishing	No	450°C, 24hr	450°C, 24hr	450°C, 24hr
Interface treatment	450°C, 1hr	200°C, 1hr	450°C, 1hr	450°C, 1hr
Sample broke when cold	Yes	No, but it broke after tensioning.	Yes	No

Table A.2: Summary of the information for the 4 samples in this study.

B. Heat capacity measurements for samples #1 and #2

Figure B.1 and Figure B.2 show C_{ac}/T against temperature up to the strain in peak T_c for samples #1 and #2, respectively. T_c is enhanced as the strain is applied up to $\approx -0.55\%$. The inhomogeneity on these two samples is larger than that in samples #3 and #4. This effect is reflected in the width of the superconducting transitions at the medium strains. Besides, the normal state heat capacity is enhanced as the strain is applied. For the detail of the discussion on the normal state heat capacity, please see Chapter 4.8.

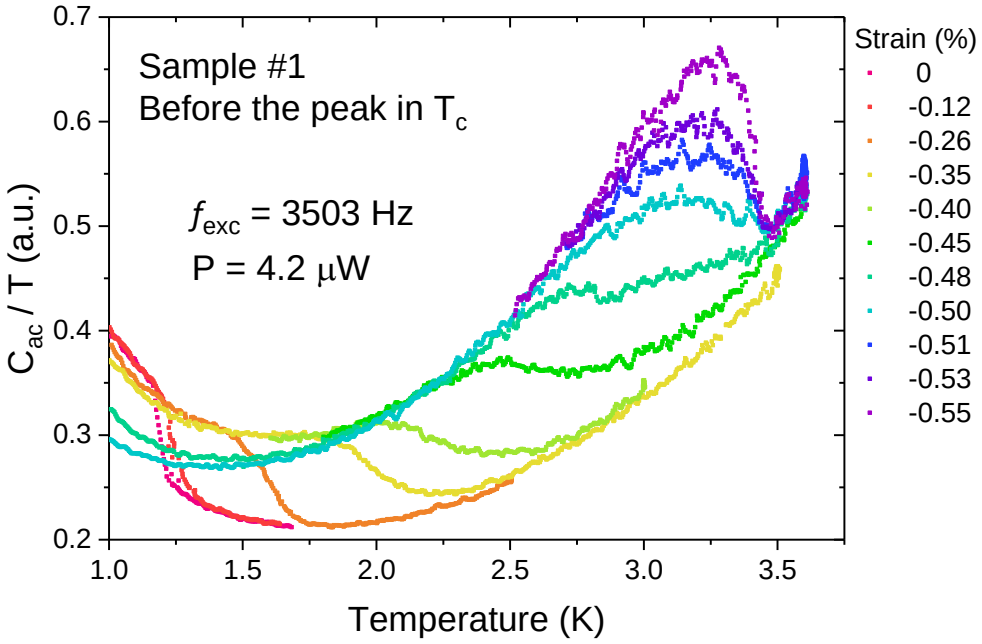

Figure B.1: C_{ac}/T against temperature for sample #1 at a series of strains before the peak in T_c.

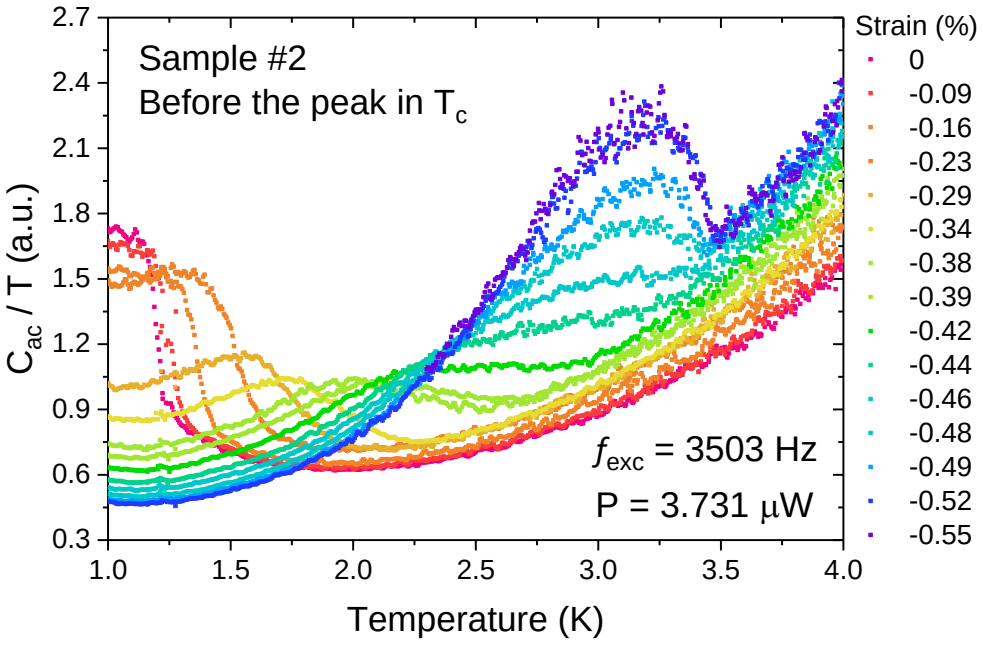

Figure B.2: C_{ac}/T against temperature for sample #2 at a series of strains before the peak in T_c.

C. Strain sweeps for sample #3

Figure C.1 shows C_{ac} as a function of strain for sample #3 at different runs. There is about 15% difference in C_{ac}. The temperature ramps in Chapter 4.3 were measurements at the first run. The normal state C_{ac} fits the data shown in Figure C.1(a). However, the strain sweeps shown in Chapter 4.8 are from the second runs, in which the value of C_{ac} are higher. The time gap between the first and the second run was more than half a year. Small changes of the measurement configurations can be expected, e.g. the thermal properties in the sample. Therefore, the difference in C_{ac} between the first and the second runs is not unreasonable.

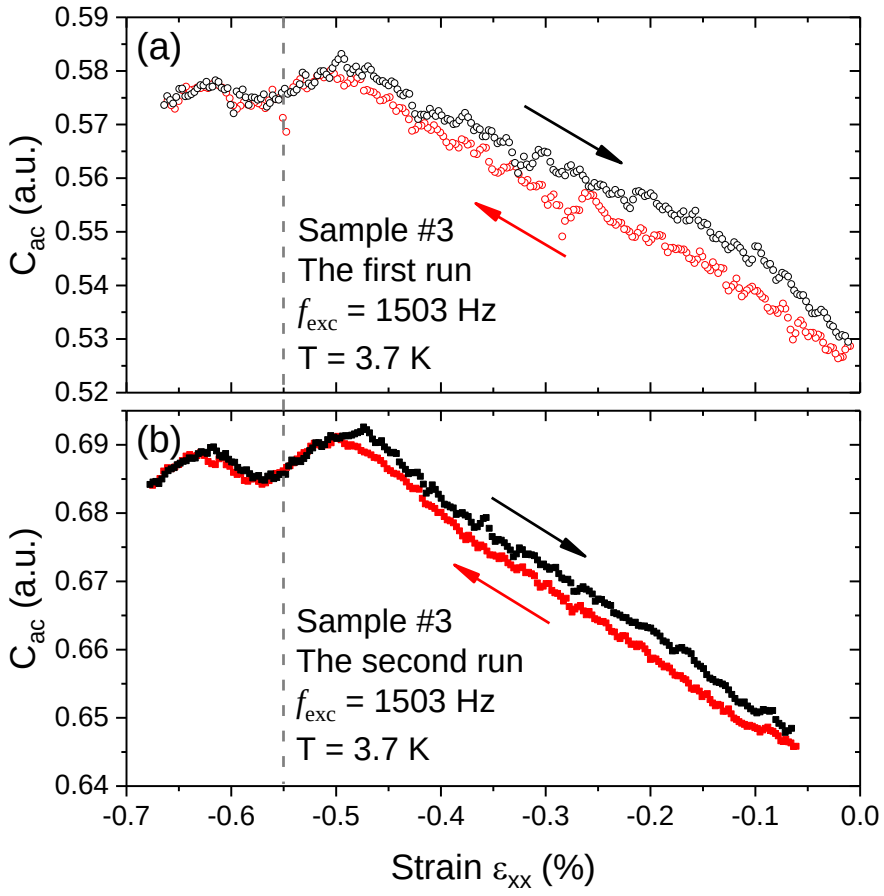

Figure C.1: C_{ac} against strain in the normal state for sample #3 with different runs. The arrows indicate the directions of the sweeps. The dashed line indicates the peak in T_c.

Bibliography

[1] H. K. Onnes, “The Resistance of Pure Mercury at Helium Temperatures,” *Commun. Phys. Lab. Univ. Leiden*, vol. 12, no. 120, p. 1, 1911.

[2] W. Meissner and R. Ochsenfeld, “Ein neuer Effekt bei Eintritt der Supraleitfähigkeit,” *Naturwissenschaften*, vol. 21, no. 44, pp. 787–788, Nov. 1933.

[3] J. G. Bednorz and K. A. Müller, “Possible high T_c superconductivity in the Ba-La-Cu-O system,” *Zeitschrift für Phys. B Condens. Matter*, vol. 64, no. 2, pp. 189–193, Jun. 1986.

[4] M. K. Wu *et al.*, “Superconductivity at 93 K in a new mixed-phase Y-Ba-Cu-O compound system at ambient pressure,” *Phys. Rev. Lett.*, vol. 58, no. 9, pp. 908–910, Mar. 1987.

[5] A. Schilling, M. Cantoni, J. D. Guo, and H. R. Ott, “Superconductivity above 130 K in the Hg–Ba–Ca–Cu–O system,” *Nature*, vol. 363, no. 6424, pp. 56–58, May 1993.

[6] L. Gao *et al.*, “Superconductivity up to 164 K in $HgBa_2Ca_{m-1}Cu_mO_{2m+2+\delta}$ (m =1, 2, and 3) under quasihydrostatic pressures,” *Phys. Rev. B*, vol. 50, no. 6, pp. 4260–4263, Aug. 1994.

[7] F. Steglich *et al.*, “Superconductivity in the Presence of Strong Pauli Paramagnetism: $CeCu_2Si_2$,” *Phys. Rev. Lett.*, vol. 43, pp. 1892–1896, 1979.

[8] H. R. Ott, H. Rudigier, Z. Fisk, and J. L. Smith, “UBe_{13}: An Unconventional Actinide Superconductor,” *Phys. Rev. Lett.*, vol. 50, no. 20, pp. 1595–1598, May 1983.

[9] G. R. Stewart, Z. Fisk, J. O. Willis, and J. L. Smith, “Possibility of Coexistence of Bulk Superconductivity and Spin Fluctuations in UPt_3,” *Phys. Rev. Lett.*, vol. 52, p. 679, 1984.

[10] T. T. M. Palstra *et al.*, “Superconducting and Magnetic Transitions in the Heavy-Fermion System URu_2Si_2,” *Phys. Rev. Lett.*, vol. 55, no. 24, pp. 2727–2730, Dec. 1985.

[11] Y. Kamihara *et al.*, “Iron-Based Layered Superconductor: LaOFeP,” 2006.

[12] Y. Kamihara, T. Watanabe, M. Hirano, and H. Hosono, “Iron-Based Layered Superconductor $La[O_{1-x}F_x]FeAs$ (x = 0.05−0.12) with T_c = 26 K,” 2008.

[13] F.-C. Hsu *et al.*, “Superconductivity in the PbO-type structure alpha-FeSe.,” *Proc. Natl. Acad. Sci. U. S. A.*, vol. 105, no. 38, pp. 14262–4, Sep. 2008.

[14] J. H. Tapp *et al.*, “LiFeAs: An intrinsic FeAs-based superconductor with T_c = 18 K,” *Phys. Rev. B*, vol. 78, no. 6, p. 060505, Aug. 2008.

[15] M. Rotter, M. Tegel, and D. Johrendt, “Superconductivity at 38 K in the Iron Arsenide $(Ba_{1-x}K_x)Fe_2As_2$,” *Phys. Rev. Lett.*, vol. 101, no. 10, p. 107006, Sep. 2008.

[16] Z.-A. Ren *et al.*, “Superconductivity and phase diagram in iron-based arsenic-oxides $ReFeAsO_{1-\delta}$ (Re = rare-earth metal) without fluorine doping,” *EPL (Europhysics Lett.*, vol. 83, no. 1, p. 17002, Jul. 2008.

[17] J. Bardeen, L. N. Cooper, and J. R. Schrieffer, “Theory of Superconductivity,” *Phys. Rev.*,

vol. 108, no. 5, pp. 1175–1204, Dec. 1957.

[18] C. C. Tsuei and J. R. Kirtley, "Pairing symmetry in cuprate superconductors," *Rev. Mod. Phys.*, vol. 72, no. 4, pp. 969–1016, Oct. 2000.

[19] Y. Maeno *et al.*, "Superconductivity in a layered perovskite without copper," *Nature*, vol. 372, no. 6506, pp. 532–534, Dec. 1994.

[20] T. M. Rice and M. Sigrist, "Sr_2RuO_4 : an electronic analogue of ^{3}He?," *J. Phys. Condens. Matter*, vol. 7, no. 47, pp. L643–L648, Nov. 1995.

[21] S. Margadonna *et al.*, "Pressure evolution of the low-temperature crystal structure and bonding of the superconductor FeSe (T_c=37 K)," *Phys. Rev. B*, vol. 80, no. 6, p. 064506, Aug. 2009.

[22] A. P. Drozdov, M. I. Eremets, I. A. Troyan, V. Ksenofontov, and S. I. Shylin, "Conventional superconductivity at 203 kelvin at high pressures in the sulfur hydride system," *Nature*, vol. 525, no. 7567, pp. 73–76, Aug. 2015.

[23] J.-P. Locquet, J. Perret, J. Fompeyrine, E. Machler, J. W. Seo, and G. Van Tendeloo, "Doubling the critical temperature of $La_{1.9}Sr_{0.1}CuO_4$ using epitaxial strain," *Nature*, vol. 394, no. 6692, pp. 453–456, Jul. 1998.

[24] G. M. Luke *et al.*, "Time-reversal symmetry-breaking superconductivity in Sr_2RuO_4," *Nature*, vol. 394, no. 6693, pp. 558–561, Aug. 1998.

[25] J. Xia, Y. Maeno, P. Beyersdorf, M. Fejer, and A. Kapitulnik, "High Resolution Polar Kerr Effect Measurements of Sr_2RuO_4: Evidence for Broken Time-Reversal Symmetry in the Superconducting State," *Phys. Rev. Lett.*, vol. 97, no. 16, p. 167002, Oct. 2006.

[26] Y. Maeno *et al.*, "Two-Dimensional Fermi Liquid Behavior of the Superconductor Sr_2RuO_4," *J. Phys. Soc. Japan*, vol. 66, no. 5, pp. 1405–1408, May 1997.

[27] A. P. Mackenzie and Y. Maeno, "The superconductivity of Sr_2RuO_4 and the physics of spin-triplet pairing," *Rev. Mod. Phys.*, vol. 75, no. 2, pp. 657–712, May 2003.

[28] N. E. Hussey, A. P. Mackenzie, J. R. Cooper, Y. Maeno, S. Nishizaki, and T. Fujita, "Normal-state magnetoresistance of Sr_2RuO_4," *Phys. Rev. B*, vol. 57, no. 9, pp. 5505–5511, Mar. 1998.

[29] C. Bergemann, A. P. Mackenzie, S. R. Julian, D. Forsythe, and E. Ohmichi, "Quasi-two-dimensional Fermi liquid properties of the unconventional superconductor Sr_2RuO_4," *Adv. Phys.*, vol. 52, no. 7, pp. 639–725, Nov. 2003.

[30] C. Bergemann, S. Julian, A. Mackenzie, S. NishiZaki, and Y. Maeno, "Detailed Topography of the Fermi Surface of Sr_2RuO_4," *Phys. Rev. Lett.*, vol. 84, no. 12, pp. 2662–2665, Mar. 2000.

[31] A. P. Mackenzie, S.-I. Ikeda, Y. Maeno, T. Fujita, S. R. Julian, and G. G. Lonzarich, "The Fermi Surface Topography of Sr_2RuO_4," 1998.

[32] A. Damascelli *et al.*, "Fermi Surface, Surface States, and Surface Reconstruction in Sr_2RuO_4," *Phys. Rev. Lett.*, vol. 85, no. 24, pp. 5194–5197, Dec. 2000.

[33] K. M. Shen *et al.*, "Evolution of the Fermi Surface and Quasiparticle Renormalization through a van Hove Singularity in $Sr_{2-y}La_yRuO_4$," *Phys. Rev. Lett.*, vol. 99, no. 18, p. 187001, Oct. 2007.

[34] A. P. Mackenzie *et al.*, "Extremely Strong Dependence of Superconductivity on Disorder in Sr_2RuO_4," *Phys. Rev. Lett.*, vol. 80, no. 1, pp. 161–164, Jan. 1998.

[35] K. Ishida *et al.*, "Spin-triplet superconductivity in Sr_2RuO_4 identified by ^{17}O Knight shift," *Nature*, vol. 396, no. 6712, pp. 658–660, Dec. 1998.

[36] M. Tinkham, *Introduction to Superconductivity: Second Edition*. 2004.

[37] V. P. Mineev and K. V Samokhin, *Introduction to unconventional superconductivity*. 1999.

[38] S. NishiZaki, Y. Maeno, and Z. Mao, "Changes in the Superconducting State of Sr_2RuO_4 under Magnetic Fields Probed by Specific Heat," *J. Phys. Soc. Japan*, vol. 69, no. 2, pp. 572–578, Feb. 2000.

[39] T. Nomura and K. Yamada, "Detailed Investigation of Gap Structure and Specific Heat in the *p* -wave Superconductor Sr_2RuO_4," *J. Phys. Soc. Japan*, vol. 71, no. 2, pp. 404–407, Feb. 2002.

[40] T. Nomura, "Theory of Transport Properties in the *p*-Wave Superconducting State of Sr_2RuO_4 –A Microscopic Determination of the Gap Structure–," *J. Phys. Soc. Japan*, vol. 74, no. 6, pp. 1818–1829, Jun. 2005.

[41] A. Steppke *et al.*, "Strong peak in T_c of Sr_2RuO_4 under uniaxial pressure," *Science*, vol. 355, no. 6321, p. eaaf9398, Jan. 2017.

[42] Y. Maeno, S. Kittaka, T. Nomura, S. Yonezawa, and K. Ishida, "Evaluation of Spin-Triplet Superconductivity in Sr_2RuO_4," *J. Phys. Soc. Japan*, vol. 81, no. 1, p. 011009, Jan. 2012.

[43] D. A. Wollman, D. J. Van Harlingen, W. C. Lee, D. M. Ginsberg, and A. J. Leggett, "Experimental determination of the superconducting pairing state in YBCO from the phase coherence of YBCO-Pb dc SQUIDs," *Phys. Rev. Lett.*, vol. 71, no. 13, pp. 2134–2137, Sep. 1993.

[44] C. C. Tsuei *et al.*, "Pairing Symmetry and Flux Quantization in a Tricrystal Superconducting Ring of $YBa_2Cu_3O_{7-\delta}$," *Phys. Rev. Lett.*, vol. 73, no. 4, pp. 593–596, Jul. 1994.

[45] J. R. Kirtley, C. C. Tsuei, A. Ariando, C. J. M. Verwijs, S. Harkema, and H. Hilgenkamp, "Angle-resolved phase-sensitive determination of the in-plane gap symmetry in $YBa_2Cu_3O_{7-\delta}$," *Nat. Phys.*, vol. 2, no. 3, pp. 190–194, Feb. 2006.

[46] K. D. Nelson, Z. Q. Mao, Y. Maeno, and Y. Liu, "Odd-parity superconductivity in Sr_2RuO_4," *Science*, vol. 306, no. 5699, pp. 1151–4, Nov. 2004.

[47] I. Žutić and I. Mazin, "Phase-Sensitive Tests of the Pairing State Symmetry in Sr_2RuO_4," *Phys. Rev. Lett.*, vol. 95, no. 21, p. 217004, Nov. 2005.

[48] E. Hassinger *et al.*, "Vertical Line Nodes in the Superconducting Gap Structure of Sr_2RuO_4," *Phys. Rev. X*, vol. 7, no. 1, p. 011032, Mar. 2017.

[49] J. R. Kirtley *et al.*, "Upper limit on spontaneous supercurrents in Sr_2RuO_4," *Phys. Rev. B*,

vol. 76, no. 1, p. 014526, Jul. 2007.

[50] C. W. Hicks *et al.*, "Limits on superconductivity-related magnetization in Sr_2RuO_4 and $PrOs_4Sb_{12}$ from scanning SQUID microscopy," *Phys. Rev. B*, vol. 81, no. 21, p. 214501, Jun. 2010.

[51] P. J. Curran, S. J. Bending, W. M. Desoky, A. S. Gibbs, S. L. Lee, and A. P. Mackenzie, "Search for spontaneous edge currents and vortex imaging in Sr_2RuO_4 mesostructures," *Phys. Rev. B*, vol. 89, no. 14, p. 144504, Apr. 2014.

[52] P. J. Curran, V. V. Khotkevych, S. J. Bending, A. S. Gibbs, S. L. Lee, and A. P. Mackenzie, "Vortex imaging and vortex lattice transitions in superconducting Sr_2RuO_4 single crystals," *Phys. Rev. B*, vol. 84, no. 10, p. 104507, Sep. 2011.

[53] D. F. Agterberg, "Vortex Lattice Structures of Sr_2RuO_4," *Phys. Rev. Lett.*, vol. 80, no. 23, pp. 5184–5187, Jun. 1998.

[54] Z. Q. Mao, Y. Maeno, S. NishiZaki, T. Akima, and T. Ishiguro, "In-Plane Anisotropy of Upper Critical Field in Sr_2RuO_4," *Phys. Rev. Lett.*, vol. 84, no. 5, pp. 991–994, Jan. 2000.

[55] K. Deguchi, M. A. Tanatar, Z. Mao, T. Ishiguro, and Y. Maeno, "Superconducting Double Transition and the Upper Critical Field Limit of Sr_2RuO_4 in Parallel Magnetic Fields," *J. Phys. Soc. Japan*, vol. 71, no. 12, pp. 2839–2842, Dec. 2002.

[56] S. Yonezawa, T. Kajikawa, and Y. Maeno, "First-Order Superconducting Transition of Sr_2RuO_4," *Phys. Rev. Lett.*, vol. 110, no. 7, p. 077003, Feb. 2013.

[57] S. Yonezawa, T. Kajikawa, and Y. Maeno, "Specific-Heat Evidence of the First-Order Superconducting Transition in Sr_2RuO_4," *J. Phys. Soc. Japan*, vol. 83, no. 8, p. 083706, Aug. 2014.

[58] A. Ramires and M. Sigrist, "Identifying detrimental effects for multiorbital superconductivity: Application to Sr_2RuO_4," *Phys. Rev. B*, vol. 94, no. 10, p. 104501, Sep. 2016.

[59] M. Sigrist, R. Joynt, and T. M. Rice, "Behavior of anisotropic superconductors under uniaxial stress," *Phys. Rev. B*, vol. 36, no. 10, pp. 5186–5198, Oct. 1987.

[60] C. W. Hicks *et al.*, "Strong increase of T_c of Sr_2RuO_4 under both tensile and compressive strain.," *Science*, vol. 344, no. 6181, pp. 283–5, Apr. 2014.

[61] A. M. Clogston, "Upper Limit for the Critical Field in Hard Superconductors," *Phys. Rev. Lett.*, vol. 9, no. 6, pp. 266–267, Sep. 1962.

[62] A. P. Mackenzie, T. Scaffidi, C. W. Hicks, and Y. Maeno, "Even odder after twenty-three years: the superconducting order parameter puzzle of Sr_2RuO_4," *npj Quantum Mater.*, vol. 2, no. 1, p. 40, Dec. 2017.

[63] A. W. Rost, "Magnetothermal properties near quantum criticality in the itinerant metamagnet $Sr_3Ru_2O_7$," University of St Andrews, 2009.

[64] R. Bachmann *et al.*, "Heat Capacity Measurements on Small Samples at Low Temperatures," *Rev. Sci. Instrum.*, vol. 43, p. 205, 1972.

[65] P. F. Sullivan and G. Seidel, "Steady-State, ac-Temperature Calorimetry," *Phys. Rev.*, vol. 173, no. 3, pp. 679–685, Sep. 1968.

[66] I. Peroni, E. Gottardi, A. Peruzzi, G. Ponti, and G. Ventura, "Thermal conductivity of manganin below 1 K," *Nucl. Phys. B - Proc. Suppl.*, vol. 78, no. 1–3, pp. 573–575, Aug. 1999.

[67] J. R. Olson, "Thermal conductivity of some common cryostat materials between 0.05 and 2 K," *Cryogenics (Guildf).*, vol. 33, no. 7, pp. 729–731, Jul. 1993.

[68] C. Y. Ho, R. W. Powell, and P. E. Liley, "Thermal Conductivity of the Elements," *J. Phys. Chem. Ref. Data*, vol. 1, no. 2, pp. 279–421, Apr. 1972.

[69] M. A. Tanatar, M. Suzuki, S. Nagai, Z. Q. Mao, Y. Maeno, and T. Ishiguro, "Anisotropy of Magnetothermal Conductivity in Sr_2RuO_4," *Phys. Rev. Lett.*, vol. 86, no. 12, pp. 2649–2652, Mar. 2001.

[70] K. Deguchi, M. A. Tanatar, Z. Mao, T. Ishiguro, and Y. Maeno, "Superconducting Double Transition and the Upper Critical Field Limit of Sr_2RuO_4 in Parallel Magnetic Fields," *J. Phys. Soc. Japan*, vol. 71, no. 12, pp. 2839–2842, Dec. 2002.

[71] D. S. Jin, S. A. Carter, B. Ellman, T. F. Rosenbaum, and D. G. Hinks, "Uniaxial-stress anisotropy of the double superconducting transition in UPt_3," *Phys. Rev. Lett.*, vol. 68, no. 10, pp. 1597–1600, Mar. 1992.

[72] D. S. Jin, A. Husmann, and T. F. Rosenbaum, "Controlled Symmetry Breaking in Superconducting UPt_3," pp. 1775–1778, 1997.

[73] J.-H. Chu *et al.*, "In-Plane Resistivity Anisotropy in an Underdoped Iron Arsenide Superconductor," *Science*, vol. 329, no. 5993, pp. 824–6, Aug. 2010.

[74] C. F. Miclea, F. M. Grosche, J. Sichelschmidt, G. R. Stewart, G. Sparn, and F. Steglich, "Unconventional superconductivity in UBe_{13} probed by uniaxial stress," *Phys. B Condens. Matter*, vol. 312–313, pp. 97–99, Mar. 2002.

[75] P. H. P. Reinders, B. Wand, F. Steglich, G. Fraunberger, G. R. Stewart, and G. Adrian, "Specific-Heat Measurements on UBe_{13} under Uniaxial Pressure," *Europhys. Lett.*, vol. 25, no. 8, pp. 619–624, Mar. 1994.

[76] O. M. Dix, A. G. Swartz, R. J. Zieve, J. Cooley, T. R. Sayles, and M. B. Maple, "Anisotropic Dependence of Superconductivity on Uniaxial Pressure in $CeIrIn_5$," *Phys. Rev. Lett.*, vol. 102, no. 19, p. 197001, May 2009.

[77] M. Shayegan, K. Karrai, Y. P. Shkolnikov, K. Vakili, E. P. De Poortere, and S. Manus, "Low-temperature, *in situ* tunable, uniaxial stress measurements in semiconductors using a piezoelectric actuator," *Appl. Phys. Lett.*, vol. 83, no. 25, pp. 5235–5237, Dec. 2003.

[78] J.-H. Chu, H.-H. Kuo, J. G. Analytis, and I. R. Fisher, "Divergent nematic susceptibility in an iron arsenide superconductor.," *Science*, vol. 337, no. 6095, pp. 710–2, Aug. 2012.

[79] A. M. Simpson and W. Wolfs, "Thermal expansion and piezoelectric response of PZT Channel 5800 for use in low-temperature scanning tunneling microscope designs," *Rev. Sci. Instrum.*, vol. 58, no. 11, pp. 2193–2195, Nov. 1987.

[80] C. W. Hicks, M. E. Barber, S. D. Edkins, D. O. Brodsky, and A. P. Mackenzie, "Piezoelectric-based apparatus for strain tuning.," *Rev. Sci. Instrum.*, vol. 85, no. 6, p. 065003, Jun. 2014.

[81] J. Paglione *et al.*, "Elastic tensor of Sr_2RuO_4," *Phys. Rev. B*, vol. 65, no. 22, p. 220506, May 2002.

[82] M. E. Barber, *Uniaxial Stress Technique and Investigations of Correlated Electron Systems*. Springer, 2018.

[83] F. Pobell, *Matter and methods at low temperatures*. Springer, 2007.

[84] N. Pearlman and P. H. Keesom, "The Atomic Heat of Silicon below 100°K," *Phys. Rev.*, vol. 88, no. 2, pp. 398–405, Oct. 1952.

[85] "High Frequency Cryogenic Transformer." [Online]. Available: http://www.cmr-direct.com/en/product/download/get?download_id=35.

[86] K. Deguchi, Z. Q. Mao, and Y. Maeno, "Determination of the Superconducting Gap Structure in All Bands of the Spin-Triplet Superconductor Sr_2RuO_4," *J. Phys. Soc. Japan*, vol. 73, no. 5, pp. 1313–1321, May 2004.

[87] M. E. Barber, A. S. Gibbs, Y. Maeno, A. P. Mackenzie, and C. W. Hicks, "Resistivity in the Vicinity of a van Hove Singularity: Sr_2RuO_4 under Uniaxial Pressure," *Phys. Rev. Lett.*, vol. 120, no. 7, p. 076602, Feb. 2018.

[88] Y.-C. Liu, F.-C. Zhang, T. M. Rice, and Q.-H. Wang, "Theory of the evolution of superconductivity in Sr_2RuO_4 under anisotropic strain," *npj Quantum Mater.*, vol. 2, no. 1, p. 12, Dec. 2017.

[89] N. R. Werthamer, E. Helfand, and P. C. Hohenberg, "Temperature and Purity Dependence of the Superconducting Critical Field, H_{c2} . III. Electron Spin and Spin-Orbit Effects," *Phys. Rev.*, vol. 147, no. 1, pp. 295–302, Jul. 1966.

[90] D. G. Cahill, "Thermal conductivity measurement from 30 to 750 K: the 3ω method," *Rev. Sci. Instrum.*, vol. 61, no. 2, pp. 802–808, Feb. 1990.

[91] Y. Aoki *et al.*, "Time-Reversal Symmetry-Breaking Superconductivity in Heavy-Fermion $PrOs_4Sb_{12}$ Detected by Muon-Spin Relaxation," *Phys. Rev. Lett.*, vol. 91, no. 6, p. 067003, Aug. 2003.